Thin organic coatings for hot dip galvanised steel and cold rolled products.

Glover, Carol

Thin Organic Coatings for Hot Dip Galvanised Steel and Cold Rolled Products.

Carol Glover

Submitted to the University of Swansea in fulfilment of the requirements for the Degree of Doctor of Engineering

ProQuest LLC.
789 East Eisenhower Parkway
P.O. Box 1346
Ann Arbor, MI 48106 – 1346

DECLARATION

This work has not previously been accepted in substance for any degree and is not being concurrently submitted in candidature for any degree.

Signed ... . (candidate)

Date .....25/04/2014.....

STATEMENT 1

This thesis is the result of my own investigations, except where otherwise stated. Where correction services have been used, the extent and nature of the correction is clearly marked in a footnote(s).

Other sources are acknowledged by footnotes giving explicit references. A bibliography is appended.

Signed .. .. (candidate)

Date .....25/04/2014.....

I hereby give consent for my thesis, if accepted, to be available for photocopying and for inter-library loans **after expiry of a bar on access approved by the Swansea University.**

Signed .. .. (candidate)

Date .....25/04/2014.....

Acknowledgements

Firstly, I would like to thank Dr Geraint Williams and Neil Craik for their supervision and support throughout the project, it would not have been possible without them.

Thanks to EPSRC and TATA Steel UK for sponsoring the project.

Thanks also to Professor Dave Worsley for giving me the opportunity to make the transition to Materials Engineering and complete the EngD, it has been a wonderful experience.

Also to those who have provided academic support and inspiration over the years, especially Zak Barratt, Andrew Robinson, Trystan Watson, Jon Elvins and Neil McMurray.

Contents

Chapter 1

Introduction

1.1 Thesis aims and objectives

The research themes in the current thesis stem from collaboration with an industrial project in which thin organic coatings (TOCs) were being developed for application as primer coatings for cold rolled (CR) and hot dip galvanised (HDG) steels. As current legislation requires the replacement of chromate, a known carcinogen, with environmentally friendly alternatives there is a need to develop inhibitors that may provide corrosion protection to an equally high standard. Electrochemical techniques have been employed to assess inhibitors in both immersion situations and in-coating with the presence of a penetrative electrolyte.

Chapter 3 A study using the SKP technique where the effect of in-coating phenyl phosphonic acid (H_2PP) for the prevention of corrosion-driven underfilm delamination on HDG substrates is studied. Experiments are carried out in the presence of large defects and the possibility of inhibitor leaching is explored.

Chapter 4 Results are presented from an extensive study using the Scanning vibrating electrode technique (SVET), backed up by open circuit potential (OCP) measurements to, firstly, determine the corrosion activity on HDG when fully immersed in electrolyte in the full range of pH. These results are then used as a baseline to compare the effectiveness of H_2PP and sodium phosphate inhibitors when added to the electrolyte.

Chapter 5 A further study on the inhibitor H_2PP is carried out on iron substrates. Both cathodic and anodic delamination process are studied. Results obtained using the Scanning Kelvin probe (SKP) are presented where the effect on cathodic delamination of in-coating additions of the H_2PP inhibitor made to a polyvinylbutyral (PVB) model primer coating is studied. This is done in two ways, the first being in the presence of a large defect and the second a realistic scribed defect experiment. Subsequent SVET experiments are presented where the influence of H_2PP on the corrosion of bare iron fully immersed in electrolyte containing the inhibitor is assessed. Finally, the effect of in-coating H_2PP additions on the anodic delamination process filiform corrosion is studied.

Chapter 6 Firstly, an alternative study utilises the SKP, which features profoundly in this thesis, to assess the interaction of PEDOT:PSS films with a range of metal surfaces. Secondly, an assessment of the effectiveness of PEDOT on preventing underfilm

delamination on both HDG and iron substrates is presented. On iron both cathodic and anodic FFC delamination are studied.

Chapter 7 An exploration of the use of time-lapse photography as an alternative, or complementary, technique for assessing the corrosion prevention of thin organic coatings (TOCs) under development. The aim is to provide a technique that achieves accurate results with a fast throughput when compared with industry standard humidity tests. A range of coated products is tested, from laboratory to the pilot-line phase, to fully explore the validity of the technique.

1.2 General corrosion theory

Most metals naturally exist as an ore. This is a state where the metal is chemically bound with another compound, typically an oxide, a sulphide or a carbonate. The extraction of a pure metal requires an input of energy. For example, iron can be extracted from its ore, hematite (Fe_2O_3), by heating with a reducing agent in the blast furnace at a temperature of 1600°C. The resulting pure metal has an increased energy state when compared to the original ore resulting in a thermodynamic drive to return to the original, lower energy state. A pure metal is unstable in air and a return to the lower energy state is facilitated by reactions with components found in the environment.

1.2.1 Electrochemistry of corrosion

Corrosion is the unwanted transformation of a metal back to its natural, lower energy state. When corrosion occurs, a wet corrosion cell is established consisting of four critical components: an anodic reaction site, a cathodic reaction site, an electrolyte and an electrical connection. The natural environment provides salt solution electrolytes in the form of seawater or rain. The conducting solutions reduce the activation energy $*\Delta G$ pathway between the pure metal and its corrosion products thus allowing the onset of corrosion.

The aforementioned electrical connection of a corrosion cell can be in the form two separate surfaces with an external circuit or two dissimilar metals joined together. However, it is typical that anodic and cathodic reaction sites will initiate on the same metal surface where this is sufficient to act as an electrical connection. It is noted that anodic and cathodic sites may be seen to be spatially inseparable on the corroding surface. Where the anode and cathode surfaces are small, very numerous and change places at short intervals of time, this is described as 'general' corrosion. Where anodic and cathodic sites are spatially distinct, the corrosion is described as 'localised'. As anodic activity is focused in small, discrete areas, this type of corrosion is particularly damaging.

The anodic reaction is:

$$m_{(s)} \rightleftharpoons m^{n+}{}_{(aq)} + ne^- \qquad (1.1)$$

where the anodic oxidation of the metal surface results in the production of metal ions and a release of electrons. The metal ions produced in the anodic reaction can react with other species to form the build-up of an insoluble residue that adheres to the metal surface. This blocks electrolyte contact with the metal surface and results in the retardation of the corrosion rate.

The anodic reaction occurs simultaneously with the cathodic reaction. Electrons released in the anodic reaction are transported through the metal surface and consumed at the cathodic reaction site. There are several possible cathodic reactions that can take place during the corrosion of a metal. In aerobic conditions at alkaline or near neutral solutions the cathodic reaction is the reduction of dissolved oxygen:

$$2H_2O_{(aq)} + O_{2(g)} + 4e^- \rightleftharpoons 4OH^-_{(aq)} \qquad E^\theta = +1.23 \text{ V (vs. SHE)[1]} \qquad (1.2)$$

However, at sufficiently low pH, cathodic reactions may occur as follows:

$$O_{2(g)} + 4H^+_{(aq)} + 4e^- \rightarrow \rightleftharpoons 2H_2O_{(aq)} \qquad E^\theta = +1.23 \text{ V (vs. SHE)[1]} \qquad (1.3)$$

In acidic conditions Hydrogen evolution may occur:

$$2H^+_{(aq)} + 2e^- \rightleftharpoons H_{2(g)} \qquad E^\theta = +0.00 \text{ V (vs. SHE)[1]} \qquad (1.4)$$

The reduction of metal ions:

$$Fe^{3+}_{(aq)} + e^- \rightleftharpoons Fe^{2+}_{(aq)} \qquad E^\theta = -0.44 \text{ V (vs. SHE)[1]} \qquad (1.5)$$

The deposition of metal:

$$Cu^{2+}_{(aq)} + 2e^- \rightleftharpoons Cu_{(s)} \qquad E^\theta = -0.34 \text{ V (vs. SHE)[1]} \qquad (1.6)$$

Fig 1.1 shows a schematic of a typical wet corrosion cell depicting a corroding metal surface under a droplet of water. This illustrates the connection between anode and cathode by the ionic current flux in the water droplet electrolyte and the flow of electrons through the metal surface. The locations of anodic and cathodic sites, in this example, are established due to local differences in the concentration of oxygen. The region in the centre of the droplet acts solely as an anode as low oxygen diffusion through the long pathway from the edge of the droplet means replenishment is not sufficient to sustain a cathodic region. The cathodic region circles the outskirts of the

droplet and, as the anodic region spreads radially outwards from the centre, a ring of corrosion product is formed. Other ways in which cathodic and anodic regions become established are due to local differences in the composition of the metal surface, local differences in pH and local differences in the permeability of a passive layer such as a surface oxide.

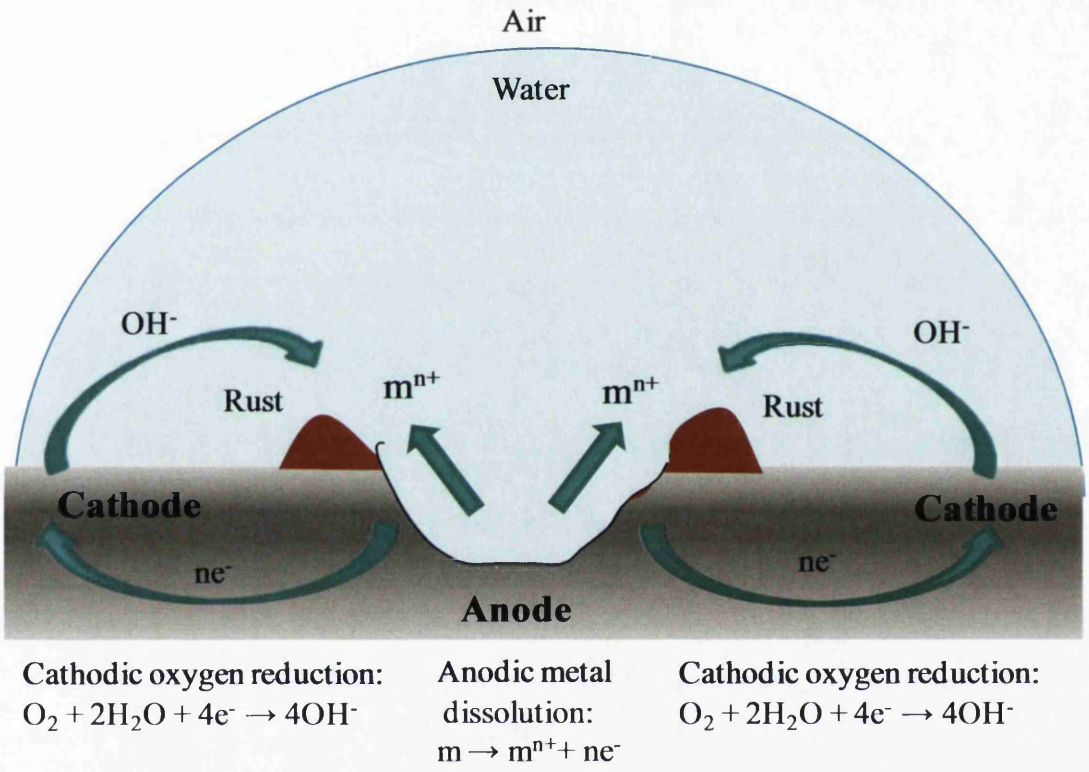

Fig1.1 Schematic diagram of a typical aqueous corrosion cell.

1.2.2 Kinetics of corrosion

A 'polyelectrode' occurs where both anodic and cathodic activity occurs on a single metallic surface where more than two couples, that are not in mutual thermodynamic equilibrium, act simultaneously at a single electrode surface [2]–[4]. It is stated in Wagner and Trauds' additivity principle that the total current flowing into an external circuit is the sum of the currents due to individual couples present on the corroding surface [5]. Therefore, where free corrosion takes place:

$$\Sigma i_{anodic} = -\Sigma i_{cathodic} = i_{corr} \qquad (1.7)$$

where i_{anodic} is the partial current density due to any anodic process, $i_{cathodic}$ is the partial current density due any cathodic process and i_{corr} is the rate of corrosion expressed in

current terms. Due to the potential dependence of electrochemical current, any given corroding metal will adopt a unique potential termed the 'free corrosion potential', E_{corr}.

Tafel defined the mathematical relationship between current density, i, and potential, E, stating [6]:

$$i_{anodic} \propto \exp(E) \tag{1.8}$$

and

$$i_{cathodic} \propto \exp(-E) \tag{1.9}$$

A Tafel plot is a graph of E against lg (current density) and may be plotted for each electrode process to give a straight line. Fig 1.2 shows a combination of Tafel plots where individual electrode processes have generated a mixed potential. This plot is known as an Evans diagram which represents a simple corrosion process for a metal in contact with an aerated electrolyte. As ions enter solution, due to the corroding of the metal at the anodic site, an excess of electrons flows to the cathodic site. Upon the advancement of corrosion the anodic region becomes less negative and results in the upward shift of potential by the amount η_a, anodic polarisation. The opposite effect is the cathodic polarisation η_c, where the cathodic reagion becomes more negative and its potential is shifted down by this amount. The Evans diagram in Fig 1.3 depicts the described positive and negative shifts in respective anodic and cathodic polarisation. The intersection of the depicted Tafel slopes shows the point at which anodic and cathodic current densities are equal; that is, their sum is zero. The free corrosion current density, i_{corr}, as stated in equation 1.7, is defined by this point. Further to this, the free corrosion potential, E_{corr}, for the system may also be obtained from the Evans diagram.

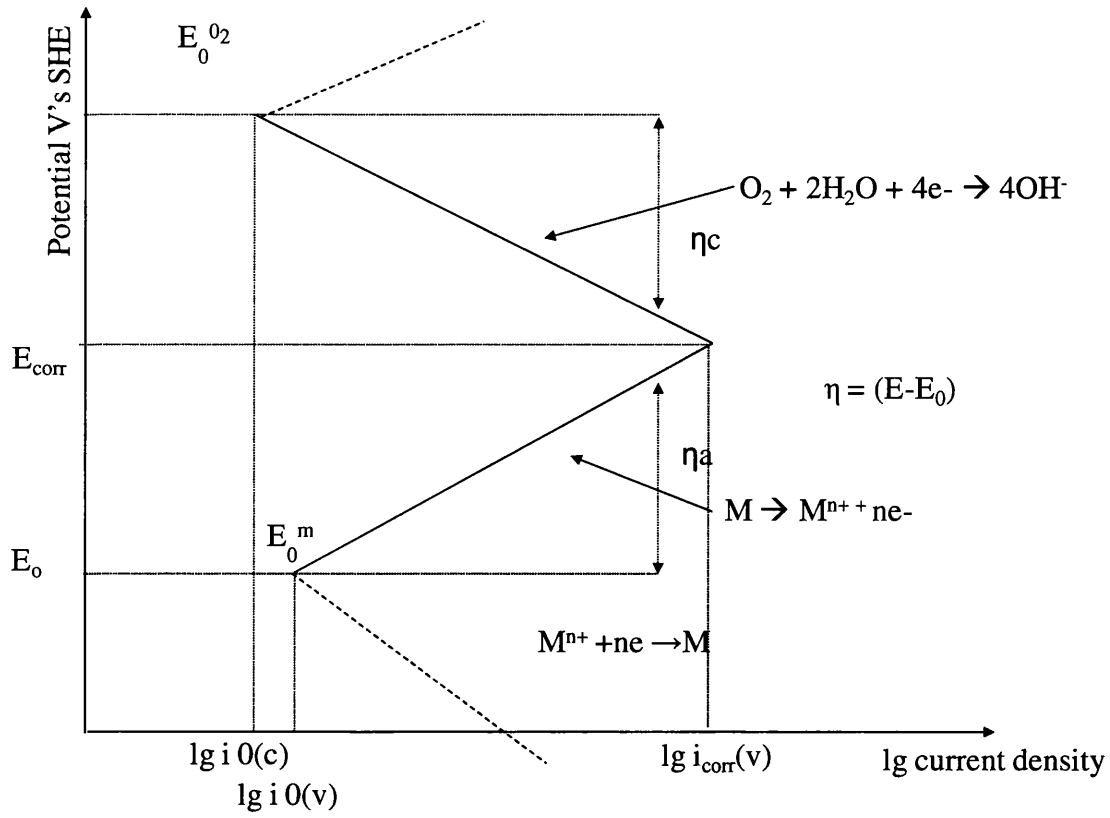

Fig.1.2 Evans diagram for a metal immersed in an aerated electrolyte.

1.2.3 Pourbaix diagrams

A great influence of electrochemical studies was Marcel Pourbaix who introduced the 'Pourbaix Diagram' where the affect of pH and potential on the stability of different species is mapped. An arbitrary division is made between a corroding and non-corroding state whereby when a concentration of a metal's ions is $\geq 10^{-6}$M in solution the metal is said to be undergoing corrosion. Where the concentration of ions is less than this value, the metal is said to be in an immune phase. It was shown in equation (1.1) that soluble metal ions pass into solution in a metal dissolution corrosion reaction; however, this is not representative of all corrosion reactions. Many corrosion products are insoluble and lead to the formation of a film that blocks the corroding surface from the electrolyte. Where this occurs the metal surface is described as 'passive' due to the substantial reduction of corrosion rate. The Pourbaix diagrams show the reaction condition of a metal, under varying conditions of pH and potential where several reactions, dependent on electrolyte pH, may occur at once.

Figs 1.3 and 1.4 show simplified Pourbaix diagrams for iron and zinc in water respectively. It can be observed that, for both metals, the corrosive state occurs under conditions of neutral pH and no impressed potential. It can also be seen that a variation of electrolyte pH or potential suppression can alter the state of the metals to regions of passivity or immunity.

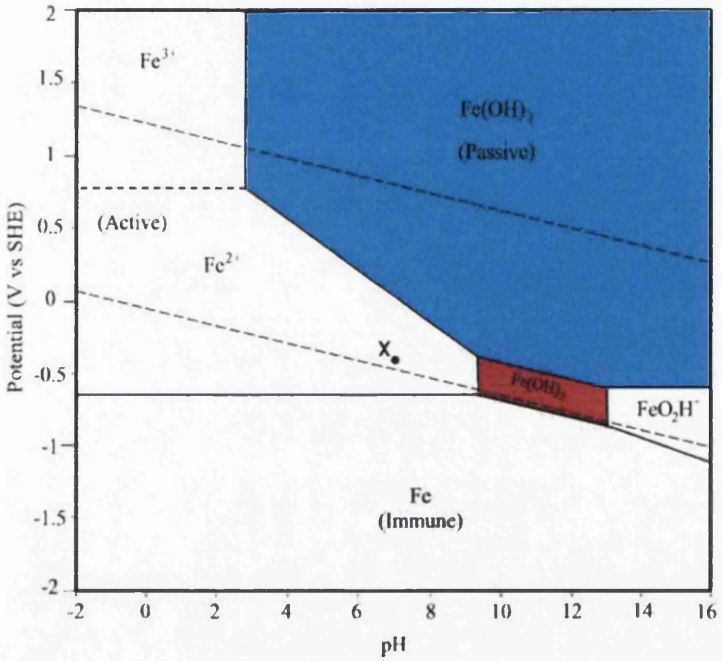

Fig 1.3 Simplified Pourbaix diagram for Iron in water.

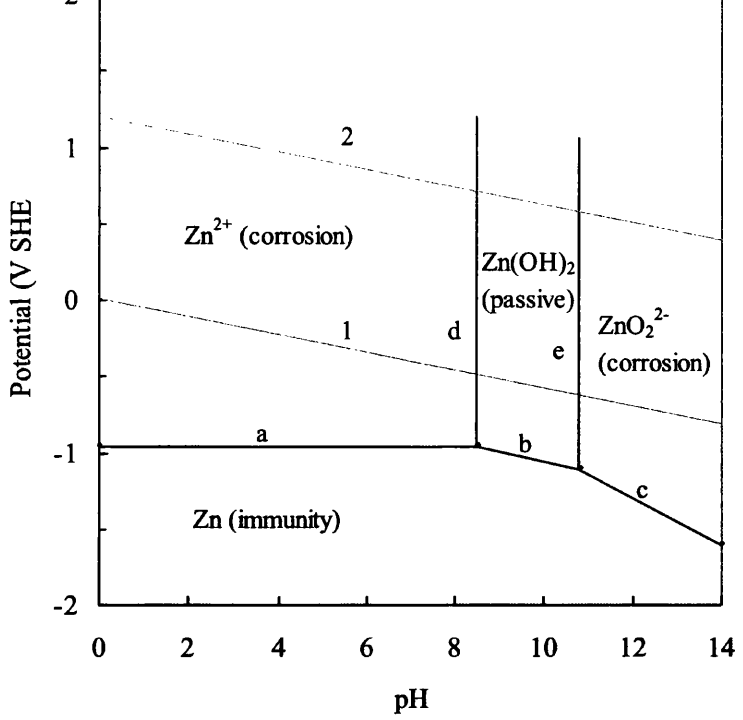

Fig1.4 Pourbaix diagram for zinc in water where (1) shows the reduction of hydrogen producing hydrogen gas and (2) shows the oxidation of water liberating oxygen. The area between (1) and (2) represents the conditions where water is stable.

1.2.4 Redox Potentials and Corrosion Potentials

Where a metal is immersed in aqueous solution containing ions of the same metal a dynamic equilibrium will be reached whereby both oxidised and reduced states of a system are present in the solution. Due to an abundance of metal cations present in solution in close proximity to the metal surface, and a negative charging of the metal due to the remaining electrons, a so-called electrochemical double layer persists. The layer means that the metal will have a different potential to the solution known as the Galvani Potential (Φ). The difference in Galvani potential between metal and solution is known as the electrode potential (E). A relationship exists between the electrode potential and the effective metal ion concentration in the solution i.e. activity of the metal ion. It is represented by the Nernst equation,

$$E = E^{\circ} - \frac{RT}{zF} \ln \frac{[\text{products}]}{[\text{reactants}]} \qquad (1.10)$$

where E is the non-equilibrium potential generated by the reaction, [reactants] and [products] are the molar concentrations of the oxidant and reductant respectively. R is

the gas constant (8.31 J mol^{-1} K^{-1}), T is temperature (Kelvin), z the number of electrons involved in the redox reaction and F is Faraday's constant (96494 C mol^{-1}).

Using Equation 1.10 the standard electrode potential of all metals can be calculated and used to generate a table of standard reduction potentials, as shown in Table 1.1. Where two metals are coupled the metal with the more positive standard electrode potential (i.e. positioned higher up in the table), is more likely to be reduced. The metal with the more negative electrode potential is more likely to be oxidised.

Table 1.1 Standard reduction potentials for some common metals [1]

Metal	Half-reaction	E^o / V vs SHE
Pt	$Pt^{2+}_{(aq)}+2e^- \rightarrow Pt_{(s)}$	+1.20
Ag	$Ag^{+}_{(aq)}+e^- \rightarrow Ag_{(s)}$	+0.80
Fe	$Fe^{3+}_{(aq)}+e^- \rightarrow Fe^{2+}_{(aq)}$	+0.77
Cu	$Cu^{2+}_{(aq)}+2e^- \rightarrow Cu_{(s)}$	+0.34
Ni	$Ni^{2+}_{(aq)}+2e^- \rightarrow Ni_{(s)}$	-0.26
Fe	$Fe^{2+}_{(aq)}+2e^- \rightarrow Fe_{(s)}$	-0.44
Zn	$Zn^{2+}_{(aq)}+2e^- \rightarrow Zn_{(s)}$	-0.76
Al	$Al^{3+}_{(aq)}+3e^- \rightarrow Al_{(aq)}$	-1.68
Mg	$Mg^{2+}_{(aq)}+2e^- \rightarrow Mg_{(s)}$	-2.38

1.2.5 Localised Corrosion

The major types of localised corrosion, relevant to the current study, that affect zinc coated and cold rolled steels are discussed in this section.

1.2.5.1 Corrosion of dissimilar metals

Where two different metals are coupled in the presence of an electrolyte a wet corrosion cell results. As described in Section 1.1, a corroding metal adopts a unique free corrosion potential E_{corr} in a given electrolyte. This allows for the classification of metals in an electrochemical series where the value of E_{corr} for each material is listed in order of relative reactivity or nobility as given in Table 1.1 in Section 1.2.4. The higher the free corrosion potential value the more noble the metal. Therefore, where two different metals are coupled in the presence of electrolyte the more reactive metal, i.e.

the metal with the lower E_{corr}, will become the anode and corrode. This is in preference to the more noble metal with the higher E_{corr} that becomes the cathode. A greater difference in potential between the two materials results in a faster anodic corrosion rate. This forms the basis of steel protection by coating with zinc, which is more reactive.

1.2.5.2 Differential aeration

Differential aeration corrosion results from any differences in oxygen concentration on the metallic surface as the cathodic reaction is the reduction of oxygen. An area of metal surface abundant in oxygen will become the cathodic region and an area depleted of oxygen will act as the anode in the cell. Such differences in oxygen concentration are typical in narrow crevices regions such as under a partially delaminated paint film or in a crack within the metal bulk. Due to the low solubility of O_2 in water, its diffusion to such depths is limited and so crevices are susceptible to anodic metal dissolution where the corresponding cathodic activity will typically become concentrated at the crevice opening or on an exposed surface. As in pitting corrosion, a lowering of pH and increase of anion concentration, such as Cl^-, may occur within the crevice thus increasing the rate of metal dissolution. Fig 1.5 shows the schematic of a corrosion cell where differential aeration drives the corrosion beneath the water droplet.

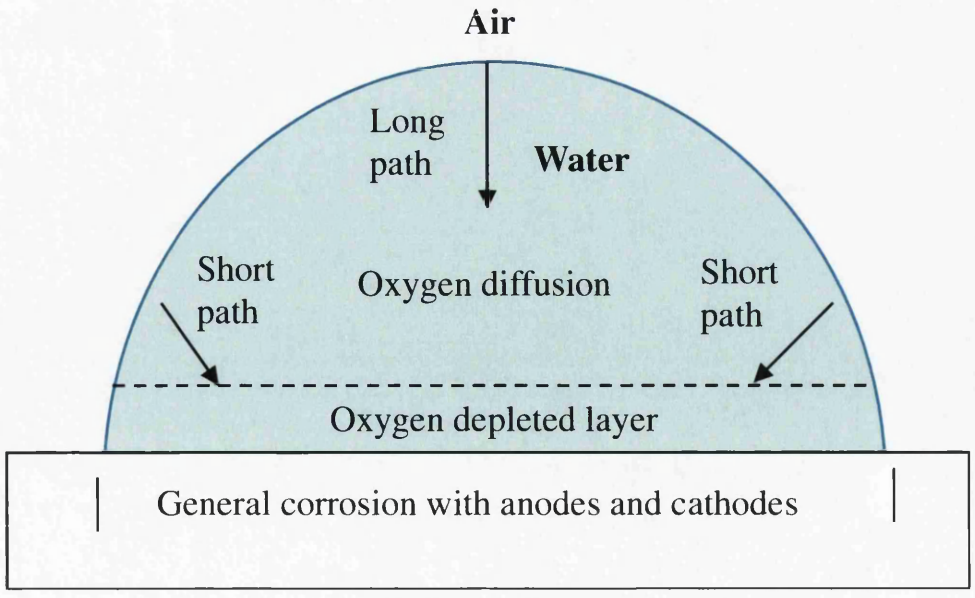

Fig.1.5 Scematic diagram showing differential aeration under a drop of water

1.3 Coatings for protection against corrosion

1.3.1 Sacrificial coating protection

Sacrificial coating protection constitutes the application of a more reactive metal to the metallic substrate in need of protection. The more reactive metal will corrode preferentially to sacrificially protect the underlying substrate; this principal was described in section 1.2.5.1 where the corrosion of dissimilar metals was discussed. Due to the steeper cathodic polarisation curve of the reactive metal coating, in comparison to the lesser reactive metal substrate, an increase in the cathodic overpotential of the surface occurs and the corrosion potential becomes more negative than the substrate [7].

Zinc is the sacrificial coating material most widely used in industry along with various coatings based on this metal. The respective free corrosion potentials of zinc and iron in seawater are -1.05 V vs SCE and -0.65 V vs SCE. According to the theory described in section 1.2.5.1 it can be stated that zinc, being more reactive, will corrode more readily than iron upon exposure to an electrolyte. In the event that a zinc coated steel sample containing a penetrating defect comes into contact with corrosive media, the zinc would corrode preferentially by becoming the anode and the underlying steel would become the cathode. Thus, metal dissolution would only occur on the zinc coating leaving the steel sacrificially protected. Further to this zinc ions readily react with hydroxide ions found in electrolyte. This produces insoluble zinc hydroxide that tends to form a layer at the defect thus blocking the steel cathode and reducing the corrosion rate.

The Evans diagram shown in fig 1.6 summarises the affect of connecting the two metals. It can be observed that the corrosion rate of the zinc coated steel ($I_{corr\ Zn\ coating}$) is lower than that of uncoated steel ($I_{corr\ uncoated\ Fe}$). This is because the cathodic overpotential of the surface is increased by the zinc coating and the exchange current density of dissolved oxygen on zinc ($I_{0c\ Zn}$) is lower than that on iron ($I_{0c\ Fe}$). Where a scratch is present and the iron is exposed to a corrosive environment the electrode potential of the exposed iron will be equal to the corrosion potential of the zinc ($E_{corr\ Zn}$). This is due to the cathodic polarisation of the surrounding zinc. The corrosion rate of the exposed iron will, therefore, be reduced substantially $I_{corr\ exposed\ Fe}$ when compared

with uncoated iron $I_{corr\ uncoated\ Fe}$. It can be concluded that zinc coatings are of extreme importance with regards to corrosion prevention as they can considerably extend the lifetime of steel products.

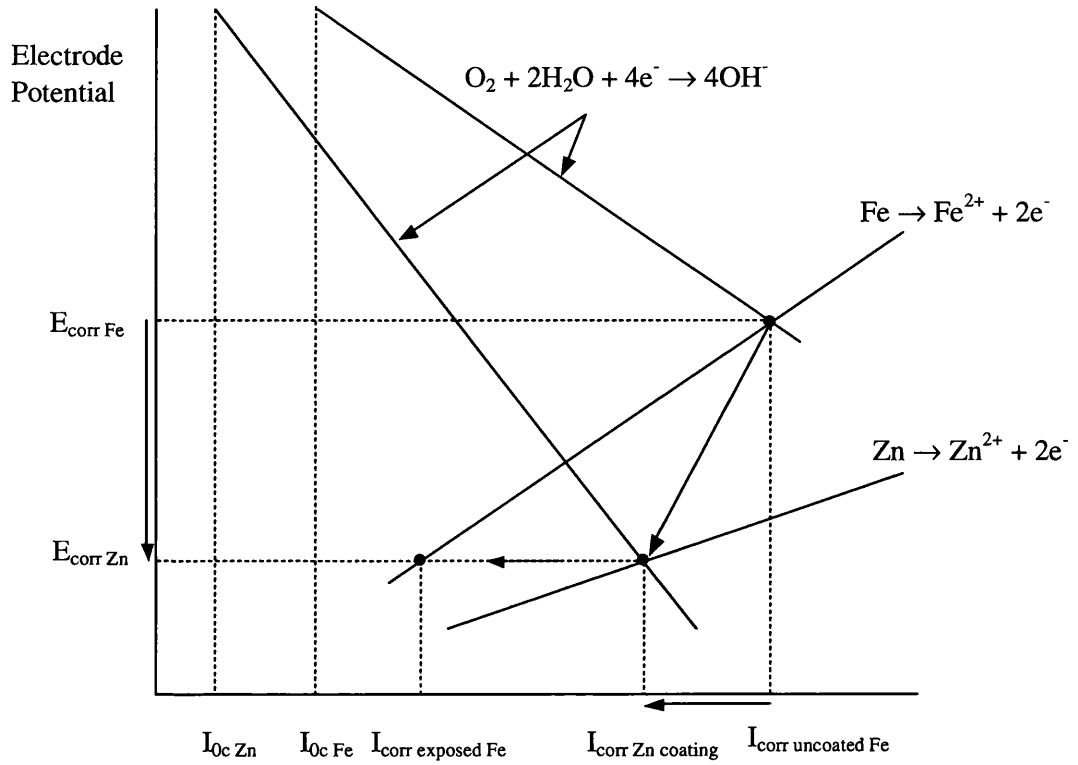

Fig 1.6 Evans diagram for zinc coated steel where a small scratch exposes a small quantity of steel showing sacrificial protection. The zinc coating provides cathodic control protection by cathodically polarising the exposed iron reducing the corrosion current of the steel, $I_{corr\ exposed\ Fe}$ [7].

1.3.2 Barrier coatings

Barrier coatings are the most basic form of corrosion protection and simply act, as the name suggests, as a barrier to air (i.e. oxygen) and electrolyte. Typical organic barrier coatings are paints, plastic laminates and enamels. These coatings can only protect against corrosion if they remain undamaged. Without any form of protection the underlying metal can become severely corroded if a penetrating defect results in exposure to a corrosive environment. Corrosion in this instance can be particularly severe as the presence of a partially delaminated film can be likened to a crevice and result in pitting corrosion.

1.3.3 The traditional coating system

A typical coating system for cold rolled (CR) steel can be observed in cross-sectional diagram shown in fig. 1.7. A typical system consists of a pre-treatment, a primer layer, where inhibitor pigment is typically added, and a top coat that provides a barrier protection and good aesthetics to the final product.

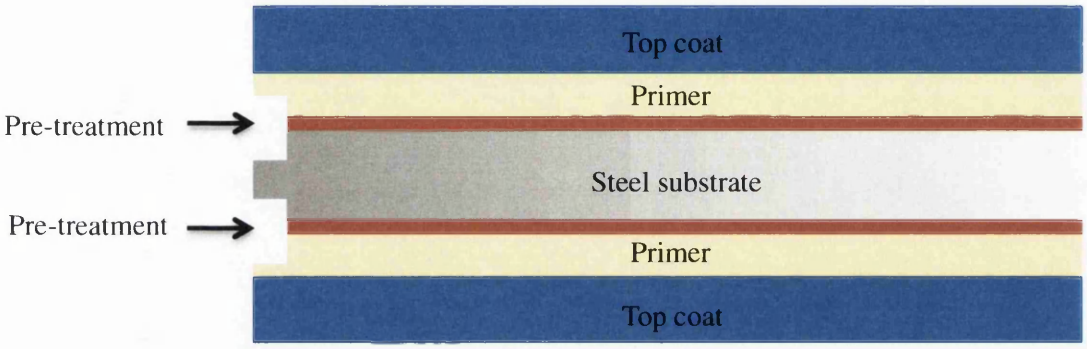

Fig 1.7 A cross section of a traditional coating system

1.3.4 Thin organic coatings (TOCs)

Thin organic coatings (TOC) have become an area of interest in the steel industry as they present an opportunity to reduce both the cost and the environmental impact of the finishing process. Although TOCs are generally used as temporary protection, there is potential for the replacement of the pre-treatment and primer layers (shown in fig 1.9) with a single TOC that is <1 μm in thickness. Furthermore, coating oils, such as those used on cold reduced steels for some markets, would no longer need to be applied. A schematic showing the stations found on a typical coating line is shown in fig 1.10. The major advantage of converting to the use of TOCs is the relief of several coating line stations such as degreasing and those involving the pre-treatment and primer application stages. Removal of these stages reduces the use of materials, electricity and man power as well as a reduction of waste. These factors also present an opportunity to lower product prices. The use of TOCs presents an opportunity to increase through-put as finishing time will decrease with a reduction in stages. A reduction in environmental impact can help to encourage a positive company reputation. In order for such a replacement to be viable a TOC must fulfill the following criteria:

1. Good adhesion to the substrate
2. Good adhesion to the top coat (i.e. good post paintability)
3. Offer corrosion resistance (i.e. contain inhibitor pigment)
4. Exhibit optimal lubricity for ease of application
5. Cost effective

The development of TOCs is discussed in Chapter 7 where an alternative to industry standard corrosion testing techniques is assessed.

1.3.5 Traditional in-coating inhibitors for protection against corrosion

To add further protection to metallic substrates, inhibitor pigments are added to barrier coatings. Such substances provide inhibition when in contact with aqueous solution and can prevent either the anodic or cathodic reaction leading to a retardation of the corrosion process. Typically, corrosion inhibitors are added to the primer layer which is applied directly to the bare, or pre-treated, metal substrate. The two types of inhibition mechanism, anodic and cathodic, will be discussed here. The traditional inhibitors chromate and phosphate will also be discussed. Section 1.7 expands on corrosion inhibition with particular focus on in-coating inhibitors for underfilm delamination.

1.3.6 Anodic Inhibitors

Two types of anodic inhibitor exist; the first of these are anodic precipitation inhibitors that form insoluble salts with the metal cations that are generated by the anodic reaction. A protective barrier film is formed by the insoluble salts that blocks mass transport to the underlying anode thus limiting further corrosion. Chromates and phosphates are examples of anodic precipitation inhibitors [8-9].

The second type is the anodic oxidising inhibitor (also termed cathodic depolarisers); these work by the removal of electrons from the electrochemical cell by providing an alternative cathodic reaction to oxygen reduction. This causes a shift in free corrosion potential where the substrate is polarised to the metal's passive region whereby the formation of a stable and insoluble oxide or hydroxide layer protects the metal substrate from further corrosion activity.

It is highly important that anodic inhibitors are present in sufficient quantity as, where a whole anodic region is not fully blocked; it results in a situation where a small anode is

coupled with a large cathode. This can lead to highly detrimental results as the anodic metal dissolution will be accelerated [10].

1.3.7 Cathodic Inhibitors

Cathodic inhibitors work by the precipitation of an insoluble salt film formed by a reaction between cations, from the inhibitor, and the hydroxide ions generated by the cathodic oxygen reduction reaction in the electrochemical corrosion cell. The resultant insoluble film blocks the cathodic reaction site. The main inhibitors of this type are rare earth metals [11].

1.3.7.1 Chromate

Chromate is the traditional inhibiting pigment used for the protection of steel against corrosion. However, despite its superior corrosion protection, the toxicity of chromate (which is described in Section 1.3.8) means that the search for a competitive alternative is of high importance industrially. The inhibitory mechanism achieved by chromate-based conversion coatings is attributed to the replacement of the cathodic reaction with the reduction of Cr(VI) to a solid Cr(III) oxide r at the cathode. The reaction is as follows:

$$2CrO^{2-}_4 + 5H_2O + 6e^- \rightleftharpoons Cr_2O_3(s) + 10OH^- \qquad (1.10)$$

On iron, this reduction reaction occurs at oxidation sites where the anodic dissolution of iron occurs. This is represented by:

$$Fe \rightleftharpoons Fe^{2+} + 2e^- \qquad (1.11)$$

On iron substrates chromium oxides (i.e. Cr_2O_3) have been shown to be thermodynamically stable above pH 5. However, it has been reported that the oxidizing power of Cr(VI) ions result in the enhancement of corrosion in acidic solutions [12]. The term 'zinc yellow' describes a classic chromate pigment that consists of a mixed salt of zinc chromate, potassium chromate and zinc hydroxide. The hydroxyl ion from the zinc hydroxide reinforces the mode of action of the chromate by raising the pH and, therefore, enhancing the stability of Cr(III) salts. Further to this, a precipitation of $Zn(OH)_2$ at cathodic sites occurs creating a protective layer enhancing the inhibitory effect.

Bastos et al measured the open circuit potential (OCP) of iron, over time, immersed in an experimental electrolyte where chromate additions had been made [13]. A potential much higher than that of the control sample was observed immediately upon immersion. This indicates the rapid formation of a passivating chromate layer.

The inhibitory effects of chromate will be considered further in Section 1.5.1 where its effect on preventing underfilm coating delamination will be discussed.

1.3.7.2 Phosphate

A close competitor to chromate is zinc phosphate that is used in both conversion-coating formulations and as anti-corrosion pigments for paints. Phosphate coatings are typically applied by immersion where a series of tanks are used to carry out the degreasing, phosphating and all subsequent rinsing stages. Phosphating treatments are suitable for both cold rolled steel and HDG steel, amongst others [14]. Dilute phosphoric acid solutions of iron, manganese and zinc primary phosphates form the bases of any conventional phosphate coating process. The following equation shows the reaction that occurs at local anodes on the iron surface between the iron itself and free phosphoric acid in solution:

$$Fe + 2H_3PO_4 \rightleftharpoons Fe(H_2PO_4)_2 + H_2 \qquad (1.12)$$

The products of this reaction are soluble primary ferrous phosphate and the evolution of hydrogen gas. This results in a local depletion of phosphoric acid at the metal/solution interface. However, the dissociation of the primary metal phosphates in solution result in the following reactions:

$$Me(H_2PO_4)_2 \rightleftharpoons MeHPO_4 + H_3PO_4 \qquad (1.13)$$

$$3MeHPO_4 \rightleftharpoons Me_3(PO_4)_2 + H_3PO_4 \qquad (1.14)$$

$$3Me(H_2PO_4)_2^- \rightleftharpoons Me_3(PO_4)_3 + 4H_3PO_4 \qquad (1.15)$$

Reaction (1.12) causes the neutralization of free phosphoric acid thus pushing the position of equilibrium in Reactions (1.13), (1.14) and (1.15) towards the right. This leads to the deposition of sparingly soluble secondary phosphates and insoluble tertiary phosphates that form cathodic blocking layers.

Phosphate pigments are considered to be more affecting at low pH due to the increased solubility of zinc in acidic media [15]. Bastos et al showed the effective corrosion inhibition of phosphate inhibitors on both zinc and iron surfaces but, in comparison to the instantaneous action of chromate, total protection of either surface took several hours to achieve. In both cases the measured open circuit potential, where zinc phosphate was added to an experimental electrolyte, was relatively similar to that of the uninhibited case. This is in contrast to chromate additions where the OCP was substantially increased as described in the previous section. As the current leading alternative to chromate, sodium phosphate inhibitor will be the basis for comparison in the studies presented within the current work [13,16] .

1.3.8 The hazards of chromium compounds

Hexavalent chromium is known to be extremely detrimental to living systems causing problems such as kidney and liver damage and, most notably, the direct damage of DNA [17-18]. Katz et al state that the oxidation state is the critical factor upon assessment of chromium compound activities. Compounds of hexavalent chromium are generally more toxic than trivalent chromium; the latter being the most stable and abundant of the oxidation states (+2, +3, +4, +5 and +6) [19]. The notion that hexavalent chromium is the most hazardous is attributed to high membrane transport and strong oxidising power. Where testing has been carried out on animals hexavalent chromium has been shown to cause tissue damage, irritative lesions of both skin and the respiratory tract and the formation of tumours at the site where injection of the compound is administrated.

Conversely, Katz states that trivalent chromium compounds in both soluble and insoluble form, are not usually active carcinogens. Shumilla et al suggests that although Cr(III) is not considered harmful as it does not have the ability to enter cells as readily as Cr(VI). However, upon contact with a cell, an insoluble form of Cr(VI) will readily enter and be subsequently reduced to Cr(III) and, in this way, the compound has found to be damaging to DNA. It is suggested that Cr(VI) acts as a "Trojan Horse" for the damaging Cr(III) [17-18].

1.4 Underfilm corrosion phenomena

As described in Section 1.3, organic coatings are primarily used to accommodate the use of metals for industrial practices where their mechanical properties may be utilised without the constraints of deficiencies caused by corrosion. The role of an organic coating is to prevent corrosion by providing a barrier against potentially destructive ions and also by improving the adhesion of the topcoat to the substrate. Furthermore, upon damage of a coating system, where a defect penetrates through to the substrate, an adequate organic coating blocks the ionic path between a local anode and a local cathode along the substrate/polymer coating interface. In the event of ingress of electrolyte beneath the organic coating the last line of defence provided by the coating is the release of corrosion active pigments and inhibitors that may leach out into the intrusive electrolyte.

The current section discusses the two forms of corrosion phenomena that occur on organically coated metallic substrates. These are cathodically driven underfilm delamination and anodically driven filiform corrosion (FFC) where respective destructive and aesthetic damage are major issues for the steel industry. The kinetics and theory is described in depth along with the background of atmospheric corrosion. Further to this, current methods of prevention for the two phenomena are summarised with a focus on chromate and its potential replacements.

1.4.1 Atmospheric corrosion

Atmospheric corrosion occurs upon the covering of a metal substrate with an electrolyte. As described in Section 1.2.1 corrosion may only occur in the presence of the four key electrochemical cell components: an anode, a cathode, a medium for ionic flow and an electrical connection.

The first stage of atmospheric corrosion is the generation of cations, the product of metal dissolution shown by Reaction (1.16). These cations enter the electrolyte layer creating a concentrated region of electrons. A reduction reaction, shown in Reaction (1.17), takes place where molecular oxygen, which has diffused through the electrolyte, receives the electrons resulting in the production of hydroxide ions. The final stage of

atmospheric corrosion is the combining of metal ions and hydroxide ions to produce the resulting solid corrosion product. The anodic reaction is as follows:

$$m \rightleftharpoons m^{n+} + ne^- \quad (1.16)$$

and the cathodic reaction is either:

$$O_2 + H_2O + ne^- \rightleftharpoons nOH^- \quad (1.17)$$

or:

$$2H^+ + 2e^- \rightleftharpoons H_2 \quad (1.18)$$

Over time this corrosion product, an electron conducting oxide layer (in the case of iron or zinc), spreads over the entire metal surface. This blocks the electrolyte from contact with the metal substrate thus inhibiting further metal dissolution. However, although reduced, further corrosion is still possible through the diffusion of molecular oxygen through the layer of corrosion product.

The rate of atmospheric corrosion increases with decreasing electrolyte thickness as the rate-determining factor is the rate of molecular oxygen diffusion through the electrolyte layer.

1.4.2 Cathodic delamination

The specification for any coating system providing corrosion protection for a metallic product includes protection against loss of coating adhesion in the inevitable event of penetrative damage. A penetrative coating defect leaves the exposed metallic substrate vulnerable to electrolyte that, upon contact, can result in the establishment of an electrochemical corrosion cell. The result is delamination of the coating system that can continue to spread away from the defect. Fig 1.8 illustrates the mechanism by which delamination occurs. The general mechanism for an iron or zinc surface involves anodic metal dissolution at the site of the exposed substrate in the vicinity of the defect shown in Equation (1.16) in Section 1.4.1. This couples with cathodic molecular oxygen reduction at the delamination front by the ingress of electrolyte underneath the coating resulting in its detachment from the substrate. The oxygen reduction reaction leads to the formation of hydroxyl ions which render the interface high in pH; this is represented by Equation (1.17) in Section 1.4.1. Other reactive intermediate products are formed during oxygen reduction that, through a chemical attack on the electrolyte,

produce a hydrogel, a network of hydrophilic polymer chains, which is thought to be the medium of initial underfilm ingress. Rapid diffusion through the hydrogel is possible but a smaller diffusion rate is observed when compared to an aqueous solution [20]. Fürbeth et al established, using the SKP technique and small-spot photoelectron spectroscopy analysis, that the formation of a galvanic element is caused by the migration of cations from the defect to the delamination front [21]. Auger analysis has shown that external electrolyte anions remain localised to the defect zone [20].

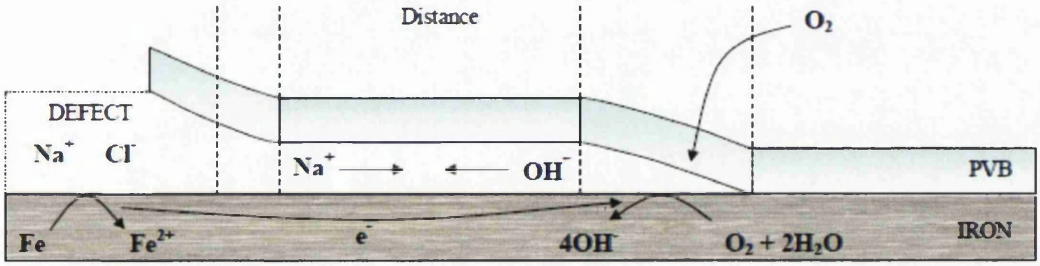

Fig1.8 Schematic representation of the E_{corr} measured in relation to a delamination cell

Underfilm delamination of a polymer-coated metal surface has been extensively studied, with the SKP technique being the primary method of investigation [9,22]. In order to discuss underfilm delamination in detail, a typical potential profile mapped using the SKP in an atmosphere of 93% relative humidity is shown in fig 1.9. A full description of the SKP technique and sample preparation can be found in Section 1.12. A typical potential profile has four distinguishable phases. They are as follows:

1. The defect region: where anodic metal dissolution takes place.
2. Region of gradual potential increase: this results from ohmic resistance to the galvanic current linking the delamination front to the defect.
3. Cathodic delamination region: observed as a sudden step in potential, where the reactions responsible for the loss of coating adhesion occur.
4. The intact interface defined by an anodic plateau. This plateau is the result of electronic conductivity from the oxide-covered substrate on which electron transfer reactions (ETRs) take place [23].

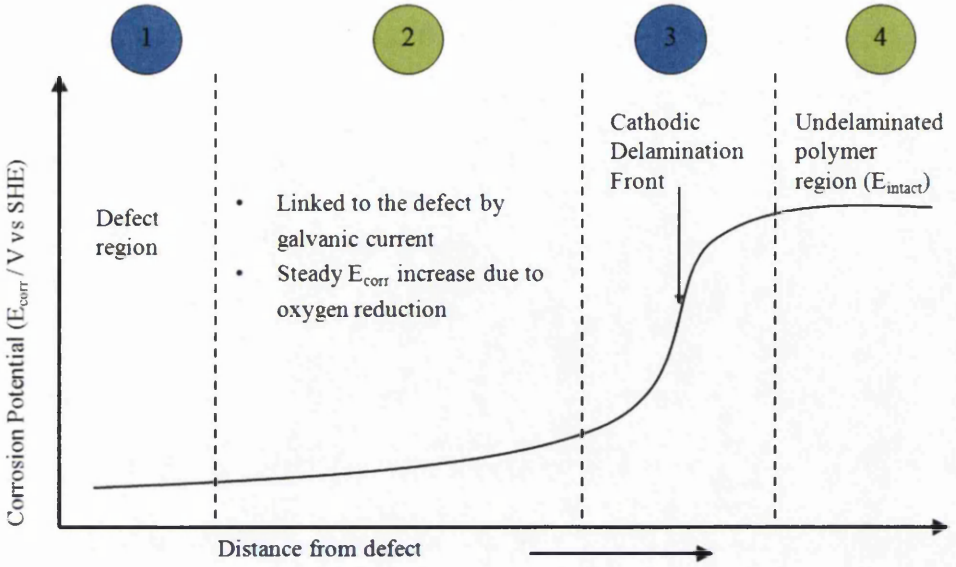

Fig 1.9 A typical E_{corr} profile showing underfilm delamination plotted using the SKP technique

1.4.3 Mechanisms of cathodic delamination of organic coatings from iron and zinc surfaces

Various theories have been put forward in current literature regarding the mechanism for loss of adhesion of an organic coating from a metallic substrate [23]. In 1976, Leidheiser and Kendig first described an elevated pH in the delaminated region, parabolic delamination rate kinetics and a sharp drop in corrosion potential at the point of coating disbondment [24]. This section will cover these theories in detail with focus on zinc and iron substrates. It is noted that, for any given system, there may exist several mechanisms of disbondment but it is that which proceeds at the fastest rate that is considered the governing mechanism [25]. Grundmeier et al suggest that there are three crucial governing properties to consider. These are:

1. The electron-transfer properties at the substrate/coating interface;
2. The oxide redox properties between metal and polymer;
3. Chemical stability of the interface with regards to potentially damaging species formed during ETRs.

The aforementioned points will be discussed with regards to the mechanism by which delamination occurs on iron and zinc substrates. Many similarities between the two metals are apparent however, when tested using SKP apparatus in the absence of oxygen, subtle differences are observed. The main distinction between the two is the

effect of an elevated pH on the metal oxides. Iron oxide is highly stable in alkaline media whilst zinc oxide is both unstable and highly soluble; the relevance of which refers to the production of hydroxyl ions from the cathodic oxygen reduction reaction described in Section 1.4.2. The mechanisms of organic coating delamination from both substrates will be discussed.

The anodic plateaux observed in region four of the E_{corr} profile (shown in fig 1.12) results from high electronic conductivity of a surface oxide where ETRs take place. This can be observed on both iron and zinc substrates which display highly conducting and semi-conducting oxides respectively. Oxygen can diffuse to the metal surface and will be reduced in correspondence to the oxidation of the surface oxide. However, with no electrolyte present, no ion transfer reactions take place and no corrosion will occur. Above a certain anodic potential the oxygen reduction rate is very small so no further anodic potential shifts are observed. There is a difference in potential of around 500 mV between zinc oxide and iron oxide with the former being more negative. This is true for zinc oxide only in the presence of oxygen. Where oxygen is removed, a rapid decrease of the electrode potential on the intact interface is observed. An iron oxide surface under the same conditions will remain stable for a comparatively long period of time. It is suggested by Grundmeier et al that this could be due to the different donor densities of both oxides. Zinc oxides generally exist as single valance states only; it is therefore understandable that a cathodic potential shift would be possible with minimal charge. In contrast, at an iron-polymer interface, a large proportion of Fe^{3+} states must be transformed into Fe^{2+}; this substantially limits any chance of a cathodic potential shift. Grundmeier et al put forward a theory suggesting that, when the oxide is reduced and the metal substrate concurrently oxidised, the redox reaction is the cause of coating adhesion loss on iron [23].

As previously stated, the oxygen reduction reaction that occurs at the metal-polymer interface in a delamination corrosion cell substantially increases the pH of the underfilm electrolyte. In such conditions an iron oxide layer is stable and so anodic behaviour is not observed in any region other than the exposed defect zone, thus ruling out metal dissolution as a possible delamination mechanism. However, oxidative destruction at an iron-polymer interface, in particular base-catalysed polymer degradation, base-catalysed hydrolysis of interfacial bonds and polymer attack, can be attributed to

intermediate radicals that form during the oxygen reduction reaction leading to loss of coating adhesion [22-23]. This implies that the instability of the interface is directly linked to the rate at which oxygen reduction occurs. However, for a polymer-coated zinc surface, the opposite is true.

Zinc oxides are unstable within an alkaline environment [23]. Experimental research, conducted by Furbeth et al using Auger electron spectroscopy (AES) sputter profiles, has revealed the substantial growth of oxide scale in the delaminated region [26]. This indicates that anodic reactions can take place within this region during a standard delamination experiment. This is confirmed by a study of potential profiles from SKP experiments, in which the atmosphere has been suddenly converted from air to argon, that show an inverse in polarity between the defect and the delamination front. In an oxygen-free environment, no oxygen reduction will take place and the galvanic element disappears. Thus, the potential becomes reliant on the Zn/Zn^{2+} couple within the defect and a $Zn/Zn(OH)^{2-}_4$ couple at the metal-polymer interface [23]. It is suggested that a pH buffering in the delaminated area would result from the establishment of an equilibrium between hydroxyl ion formation and the reaction with zinc. This implies a reduction in the path of charge transfer between local anode and the local cathode (region of ion incorporation) potentially leading to a higher delamination rate when compared with iron.

Williams et al [9] also suggest that, at an elevated pH, the oxidation of zinc leads to the formation of solid zinc hydroxide product $Zn(OH)_2$ generated by the following reaction:

$$Zn_{(s)} + 2H_2O \rightleftharpoons Zn(OH)_{2(s)} + 2H^+(aq) + 2e^- \qquad (1.19)$$

The amphoteric nature of $Zn(OH)_2$ results in its dissolution at high pH leading to the formation of zincate (ZnO_2^{2-}) and bizincate ($HZnO_2^-$) corrosion products, shown in Reactions (1.20) and (1.21) respectively. This is due to aforementioned anodic activity that eventually occurs in the delaminated region.

$$Zn(OH)_2(s) \rightleftharpoons HZnO_2^-(aq) + H^+(aq) \qquad (1.20)$$

$$Zn(OH)_2(s) \rightleftharpoons ZnO_2^-(aq) + 2H^+(aq) \qquad (1.21)$$

At pH 10.37 or higher, such as is found in the delaminated underfilm region, a bare zinc surface exposed by the dissolution of zinc(hydr)oxide could also be directly oxidized to bizincate via the following reaction [9,26]:

$$Zn(s) + 2H_2O \rightleftharpoons HZnO_2^-(aq) + 3H^+(aq) + 2e^- \qquad (1.22)$$

It can be concluded that the governing mechanism for adhesion loss on iron is due to cathodic delamination in which polymer attack by reactive intermediates generated from the oxygen reduction reaction results in the breaking of interfacial bonds and polymer degradation. The stability of the metal-polymer interface is directly linked to the rate of oxygen reduction. In contrast, the governing mechanism for coating adhesion loss on a zinc substrate is due to the formation of the galvanic element. An anodic reaction results from the alkalisation of the zinc-polymer interface in the delaminated region. This leads to the growth of a thick oxide in the delaminated region resulting in a reduced ionic pathway to the delamination frontier thus increasing the delamination rate. The difference in disbondment mechanism between zinc oxide and iron oxide can therefore be attributed to a different level of stability when in an alkaline environment.

1.4.4 Characterisation of underfilm delamination kinetics of uninhibited coatings

In order to study the effectiveness of in-coating inhibitors on underfilm delamination, the delamination kinetics of uninhibited coatings must first be characterised. Any literature concerned with underfilm delamination typically contains details of control experiments in which the baseline kinetics have been established for the particular substrate-coating type to be studied. This allows the characterisation of that particular delamination cell. The current discussion refers to reported delamination kinetics of uninhibited PVB coatings applied to iron and HDG (zinc) substrates, where delamination is initiated by 5% aqueous NaCl electrolyte and experiments are carried out at 93% relative humidity.

The measurable distance from defect to delamination front can be established using an SKP-derived E_{corr} profile. The delamination front is located at the inflection point where a steep change in potential is observed; this was illustrated in Fig 1.12. The background of this widely accepted theory is described in section 1.4.2. The time dependence of the position of the delamination is then used to analyse underfilm delamination kinetics. The relationship between delaminated distance (x_{del}) and any

given time (t_{del}), after addition of electrolyte to the defect, has been defined previously with the following equation:

$$x_{del} = k_{del}(t_{del} - t_i)^{1/2} \quad (1.23)$$

where k_{del} is the delamination rate constant [28]. Plotting x_{del} vs $(t_{del} - t_i)^{1/2}$ allows the delamination kinetics to be characterised. The term t_i is the time taken for either parabolic or linear kinetics to become established. At the time of electrolyte addition to the defect, the sample has spent sufficient time in the humidity chamber to allow the full hydration of the coating. The onset of definable delamination kinetics at time t_i is the time at which interfacial ionic concentration reaches a level where cathodic oxygen reduction is supported. Section 1.4.5.2 expands on this where the effect of electrolyte concentration on delamination rate is discussed.

It is extensively reported that, for the delamination of an unpigmented PVB coating from an iron or HDG substrate plotted as x_{del} vs. $(t_{del} - t_i)^{1/2}$, linear kinetics are observed [9,26,27,29]. The rate-determining step for the observed delamination kinetics of uninhibited coatings is regarded as the transport of electrolyte cations travelling from the defect, parallel to the interface, to the delamination front. Equation 1.23 is not a result of the transport of ions penetrating the coating in a perpendicular direction, as this diffusion path is independent of distance to the defect.

Leng et al showed that, by differentiating a series of potential profiles taken from any typical delamination experiment using SKP, the delamination front could be obtained exactly by the maximum value of the resulting peak. The various parameters, such as height, width and position of this peak reveal the characteristics of the delamination cell when considered with respect to time. Leng demonstrates how the delamination process can be quantified in several ways [20]. It was observed that, with increasing delamination time, the peak height gradually decreased. It was suggested that, during this time, the highly alkaline corrosion conditions in the vicinity of the delamination front begin to distribute through the already delaminated region. Progression over longer periods of time can result in the delamination front becoming indistinguishable. The rate at which this E_{corr} distribution occurs can be quantified by the measurement of peak height plotted against time.

Leng attributes the width of the peak to the direct distance measurement between the change in electrochemistries between the intact and already delaminated surfaces. The width of the peak is reported to remain relatively constant over long periods of time. Leng states that this region may also be determined by considering the ability of the specified ions to diffuse into the intact polymer and the time required for the oxygen reduction reaction to cause the destruction of the interface.

In summary, several quantifiable characteristics exist with regards to delamination cell potential profiles established for inhibitor-free delamination experiments. From this, any effects of inhibitor additions made to the protective coating may be determined where inconsistencies with the uninhibited profiles are observed.

1.4.5 Factors effecting delamination rate of uninhibited coatings

In the previous section it was stated that the rate-determining step for the delamination of unpigmented coatings is regarded as the transport of electrolyte cations travelling from the defect, parallel to the interface, to the delamination front. The rate-determining step is in any complex process is always the slowest step. Before considering the effect of inhibitor additions made to a polymeric coating on the rate of its delamination from a metal substrate, the effects on the delamination rate of those parameters that will remain consistent in a standard delamination experiment must first be understood. The influence of the initiating external electrolyte on coating delamination rate, with regards to composition and concentration, is discussed for a delamination cell on iron and zinc substrates.

1.4.5.1 Influence of the external electrolyte composition on delamination rate

Cation type has proven highly significant in the study of underfilm mass transport mechanism. As described in section 1.4.2, it has been reported that, upon the establishment of a delamination cell, only cations are present in the delaminated region; anions remain localized to the defect. Leng et al experimented with alkali-halide chloride salt electrolytes and showed that, when plotting delamination distance vs. $(t - t_i)^{1/2}$, the delamination rate could be ranked in the order $Cs^+ > K^+ > Na^+ > Li^+$ [20]. This ranking order correlates to the mobility ranking of the listed cations when in aqueous electrolyte. For example, the small Li^+ ion displayed the lowest delamination rate and has the lowest mobility in aqueous electrolyte due to a large, strongly bound hydration

shell. Leng concludes that the rate-determining step for the delamination of simple unpigmented polymeric coatings is the transport of cations along the substrate/coating interface. However, Leng also reports that the observed diffusion coefficients recorded for cations at the metal-polymer interface are substantially smaller than those recorded in water. This leads to the assumption that the cations migrate via a thin gel-like layer, as referred to in section 1.4.2, which results from the chemically destroyed polymer. Although mechanical adhesion to the substrate is severely limited, the swollen polymeric structure limits cation mass transport, hence the reduction in measured mobility values at the interface when compared with those in water.

Further experiments were carried out by Leng et al to determine the influence of anion type on the delamination rate. It was found that the delamination rate differed very little when electrolytes of NaBr, NaF, NaCl and $NaClO_4$ were used to initiate delamination. The anions in a cathodic delamination cell remain localized to the defect region; using ESCA studies, Furbeth et al proved this [31]. In contrast to cations, which migrate to the delamination front to balance the negative charge created by the cathodic oxygen reduction reaction, anions have no role to play and can be considered negligible with regards to delamination rate.

1.4.5.2 Influence of electrolyte concentration on delamination rate

Leng et al have studied the effect of electrolyte concentration on the underfilm delamination rate of a polymeric coating [20]. The SKP technique was used to study the delamination of polymeric coatings where varying concentrations of NaCl were added to deionised water applied to the sample defect. It was found that, where deionised water with NaCl content below 0.05 M was added, no coating delamination was observed using the SKP; this was verified using mechanical de-adhesion testing. This highlights a minimum requirement of ions at the metal-polymer interface necessary for the establishment of the galvanic effect. Without sufficient ion content electrochemical reactions are impeded by the domination of an extended diffuse double layer as a result of the lack of ions incorporated into the interface. Hence, as described in section 1.4.4, equation (1.20) must incorporate t_i as up to this point interfacial ionic concentration has not reached the required level to support cathodic oxygen reduction.

Leng also found that increasing the NaCl concentration upwards of 0.05 M the delamination rate progressively increased. When plotting delamination distance x_{del} vs. $(t_{del} - t_i)^{1/2}$, all experiments revealed linear kinetics up to a time of 15 h. Leng states that, unlike electrolyte composition, the linear kinetics cannot be attributed to ion mobility. It is suggested that the observed kinetics are influenced by a permeation coefficient [20].

1.4.6 Filiform Corrosion

1.4.6.1 Background to filiform corrosion

First reported in scientific literature in 1944 by Sharman, filiform corrosion (FFC) is considered a type of atmospheric corrosion and was first observed on lacquered tobacco cans [32]. The characteristic thread-like corrosion product deposited under organic films is primarily known to affect organic-coated aluminium and iron (steel) substrates. The effects of FFC are largely superficial with the main detrimental effect of the mechanism being aesthetic. This in itself is unacceptable within the organic-coated metal product market but, more importantly, in some instances FFC is a precursor to more serious, structural problems. The first example of this kind was found in the aeronautical industry where aeroplanes exposed to tropical atmospheres experienced corrosion on the rivet heads and at the edges of aluminium sheets. Cracking in the paintwork caused by flight vibrations resulted in the onset of FFC that eventually lead to corrosion in crevices surrounding the rivets. The result was crack development in highly stressed zones from FFC trails [33]. FFC was able to develop undetected below the lacquer coating and was noticed only when the problem became dangerous in nature. It is, therefore, of great importance that organic coatings provide resistance against FFC in the event that the metallic product to be is exposed to the conditions under which FFC may occur.

1.10. Photographic image of filiform corrosion on an aluminium substrate [34]

1.4.6.2 Factors effecting filiform corrosion

FFC is initiated by the penetration of soluble ionic species, such as chloride ions, through a defect or coating weak spot to the underlying substrate. It has been reported that FFC on iron may initiate by a wide range of anions where the effectiveness of particular salts at doing so is regardless of its hygroscopic characteristics. FFC only occurs at humidity in the range 60 - 95%. Where relative humidity is close to the saturation point, i.e. above 95%, blistering is typically observed in place of FFC [33]. Further to this, oxygen must be present for FFC to occur as corrosion processes require a redox reaction; FFC does not occur in inert atmospheres [35]. It has been shown elsewhere that an increase in temperature from ambient conditions results in an increase in FFC growth rate [33].

1.4.6.3 Filiform corrosion mechanism – Phase one

McMurray et al showed that, on iron substrates, a phase of cathodic coating disbondment precedes FFC where initiation is achieved by the addition of group (I) chloride salt electrolytes to a penetrative defect [36]. Whilst the progressive depletion of the group (I) cations occurs, due to migration to the site of cathodic delamination, Cl^- anions remain in the vicinity of the defect. The electrochemical cell is completed by the anodic dissolution of Fe^{2+} cations at the defect. Upon the eventual exhaustion of all group (I) cations and, hence, the halting of cathodic delamination, the remaining Fe^{2+} and Fe^{3+} chlorides at the defect site begin the onset of Phase two, FFC.

A study by McMurray et al recorded observations of cathodic delamination and subsequent FFC initiated by a range of aqueous group (I) chloride salts[36]. Unlike

initiation with the other group (I) chloride salt electrolytes, $FeCl_2$ electrolyte resulted in no initial cathodic disbondment. Instead a layer of thick, dark brown precipitate was observed on the coating defect. It was suggested that, through contact with atmospheric O_2, Fe^{2+} cations are oxidised to Fe^{3+}. It is known that the precipitation of an insoluble solid $Fe(OH)_3$ is the result of a tendency of Fe^{3+} aquacations to undergo hydrolysis to produce a series of mono and polynuclear hydroxyl-complexes. The lack of a cathodic delamination phase prior to the onset of FFC can be attributed to the polyvalent Fe^{3+} aquocation rendered incapable of carrying current through the alkaline underfilm electrolyte layer. After a 40 h period the initiation of FFC was observed where the filament propagation rate was similar to those initiated by other group (I) chloride salts. [36].

1.4.6.4 Filiform corrosion mechanism – Phase two

The mechanism for Phase two filament growth is presented by Keashe [37] and further demonstrated by Ruggeri and Beck [38]. The theory attributes the delamination of the coating, caused by FFC, to an anodic mechanism. A filiform filament is made up of an electrolyte-filled head, including metal cations and aggressive Cl^- anions, and a filament tail consisting of inert corrosion product. The head acts as the active corrosion cell and travels across the metal substrate leaving behind the dry, porous corrosion product that makes up the tail. As a result of cation hydrolysis, the leading edge of the filament head displays a very low pH, typically between pH 1 and pH 4. Conversely, the back of the head is of extremely high pH; this was measured by Slabaugh as pH 12 on an iron substrate [35].

The initiation of FFC is thought to be by osmosis on the basis that it only occurs when exposed to a humidity above 65% [39]. Where a penetrative defect allows the entry of electrolyte containing a soluble salt, a small liquid aggregate will form. This is due to the high affinity of the ions for water. Upon the build-up of molecules a formation of liquid occurs such that any further liquid penetrating the coating is retained due to the vapour pressure of the concentrated electrolyte [40]. The beginning of anodic iron dissolution then occurs releasing Fe^{2+} ions into the solution. Furthermore, the displacement of oxygen occurs in the same region. Where low oxygen concentration is present, within a differential aeration cell, the acidification of the electrolyte is a typical

response; this oxygen deficient site forms the basis of the anode and the surrounding area forms the cathode. The diffusion of oxygen and water through the porous tail into the filament head causes a differential aeration cell and the separation of the anode and cathode. The imbalance of oxygen supply to the area of iron dissolution allows the further development of the anode and the cathode. The oxygen deficient area at the front of the head becomes the anode and the oxygen rich area at the back of the head, supplied by the porous tail, becomes the cathode. Upon the full development of the oxygen concentration cell, the region at the front of the head anodically undermines the coated substrate allowing for the propagation of the filaments.

Williams et al show that a potential gradient exists between the front and back of the filament head where anions migrate to the front and cations migrate to the back [36]. The Fe^{2+} formed in the oxidisation of the iron, as in equation (1.24), at the front of the head migrates to the back of the head. Further oxidisation of the cation then occurs as it is exposed to a higher oxygen concentration. This cathodic reaction is shown in equation (1.25).

$$Fe \rightleftharpoons Fe^{2+} + 2e^- \qquad (1.24)$$

$$4Fe^{2+} + O_2 + 2H_2O \rightleftharpoons 4Fe^{3+} + 4OH^- \qquad (1.25)$$

A colour change between anodic and cathodic regions can be observed where a 'V' shaped boundary between ferrous and ferric ions exists.

1.4.6.5 Alternative FFC mechanism

An alternative mechanism by which FFC initiates and propagates has previously caused some dispute amongst authors regarding the location of the cathodic site. The opposing proposals suggests that cathodic activity occurs either in the narrow region at the very front of the filament head [30,38,39] or even preceding the filament head a small distance ahead of the leading edge [40-41]. Funke proposed a mechanism by which a cathodic region lies a distance in front of the filament head and is able to grow due to a generation of underfilm hydroxyl ions. It was suggested that this occurs until the cathodic region reaches a size where it merges with the filament head. From this hydroxyl ions are said to migrate in the direction of the anode while electrolyte cations present in the head migrate towards the preceding cathode. A polarity reversal results where the front region, originally cathodic, is now the filiform head anodic leading

edge. The process is said to repeat resulting in the segmented appearance of the filament tails.

Various counter arguments to this hypothesis include the notion that the described model is inconsistent with the asymmetric separation observed between corrosion cell anodic and cathodic zones. Ruggieri and Beck also point out that the alternative mechanism implies that the ionic current must flow from the anode through the coating to reach the anterior cathodic region [38]. It is suggested that high resistance of the undelaminated coating would limit cathode size. A lack of experimental evidence to prove the existence of the region cathodic detachment preceding filament advancement is typically taken as an argument against its validity. However, Williams et al suggest that, although it is not a filament propagation rate determining process in FFC on iron, it should be considered an important factor in the lateral spread of filament head electrolyte [36].

1.5 Recent work on inhibitors for the prevention of the underfilm delamination of organic coatings

Extensive research published by various authors outlines the prevention of corrosion-driven underfilm delamination by in-coating inhibitor additions and pre-treatments; these will be discussed within the current section. Due to legislative pressure to replace the traditional chromate-based inhibitor systems, non-toxic, alternative inhibitors are of particular importance for industrial applications.

As described in Section 1.4.2, an electrochemical delamination cell is established by the coupling of a cathodic oxygen reduction reaction at the delamination front with anodic metal dissolution at a defect. In the delamination of unpigmented coatings an underfilm pH of > 10 contributes to the hydrolysis of interfacial bonds, polymer degradation and, in the case of HDG, dissolution of the amphoteric zinc (hydr)oxide film. Reported delamination kinetics suggest that the rate-determining step in an uninhibited delamination cell is the migration of cations from the external electrolyte to the delamination front. The mechanism by which chromate acts so efficiently to prevent the aforementioned cathodic disbondment process will be discussed along with a selection of potential replacement inhibitor systems.

1.5.1 The inhibition of corrosion-driven underfilm delamination by chromate

The cathodic inhibitory properties of chromate have been reported extensively in various literature [9,42,43]. In-coating chromate ($SrCrO_4$) additions have been proven to reduce both underfilm delamination and delamination cell currents to a minimum. This has been shown at volume fractions (φ_{sc}) of ≥ 0.064 when added to a PVB coating applied to HDG substrates [9]. The dominant inhibition mechanism from such findings is considered to be the replacement of the oxygen reduction reaction by self-limiting chromate anion reduction (Reaction 1.26). This acts as a cathodic depolarizer following the diffusion of $CrO4_4^{2-}$ anions from the coating directly into the underfilm electrolyte layer. Furthermore, the resulting insoluble Cr(III) (hydr)oxide ($Cr(OH)_3$) precipitate acts to reinforce any passive zinc(hydr)oxide layer that may be present at the zinc surface.

$$2CrO4_4^{2-} + 10H_2O + 6e^- \rightleftharpoons 2Cr(OH)_3(s) + 10OH^- \quad (1.26)$$

Further to this it has been shown that a zinc surface, within the already delaminated region, becomes increasingly passive over the duration of the experiment [47]. This was shown by an increase in potential in the area from values of -0.6 V vs. SHE, typical for a freely corroding zinc surface at the defect margin, to ca. -0.35 V vs. SHE [9]. This passivation is attributed to a combination of high underfilm pH and the diffusion of $CrO4_4^{2-}$ anions into the electrolyte layer. A reported decrease in rates of anodic zinc dissolution in region (I) of fig 1.12 contributes to, but does not govern, the overall reduction in delamination rate.

In contrast to the highly effective inhibitory action of in-coating $SrCrO_4$, anions of the same pigment ($CrO4_4^{2-}$) added to the electrolyte were found to reduce the delamination of an unpigmented coating by a conservative < 25%. A passivation of the exposed zinc surface at the defect was observed and anodic zinc dissolution was profoundly inhibited exclusively in this region. The reason delamination was able to progress was due to the persistent zinc dissolution in the defect/coating margin region. The authors assigned this finding to be consistent with previous findings that showed the substantial exclusion of $CrO4_4^{2-}$ anion migration from the underfilm electrolyte layer by the delamination cell electric field [9].

1.5.2 The inhibition of corrosion-driven underfilm delamination by smart-release coating systems

'Smart-release' inhibitor systems, also known as nanocontainer-based technologies, have obtained substantial recognition as a credible alternative to in-coating corrosion inhibitor pigments based on sparingly soluble chromate. The attraction of such systems is as follows:

1. They have the ability to release stored inhibitor species and sequester aggressive ions. This occurs only upon intrusion by corrosive electrolyte. This is a major advantage with respect to environmental concerns as sparingly soluble chromate based pigments continuously leach their constituent ions when in contact with aqueous media resulting in long-term environmental damage.
2. It is potentially possible to incorporate either inorganic or organic ionic species that may act as corrosion inhibitors. This relieves the limitations of only incorporating sparingly soluble salts.

The release of stored inhibitor species may be triggered in three ways. The first is by the presence of aggressive ions that initiate a subsequent ion-exchange process. The second trigger is by an alteration in substrate potential, this type of system is typically achieved by the incorporation of a conducting polymer (CP). CPs such as polypyrrole (Ppy) have been shown to prevent corrosion at a defect by the release of inhibiting anions only when the defect potential falls beneath a threshold value [44-45].

The final type of smart-release system triggers anion-release when a change in local pH is realised. These include coatings based on meso-porous silica [49], hydroxyapatite [50] and layer-by-layer deposited polyelectrolytes [51]. Extensive study has successfully shown that, on a range of metallic substrates, a self-healing effect to a penetrating coating defect can be achieved the results of which are comparable to industry standards [28].

1.5.3 Ion-exchange pigments for the inihibiton of corrosion driven underfilm delamination

A major contender for the replacement of chromate under investigation is the use of ion-exchange minerals as smart-release pigments for incorporation within a polymer binder

[28], [52]–[57]. The inhibitory mechanism against delamination of such a system takes effect only in the presence of a potentially damaging aqueous environment where inhibitor species are released and aggressive chloride and H^+ ions are sequestered. The main contenders for the replacement of chromate based systems will be described in this section.

1.5.3.1 Rare earth metal cation-exchanged bentonite pigment

Various literature documents the substantial study of exchange cations for naturally occurring bentonite (a.k.a Wyoming) clay [56,57,58]; a comparatively low-cost pigment that exhibits no negative connotations on the environment. The key characteristic of bentonite clays, with regards to their inhibitory qualities within the highly alkaline rendered conditions of a delamination cell, is their intrinsic cation exchange properties that have substantial independence from pH [61].

Williams et al explored the exchange of bentonite clays with a range of divalent alkali earth metal cations: Mg^{2+}, Ca^{2+}, Sr^{2+} and Ba^{2+} and trivalent rare earth metal cations Y^{3+} and Ce^{2+} [29]. A significant enhancement in the resistance of cathodic delamination in organic coatings adherent to iron surfaces was demonstrated when compared with experiments on uninhibited coatings. The proposed inhibitory mechanism was the reduction of underfilm electrolyte conductivity by underfilm cation exchange and precipitation of sparingly soluble hydroxides. Delamination kinetics were consistent with underfilm cation migration as the rate determining step. Interestingly, it was observed that the cations with more soluble hydroxides provided superior inhibition to underfilm delamination than those with less soluble hydroxides. It was suggested that a less soluble hydroxide might result in excess precipitation that acts to suppress further cation exchange.

1.5.3.2 Zn^{2+}-exchanged bentonite pigment

Zn^{2+}-exchanged bentonite pigment dispersed in a PVB coating have been shown to significantly decrease the delamination rate of coatings applied to a HDG substrate. Cation exchange has been shown to occur between Na^+ ions in the underfilm electrolyte and the Zn^{2+}-Ben pigmented coating. The governing mechanism, suggested by Williams et al, is thought to be the suppression of cathodic oxygen reduction; this was

shown in two ways [62]. Firstly, with increasing levels of in-coating exchangeable Zn^{2+}, the E_{intact} was shown to become progressively depressed when compared to those values observed in the uninhibited case. Secondly, analysis of the delamination rate revealed a change from the parabolic kinetics (where x_{del} was plotted against $(t_{del} - t_i)$), seen in the control experiment, to linear kinetics upon addition of inhibitor pigment. It is suggested that a cathodic blockade results from the aquo-cation hydrolysis of exchanged Zn^{2+} that produces a buffering of the underfilm pH. The dissolution of amphoteric zinc (hydr)oxide at the delamination cell cathode is thus prevented and reinforced to further obstruct interfacial electron transfer [61].

1.5.3.3 Ce^{3+} cation-exchanged bentonite and silica

Dispersions of Ce^{3+} cation-exchange pigments based on silica and bentonite in PVB coatings applied to HDG substrates have been shown to significantly retard, but not completely halt, cathodic delamination. The mechanism is ascribed to an increase in under-film resistivity by the displacement of underfilm electrolyte by solid $Ce(OH)_3$ via Reaction 1.27.

$$Ce^{3+}(aq) + 3H_2O(aq) \rightleftharpoons Ce(OH)_3(s) + 3H^+(aq) \qquad (1.27)$$

The consequence of this deposit is the increase in length and tortuosity of the pathway in which delamination cell ions must migrate. The mechanism was derived from the delamination kinetics that remained parabolic (where x_{del} was plotted against $(t_{del} - t_i)$), where inhibitor was added, denoting that mass transport control remains the rate-determining step. Williams et al suggest that the rate of exchange of $Ce^{3+}(aq)$ ions with $Na^+(aq)$ from the experimental electrolyte lags behind the advancing delamination front. The majority of Ce^{3+} ions that enter the highly alkaline electrolyte form a $Ce(OH)_3$ precipitate in close proximity to the defect and the delaminated zone. Oxygen reduction at the delamination cell cathode is free to continue as no coherent cathodic film capable of stifling the reaction is formed [29].

1.5.3.4 Ca^{2+} cation-exchanged silica

A commercially available cation-exchange pigment based on exchangeable calcium-containing silica (SiO_2) pigment has been shown to exhibit an equivalent level of inhibition as that of chromate pigments [63]. It is prepared via the treatment of SiO_2

powder with aqueous calcium hydroxide ($Ca(OH)_2$). Three inhibitory mechanisms have been proposed:

1. The acid-base reaction of calcium hydroxide with –OH groups on the SiO_2 particle surface produces exchangeable Ca^{2+} cations.
2. An interaction between Ca^{2+}-silica and the binder resulting in an improvement of cross-linking
3. The formation of a protective film at the point of metal contact facilitated by the established mobility of silica and calcium during the permeation process [63]–[65].

1.5.3.5 Anion-exchange hydrotalcite clay

The white, anionic clay hydrotalcite (HT) is commercially available in a range of chemical compositions and crystallographic parameters. Such clays are all termed 'hydrotalcite' or 'layered double hydroxides' (LDH) and are either natural or synthetic lamellar mixed hydroxides that contain exchangeable anions. Specifically, HT in the form $Mg_6Al_2(OH)16CO_3.4H_2O$ and hydrotalcite-like compounds have been shown previously to act effectively as halogen scavengers within a polymer coating system. Within an aqueous system they have been shown to act as halide getters [66]. Both hydrotalcites and calcined hydrotalcites have also been shown to neutralise aqueous acids [67].

1.5.4 Intrinsically conducting polymers as inhibitors of underfilm delamination

Intrinsically conductive polymers (ICPs), also referred to as π-conjugate polymers, have been extensively studied due to their potential utilisation within electronic, electrochemical and optical applications [68]. ICPs are discussed further in Section 1.6. The majority of literature that discusses the use of ICPs with regards to corrosion protection focuses on the redox active polymers, in particular polypyrrole, polyaniline and polythiothene [41,42,61,62]. The following suggestions for the incorporation of ICPs into an effective coating system have been proposed within the available literature:

1. Single layer primer

The electro-deposition of ICPs directly onto metallic surfaces is the established method of application [71]. Further to this, the addition of low concentration, anti-corrosive pigments is proven to improve corrosion resistance where it is theorised that no further coating layers are required [72].

2. Primer layer in a conventional coating system

   It has been suggested that superior corrosion protection can be achieved where a topcoat overlays an ICP primer layer [73]–[75].

3. Conventional polymer binder/ICP blend

   Various authors have reported improved corrosion protection on iron where, in particular, polyaniline has been mixed with polyurethane or alkyd resins [73-74].

4. Replacement of anticorrosion pigments with ICPs.

   Low concentration additions (< 1% wt.%) of an ICP to traditional paint formulation have been reported to show improved corrosion resistance when compared with uninhibited paints [65-66].

Despite the positive points mentioned above, the use of ICP for corrosion protection is a contentious issue. It is suggested by Rohwerder et al that, depending on the coating system and the corrosive conditions, an ICP may provide excellent protection or, alternatively, may cause the unwanted acceleration of corrosion [22]. The proposed inhibition mechanisms of such ICPs are as follows:

1. The ennobling mechanism – when applied in their oxidised form, conductive redox polymers such as polyaniline and polypyrrole act as an oxidiser to improve the oxide layer at the substrate-coating interface. It is also suggested that they provide anodic protection by maintaining the substrate in the passive region where a defect has led to substrate exposure to the external environment.
2. The shifting of the oxygen reduction site from the substrate-coating interface purely into the polymer coating. This acts to spread the produced radicals (such as the OH^- radical that promotes the loss of adhesion) over the coating in order to reduce the radical content at the interface.

However, Rohwerder also reports that, in a situation where a large defect exists, whilst some CP coatings continue to provide good protection, others have been found to fail [78]. In an immersion situation where the whole surface area of the defective coating is

in contact with the electrolyte the ICP is active. In this instance the reduction current of the ICP would typically be higher than the current required to overcome the critical passivation current density in the defect. In contrast, a delamination scenario would stand only a small chance of the ICP reduction current being higher than required to overcome the critical passivation current density. This is due to the limited portion of the active ICP available to passivate the comparatively large area of underlying substrate exposed to the penetrating electrolyte at the defect.

Rohwerder et al suggest that an important factor that affects whether polarisation will lead to the protection against, or enhancement of, corrosion is the coupling between the ICP and the metal onto which it is coated. Protection may only be observed where the ICP is capable of providing oxidation power high enough to raise the corrosion current of the metal over the critical passivation current density. Where this can not be achieved, the acceleration of corrosion is likely. Specific cases where ICPs have been incorporated into coating systems will be discussed in the proceeding sections [22].

1.5.4.1 The effect of polyaniline on underfilm delamination

The electrically conductive emeraldine salt (ES) of polyaniline (PAni) was first reported to be an effective inhibitor against corrosion by DeBerry in 1985 [79]. The PAni ES is produced via the proton doping of partially oxidised PAni emeraldine base (EB) using Bronsted acids [80]. Within the available literature the comparable effectiveness of dopant type, doped (conductive) and undoped (non-conductive) PAni ES is a contentious issue with regards to the protection of carbon steel [81]. Certain publications suggest that an enhancement in protection is achieved by doping with anions with their own inhibitory qualities; the ability to form a salt layer on the substrate is shown to be beneficial [82]–[86]. Contrary to this, several studies have contested the need for doping and suggested that the protection qualities of PAni EB are superior [86]–[91].

A readily available version if PAni, paratoluenesulphonic acid (PAni-PTS), is widely used commercially [68,89]. A major drawback of PAni-PTS, however, is its intractable nature through which adhesion to metal surfaces is limited [71]. Application of PAni ES to metallic substrates is traditionally carried out by electrodeposition or via the

deposition of water-borne dispersions. Several studies report the successful dispersion of PAni into a conventional polymer binder [85,90]. Williams et al studied the effect of PAni-PTS on underfilm delamination when dispersed in a PVB coating applied to HDG substrates [94]. It was hypothesised that, by dispersing in a non-conducting polymer matrix such as PVB, PAni-PTS could be utilised without any issues with adhesion loss. PAni-PTS dispersions of $\varphi_{pa} \geq 0.2$ in PVB were found to profoundly inhibit underfilm delamination over a 48 h period. The proposed inhibition mechanism, in this instance, was the stifling of the cathodic oxygen reduction reaction by the formation of a PAni-PT-induced zinc oxide layer at the zinc-coating interface. This oxide layer was found to form at a thickness proportional to φ. The zinc layer was also found to remain unharmed by the highly alkaline underfilm conditions by a pH buffering mediated by the PAni-PTS additions.

The effective inhibition of cathodic delamination on iron substrates by PAni doped with various acids, *p*-toluenesulfonic (H-*p*TS), camphorsulfonic (H-CS), phosphoric (H_3PO_4) and phenylphosphonic (H_2-PP) was proven in an SKP study. A progressive increase in substrate potentials, by up to 0.36 V, with increasing PAni volume fraction (φ_{pa}) was observed from PVB/PAni ES coatings. Such coatings also induced the growth of an interfacial iron oxide or salt film. This is in contrast to PAni EB coatings where E_{intact} is shown to be independent of φ_{pa} indicating that no electron transfer takes place between the iron substrate and the electrically non-conducting PAni EB.

The mechanism by which oxide growth occurs, proposed by Holness et al, suggests that the oxide layer behaves as a hydrous polyelectrolyte containing the LB/ES redox couple shown in Reaction (1.28) [95]. A^- represents the relevant dopant anion.

$$PAni^{+\cdot}A^-(ES) + e^- \rightleftharpoons PAni(LB) + A^- \quad (1.28)$$

$$Fe \rightleftharpoons Fe^{2+} + 2e^- \quad (1.29)$$

$$2Fe^{2+} + 3H_2O \rightleftharpoons Fe_2O^3 + 3H^+ + 2e^- \quad (1.30)$$

The underlying substrate is polarized to potentials at which the spontaneous oxidation of iron occurs, shown in Reaction (1.29). Further to this the Fe^{2+}, which exists transiently as the dopant anion salt, undergoes oxidative hydrolysis at the iron surface via Reaction (1.30). A hydrous layer of Fe^{III} (hydr)oxide is produced which is able to thicken linearly with time due to no significant impedance of the anodic current. A

cyclic re-oxidation of air-sensitive LB moieties to ES through coupling with cathodic oxygen reduction means the PAni redox state is maintained.

The dominant inhibition mechanism for PAni ES coatings is considered to be the relocation of the cathodic oxygen reduction reaction from the ennobled substrate onto the coating ES. This mechanism was also observed by Tallman et al where polypyrrole-PAni duplex coatings were electropolymerised onto HDG substrates [71]. The before-mentioned reduction of PAni ES to PAni LB partially, or wholly, replaces the cathodic oxygen reduction reaction within the delamination zone. The re-oxidation of PAni LB is able to take place until the alkalization of the underfilm region occurs. At which point the reaction product becomes non-protective PAni EB.

The PAni-dopants that displayed the most effective delamination prevention were PAni-HPP and PAni- H_3PO_4; the formation of FePP and $Fe_3(PO_4)_2$ salt films were observed respectively. Williams suggests that the salt films hindered electron transfer between PAni-ES and the iron substrate. This "secondary" barrier decreases the rate of PAni-ES reduction at the delamination front. Due to an eventual depletion, ES can only act to retard cathodic delamination, albeit substantially, but with the addition of these particular dopant salts a complete prevention can be achieved.

In summary the suggested inhibition mechanisms, assigned by various authors, for the protection of carbon steel by PAni includes:

1. Substrate ennoblement
2. The formation of a passive oxide film
3. The relocation of the cathodic oxygen reduction reaction from the ennobled substrate onto the coating ES
4. The precipitation of an insoluble metal salt resulting in anodic inhibition where a dopant anion is present

1.5.4.2 The effect of polypyrrole on underfilm delamination

Paliwoda-porebska et al found that an unmodified coating, based on the conducting redox polymer polypyrrole (Ppy), employed for protection against underfilm delamination from a large defect, the acceleration of delamination is observed [48]. The resultant accelerated breakdown of the coating is due to a fast oxygen reduction reaction

and a failure to passivate the defect region. It was suggested that the fast reduction process is caused by high cation mobility in the reduced polymer. As the delamination progresses it is thought that the coating becomes increasingly accommodating for fast cation transport.

Where a Ppy coating was doped with MoO_4^{2-}, it was found that no inhibition of delamination was observed. It was theorised that this was due the over-oxidation of Ppy due to the highly alkaline rendered interface between the metal and the polymer.

Where Ppy was doped with the anion $[PMo_{12}O_{40}]^{3-}$, significant inhibition of delamination was observed through on-demand release. A partial passivation of the defect was observed where iron dissolution was inhibited by the accumulation of MoO_4^{2-} anions. The successful inhibition in this case was also achieved by the decomposition reaction of the $[PMo_{12}O_{40}]^{3-}$ anion which provided significant buffering of the high pH at the delamination front. In the MoO_4^{2-} dopant case described above, this buffering does not take place and inhibition can not be achieved.

1.6 Previous literature on relevant inhibitor materials

1.6.1 Corrosion inhibition by Phenyl phosphonic acid

Phenyl phosphonic acid (H_2PP) is studied intensely in the current thesis with regards to its effect on inhibition of corrosion on industrially important materials; namely iron and HDG. Previous studies have shown the effective inhibition of filiform corrosion (FFC) on aluminium where H_2PP is added to a polyvinylbutyral (PVB) coating. Inhibition of filament advancement beyond 1.5 mm was achieved at the critical level of 0.5%; it was observed that H_2PP additions above this level made no further improvement. It was suggested that electrochemically active sites were sufficiently blocked by HPP^- and PP^{2-} anion adsorption where H_2PP was present at this level. Coleman et al found that H_2PP acts to suppress the E_{corr} in the undelaminated region by values up to 0.35 V [96]. This was attributed to the described HPP^- and PP^{2-} anion adsorption on the oxide-covered aluminium surface. This observation coincided with a reduction in FFC filaments [96]. A further suggestion is that the formation of a metal/H_2PP salt layer acts to prevent the propagation of the initiated filaments.

H_2PP was used in a study by Williams et al where polyaniline (PAni) emeraldine salts (ES) in a PVB coating were doped with the inhibitor. Whilst the study concerns the effectiveness of PAni ES at preventing underfilm delamination it is also shows that an H_2PP dopant provides a secondary barrier by the formation of a FePP salt film. This is shown to hinder the oxidation reaction of the iron substrate assuming the ions exceed the estimated solubility product (K_{sp}) value which was given as $K_{sp} = 10^{-7.9\pm0.3}$ from a titration experiment [80].

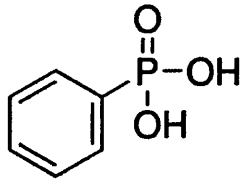

Fig 1.11 The atomic structure of phenyl phosphonic acid

1.6.2 Conducting Polymers

The concept of conducting polymers was first introduced by Hatano et al in the 1960s where a study revealed the conductive properties of polyacetylene. Since 1977, where Shirakawa, MacDiarmid and Heeger proved the possibility of increased conductivity of said polymer via exposure to halogen vapour, the newly classified 'intrinsically (inherently) conducting polymers' (ICP) have become a highly researched subject for applications in a wide span of industrial sectors. With observed electrical properties close to that of copper, ICPs were also referred to as 'organic metals'. Fig 1.12 shows the chemical structures of some common π-conjugated polymers.

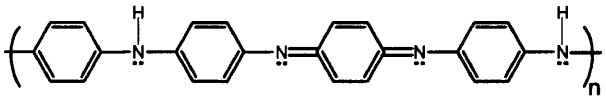

Polyaniline (PAni)

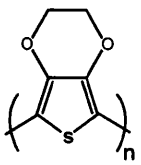

Poly (3,4-ethyldioxythiophene) (PEDOT)

trans–polyacetylene (t-PA)

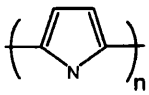

Polypyrrole (PPy)

Fig 1.12 The atomic structure of various conducting polymers

Conducting polymers can be grouped into either ionically or electronically conductive depending on the type of charge transport carrier. As the name suggests, in ionically conducting polymers ions are responsible for the conduction of electricity; a typical application is the electrolyte in a solid-state battery. Electrically conducting polymers can be further divided into two categories; intrinsic and extrinsic. An extrinsically conducting polymer is able to conduct due to the addition of conductive fillers e.g. graphite or metal particles.

1.6.3 Poly (3,4-ethyldioxythiophene) (PEDOT)

PEDOT is currently the most widely used ICP due to its performance with regards to conductivity, processablity and stability. Compared with other thiophenes, PEDOT displays good electrochemical, ambient and thermal stability of its electrical properties. However, pristine PEDOT is neither soluble nor dispersible, due to a formation of undesirable products formed in the polymerisation reactions; processablitlity in unaltered PEDOT is poor.

In 1989, a way of rectifying these problems was achieved by the polymerisation of the EDOT monomer in aqueous poly(styrenesulfonic acid) (PSS). PSS itself has no oxidising effect so is not considered to be a dopant. However, due to a much higher molecular weight, PSS and the corresponding polyanion were found to function sufficiently as the counterion for positively charged, doped PEDOT. PSS acts to keep the PEDOT chain segments dispersed in the aqueous medium. The resulting PEDOT:PSS complex was found to display highly stable micro-dispersive properties in water where PEDOT is in its oxidised state. The final product is processable on a large scale and may be applied via a range of industrial techniques to produce a thin,

transparent, conducting film. Aqueous dispersions of commercial grade PEDOT:PSS typically have a work function of ca. 5.2 eV. Due to the PSS content the dispersion typically displays a pH value between 1.5 and 2.5 at room temperature.

1.6.4 Corrosion inhibition by PEDOT

To date, Poly(3,4-ethylenedioxythiophene) (PEDOT) has been used within photographic film, antistatic coatings, printed circuit boards, inorganic electroluminescent lamps amongst others (ref:). PEDOT has proved useful in such a wide range of applications due to its high conductivity and uniquely high stability when in the oxidised state. An essential requirement of the applications listed above is effective film-forming properties. This is achieved by doping with poly(styrene sulfonic acid) (PSS) which promotes the formation of a water-soluble polyelectrolyte system [68]. Armelin et al studied the effectiveness of PEDOT:PSS as an anticorrosive additive in low concentrations (**0.3 wt.%**) in a conventional epoxy paint formulation for steel [69]. It was found that PEDOT:PSS additives provided a significant improvement in corrosion protection when compared with the unmodified paint formulation in an accelerated corrosion assay using aggressive saline solution. Although various papers suggest the possible applications for PEDOT:PSS as a corrosion inhibitor available literature on the substrate is very limited at present.

1.7 Theoretical principals of the Scanning Vibrating Electrode Technique (SVET)

The relatively modern innovation of scanning electrochemical techniques is a highly effective means of studying the kinetics and mechanism of metallic corrosion in aqueous environments. This is a substantial progression from traditional techniques where a basic, unspecific picture of a corroding surface was produced. In principal, the electrochemical activity of the surface of interest may be scanned periodically with a micro tip electrode to produce a series of spatially resolved maps showing corrosion over time. This enables the identification of corrosion type and allows subtle features to be observed. Scanning is conducted at very close distances from the surface where local potential values are obtained that relate to a known co-ordinate position. The ability to spatially resolve and quantify localised differences in corrosion activity on a metallic surface, and provide details of reaction rates, is highly unique. A major benefit of such

techniques is that the scanning process does not perturb the sample in any way such that results are unaffected and highly reliable.

The predecessor of the SVET is the Scanning reference electrode technique (SRET) that uses a scanning reference electrode and a remote electrode to measure the ohmic potentials generated in solution by the passage of current from anodic to cathodic sites. The SVET is derived from the SRET and provides a considerable advancement in sensitivity and spatial resolution by measurement of the vertical component of current flux in the plane of the scan. This measurement also enables a more reliable estimate of current density [98].

As described in Section 1.2.1, the electrochemical corrosion of a metal involves the flow of ionic current from a local anodic site to a general cathodic region. The ionic current distribution through the electrolyte can be considered as lines of current flux that pass from anode to cathode. The flow of electrons through the metallic substrate completes the conducting circuit. The metallic substrate can be considered as a plane of constant potential due to its negligible resistance. Conversely, the electrolyte has a substantially higher resistance and, therefore, ohmic potential gradients are produced upon the movement of ionic current through the solution. These may be represented as a series of lines of iso-potential that lie normal to the lines of ionic current flux. This is illustrated in the schematic shown in Fig 1.13.

Both the Laplace equation (equation 1.31) and Ohm's law (equation 1.32) can be used to determine the distribution of potential and ionic current in solution; these are as follows:

$$\nabla^2 E = 0 \qquad (1.31)$$

$$i = -\square \nabla E \qquad (1.32)$$

Where E represents the electrical potential, i the current and □ the conductance of the solution.

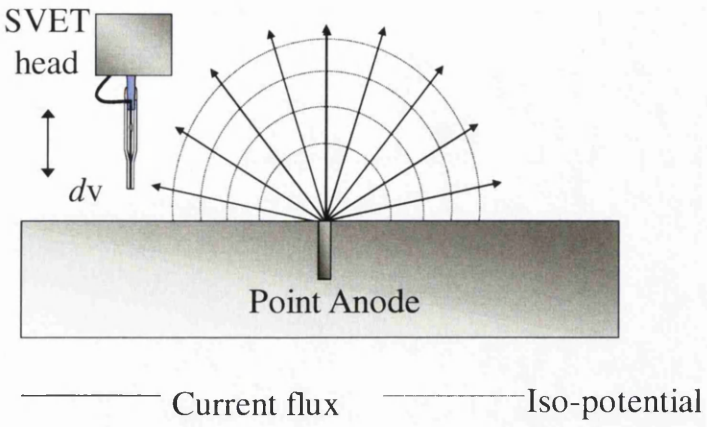

Fig 1.13 – Schematic representation of the current flux and iso-potentials generated from a point source.

Further to this, the potential at any point in three dimensional planes (x,y or z) is shown to be inversely proportional to the distance from the source for a point current source, i, situated at height z = 0 on a non-conducting x,y plane where the current drain is equal to infinity. This is given by:

$$E = \frac{i}{2\pi\kappa\sqrt{(x^2 + y^2 + z^2)}} \qquad (1.33)$$

The SVET technique is based on the scanning of a micro-tip electrode (125 μm diameter platinum wire within a glass capillary) that is vibrated mechanically at constant amplitude and frequency perpendicularly at ca. 100 μm (in the current study) above the sample surface. An alternating potential is registered, at the vibration frequency, where the vibrating tip scans over a corroding surface. This registered potential is proportional to the electric field strength or potential gradient in the direction of the vibration that arises due to ionic current flux passing through the electrolyte. Therefore, the SVET signal is directly proportional to the component of ionic current density that lies parallel to the vibration of the probe; hence, in the current study, normal to the sample surface. Due to the set distance of the vibrating micro-tip above the corroding surface, the measured signal is proportional to the vector component of the current density in the electrolyte at the height of the probe and not the surface current density [98].

By vibrating the SVET probe perpendicular to the surface, the normal electrical field strength (F) may be measured. A progression of equation 1.30, which gives the electric potential, E, at any point (x,y,z) in the electrolyte, is as follows:

$$F = \frac{dE}{dz} = \frac{iz}{2\pi\kappa(x^2 + y^2 + z^2)^{1.5}} \tag{1.34}$$

where the differentiation of equation 1.30 with respect to z has been carried out. Fig 1.14 shows the characteristically peaked shape centred about the current source that represents the distribution of normal field strength in solution across a plane of constant height above a point current source. From equation 1.31, the maximum field strength (F_{max}) at a height z will occur when the micro-tip is directly above the point source origin (i.e. x=0, y=0) and is given as follows:

$$F_{max} = -\frac{i}{2\pi\kappa z^2} \tag{1.35}$$

which, again, is recognised as the z differential of equation 1.30. It is highly critical for an SVET study that test samples are flat and contain no perturbing features. This is due to the inverse-square relationship between F_{max} and the probe height, implicit in equation 1.32 that makes the control of probe height critical in any SVET measurement. One positive feature of the SVET predecessor, SRET, is that the condition of samples is not such a concern. However, recent advances in SVET development have resulted in 3D height scanning which allows the scanning of 3D shapes whilst maintaining a constant distance from the sample surface.

In terms of accurately locating localised corrosion features, spatial resolution is of high importance; this is defined by the minimum distance between two features that is detectable by the scanning micro-tip. Theoretical spatial resolution of the SVET is determined by the calculation of signal peak width at half the maximum peak height (*whm*). If r is taken as the distance from a point current source on the x,y plane then it can be shown that:

$$r = (x^2 + y^2)^{0.5} \tag{1.36}$$

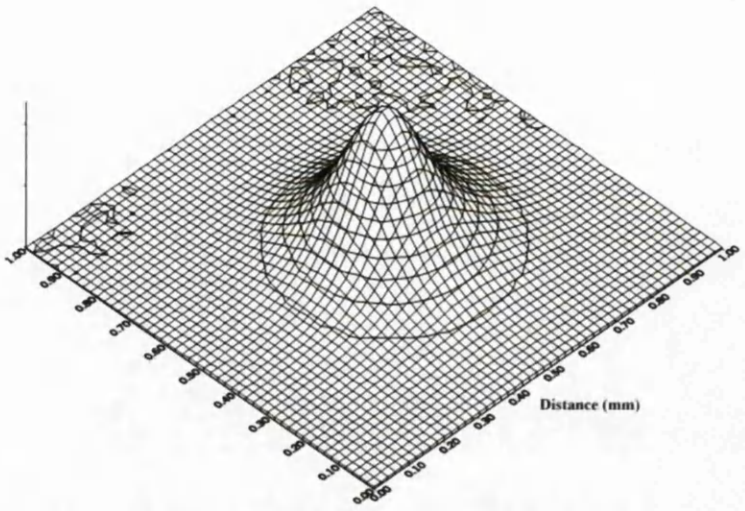

Fig 1.14 – Graphical representation of the distribution of normal field strength in solution across a plane of constant height above a point current source.

then the value of r at which the value of F falls to half of its maximum value (i.e. $0.5F_{max}$) is obtained by combining equations (1.33) and (1.34).

$$F_{max} = \frac{iz}{2\pi\kappa(r^2 + z^2)^{1.5}} \tag{1.37}$$

The ratio of equations. (1.29) and (1.31) then gives,

$$r = z(2^{2/3} - 1)^{0.5} \tag{1.38}$$

Finally, since the width of the SVET response peak is twice the value of r

$$whm = 2r = 1.533z \tag{1.39}$$

As is used throughout the current study, a scan height of 100μm would yield a theoretical spatial resolution of 153 μm. However, the actual resolution of the SVET apparatus is around 250 μm. This deviation from the theoretical resolution and the measured resolution results from the finite dimensions (i.e. the 125 μm platinum disc) of the experimental probe.

Through model studies carried out by Isaacs it has been demonstrated that the equations expressed here can be considered true when in reference to a point source [99]. When investigating the effect of probe height above a point source set in an insulating plane on the normal fields of current flux Isaacs showed that the distribution of the ionic currents emanating from the electrodes are dependent on the disk being of either

uniform current density or of a uniform potential at the surface of the disk. Scan heights are suggested to be kept above a certain limit as it was stated that when the distance between the probe and the point source approaches zero the current fields become non-linear.

1.7.1 SVET efficiency

The fixed scanning height (h) of the SVET tip has been found to be insufficient in certain situations. When scanning a corroding surface where a well established local anode is surrounded by a well distributed cathode, as in stable pitting corrosion, the distance between local anode and local cathode will be greater than h and current flux lines will cross the plane of scan and therefore be detectable. When scanning a surface where generalised corrosion is occurring and the anode-cathode distance is less than h the current flux will not cross the plane of scan and, therefore, not be detectable by the SVET; this will result in a greatly reduced efficiency of the scan [100]. This is illustrated in fig 1.15.

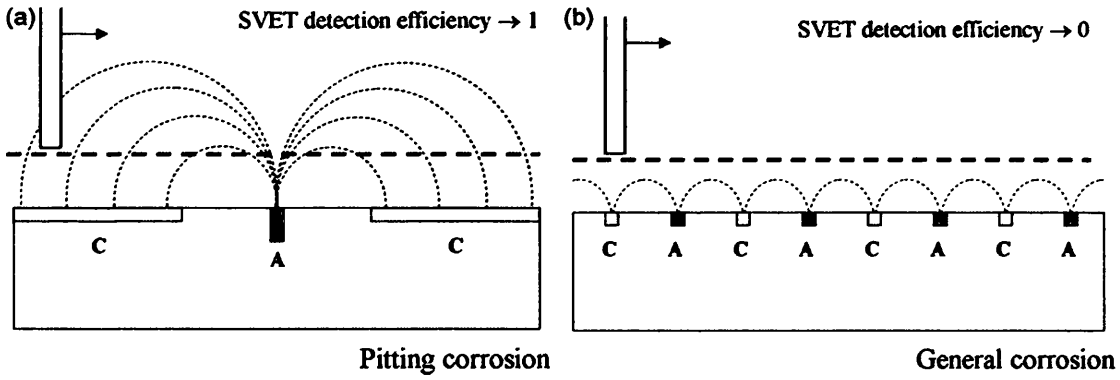

Fig.1.15 Schematic diagrams that show the SVET detection efficiency in two scenarios where (a) a local anode is surrounded by a uniformly distributed cathode where the anode-cathode distance is > h and (b) a generalised attack where the anode-cathode distance is < h [100].

1.8 Theory and principals of the scanning Kelvin probe (SKP)

Pioneered by Stratmann et el, the use of the Scanning Kelvin Probe (SKP) for the study of metallic surfaces under atmospheric conditions has allowed the advancement of investigative testing into underfilm delamination of polymeric films. One profound

benefit of the technique over traditional techniques is that, in no situation, does the sample surface need to be touched meaning damage of any kind is avoided.

In practice, atmospheric conditions are the most corrosively damaging as metal surfaces are subject to thin electrolyte layers that develop through both water adsorption and condensation. Traditional testing techniques are not suitable for testing in atmospheric corrosion conditions because an electrolytic conduction path is required to connect the scanning and reference electrodes. The SKP technique does not require a reference electrode. This allows for the electrochemical mapping of localized corrosion phenomena that occurs beneath both thin electrolyte films and intact polymer coatings. As one of the most sensitive measuring techniques in surface physics the SKP technique, or 'Kelvin's vibrating capacitor technique', has become a well established means of determining metallic work functions. Initial studies, conducted by Stratmann et al, were based on large areas; advancement in design, however, has led to lateral scanning resolutions of < 100 μm [101].

1.8.1 Principles of SKP operation

Fig 1.26 shows a schematic diagram of the SKP technique that illustrates its use in measuring surface (Volta) potential. The probe is positioned perpendicularly above the sample where the two constitute the plates of a parallel plate capacitor. The air-gap and insulating polymer (as in a delamination experiment) are the non-conducting medium present between the 'capacitor plates' and, thus, represent the capacitor dielectric. Capacitance (C) of a parallel plate capacitor can be established via the following equation:

$$C = \frac{\varepsilon \varepsilon_0 A}{d} \tag{1.40}$$

where A is the plate area, d is the distance between plates, ε_0 is the permittivity of a vacuum and ε is the dielectric constant of the capacitor dielectric. The probe electrode is vibrated relative to the sample surface in sinusoidal form at a frequency, ω, such that the distance separating the two capacitor plates, d, varies with time, t. This is represented as follows:

$$d = d_0 + d_1 \sin(\omega t) \tag{1.41}$$

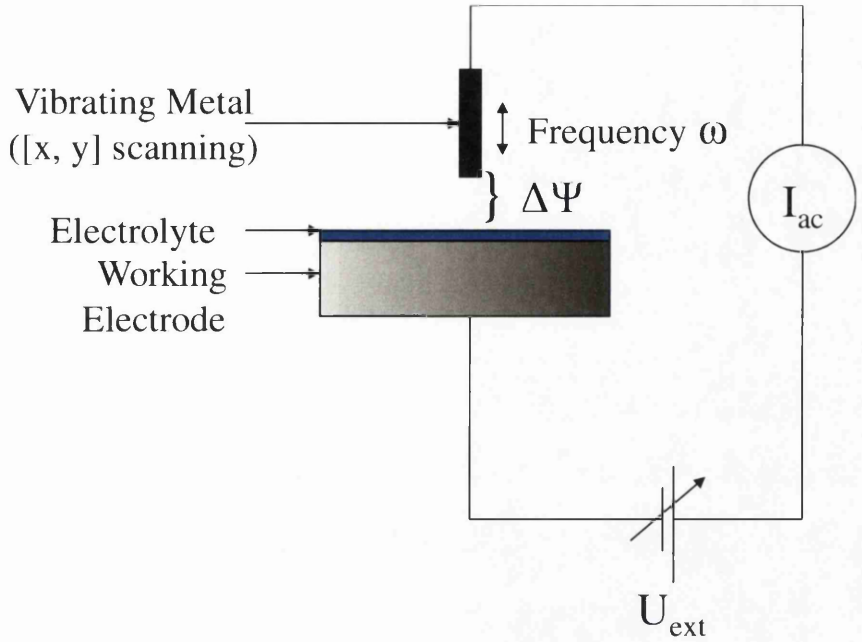

Fig. 1.16 Schematic diagram of the SKP

in which the mean plate separation is denoted by d_0, and the amplitude of vibration by d_1. A periodic fluctuation, C, is produced by probe vibration. Where any Volta (outside) potential exists between probe and sample surface, an alternating current, i, will result in the external circuit illustrated in the schematic shown in fig 1.16. This flow of current is given by:

$$i = \frac{dQ}{dt} = \Delta V \frac{dC}{dt} \tag{1.42}$$

where Q represents the electric charge on the capacitor plates. By substituting equation 1.38 and 1.39 into equation 1.40 the following is true:

$$i = -\varepsilon \varepsilon_o A \Delta V \frac{d_1 \omega \cos(\omega t)}{[d_0 + d_1 \sin(wt)]^2} \tag{1.41}$$

and, in situations where $d_0 >> d_1$ this relationship can be simplified as follows:

$$i = -\varepsilon \varepsilon_o A \Delta V \frac{d_1 \omega \cos(\omega t)}{{d_0}^2} \tag{1.42}$$

Maximum signal current (imax) is obtained when;

$$d_1 = \frac{d_0}{(2)^{-1/2}} \tag{1.43}$$

and this may be written in the form:

$$d_0 = \frac{d_{min}}{1-(\frac{1}{2}^{(-1/2)})} \tag{1.44}$$

where $d_{min} = d_0 - d_1$ = the minimum distance between the two plates.

The open circuit value of ΔV is not directly obtained from the Kelvin probe signal current. Instead, by means of adjusting the value of the externally applied DC bias voltage, E, such that the signal current is nulled i.e. made zero, the ΔV value is determined indirectly. Under such circumstances the following is true:

$$E = E_{i=0} = -\Delta V \tag{1.45}$$

If the experimentally obtained quantity $E_{i=0}$ is used to define a parameter E_{KP} where we take the following to be true: $E_{KP} = -E_{i=0}$ then E_{KP} is equivalent to the Kelvin probe-determined Volta potential difference, ΔV. The 'nulling' technique used is advantageous because the measurement doesn't perturb the sample-solution interface where an electrolyte layer is present.

1.8.2 Calibration of the scanning Kelvin probe

The conditions under which an experiment is performed have an effect on the particular physical meaning of the before mentioned value E_{KP}. For example, where measurements are taken in vacuum conditions on a pristine metal surface E_{KP} will represent the difference in work function of the sample and probe. Upon the introduction of air to an experiment the metal sample may now exhibit a surface oxide film that causes a deviation in E_{KP} values expected of the metallic work functions. Humidity is another factor that offers further deviation from a measurement of pure difference in metallic work function. With humid atmosphere comes the hydration of surface oxide layers as a consequence of water adsorption.

The complexity of the EKP interpretation increases with the presence of a conducting electrolyte film on the sample surface. In such situations the Volta potential difference measured is that between the probe electrode and the outer surface of the electrolyte film. Complexities arise due to the number of influences that may affect the electrolyte film Volta potentials. These include electrical double-layer effects at the metal-solution interface and ionic migration between localised corrosion sites causing the formation of potential gradients that set up in the solution. However, if no ionic current flow is present in solution and the electrolyte film is thicker than the electrical double layer then it may be shown that [99-100]:

$$E_{KP} = E_{corr} + \text{constant} \tag{1.46}$$

Where E_{corr} represents the free corrosion potential of the metal sample relative to a reference electrode (real of hypothetical) immersed in the film of electrolyte at the exact point of measurement.

For a polymer-coated metal substrate the half-cell potential ($E_{1/2}$) is given by:

$$E_{1/2} = \frac{\alpha_e^{ref}}{F} - \chi_{gas}^{pol} + \Delta\psi_{pol}^{ref} \tag{1.47}$$

where χ_{gas}^{pol} is the dipole potential of the polymer-gas interface and $\Delta\psi_{pol}^{ref}$ is the Volta potential difference measure between the reference probe and the polymer surface. Equation 1.44 can then be adapted for a post-delamination situation in which a layer of electrolyte exists between the metal substrate and the polymer layer. This is as follows:

$$E_{1/2} = \Delta\varphi_D + \frac{\alpha_e^{ref}}{F} - \chi_{gas}^{pol} + \Delta\psi_{pol}^{ref} \tag{1.48}$$

where $\Delta\varphi_D$ is the Donnan potential equivalent to the Galvani potential difference which becomes established between the polymer layer and the electrolyte solution ($\varphi^{sol} - \varphi^{pol}$). It can be assumed that quantities α_e^{ref}, χ_{gas}^{pol} and χ_{gas}^{pol} remain constant over time where the gas-phase composition remains unchanged.

It is typical to express the free corrosion potential, E_{corr}, of a metallic surface with respect to a reference electrode such that:

(1.49)

$$E_{corr} = E_{1/2} + E_{1/2}^{ref}$$

where $E_{1/2}$ is the half-cell potential defined in equations 1.44 – 1.46 and $E_{1/2}^{ref}$ is the half-cell potential of the reference electrode. Equation 1.46 may be used to rewrite equations 1.47 and 1.48, where A and B are constants, as follows:

$$E_{corr} = A + \Delta\psi_{sol}^{ref} \tag{1.50}$$

for the bare substrate-electrolyte interface

$$E_{corr} = B + \Delta\psi_{pol}^{ref} \tag{1.51}$$

for both the substrate-intact polymer interface and the substrate-delaminated polymer interface.

The values of A and B may be individually determined by the simultaneous measurement of E_{corr} (vs. a standard reference electrode) with $\Delta\psi_{sol}^{ref}$ and $\Delta\psi_{\square ol}^{ref}$ (using the Kelvin probe) respectively.

1.9 References

[1] K. Tretheway and C. John, *Corrosion for science and engineering*. 1995.

[2] R. Parsons, *Pure Appl. Chem*, vol. 37, no. 512, 1974.

[3] J. O. Bockris, *Modern Aspects of Electrochemistry*, 1959.

[4] P. Van Rysselberghe, *Electrochim. Acta*, vol. 9, no. 11, pp. 1343–1371, 1964.

[5] C. Wagner and W. Traud, *Electrochem. Acta*, vol. 44, p. 391, 1938.

[6] J. Tafel and Z. Physik, *Chem*, vol. 641, p. 50, 1905.

[7] I. Suzuki, *Marcel Dekker Pub. N.Y*, 1989.

[8] E. Matteson, *Basic corrosion technology for scientists and engineers*. 1996.

[9] G. Williams and H. N. McMurray, *J. Electrochem. Soc.*, vol. 148, no. 10, B377, 2001.

[10] S. M. Powell, H. N. Mcmurray, and D. A. Worsley, *Iron and Steel making* 1040–1051, 1999.

[11] A. J. Aldykiewicz, H. S. Isaacs, and A. J. Davenport, *Electrochem. Soc.*, 1995.

[12] a. Amirudin, C. Barreau, R. Hellouin, and D. Thierry, *Prog. Org. Coatings*, vol. 25, no. 4, 339–355, 1995.

[13] a. C. Bastos, M. G. Ferreira, and a. M. Simões, *Corros. Sci.*, vol. 48, no. 6, pp. 1500–1512, 2006.

[14] L. L. Shreir, G. T. Burstein, and R. A. Jarman, *Corrosion*. 1994.

[15] J. A. Burkill, J. E. O. Mayne, and J. Oil, *Colloid. Chem. Assoc.*, vol. 48, 341, 1965.

[16] A. C. Bastos, M. G. S. Ferreira, and A. M. Simões, *Prog. Org. Coatings*, vol. 52, no. 4, 339–350, 2005.

[17] N. F. Izmerov, *(Ed) IRPTC Scientific Review-UN Environmental Programme;*, 1982.

[18] J. A. Shumilla, K. E. Wetterhahn, and a Barchowsky, *Arch. Biochem. Biophys.*, vol. 349, 356–62, 1998.

[19] S.A. Katz, *Environ. Health Perspect.*, vol. 92, 13–6, 1991.

[20] A. Leng, H. Streckel, K. Hofmann, and M. Stratmann, *Corros. Sci.*, vol. 41, no. 3, 599–620, 1998.

[21] W. Fürbeth and M. Stratmann, *Prog. Org. Coatings*, vol. 39, 23–29, 2000.

[22] M. Rohwerder and A. Michalik, *Electrochim. Acta*, vol. 53, no. 3, pp. 1300–1313, 2007.

[23] G. Grundmeier, W. Schmidt, and M. Stratmann, *Electrochim. Acta*, vol. 45, 2515 – 2533, 2000.

[24] H. Leidheiser and M. Kendig, *Eng. Chem. Prod. Res. Dev.*, vol. 17, no. 1, 54–55, 1978.

[25] G. Williams and N. McMurray, *Shreir's Corros.*, vol. 2, 988–1004, 2010.

[26] W. Fürbeth and M. Stratmann, *Corros. Sci.*, vol. 43, no. 2, pp. 207–227, 2001.

[27] W. Fürbeth and M. Stratmann, *Corros. Sci.*, vol. 43, no. 2, 243–254, 2001.

[28] G. Williams, S. Geary, and H. N. McMurray, *Corros. Sci.*, vol. 57, 139–147, 2012.

[29] G. Williams, H. N. McMurray, and D. A. Worsley, *J. Electrochem. Soc.*, vol. 149, 4, B154, 2002.

[30] R. J. Holness, G. Williams, D. A. Worsley, and H. N. Mcmurray, *J. Electrochem. Soc.*, 152, 2, B425–B433, 2005.

[31] W. Fürbeth and M. Stratmann, *Prog. Org. Coatings*, 39,. 1, 23–29, 2000.

[32] C. F. Sharman, *Nature*, no.153, 621, 1944.

[33] A. Bautista, *Prog. Org. Coatings*,28, 49–58, 1996.

[34] J. Coleman, A, H. N. McMurray, G. Williams, A. Afseth, and G. M. Scamans, *Electrochem. Solid-State Lett.*, v 10, 5, C35, 2007.

[35] W.H. Slabaugh, *Paint Technol.*, 44, 76, 1972.

[36] G. Williams and H. N. Mcmurray, *Electrochem. commun.*, 5, 871–877, 2003.

[37] H. Keashe, *Werkstoffe Korros*, vol. 10, 668, 1959.

[38] R. Ruggeri and T. Beck, *NACE*, 39,452, 1983

[39] H. Leidheiser, in *NACE*, 38(7) 374, 1982

[40] W. Funke, *NACE*, , 29–46, 1981

[41] H. J. W. Lenderink, *Techniche University Delft*, The Netherlands, 1995.

[42] P. P. Leblanc and G. S. Frankel, *J. Electrochem. Soc.*, vol. 151, 3, B105, 2004.

[43] W. Funke, *Prog. Org. Coatings*,vol. 9, 1, 29–46, 1981.

[44] W. Funke, *Ind. Eng. Chem. Prod. Res. Dev.*, vol. 24, 3, 343–347, 1985.

[45] J. Zhao, *J. Electrochem. Soc.*, vol.145, 7, 2258, 1998.

[46] I. L. Rosenfeld, *Corros. Inhib,* 145, 1981.

[47] A. Leng, *Corros. Sci.*, vol. 41, 3, 547–578, 1998.

[48] G. Paliwoda-porebska, M. Stratmann, and M. Rohwerder, *Corros. Sci.*, vol. 47, 3216–3233, 2005.

[49] D. Borisova, H. Möhwald, and D. G. Shchukin, *ACS Nano*, vol. 5, 3, 1939–46, 2011.

[50] D. Snihirova, S. V Lamaka, M. Taryba, A. N. Salak, S. Kallip, M. L. Zheludkevich, M. G. S. Ferreira, and M. F. Montemor, *ACS Appl. Mater. Interfaces*, vol. 2, 11, 3011–22, 2010.

[51] D. V. Andreeva, E. V. Skorb, and D. G. Shchukin, *ACS Appl. Mater. Interfaces*, vol. 2, 7, 1954–1962, 2010.

[52] R. G. Buchheit, H. Guan, S. Mahajanam, and F. Wong, *Prog. Org. Coatings*, vol. 47, 3–4, 174–182, 2003.

[53] G. Williams and H. N. McMurray, *Electrochem. Solid-State Lett.*, vol. 6, 3, B9, 2003.

[54] H. N. McMurray and G. Williams, *Corrosion*, vol. 60, 3, 219–228,. 2004.

[55] S. P. V. Mahajanam and R. G. Buchheit, *Electrochem. Solid-State Lett,* 2012.

[56] M. L. Zheludkevich, S. K. Poznyak, L. M. Rodrigues, D. Raps, T. Hack, L. F. Dick, T. Nunes, and M. G. S. Ferreira, *Corros. Sci.*, vol. 52, 2, 602–611, 2010.

[57] J. Tedim, S. K. Poznyak, A. Kuznetsova, D. Raps, T. Hack, M. L. Zheludkevich, and M. G. S. Ferreira, *ACS Appl. Mater. Interfaces*, vol. 2, 5, 1528–35, 2010.

[58] S. Bohm, H. N. McMurray, D. A. Worsley, and S. M. Powell, *Mater. Corros.*, vol. 52, 12, 896–903, 2001.

[59] G. Williams, H. N. McMurray, and D. A. Worsley, *J. Electrochem. Soc.*, vol. 149, 4, B154, 2002.

[60] H. N. McMurray, D. Williams, G. Williams, and D. Worsley, *Corros. Eng. Sci. Technol.*, vol. 38, 2, 7, 2003.

[61] G. Williams, H. N. McMurray, and M. J. Loveridge, *Electrochim. Acta*, vol. 55, 5, 1740–1748, 2010.

[62] G. Williams, H. N. McMurray, and M. J. Loveridge, *Electrochim. Acta*, vol. 55, 5, 1740–1748, 2010.

[63] L. W. Vasconcelos, I. C. P. Margarit, O. R. Mattos, F. L. Fragata, A. S. B. Sombra, *Corros. Sci.*, vol. 43, 12, 2291–2303, 2001.

[64] M. Zubielewicz, W. Gnot, *Prog. Org. Coatings*, vol. 49, 4, 358–371, 2004.

[65] R. . Howard, I, Zin, J. Scantlebury, and S.Lyon, *Prog. Org. Coatings*, vol. 37, 1–2,. 83–90, 1999.

[66] S. Miyata, *Clay Miner.*, 1983.

[67] T. Kameda, Y. Miyano, T. Yoshioka, M. Uchida, and A. Okuwaki, *Chem. Lett.*, vol. 29, 1136–1137, 2000.

[68] C. Ocampo, E. Armelin, F. Liesa, C. Alemán, X. Ramis, and J. I. Iribarren, *Prog. Org. Coatings*, vol. 53, 3, 217–224, 2005.

[69] E. Armelin, Á. Meneguzzi, C. A. Ferreira, and C. Alemán, *Surf. Coatings Technol.*, vol. 203, 24, 3763–3769, 2009.

[70] J. Birgerson, X. Crispin, G. Greczynski, W. Osikowicz, A. W. D. Van Der Gon, W. R. Salaneck, and M. Fahlman, vol. 139, 1–10, 2003.

[71] T. D. E, G. Spinks, A. Dominis, and G. G. Wallace, *Solid State Electrochem*, vol. 6, 73, 2002.

[72] D. M. Lenz, M. Delamar, and C. A. Ferreira, *Prog. Org. Coatings*, vol. 58, 1, 64–69, 2007.

[73] T. Schauer, A. Joos, L. Dulog, and C. . Eisenbach, *Prog. Org. Coatings*, vol. 33, 1, 20–27, 1998.

[74] D. E. Tallman, Y. Pae, and G. P. Bierwagen, *Corrosion*, vol. 56, 4, 401–410, 2000.

[75] V. J. Gelling, M. M. Wiest, D. E. Tallman, G. P. Bierwagen, and G. G. Wallace, *Prog. Org. Coatings*, vol. 43, 1–3, 149–157, 2001.

[76] J. I. I. Laco, F. C. Villota, and F. L. Mestres, *Prog. Org. Coatings*, vol. 52, 2, 151–160, 2005.

[77] A. F. Baldissera and C. A. Ferreira, *Prog. Org. Coatings*, vol. 75, 3, 241–247, 2012.

[78] M. Rohwerder, L. M. Duc, and a. Michalik, *Electrochim. Acta*, vol. 54,. 25, 6075–6081, 2009.

[79] D. DeBerry, *Electrochem Soc*, vol. 132, 1022, 1985.

[80] G. Williams, a. Gabriel, a. Cook, and H. N. McMurray, *J. Electrochem. Soc.*, vol. 153, 10, B425, 2006.

[81] E. Akbarinezhad, M. Ebrahimi, and H. R. Faridi, *Prog. Org. Coatings*, vol. 64, 4, 361–364, 2009.

[82] P. J. Kinlen, Y. Ding, and D. C. Silverman, *Corrosion*, vol. 58, 6, 490–497, 2002.

[83] A. Cook, A. Gabriel, D. Siew, and N. Laycock, *Curr. Appl. Phys.*, vol. 4, 2–4, 133–136, 2004.

[84] J. E. Pereira da Silva, S. I. Córdoba de Torresi, and R. M. Torresi, *Corros. Sci.*, vol. 47, 3, 811–822, Mar. 2005.

[85] M. Kendig, M. Hon, and L. Warren, *Prog. Org. Coatings*, vol. 47,3–4, 183–189, 2003.

[86] A. J. Dominis, G. M. Spinks, and G. G. Wallace, *Prog. Org. Coatings*, vol. 48, 1, 43–49, 2003.

[87] M. Fahlman, S. Jasty, and A. J. Epstein, *Synth. Met.*, vol. 85, 1–3, 1323–1326, 1997.

[88] A. Talo, O. Forsén, and S. Yläsaari, *Synth. Met.*, vol. 102, 1–3, 1394–1395, 1999.

[89] A. Mirmohseni and A. Oladegaragoze, *Synth. Met.*, vol. 114, 2, 105–108, 2000.

[90] A. M. Fenelon and C. B. Breslin, *Surf. Coatings Technol.*, vol. 190, 2–3, 264–270, 2005.

[91] M. Tiitu, A. Talo, O. Forsén, and O. Ikkala, *Polymer (Guildf).*, vol. 46, 18, 6855–6861, 2005.

[92] B. Wessling, *Mater. Corros. und Korrosion*, vol. 47, 8, 439–445,1996.

[93] A. B. Kaiser, C.-J. Liu, P. W. Gilberd, B. Chapman, N. T. Kemp, B. Wessling, A. C. Partridge, W. T. Smith, and J. S. Shapiro, *Synth. Met.*, vol. 84, 1–3, 699–702, 1997.

[94] G. Williams, R. J. Holness, D. A. Worsley, and H. N. McMurray, *Electrochem. commun*, vol. 6, 6, 549–555, 2004.

[95] R. J. Holness, G. Williams, D. A. Worsley, and H. N. McMurray, *J. Electrochem. Soc.*, vol. 152, 2, B73, 2005.

[96] A. J. Coleman, H. N. Mcmurray, G. Williams, A. Afseth, and G. M. Scamans, *J. Electrochem. Soc.*, 2007–2010, 2007.

[97] S. K. Ghosh, *functional coatings by polymer microencapsulation.* 2006.

[98] H. McMurray and D. Worsley, *Adv. Chem. Kinet.*, vol. 4, 1997.

[99] H. Isaacs, *Electrochem. Soc*, vol. 138,. 722–728, 1991.

[100] G. Williams, A. J. Coleman, and H. N. McMurray, *Electrochim. Acta*, vol. 55, 20, 5947–5958, 2010.

[101] M. Stratmann, H. Streckel, and R. Feser, *Corros. Sci.*, vol. 32, 4, 467–470, 1991.

[102] M. Stratmann, *Corros. Sci.*, vol. 27, 8, 869–872, 1987.

[103] K. Doblhofer and M. Cappadonia, *J. Electroanal. Chem. Interfacial Electrochem*, vol. 243, 2, 337–342, 1988.

Chapter Two.

Experimental Procedures.

2.1 Materials

The studies in this thesis involve corrosion testing both by immersion of bare metal substrates and observing the corrosion on a metal surface underneath an organic coating. The current section outlines the key materials used to create the samples so the relevant experiments could be carried out. This includes both metal substrates and their coatings. Table 2.2 given in Section 2.8 at the end of the current chapter lists all other materials used.

2.1.1 Metals

All metals used throughout this study were used as substrate material. All hot dip galvanised (HDG) steel was supplied from a single batch by Tata Steel UK and comprised of 0.7 mm gauge mild steel coated on both side with a 20 μm zinc layer. All iron samples used were provided by Goodfellow Metals Ltd and were pre-cut 50 mm x 50 mm coupons of iron foil (99.9% Fe) of 1.5 mm thickness.

2.1.2 Organic coatings

Poly vinyl butyral-co vinyl alcohol (PVB), MW ~70,000-100,000, was used as a model coating for all delamination experiments and was obtained from Sigma-Aldrich Chemical Co. As PVB is soluble in ethanol it is possible to be used to make a liquid of controlled viscosity. PVB shows good adhesion to metal substrates due to a consistency of hydrophilic and hydrophobic monomers. PVB was chosen for the current study as it is simple to prepare and apply to a substrate and is of low risk to health. The structure of PVB is given in fig 2.1.

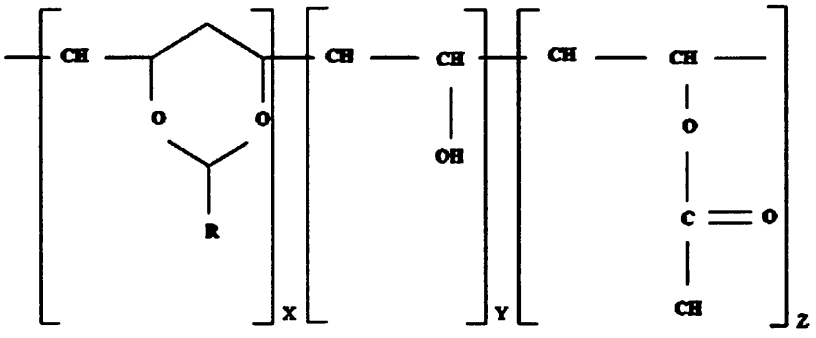

R = CH_2-CH_2-CH_3
X = No. of vinyl acetal groups
Y = No. of vinyl alcohol groups
Z = No. of vinyl acetate groups

Fig 2.1 The structure of PVB.

2.1.3 Sample Preparation

HDG steel and iron samples were prepared for experiments by, firstly, being cut using a guillotine into coupons of 50 mm x 50 mm if not already the correct size. Polishing was then carried out using 5 μm alumina powder to remove any surface oxide before subsequent rinsing with water to remove any powder residue. Finally a degreasing with ethanol was carried out to ensure a clean surface followed by air-drying.

2.2 The Scanning Kelvin probe (SKP)

The SKP technique is employed in Chapters 3, 5 and 6 for the assessment of corrosion underneath organic coatings in atmospheric conditions. The phenomenon of cathodic delamination of an organic coating from a metallic substrate has been studied. Through measuring the external potential at localised points over a sample surface an electrochemical map of the sample surface can be created and from this the coating delamination kinetics can be established.

2.2.1 Sample Preparation

In the current thesis, SKP experiments have been carried out using two types of sample set-up. In both cases samples were initially prepared as described in section 2.1.3.

2.2.1.1 Standard delamination cell

The standard sample preparation method is taken from the methods developed by Stratmann et al for the measurement of underfilm delamination [1]. A clear adhesive tape was used to cover a 15 mm x 50 mm area adjacent to one edge of the sample. Two strips of Tesla adhesive insulating tape (supplied by RS), of thickness 30 μm, were placed parallel to each other and normal to the clear tape at the edges of the sample. This left a bare strip of metal in the centre of sample of size 35 mm x 20 mm that acts as a trough for the organic coating. Approximately 0.5 cm^3 of a 15.5% w/w ethanolic PVB solution, containing the desirable amount of phenyl phosphonic acid (H_2PP) where necessary, was then deposited onto the clear tape and cast into a thin film using a glass rod which was pulled across the exposed area. The adhesive tape acted as a height guide allowing for the even coating distribution at a final dry film thickness of ~10 μm. The dry film thickness was measured in three separate areas before each experiment

using a Dektak profileometer supplied by Veeco. This process is shown in figure 2.2. The film was then allowed to dry in air over a 30 min period. The clear tape was then scribed at the edges and pulled back into a raised lip leaving an exposed area of 20 mm x 15 mm of the bare metal. A well for electrolyte was created using non-corrosive silicon sealant supplied by RS. This is shown in fig 2.12(b).

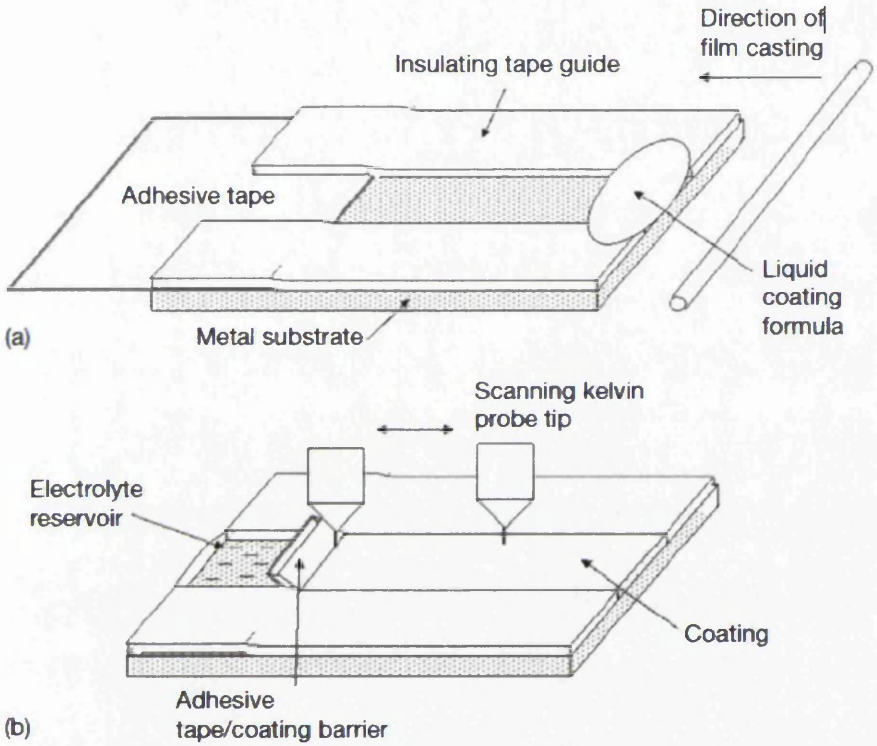

Fig 2.2 Representation of a) the bar coating process for the application of the PVB coating and b) the final sample with the defect and electrolyte well created from non-corrosive silicone rubber.

2.2.1.2 Scribed defect delamination cell

The sample preparation for this experiment was taken from a study by Williams et al [2] where both underfilm delamination and the resulting filiform corrosion (FFC) were assessed using this method. The method to be described was used for underfilm delamination. Samples were initially prepared as described in sections 2.2 and 2.3. A 15.5% w/w ethanolic solution of PVB, containing the relevant amount of H_2PP where necessary, was bar-cast onto a clean sample where strips of Tesla adhesive insulating tape, of thickness 30 μm, had been placed parallel to each another on two of the sample edges. The tape acted as a trough for the PVB which, after being allowed to dry in air for 30 minutes, had a dry film thickness of ~10 μm. A 2 mm long penetrative linear defect was scribed into the PVB layer using a scalpel blade.

2.2.2 SKP Apparatus

Fig 2.3 shows a typical schematic representation of the SKP apparatus. The sample holder, housed within the stainless steel chamber, was connected to an external tri-axial motor stage and reference probe. The whole system was computer controlled and data was collected on the computer.

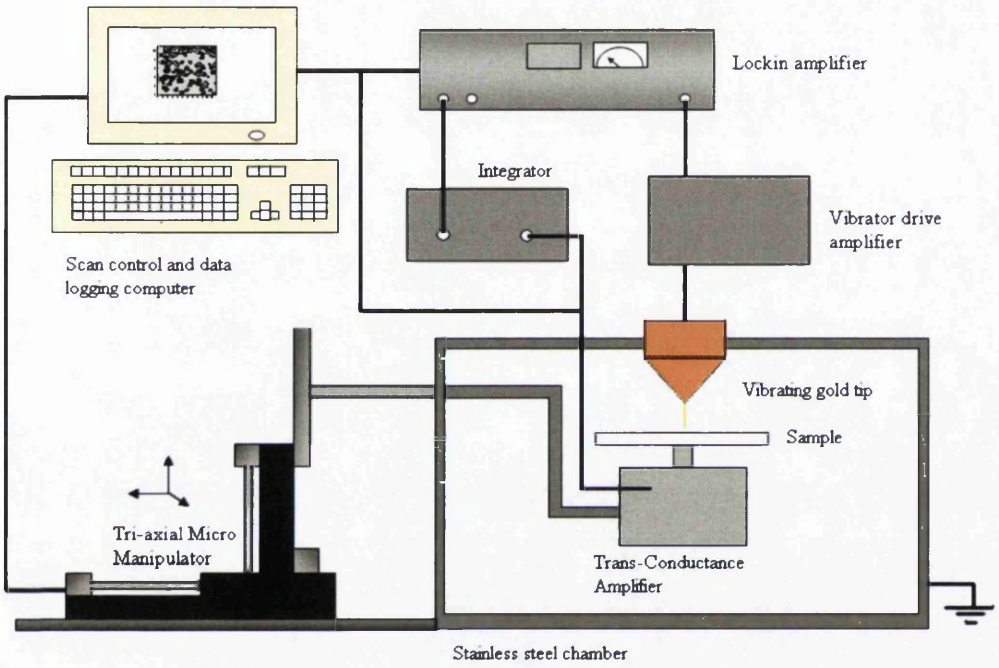

Fig 2.3 Schematic diagram of the SKP apparatus set up.

The reference probe consisted of 125 μm diameter 99.99% gold wire that was vibrated normal to the sample surface. Probe vibration was achieved via a glass push rod connected to an audio loud speaker. The speaker was driven at frequency of 280 Hz via the oscillator function on a lock-in amplifier that maintained an amplitude of 40 μm as measured via a strobe light. The periodic variation in capacitance, between the sample and reference probe that results in a generated a.c. current, was initially amplified and converted to a.c. voltage. A feedback circuit was created where a corresponding d.c. output was sent from the amplifier to an integrator where the d.c. bias voltage applied to the sample was adjusted so as to automatically null it. The integrator made the finite changes to equalise the Galvani Potentials of the probe and the specimen to nullify the a.c. current. When the integrator alters the bias d.c. voltage, the system determines the effect it has on the a.c. current, gradually with smaller and smaller changes the system

reaches null conditions. Once the stable condition is reached the integrator sends the magnitude of the reverse bias required, converted to a digital signal by the lock-in amplifier to the computer.

2.2.3 Operation of the SKP

After calibration of the SKP (described in Section 2.2.4) the test sample was mounted on the 'stage' in the stainless steel chamber and levelled manually. The first step in levelling was to position the probe over one end of the sample area and incrementally reduce the distance between sample and probe by raising the sample up to the probe. At the point of contact between sample and probe an overload signal was read on the lock-in amplifier. The sample was subsequently lowered so that a distance of 100 μm separated it from the probe and was then moved to the opposite end of the scan area. The same procedure was repeated where the distance between probe and sample was incrementally decreased until an overload was again registered. The required distance the sample needed to be raised to touch the probe was registered. The sample stage was then adjusted accordingly until both extremities of the scan area were equidistant from the probe in a vertical direction. Upon achieving a level sample, sample and probe were separated by 100 μm; this was the scanning height. It was highly important to ensure the sample was correctly levelled to allow a constant scan height during the experiment.

All delamination experiments were carried out at room temperature and the humidity of the chamber was maintained at 95% relative humidity by the incorporation of electrolyte reservoirs in the chamber. Before each scan the sample was left without the addition of electrolyte inside the closed stainless steel chamber to allow the correct humidity to be established and the full hydration of the coating. In all standard delamination cells 5% w/w $NaCl_{(aq)}$ was used as the initiating electrolyte in the sample well. The Spatial resolution of the Volta potential can then be achieved by scanning the sample area along four 12 mm lines to the defect boundary. Scans were carried out immediately after the addition of electrolyte and then at regular intervals as specified in the relevant chapter. The computer recorded a data grid for each scan.

2.2.4 Calibration of the SKP

SKP was calibrated in terms of electrode potential using a comparison with known standard redox couples Ag/Ag^{+}, $Cu/Cu2^{+}$, Fe/Fe^{2+}, and Zn/Zn^{2+} couples according to an

established calibration procedure. Calibration cells consisted of machined wells ~15 mm in diameter and 5 mm deep in disks of the respective metal. The wells were then filled with 0.5 mol dm^{-3} aqueous solution of the respective metal chloride salt or, in the case of silver, 0.5 mol dm^{-3} nitrate salt. Values for E_{KP} were obtained by vibrating the probe in a position ~100 μm above the electrolyte meniscus in the centre of the well. The electrode potential was simultaneously measured vs. SCE using a Solartron 1280 potentiostat.

When using SKP to carry out experiments on an organically coated metal sample, the effect of the coating must also be accounted for. The calibration of the PVB film has been carried out elsewhere and found to amount to an offset of -220 mV. In brief, a self-supporting PVB film of the coating is produced and placed over the calibration disk so that it is in contact with the electrolyte meniscus. The polymer film is then allowed to equilibrate with electrolyte 6 hours prior to the E_{KP} measurements. These measurements were obtained by the same procedure described above.

After scanning, calibration of the obtained data was carried out using the following equation:

$$\mathbf{E_{corr} = E_{kp} + constant} \qquad (2.1)$$

If calibration using the Cu/Cu^{2+} redox couple is considered, where the known E_{corr} for Cu is 298 mV, the value of the Cu/Cu^{2+} measured by the SKP thus allows the constant to be calculated. As described above, a material specific offset must be factored into the final calibration calculation when data is obtained from scanning above an organic coating. In the case of PVB this value is -220 mV. An example of a calibration calculation is given below where 250mV is an example of an experimentally obtained reading for a Cu/Cu^{2+} redox couple:

298 = -250 + constant

548 = constant

Then taking into consideration the PVB-

548-220

= 328 mV

Therefore, where the value of 250 mV is obtained using the described calibration technique, a final value of 328 mV must be added to the Kelvin Potential recorded via the experiment.

2.2.5 Scanning Kelvin probe analysis

Data was then be extrapolated via Microsoft Excel in the form of time dependant E_{corr} vs. Distance plots. From this the distance of potential change that results from a delamination front was measured. This then allowed the delamination kinetics to be plotted in terms of distance against time.

2.3 Use of the Scanning Vibrating Electrode technique for the evaluation of corrosion behaviour

A wealth of previous studies exist where the SVET has been employed to gain a greater understanding of the mechanisms of corrosion that occur on metal surfaces fully immersed in solution [3–6]. Locally occurring corrosion events may be resolved in SVET by the use of a movable micro-tip electrode. An alternating potential is detected at the vibration frequency proportional to the potential gradient in the same direction as the vibration that emanates from the current source in solution [3]. Due to this the SVET translates extremely well to localised corrosion study as anodic events occurring on a galvanised surfaces in chloride electrolytes can be considered point current sources. The SVET can be utilised to assess the corrosion behaviour of a variety of metallic coating systems and has the ability to determine the location and intensity of anodic and cathodic events occurring on the surface of the metal in question. Time dependant metal loss and anodic current density can be semi-quantified allowing for the comparison of different systems i.e. coating systems or electrolyte inhibitor additions.

2.3.1 SVET for the study of corrosion occurring on fully immersed, bare metallic surfaces

A constant scan height of 100 μm was set for the glass encased 125 μm platinum wire SVET microtip which scanned across the corroding sample surface submerged in the electrolyte (5% w/v NaCl for all tests where inhibitor additions were made to the relevent electrolyte). The SVET scanned over the surface twice hourly for a total of 24 h in each experiment. A 24 h representation of the corrosion activity at the surface could then be created for analysis [7]. The dissolved oxygen concentration in bulk solution

was assumed to be the equilibrium concentration for air saturated water constant of 2.8 x 10^{-4} mol dm^{-3} [3]. The SVET probe was vibrated normal to the sample surface at a frequency of 140 Hz with amplitude of 30 μm. The amplitude of tip vibration was measured by viewing the tip under a microscope with applied light from a stroboscope. This served to slow the visible motion of vibration so an amplitude measurement could be taken easily. Control of the frequency and probe signal measurement was carried out by the use of a lockin amplifier (Perkin Elmer EG & G model 7625) and digital signal averaging (typically of ten successive measurements) was carried out to enhance the signal-to-noise ratio. Movement of the probe over the sample surface was controlled by the use of linear bearings driven by stepper motor on a tri-axial micromanipulator platform supplied by Time and Precision Ltd. The SVET tip was held in a Teflon holder that attaches to a glass push rod. The push rod attaches to the cone of a speaker that serves to provide the vibration to the tip. The speaker and push rod are encased in a mu-metal box that acts to reduce electromagnetic leakage to a minimum.

2.3.2 Sample preparation for SVET

All metal samples were prepared as described in section 2.1.3. An area of ca. 10 mm x10 mm (the exact size of which was noted in each case) was isolated in the centre of the coupon using insulating extruded PTFE self-adhesive tape so that only the scan area was exposed. For any given test corrosion was observed on the scan area only and not anywhere else on the sample for the duration of a 24 h scan.

2.3.3 SVET Calibration

The component of current flux normal to the sample surface generated by a current source in solution is measured by the SVET. This is achieved via the vibration of the micro-tip above the point current source at constant height, frequency and vibration. The potential measured by the SVET micro-tip is proportional to the electrical field strength, F, or potential gradient in the direction of vibration. Eq 2.2 details how the field strength, F, varies with distance from the point source (i).

$$F = \frac{dE}{dz} = \frac{iz}{2\pi\kappa(x^2 + y^2 + z^2)^{1.5}} \qquad (2.2)$$

K = conductivity of the electrolyte

x,y and z are distances in the horizontal and vertical planes.

$$F_{max} = \frac{i}{2\pi\kappa z^2} \qquad (2.3)$$

The value of F will therefore be at its maximum when the microtip is directly above the point source shown by Eq 2.2.

By Ohm's law, the current flux density along the axis of probe vibration (j_z) is related to the peak-to-peak SVET voltage signal (V_{pp}) by the following:

— (2.4)

where k is solution conductivity and the SVET calibration factor may be defined as $G=k/A_{pp}$. In practice, calibration was carried out by the use of a two compartment cell; this is shown schematically in fig 2.4.

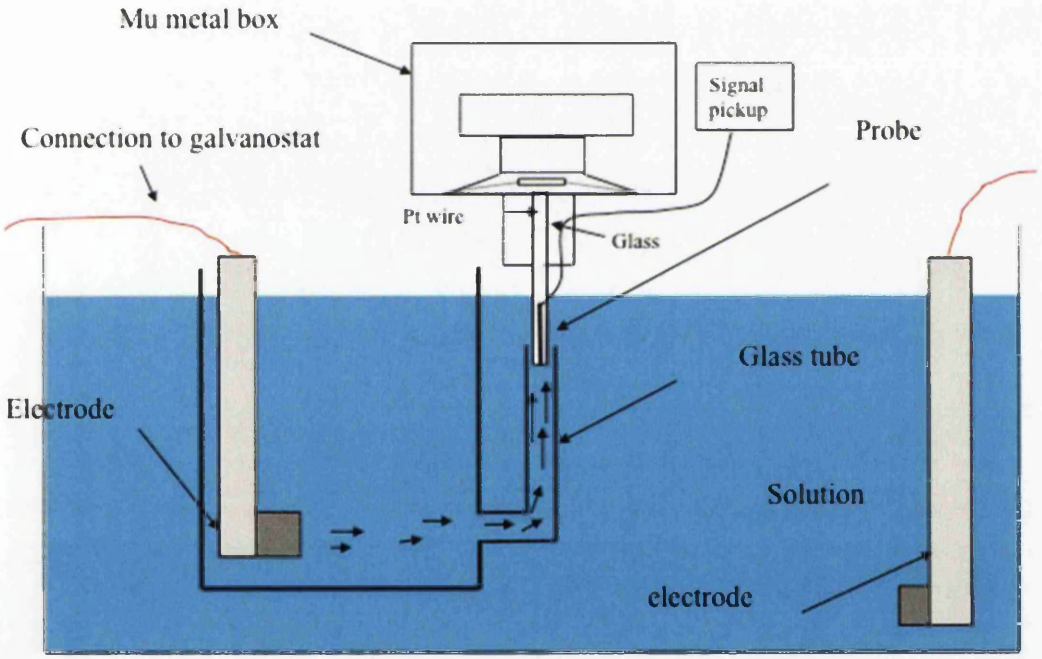

Figure 2.4 Schematic representation of the calibration instrumental set-up

A 1 cm^2 Pt electrode was placed in each compartment of the cell and compartments were linked by an electrolyte-filled glass tube, vertical in orientation, 70 mm in length and 5mm in internal diameter. The SVET tip was placed ca. 5 mm downwards inside the glass tube and a nanogalvanostat was employed to pass a range of currents through the tube. At this position, current flux density was constant across the diameter of the tube and equal to the cell current divided by the internal cross-sectional area (where the cross-sectional area of the SVET probe is deducted). An area of uniform current

density is created by the tube as lines of current flux align parallel to its length and parallel with the axis of probe vibration. The voltage was measured for each resultant current density and a linear relationship was observed as shown in fig 2.5. The instrument calibration factor was obtained from the gradient of the current density vs. recorded SVET voltage plot.

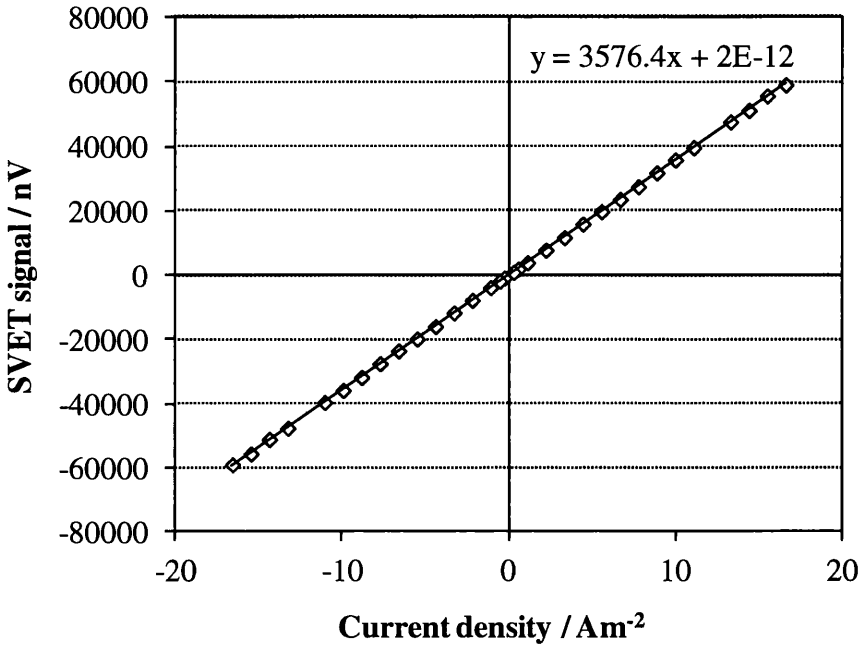

Fig 2.5 SVET calibration plot measured in 5% w/v NaCl electrolyte where signal changes linearly with current.

2.3.4 Rendering of SVET data

The SVET data was calibrated via the procedure described in the previous section in order to convert the raw data in nV into Am^2. The data was uploaded into the cartography package Surfer™ from Golden Software. False colour contour maps were created using this software for each half hourly scan allowing for the detailing of anode and cathode intensity and location. In all results throughout the study the anodic activity is defined in red and cathodic activity in blue. Signal strength is depicted by colour intensity and the scale bar provides the link between the colour depth and an exact value of current density. The position, intensity and life times of local corrosion activity occurring on the sample surface can then be monitored.

The data from the numerous current density surface plots produced in each 24 h scan was expressed in a compact manner by an estimation of time dependent evolution of local corrosion currents obtained through the numerical area integration of j_z. Numerical integration, given in Equation (2.5), provided a minimum estimate of time-dependent total anodic current (I_t) and, therefore, area-averaged anodic current density (j_t) associated with each of the current density distribution j_z maps.

$$I_t = A.J_t \geq \int_0^X \int_0^Y [j_{z(x,y)} > 0] dxdy \qquad (2.5)$$

where A is the area of the sample, X and Y are the length and width of the SVET scan. The trapezium rule employed to carry out the numerical integration allowing a single J_t value to be obtained per half hourly scan. The estimated values could then be plotted with respect to time and used for a comparative assessment of each sample [8]. Random electrical noise superimposed on the SVET signal (typically 1 μV peak-to-peak which corresponds to ±0.06 A m^{-2}) must be compensated for. Therefore, a J_{at} value carried out for a blank experiment was subtracted from each individual area-averaged anodic J_{at} current density value calculated according to Eq 2.5. A mean J_{at} value was obtained from five separate blank SVET scans carried out over a glass slide immersed in 5% w/v $NaCl_{(aq)}$.

By making the assumption that corrosion activity occurring on the sample remains constant in the interval between scans, it is possible to calculate the amount of metal lost during each experiment by utilising Faraday's law.

$$\frac{J_{at}.t}{F} \cdot \frac{A_r(Zn)}{n} \qquad (2.6)$$

F = Faraday's constant, (96487 C/mol)

n = no. of electrons lost during corrosion, which is 2 for the case of Zn

A_r = atomic weight, in the case of zinc is 65

Total metal loss for the entire 24 h experiment can, therefore, be calculated by summing the individual half-hourly mass loss values.

2.4 Filiform corrosion experiments

In all cases iron samples were prepared as described in Section 2.1.3 and 2.2.1.2 where a 10 mm penetrating scribe was made into the PVB coating containing the relevant levels of H_2PP. In all cases, FFC was initiated by introducing a volume of 2 µl of aqueous 0.005 M $FeCl_2$ to the scribe and allowing to dry in room air. Samples were then placed in an environment chamber that was maintained at a constant 93% relative humidity and 20°C. Samples were then photographed using a 600G Canon camera on a weekly basis. Photographic images were then analysed using SigmaScan Pro software, this is described in full in Section 2.6.3.

2.5 Open circuit potential (OCP) measurements

All metal samples were prepared as described in section 2.1.3. An area of ca. 10 mm x10 mm was isolated in the centre of the coupon using insulating extruded PTFE self-adhesive tape so that only this area was exposed. A small area of exposed metal was also left un-taped at the top edge of the sample so that an electrical connection could be made. The sample was immersed in 5% w/v $NaCl_{(aq)}$ electrolyte, ensuring that the exposed area for electrical connection was out of the water. This was then connected as the working electrode and held in place next to a calomel reference electrode, which was also immersed in the electrolyte. Time-dependent free corrosion potential measurements were performed using a Solartron SI 1280B Electrochemical Workstation.

2.6 Time-lapse photography

Time-lapse photography is a method adapted for the visualisation of corrosion and its progression over time. The technique is particularly useful to be used in conjunction with results from the SVET to aid the overall understanding of the corrosion process. The formation of any artefacts that may not be observed using the SVET may also be highlighted.

2.6.1 Sample preparation for time-lapse photography

All materials tested using time-lapse photography in Chapter 7 of this thesis were supplied by Tata Steel UK RD&T department. Material was received in the form of A4 sheets of cold rolled (CR) steel with a thin organic coating (TOC) applied by bar-

coating or by various methods on a pilot line; details of this will be specified where required. Material was cut into coupons of ~20 x 20 mm using a guillotine. Coupons were then covered completely using insulating extruded PTFE self-adhesive tape leaving only a 10 mm x 10mm exposed area of the organically coated metal surface.

2.6.2 Time-lapse photography apparatus and operation

A Canon G10 Power-shot camera with a close up lens was set up in the desired position using a tripod. The camera was controlled remotely using Canon software. Fluorescent lighting was used to ensure a good contrast could be achieved on the sample. Fully prepared samples, as described in section 2.6.1, were affixed to the bottom of a petri dish using double sided tape. Electrolyte of the required concentration of NaCl was added to the petri dish and the first image was taken immediately. Images were acquired at a rate of one image every 30 minutes for a duration of up to several days, exact timings are given in the relevant chapter.

2.6.3 Rendering of time-lapse photography data

The raw photographic image files were edited using the 'batch process' tool in Photoshop CS3 software to obtain an image of just the required test area. Edited images were then uploaded into SigmaScan Pro software where they were converted to grey-scale. A calibration of each image was carried out to determine a fixed size. The colour intensity threshold was then altered so that the areas of interest were highlighted, this is demonstrated in fig 2.6 and fig 2.7. The highlighted areas were subsequently measured as a percentage area of the whole image.

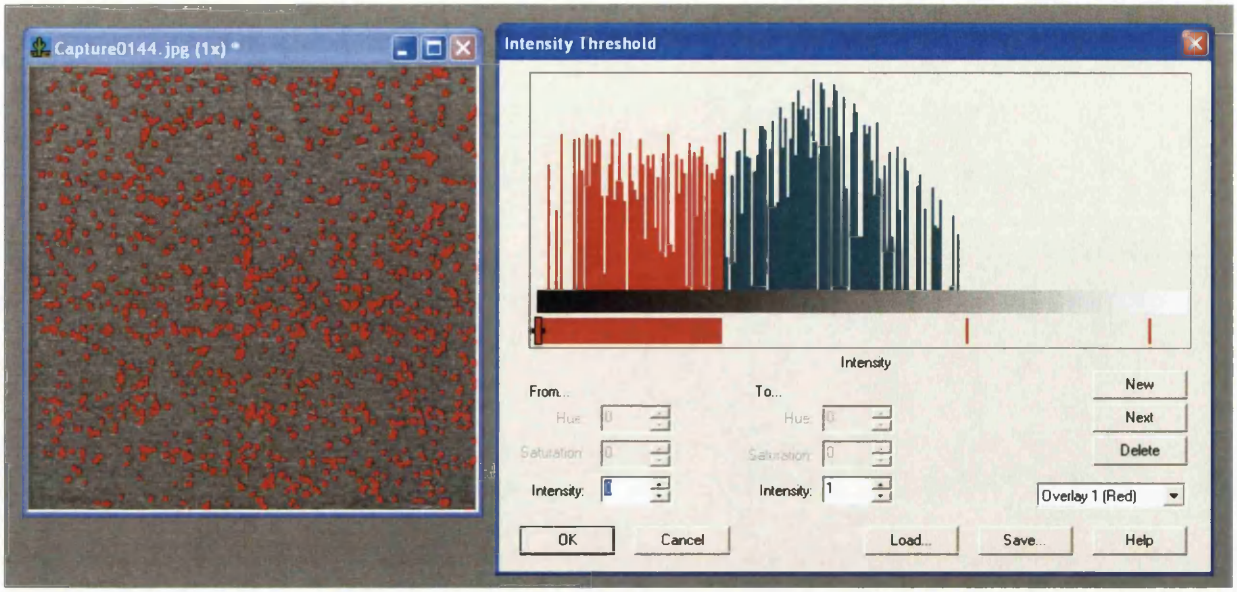

Fig 2.6 Screen shot of SigmaScan Pro software where the colour intensity threshold is adjusted to allow measurement of specific tones.

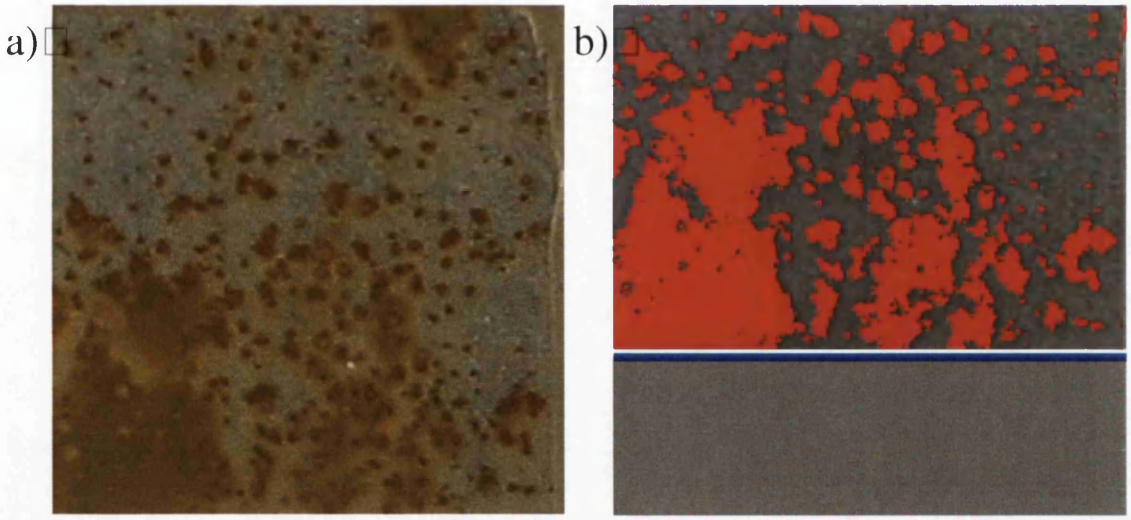

Fig 2.7 A partially corroded sample shown by (a) a photographic image and (b) the same image in grey-scale where SigmaScan Pro software has been used to highlight the corroded regions for measurement.

2.7 Atmospheric corrosion testing

Atmospheric corrosion tests were carried out to determine the resistance of materials to a humid atmosphere. In the current thesis the corrosion performance of thin organic coatings (TOC) on cold reduced (CR) steel was assessed in accordance with BS 3900 – Part F2 [9]. The degree of rusting was assessed according to ASTM D610-08 [10]. All the systems were evaluated in duplicate, with one cut edge exposed and no scribe.

2.7.1 Atmospheric corrosion testing sample preparation

Samples of CR steel were received from various pilot line trials coated on one side with a TOC. Samples were all cut to a standard size of approximately 150 mm x 80 mm. The back and edges of the sample were masked using insulating extruded PTFE self-adhesive tape. One cut edge was left exposed and no scribing was carried out.

2.7.2 Atmospheric corrosion experimental methods

Prior to exposure to a humidity chamber, samples were dried for a minimum of 16 h at a temperature of 23± 2°C and a relative humidity of 50 ± 5 % with free air circulation and protection from direct sunlight. The testing procedure commenced immediately prior to this conditioning period. Samples were held vertically in a closed humidity chamber with a cyclic fluctuation of temperature between 42°C and 48°C. The relative humidity was maintained at approximately 100% to insure the constant presence of copious condensation on the panels.

2.7.3 Evaluation of the degree of rusting for atmospheric corrosion tests

Evaluation of the degree of rusting on the CR steel panels containing a TOC was carried out with accordance to ASTM D610-08 [10]. First, the area to be evaluated was selected and the type of rust distribution was determined using the definitions defined in Table 2.1 and visual examples such as those given in fig 2.7. The percentage area rusted was then estimated using visual examples such as those shown in fig 2.8. The rust grade was then determined by the percentage of area rusted again using Table 2.1. A rust rating was assigned using rust grade 0 – 10 followed by either S for spot, G for general, P for pinpoint or H for hybrid.

Table 2.1 Scale and description of rust ratings [10].

Rust Grade	Surface Rusted (%)	Spot (S)	Visual Examples General (G)	Visual Examples Pinpoint (P)
10	Less than or equal to 0.01%		None	
9	Greater than 0.01% and up to 0.03%	9 – S	9 – G	9 – P
8	Greater than 0.03% and up to 0.1%	8 – S	8 – G	8 – P
7	Greater than 0.1% and up to 0.3%	7 – S	7 – G	7 – P
6	Greater than 0.3% and up to 1%	6 – S	6 – G	6 – P
5	Greater than 1% and up to 3%	5 – S	5 – G	5 – P
4	Greater than 3% and up to 10%	4 – S	4 – G	4 – P
3	Greater than 10% and up to 16%	3 – S	3 – G	3 – P
2	Greater than 16% and up to 33%	2 – S	2 – G	2 – P
1	Greater than 33% and up to 50%	1 – S	1 – G	1 – P
0	Greater than 50%		None	

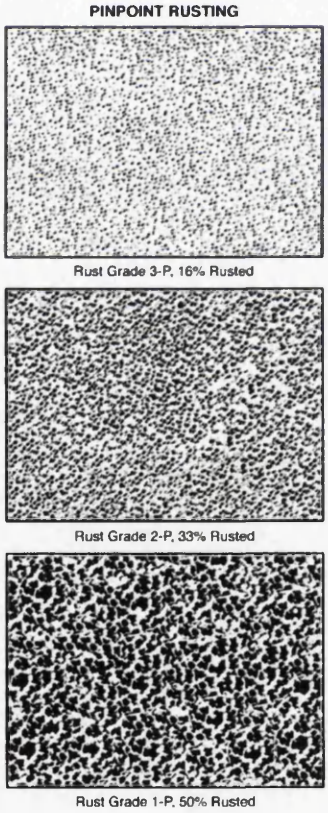

Fig 2.8 Examples of area percentages rust grades on coated samples [10].

2.8 Materials, chemicals and reagents

Table 2.2 List of materials used in current thesis

Material	Supplier	Purity
Hot dip galvanised Steel Substrate	Tata Steel UK	
Iron coupons	Goodfellow Metals Ltd	99+%
NaCl	Sigma-Aldrich	99+%
NaOH	Sigma-Aldrich	99+%
Ethanol	Sigma-Aldrich	99+%
PVB	Sigma-Aldrich	99+%
Silicon Rubber	RS	Non-Corrosive
Alumina Powder	Buehler	
PTFE tape	RS	
Phenyl phosphonic acid	Sigma-Aldrich	99+%
PEDOT:PSS	AGFA Orgacon^{TM} Inks	
Sodium phosphate	Sigma-Aldrich	99+%
Tesla tape	RS	

2.9 References

[1] M. Stratmann, A. Leng, W. Fürbeth, H. Streckel, H. Gehmecker, and K.-H. Groβe-Brinkhaus, *Prog Org Coat*, vol. 27, 1–4, 261–267, 1996.

[2] G. Williams and H. N. Mcmurray, *Electrochemistry Communications*, vol. 5, 871–877, 2003.

[3] H. N. Mcmurray, S. M. Powell, and D. A. Worsley, *British Corrosion Journal*, vol. 36, no. 1, 2001.

[4] D. A. Worsley, A. Belghazi, and S. M. Powell, *Iron and Steelmaking*, vol. 26, no. 387, 1999.

[5] K. Ogle, S. Morel, and D. Jacquet, *Elec. Chem. Soc.*, vol. 153, no. 1, B1–B5, 2006.

[6] D.Worsley, D. Williams, and J. S. Ling, *Corrosion Science*, vol. 43, no. 12, pp. 2335–2348, 2001.

[7] A. Bonnel, F. Dabosi, C. Delouis, M. Dupart, B. Kedam, and J. Tribollet, *Elec. Chem. Soc.*, vol. 130, no. 4, 753–761, 1983.

[8] G. Williams, H. N. McMurray, and R. Grace, *Electrochimica Acta*, vol. 55, 27, 7824–7833, 2010.

[9] "Test for paints - Part F2, determination of resistance to humidty (cyclic condensation)" 1989.

[10] "Standard Practice for Evaluating Degree of Rusting on Painted Steel Surfaces 1," 4–9, 2012.

Chapter Three.

Inhibition of corrosion-driven organic coating delamination on hot dip galvanised steel by phenyl phosphonic acid.

3.1 Introduction

The market for organically coated hot dip galvanised (HDG) steel products is of worldwide proportions. An integral component of the organic coating system comprises a primer layer, which provides corrosion protection to the underlying steel by means of corrosion inhibitive pigments dispersed within an organic binder. The most effective anti-corrosion pigment technologies are those based upon sparingly soluble salts of chromium (VI) anions, such as zinc or strontium chromate. However, legislative pressure to replace the traditional, highly effective, yet toxic and carcinogenic, inhibitor pigments based on chromium (VI) with credible, environmentally acceptable technologies presents a major challenge in corrosion science research [1,2]. The detrimental environmental and health risks of Cr(VI) are described in detail in Section 1.3.8. Furthermore, an industrial demand for a reduction in primer coating dry film thickness exists, driven by the need for cost savings and reduced environmental impact. Therefore, potential replacements for chromium (VI)-based inhibitors must be compatible with organic coatings of thicknesses of typically less than 10 μm.

The conventional approach to incorporating chrome-free inhibitors into an organic coating system is to disperse pigments that are sparingly soluble salts such as zinc phosphate [3–5]. The prevention of delamination by the incorporation of such pigments is attributed to several mechanisms such as improved barrier properties [6]. Precipitates of tertiary phosphates with zinc have also been reported where phosphate layers at the anodic and cathodic sites occur [7,8] hindering the access of oxygen to the substrate. Such pigments continuously leach constituent ions when in contact with aqueous media. This results in the passivation of the over-coated zinc surface, and contributes to the prevention of underfilm delamination [9], however, this uncontrolled leaching can result in long term environmental issues [10]. A recent innovation that provides a potential solution to such issues is the 'smart-release' system where the release of stored inhibitor species and the sequestration of aggressive ions occurs when contact is made with a corrosive electrolyte [11,12]. Ion-exchange pigments based on naturally occurring Wyoming Bentonite clays display this double effect where harmful chloride anions are absorbed and inhibiting ions are released [13–15]. Furthermore, the incorporation of any inorganic or organic species may be applied as they may be employed as generic 'inhibitor delivery systems'. This increases the range of inhibitors that may be included within a protective coating without the constraint of only using those ionic

species that form sparingly soluble salts. The smart release of stored inhibitor species may also be triggered by a change in the metal substrate potential. Conducting polymer coating systems, such as polypyrrole, have been shown to release inhibitor anions only, when the potential at and around the defect falls below a threshold value [16,17]. Other systems, for example those based on meso-porous silica [18], hydroxyapatite [19] and layer-by-layer deposited polyelectrolytes [20], intelligently release inhibitor species where a change in the local pH occurs. Such new technologies are discussed in full in Section 1.5.

In the current Chapter a different approach is used where the inhibitor, in its acid form, is directly dissolved into a solution of the polymer. The approach is similar to that taken for etch-primers where certain components of the primer solution cause a reaction with the metal surface and lead to the formation of a protective layer at the metal-organic coating interface. For example, Marsh et al report the increased surface area available for coating adhesion interactions where traditional chromate pigmented etch-primers are employed as anti-corrosion pre-treatments for steel [21].

For the current study an in situ scanning Kelvin probe (SKP) technique was adopted to follow the delamination kinetics of thin (ca. 10 μm) polyvinyl butyral (PVB) coatings, containing phenyl phosphonic acid (H_2PP) additions over a range of concentrations, adherent to a HDG steel substrate. The SKP technique allows the temporal and spatial resolution of potential distributions beneath intact organic coatings and has been extensively used in the study of delamination [9,11,22,23]. The principal aim has been to determine the efficiency of H_2PP as an inhibitor to corrosion-driven cathodic disbondment when dissolved in a thin PVB coating applied to a HDG steel surface. The mechanism by which H_2PP prevents cathodic disbondment is determined by analysis of delamination kinetics. Delamination testing has been carried out on both uninhibited coatings, where various levels of H_2PP have been added to the experimental electrolyte, and through in-coating additions of H_2PP.

It has been demonstrated in a recent study that H_2PP additions made to a PVB coating effectively inhibit filiform corrosion on aluminium substrates [24]. Williams et al also showed that particulate polyaniline doped with H_2PP dispersed in a PVB coating efficiently decreases the rate of cathodic disbondment on iron surfaces by up to 99% with increasing volume fractions (□) (i.e. □ ≤ 0.05) [25]. A key feature of the overall

mechanism, described by Williams, is the ability of H_2PP to form an electron transfer blocking, insoluble, salt film with divalent metal cations. The work described here investigates the influence of H_2PP on cathodic delamination when various levels of the inhibitor are dissolved in a PVB coating applied to a HDG steel substrate.

3.2 Experimental details

3.2.1 Materials

Hot dip galvanised steel samples, provided by Tata Steel UK, were a gauge of 0.7 mm mild steel coated with a zinc layer of 20 μm cut into square coupons of 50 mm x 50 mm. Polyvinyl butyral (PVB) solutions were prepared in ethanol (15.5% w/w) and the required amount of phenyl phosphonic acid (H_2PP) added and thoroughly mixed. All chemicals were supplied by Sigma-Aldrich Chemical Co. and were of analytical grade purity.

3.2.2 Sample preparation

Samples were prepared as described in Section 2.13. In the current chapter all SKP experiments were carried out using a standard delamination cell as described in Section 2.2.1.1 and well documented elsewhere in literature published by Stratmann et all [26].

3.2.3 Methods

An electrolyte of 5% w/v $NaCl_{(aq)}$ was used in all case; this concentration is typical for industry standard accelerated corrosions tests such as salt spray. Where H_2PP inhibitor was added to the electrolyte, neutralisation to pH 7 was carried out on a drop-by-drop basis using additions of an aqueous sodium hydroxide (NaOH) solution.

The SKP reference probe was scanned over the coated surface in a 12 mm line normal and adjacent with the defect-coating boundary. Scanning commenced immediately on the addition of electrolyte and thereafter at hourly intervals over a period of 24 h. A 100 μm reference probe-to-air gap was used with E_{corr} data points recorded at 20 per mm. In all delamination experiments the temperature and humidity were kept constant at 25°C and 95% r.h. The full description of SKP instrumentation, calibration procedure, set-up and subsequent analysis can be found in Sections 2.2.2 to 2.2.5.

For experiments carried out in the presence of an electrochemically deposited Zn^{2+}/ phenylphosphonate salt layer the HDG steel coupon was masked off using 90 μm thick extruded PTFE 5490 tape (3M Ltd.) leaving an exposed area of ca. 10 mm x 20 mm. The Zn^{2+}/phenylphosphonate salt layer was electrochemically deposited using a three electrode set-up where the HDG steel sample (working electrode), a calomel reference electrode (SCE) and a platinum counter electrode were immersed in aqueous solution containing 0.05 M H_2PP and 0.015 M $ZnCl_2$. A Solartron SI 1280B Electrochemical Workstation was employed to apply a 0.1 V for 30 min. The tape was then removed and the sample was lightly rinsed using distilled water. A Stratmann cell was then produced using the methods described in Section 2.2.1.1 where the deposited film was over-coated with PVB and the defect region was a bare HDG steel surface.

In those experiments that required a switch from air to N_2 inside the SKP chamber, two hoses passing through two separate dreschel bottles containing 5% w/v NaCl (aq) were fed into the chamber. Air was pumped through the dreschel bottle using a KNF Laboport vacuum pump and, when required, this was switched off and the N_2 was pumped through the other dreschel bottle from a cylinder. In both cases a Cole-Parmer valved flow meter was used to ensure equal flow rates. A Lascar EL-USB-1 data logger was kept inside the chamber at all times to record the humidity.

In order to determine the solubility product (K_{sp}) of the ZnPP salt, titrations were carried out where $ZnCl_{2(aq)}$ solutions, of various concentrations, were titrated from a burette into a beaker containing 10 ml of aqueous solution containing various concentrations of H_2PP adjusted to pH 7. The volume of $ZnCl_{2(aq)}$ solution required to produce soluble product in the beaker was recorded and the concentrations of Zn^{2+} (aq) and PP^{2-} (aq) used to give an estimate of K_{sp} according to the following.

$$K_{sp} = [Zn^{2+}\ (aq)]\ [PP^{2-}\ (aq)] \qquad (3.1)$$

3.3. Results and Discussion

3.3.1 Delamination of uninhibited PVB coatings on HDG

Three types of experiment were carried out using unpigmented PVB coatings on HDG steel. Firstly, the baseline kinetics of a delamination cell under an uninhibited PVB coating were characterised through control delamination experiments. The second type of experiment was carried out to identify the effects of PP^{2-} anions added directly to the experimental electrolyte used to initiate underfilm corrosion by application to the defect. Additions of H_2PP at levels of 0.01 M and 0.05 M, with subsequent adjustment to pH 7 were made to the 5% w/v $NaCl_{(aq)}$ electrolyte. The third type of experiment was carried out to determine the effect on delamination kinetics of an electrochemically deposited Zn^{2+}/ phenylphosphonate salt layer at the substrate-coating interface.

Fig 3.1 shows the typical time-dependent E_{corr}-distance (x) profiles established upon the addition of 5% w/v $NaCl_{(aq)}$ to the sample defect for a PVB coating delaminating from HDG steel. The characteristic steep potential drop of ca. 0.3 V indicates the location of the delamination front measured from the defect to the inflection midpoint. The recorded E_{corr} values of the undelaminated region (E_{intact}) of ca. -0.3 V to -0.4 V vs. SHE can be directly compared to those measured for uncoated HDG steel. At ca. three hours after initiation, measured E_{corr} values in the region in direct proximity to the defect approximate the equilibrium potential of Reaction 3.2 i.e. ca. -0.76 V vs. SHE.

The mechanism by which cathodic delamination occurs is described in detail in Section 1.4.2. In brief, a local cathode resulting from oxygen reduction as in Reaction 3.3, exists in the vicinity of the delamination front [4,6]. Zinc dissolution (Reaction 3.2) is constrained to the defect region. The ingress of a thin layer of electrolyte beneath the organic coating allows the passage of ionic current linking the cathodic and anodic processes. It has been shown previously that, in the absence of any inhibitors, this ionic current and, therefore, the rate of delamination, is limited by the migrational mass transport of cations (i.e. Na^+ in the current study) from the external electrolyte to the delamination front [27]. The observed sharp reduction in E_{corr} shown in fig 3.1, denoting the delamination front, can be attributed to an ingress of ions, loss of coating adhesion and the onset of Reaction 3.3.

$$Zn \rightleftharpoons Zn^{2+} + 2e^- \qquad (3.2)$$

$$O_2 + 2H_2O + 4e^- \rightleftharpoons 4OH^- \quad (3.3)$$

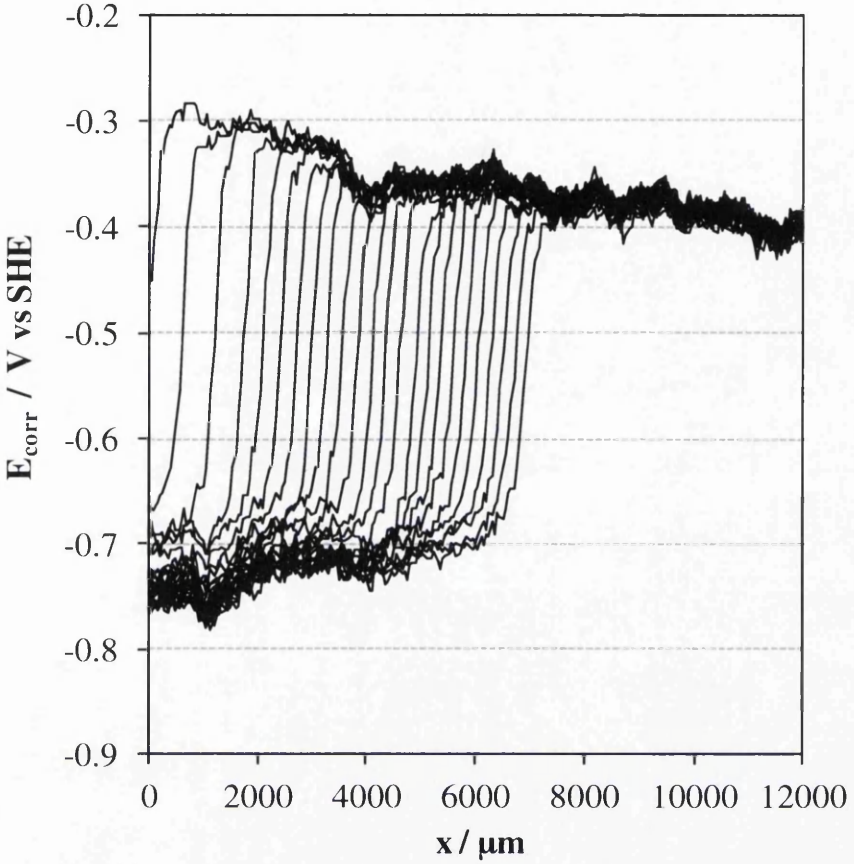

Fig 3.1 Profiles of time dependent E_{corr} measurements against distance (x) from the artificial coating defect for a HDG substrate coated with uninhibited PVB measured hourly from 0 h (left) to 24 h (right).

Reaction 3.3 results in an increased pH at the delamination front where typical values of pH 10-11 have been recorded [27]. This highly alkaline-rendered environment promotes coating disbondment through the dissolution of amphoteric layers, polymer degradation and hydrolysis of interfacial bonds. This also leads to the formation of bizincate ($HZnO_2^-$) and zincate (ZnO_2^{2-}) corrosion product from anodic activity that eventually occurs in the underfilm region (equilibrium Reactions 3.4 and 3.5).

$$Zn(OH)_2(s) \rightleftharpoons HZnO_2^-(aq) + H^+(aq) \quad (3.4)$$

$$Zn(OH)_2(s) \rightleftharpoons ZnO_2^{2-}(aq) + 2H^+(aq) \quad (3.5)$$

It is suggested by Furbeth [23] that, at elevated pH such as in the delaminated underfilm region, a bare zinc surface exposed by the dissolution of zinc(hydroxide) can be directly oxidised to bizincate via the following reaction:

$$Zn(s) + 2H_2O \rightleftharpoons HZnO_2^-(aq) + 3H^+(aq) + 2e^- \quad (3.6)$$

It is observed in fig 3.1 that the delamination frontier moves progressively away from the defect immediately upon addition of electrolyte, reaching a distance of ca. 7500 μm over a 24 h period. When additions of 0.01 M and 0.05 M H_2PP were made to the experimental electrolyte, the onset of underfilm delamination was delayed by 360 min and 900 min respectively. Fig 3.2 shows a typical plot from an experiment where an addition of 0.05 M H_2PP was made to the electrolyte. The E_{corr} at the defect boundary appears entirely similar to that of the uninhibited electrolyte case. The first profile shown on the left was recorded at 840 min and the first recorded delamination front occurred at 900 min indicating a delay in delamination until this time. Fig 3.3 shows a plot of x_{del} vs. t_{del} for the unpigmented coating experiments where x_{del} is the delamination distance and t_{del} is the delamination time following application of electrolyte. The plot shows the significant delays in delamination initiation where 0.01 M and 0.05 M of H_2PP were added to the experimental electrolyte.

Fig. 3.4 shows a plot of x_{del} vs. $(t_{del} - t_i)$, again for the unpigmented coating experiments, where t_i is the initiation period. It can be observed that parabolic kinetics are retained where H_2PP additions were made to the experimental electrolyte. This suggests that cation migration remains the rate-limiting step. A similar delamination rate constant (k_{del}) is observed for all three experiments.

The proceeding Chapter will investigate the effect of H_2PP on the corrosion of a bare HDG steel surface where additions are made to an experimental electrolyte. It is thought that, even if H_2PP additions at 0.05 M can be shown to effectively inhibit corrosion on bare HDG steel, this will not reduce the rate of underfilm corrosion once it has initiated. This is in agreement with previous work by Williams et al where additions of Na_2CrO_4 , $SrCrO_4$ and Ce^{3+} were made to the electrolyte [9,15]. It is suggested that, upon the eventual initiation of delamination, the electrolyte anions (e.g. Cl^- and PP^{2-}) are excluded from the underfilm electrolyte layer.

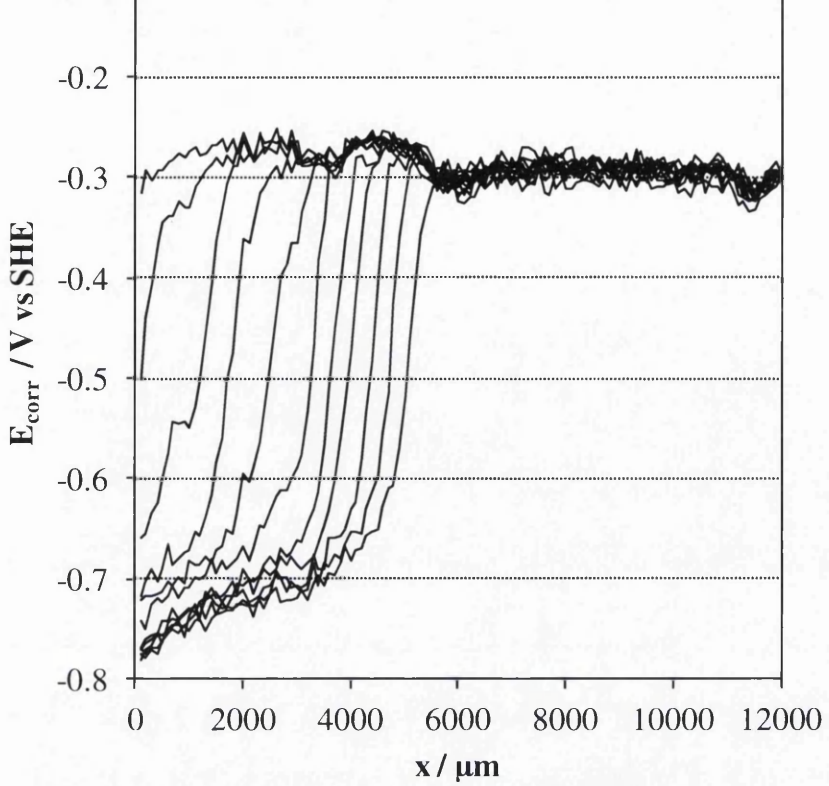

Fig 3.2 Profiles of time dependant E_{corr} measurements against distance (x) from the artificial coating defect containing 5% NaCl electrolyte with additions of 0.05 M H_2PP neutralised to pH 7 for a HDG substrate coated with uninhibited PVB measured hourly from 840 min (left) to 1440 min (right).

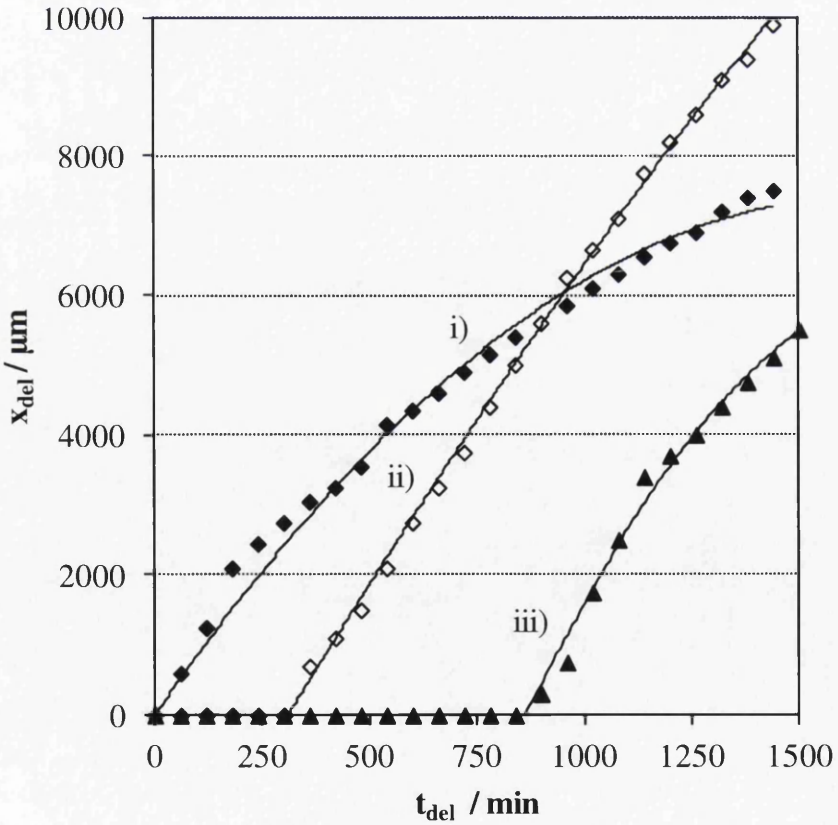

Fig 3.3 Plots of x_{del} versus t_{del} for uninhibited PVB coated HDG substrates where electrolyte adjusted to pH 7 containing concentrations of i) 0 M ii) 0.1 M and iii) 0.05 M H_2PP has been added to an external defect.

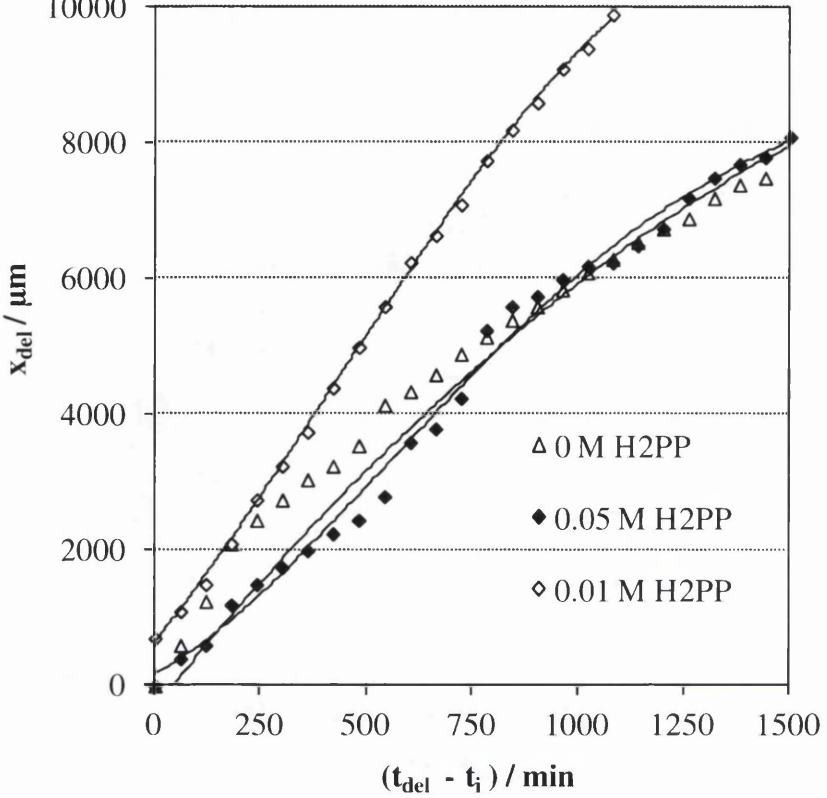

Fig 3.4 Plots of x_{del} vs. $t_{del} - t_i$ for uninhibited PVB coated HDG substrates where electrolyte adjusted to pH 7 containing concentrations of 0 M, 0.1 M and 0.05 M H_2PP has been added to an external defect.

Fig 3.5 shows the time-dependent profiles of E_{corr} measurements vs. distance (x) for the delamination of an unpigmented PVB coating on HDG steel overlaying an electrochemically deposited Zn^{2+}/phenylphosphonate layer with a thickness of ca. 10 µm. A progression of the delamination front to ca. 2000 µm is observed over 24 h. The plot shows that the E_{intact} values are wholly similar to those in the control experiment, shown in fig 3.1, however, E_{corr} values in the delaminated region are not as negative as those observed in the control experiment. These values are approximately 0.1 V vs. SHE more positive than the control experiment. This indicates that inhibition of anodic activity occurring in the delaminated zone is more effective here than in the previous experiments where the inhibitor is present in the electrolyte because PP^{2-} is excluded from this under-film region. In the current case, the pre-existing sparingly soluble ZnPP salt film in this region prevents under-film anodic activity.

Fig 3.6 shows a plot of x_{del} vs. $(t_{del} - t_i)$ for this experiment in comparison with the control experiment. It can be seen that the plot displays linear kinetics and the delamination rate has been considerably reduced. In contrast to the previous experiments no increase in t_i was observed and the onset of delamination was recorded after the first hour of initiation. All the results from experiments carried out using unpigmented coatings are summarised in Table 3.1.

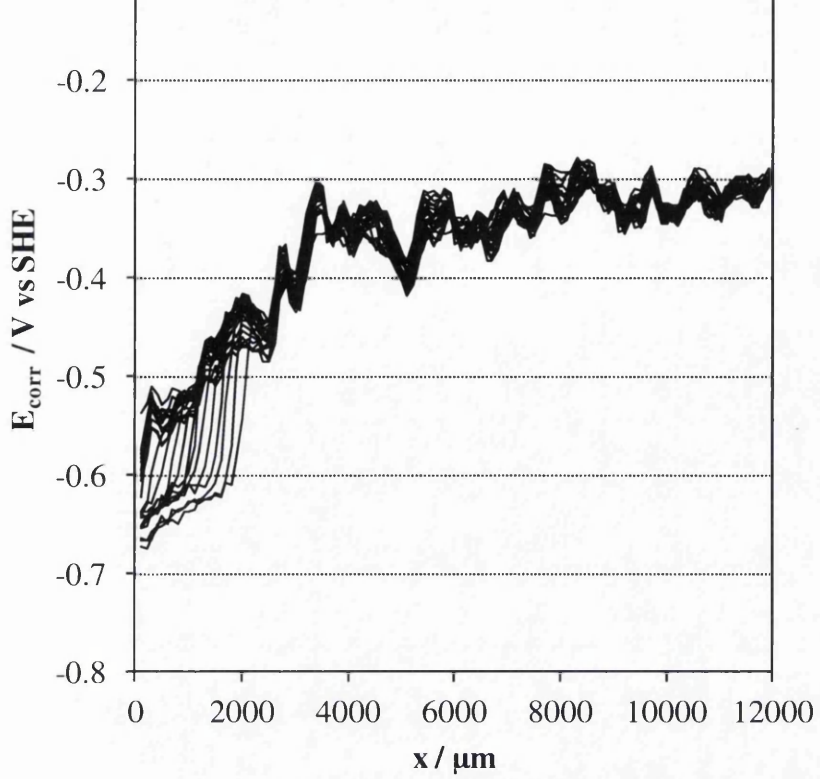

Fig 3.5 Profiles of time-dependant E_{corr} measurements against distance (x) from the artificial coating defect for a HDG substrate containing a electrochemically deposited 10µm ZnPP salt film over-coated with uninhibited PVB measured hourly from 0h (left) to 24 h (right).

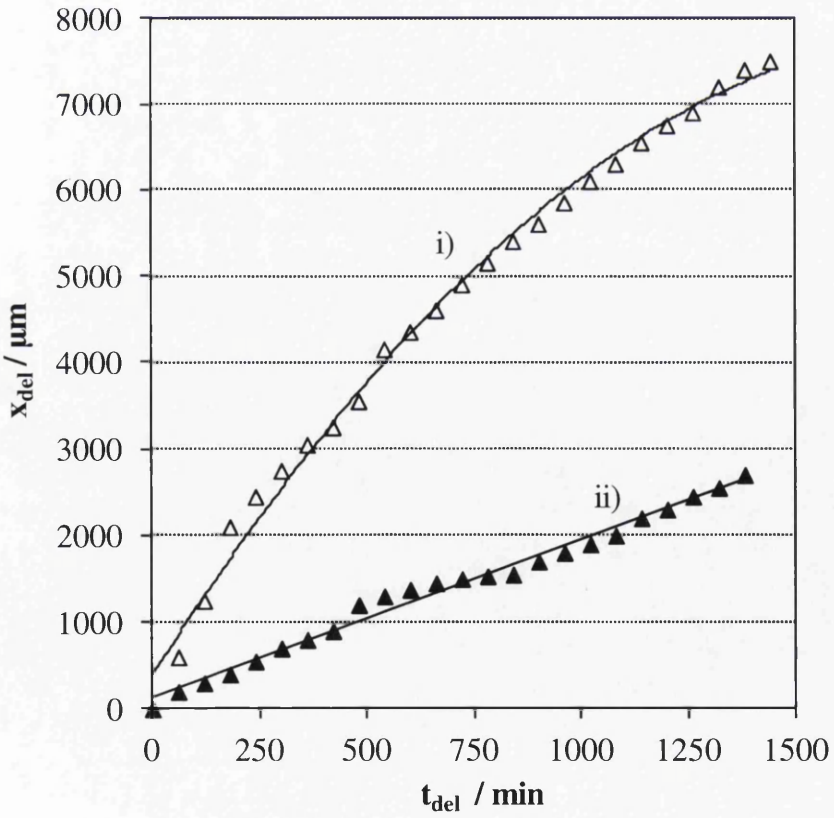

Fig 3.6 Plots of x_{del} vs. t_{del} - t_i for uninhibited PVB coated HDG substrates where i) was an unaltered control sample and ii) had a 10 µm ZnPP salt film electrochemically deposited on the sample surface prior to coating with PVB.

Table 3.1 Values of time to delamination determined for uninhibited PVB where varying concentrations of H_2PP have been added to the electrolyte adjusted to pH 7.

H_2PP (M)	t_i (mins)	k_{del}	K_{del} reduction (%)
0	0	5.4	0
0.01	360	8.8	-63
0.05	1140	4.7	13
0 (ZnPP layer)	0	1.2	78

A further SKP experiment was carried out on zinc samples coated with uninhibited PVB PVB and PVB containing 10% H_2PP additions. All experiments were conducted in 95% humidity. SKP scanning was carried out on a single point over the coated surface until a stable E_{corr} was reached; at this point the chamber was flooded with N_2. Scanning over the same point then continued until further stabilisation was achieved. Typical results are given in fig 3.7 where i) shows the result for the uninhibited coating and ii) shows the result for the coating containing 10% H_2PP additions. In both cases a substantial drop in E_{corr} takes place at the point where the chamber is flooded with N_2 (at ca. 1000 min). The reason for such a drop in E_{corr} is due to a partial reduction of the oxide layer on the metallic zinc substrate under the PVB coatings. This does not occur in a normal air environment due to the oxidising potential of oxygen [28–30]. In the case of those samples coated with PVB containing H_2PP, more negative potentials were measured in the absence of oxygen. This suggests that the in-coating H_2PP has an influence on the oxygen reduction reaction during delamination and indicates the presence of ZnPP layer that is reduced further by the underlying zinc substrate in the absence of oxygen.

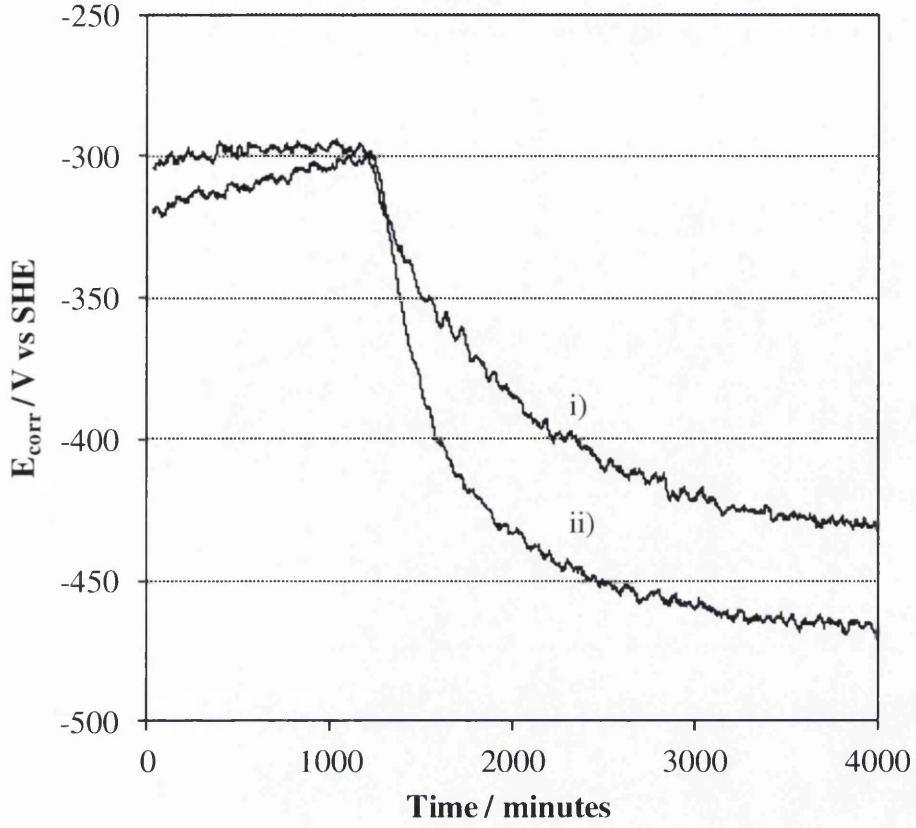

Fig 3.7 Plots of E_{corr} measurements vs. time measured on a single point of HDG surfaces coated with i) uninhibited PVB and ii) PVB containing 10% additions of H_2PP. A switch from air to an N_2 atmosphere occurred at ca. 1000 min.

3.3.2 Delamination of phenyl phosphonic acid inhibited coatings

Delamination experiments were carried out to determine the inhibition efficiency of H_2PP where additions of 0%, 2%, 5% and 10% w/w were made to a PVB coating. Figs 3.8 and 3.9 show the E_{corr} versus distance profiles measured for experiments in which additions of 5% and 10% H_2PP were made to the PVB coating respectively. In the later stages (ca. 20-24 h after initiation) of the experiment with 5% additions, measured E_{corr} values in close proximity to the defect approximate the hypothesised equilibrium potential of Reaction 3.2 i.e. ca. -0.76 V vs. SHE. In contrast, where 10% additions were made, this value is more positive indicating that the anodic reaction at the defect is inhibited, albeit partially. No variation of E_{intact} is observed at any level of H_2PP addition when compared with the control experiment suggesting that the presence of in-coating H_2PP has minimal effect on the steady-state delamination-cell potentials. Fig 3.10 shows plots of delaminated distance (x_{del}), measured starting at the defect edge, vs. (t_{del} - t_i) allowing for a comparison of delamination kinetics obtained from inhibited and uninhibited coating data. The delamination rate (k_{del}) information obtained from plot gradients in fig. 3.11 is listed in Table 3.2. All inhibited cases exhibit a substantial

reduction in k_{del} of > 71% starting at additions of 2% H_2PP. Thereafter, with increasing levels of H_2PP, k_{del} is found to decrease by small increments. The delamination initiation times (t_i) for each experiment are also listed in Table 3.2 showing that t_i is increased substantially with increasing levels of H_2PP additions. Additions of 10% H_2PP are shown to delay the onset of delamination for periods of up to approximately 20 h. The effect of t_i and k_{del} vs. % of in-coating H_2PP additions is illustrated in fig 3.12. A k_{del} value for the un-inhibited PVB was taken as an initial rate value from the first few hours of delamination.

The same change from parabolic (in the uninhibited experiment) to linear (in the inhibited experiments) kinetics has been shown in previous studies on polyaniline and smart-release bentonite-pigmented coating systems [31]. In these studies the transition to linear kinetics was ascribed to interfacial oxygen reduction at the disbondment front becoming the rate-limiting step in the corrosion-driven delamination process. It is proposed that for in-coating H_2PP additions, the transformation results from an electron transfer-blocking interfacial layer that forms when the PVB/H_2PP ethanolic solution is initially applied to a HDG steel surface. The dissociation of H_2PP dissolved in the ethanol produces H^+ cations that result in an acid etch of the zinc surface generating Zn^{2+} cations at the substrate/coating interface via Reaction 3.2. The following series of equilibria illustrate the de-protonation of H_2PP:

$$H_2PP_{(aq)} \rightleftharpoons HPP^-_{(aq)} + H^+_{(aq)} \qquad (pK_{a1} = 2.3) \qquad (3.7)$$

$$HPP^-_{(aq)} \rightleftharpoons PP^{2-}_{(aq)} + H^+_{(aq)} \qquad (pK_{a2} = 7.8)[32] \qquad (3.8)$$

Although a low pH will be produced at the coating/Zn interface when the coating is first applied, the progressive removal of H^+ by neutralisation from OH^- generated by Reaction 3.3, or by cathodic hydrogen evolution coupling with Zn dissolution, will favour further H_2PP and HPP^- dissociation according to reactions 3.7 and 3.8. Eventually, sufficiently high local concentrations of PP^{2-} will build up, allowing a subsequent reaction with underfilm Zn^{2+} ions to occur, forming a solid film of insoluble $Zn^{2+}PP^{2-}$ at the metal coating interface according to the following:

$$Zn^{2+} + PP^{2-} \rightleftharpoons [Zn^{2+}PP^{2-}]_s \qquad (3.9)$$

A solubility product (K_{sp}) value of 10^{-6} mol^2 dm^{-6} was obtained experimentally through a series of titrations. It is proposed that the resulting precipitate forms a barrier to

electron transfer and subsequently blocks the underfilm cathodic oxygen reduction reaction. Analysis of the surface should be carried out, in future work, using X-ray photoelectron spectroscopy (XPS) to verify the presence of such a salt film. Previous observations of a substantially reduced k_{del} for a PVB coated sample comprising an electrochemically deposited Zn^{2+}/phenylphosphonate layer (see fig 3.5), confirm this theory.

A second mode of inhibition which may contribute to the overall mechanism is suggested, whereby the in-coating H_2PP acts to moderate underfilm pH from its alkaline-rendered state. The first and second deprotonation steps given in Reactions 3.7 and 3.8 have pK_a values of 2.3 and 7.8 respectively, suggesting that pH buffering at these values will occur. A reservoir of H^+ cations, provided by the in-coating H_2PP, acts to neutralise the hydroxide product present in the delamination region. Firstly, this mechanism will reduce loss of coating adhesion caused by base-catalysed polymer degradation and base-catalysed hydrolysis of interfacial bonds. Secondly, lack of high pH will prevent the formation of anodic activity in the delaminated region hindering the formation of zincate and bizincate corrosion products, as shown in Reactions 3.4 – 3.5, which may contribute to adhesion loss.

A third mode of inhibition involves the leaching of H_2PP, HPP^- or PP^{2-} from the edge of the coating/defect boundary in to the $NaCl_{(aq)}$ electrolyte at the exposed zinc surface. An inhibition of Reaction 3.2 at the coating/defect boundary would be anticipated to result in a corresponding decrease of Reaction 3.3 at the delamination front. It was also shown in Section 3.3.1 that additions of H_2PP made to the external electrolyte increased the delamination initiation time by up to 20 h. Furthermore, where a $Zn^{2+}PP^{2-}$ salt film was electrochemically grown on the HDG substrate prior to coating with unpigmented PVB, there was no increase in delamination initiation time in comparison to the control experiment. This suggests that the observed increase in t_i with increasing levels of in-coating H_2PP relates to the temporary prevention of Reaction 3.2 at the coating/defect edge by the leaching of PP^{2-} from the coating into the electrolyte. To test the theory of this third possible mode of inhibition, the proceeding Chapter will determine the effect of H_2PP on the corrosion of a bare HDG surface where additions are made to an experimental electrolyte.

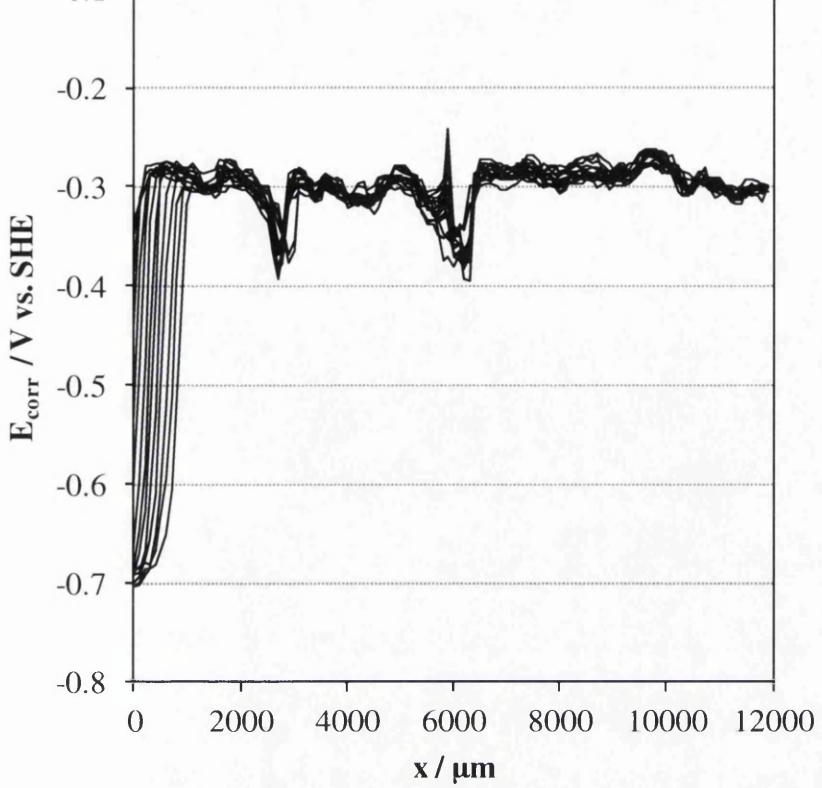

Fig 3.8 Profiles of time dependent E_{corr} V vs. SHE measurements against distance (µm) from the artificial coating defect for a HDG substrate coated with a PVB layer at a thickness of 10 µm containing 5% additions of H_2PP measured from 1440 min (left) and then at intervals of 660 min up to 1400 min (right).

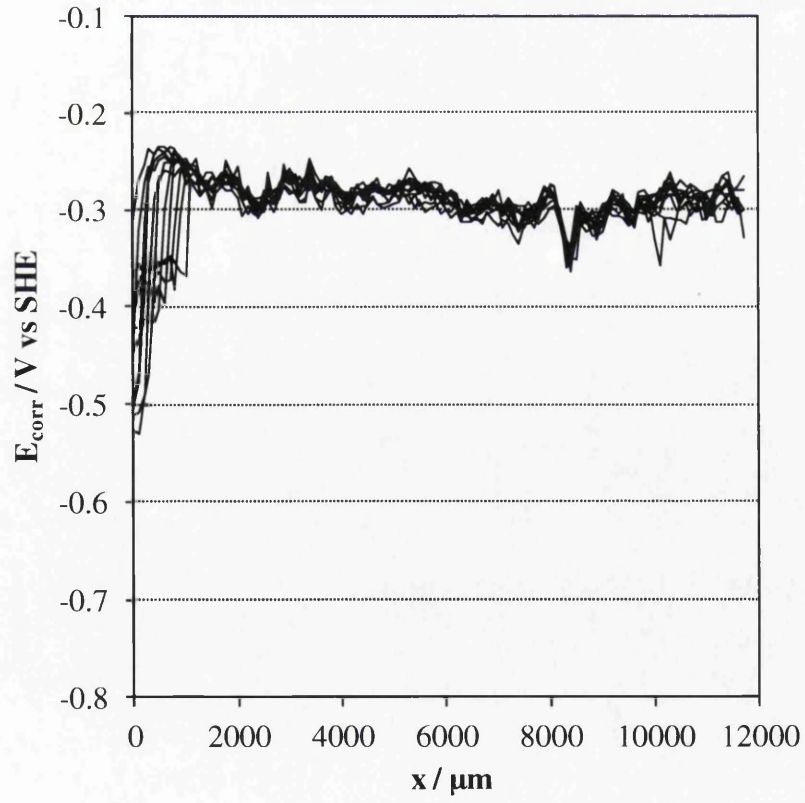

Fig 3.9 Profiles of time dependant E_{corr} V vs. SHE measurements against distance (µm) from the artificial coating defect for a HDG substrate coated with a PVB layer at a thickness of 10 µm 10% additions of H_2PP measured from 1200 min (left) and then at intervals of 180 min up to 3000 min (right).

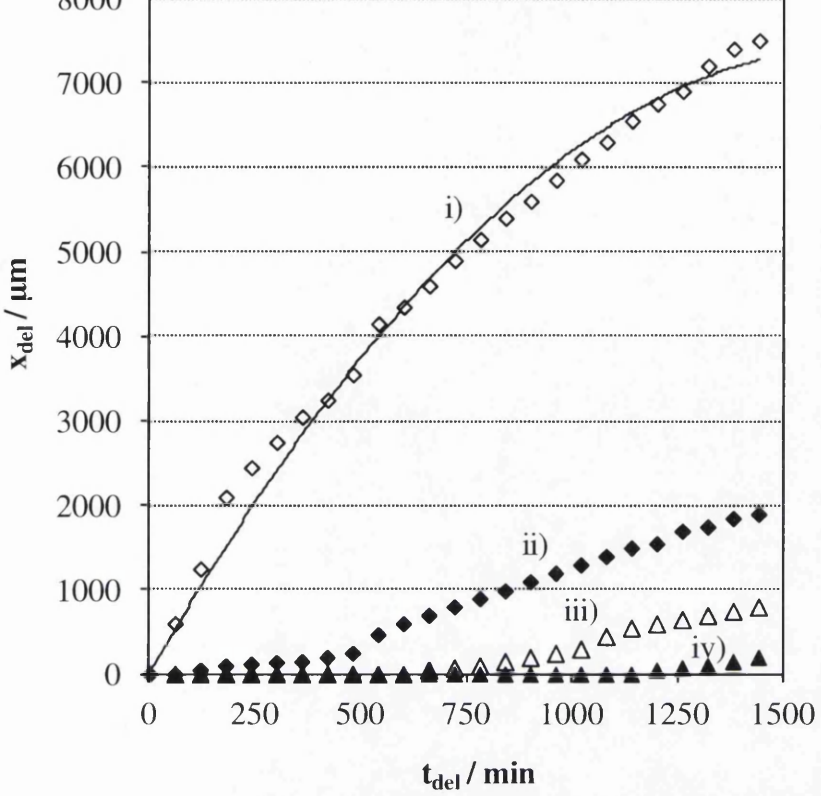

Fig 3.10 Plots of x_{del} vs. t_{del} for PVB coated HDG substrates where additions of i) 0%, ii) 2%, iii) 5% and iv) 10% H_2PP have been made to the PVB coating.

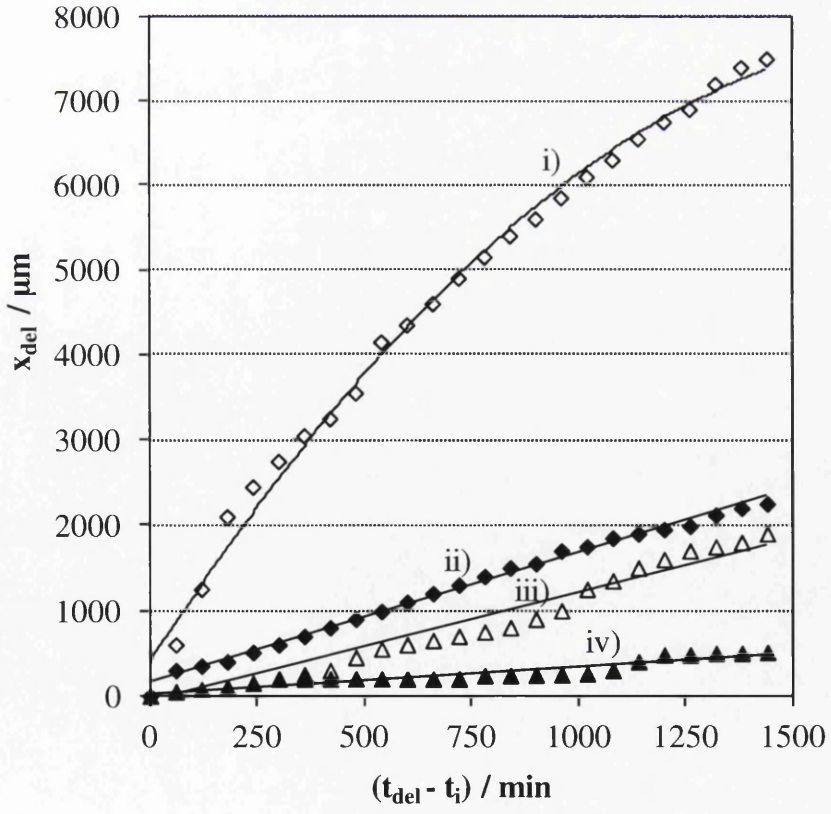

Fig 3.11 Plots of x_{del} vs. $(t_{del} - t_i)$ for PVB coated HDG substrates where additions of i) 0%, ii) 2%, iii) 5% and iv) 10% H_2PP have been made to the PVB coating.

Table 3.2 Values of parabolic rate constant and time to delamination determined for PVB coatings containing various values of H_2PP on HDG substrates.

%H_2PP	k_{del} (μm.min)	k_{del} reduction (%)	t_i (min)
0	5.4	0	0
2	1.5	72	480
5	1.3	76	660
10	0.3	94	1200

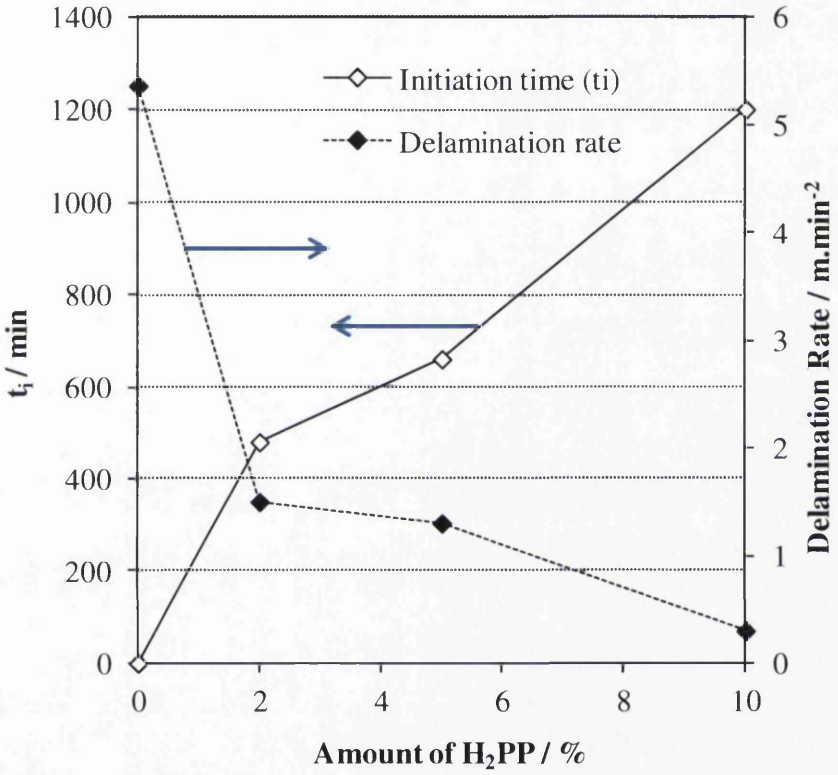

Fig 3.12 Summary plots of delamination initiation time values (t_i) and k_{del} values both plotted as a function of H_2PP levels (%) added to 10 μm PVB coatings delaminating from HDG steel substrates; the latter are plotted using a secondary y-axis.

3.4 Conclusions

Phenyl phosphonic acid (H_2PP) dissolved in a 10 μm PVB primer coating can achieve the efficient inhibition of underfilm delamination observed where additions of 5% w/v $NaCl_{(aq)}$ were made to a sample defect for a period of up to 20 h. In the absence of H_2PP, delamination progresses to a distance of ca. 7500 μm, measured from the defect site, over a period of 24 h. When H_2PP is present in the coating at a dispersion of 2% w/w, the time for delamination kinetics to become established (t_i) is increased to 480 min from 0 - 120 min where no H_2PP is present. This increases to 1200 min where 10%

w/w additions are made. It was also shown that, where additions of neutralised H_2PP were added to the external electrolyte at a level of 0.05 M the t_i was increased to 1140 min. It is suggested that dissociated PP^- ions act to suppress the anodic reaction (Reaction 3.2) at the defect site that, in turn, leads to a corresponding decrease in the cathodic reaction (Reaction 3.3) that drives forward delamination. Thus, the onset of the delamination process is inhibited for a substantial period of time.

Furthermore, when H_2PP is present in the coating (at dispersions of $\geq$ 2% w/w), the delamination rate (k_{del}) is decreased by $\geq$ 72%. Incremental reductions in k_{del} are observed with increasing levels of in-coating H_2PP. A 92% reduction in k_{del} is observed where additions of 10% w/w H_2PP are made. When plotting x_{del} vs. t_{del}, a transition from parabolic kinetics for the uninhibited coating to linear kinetics where H_2PP additions were made is observed. It is suggested that the formation of an insoluble Zn^{2+}/phenylphosphonate salt layer at the substrate/coating interface blocks the cathodic oxygen reduction reaction leading to the suppression of coating delamination. The salt layer is thought to form upon coating where the in-coating acid etches the surface causing the dissolution of Zn^{2+}. Where an electrochemically deposited Zn^{2+}/phenylphosphonate salt layer was over-coated with uninhibited PVB it was found that delamination initiated immediately but k_{del} was reduced by ~78%.

A further suggested mechanism is that the dissociation of H_2PP results in an abundance of H^+ cations that act as a buffer to neutralise the alkaline rendered underfilm region from the cathodic oxygen reduction reaction. The rate at which base catalysed polymer degradation, and interfacial bond hydrolysis, occurs is subsequently reduced. Although the combination of all three modes of inhibition contributes to a marked decrease in k_{del}, this remains non-zero even when a 10% w/w H_2PP addition is used.

3.5 References

[1] J. A Shumilla, K. E. Wetterhahn, and a Barchowsky, *Archives of biochemistry and biophysics*, vol. 349, 2, 356–62, 1998.

[2] N. F. Izmerov in *(Ed) IRPTC Scientific Review-UN Environmental Programme*, 1982.

[3] A. C. Bastos, M. G. S. Ferreira, and A. M. Simões, *Progress in Organic Coatings*, vol. 52, no. 4, 339–350, 2005.

[4] B. Amo, R. Romagnoli, V. F. Vetere, and L. S. Herna, 28–35, 1998.

[5] V. Jašková and A. Kalendová, *Progress in Organic Coatings*, vol. 75, 4, 328–334, 2012.

[6] M. Beiro, a Collazo, M. Izquierdo, X. Nóvoa, and C. Pérez, *Progress in Organic Coatings*, vol. 46, 2, 97–106, 2003.

[7] K. Aramaki, *Corroion Sci*ence vol. 43, 591–604, 2001.

[8] I. M. Zin, S. B. Lyon, and V. I. Pokhmurskii, *Corrosion Science*, vol. 45, 4, 777–788, 2003.

[9] G. Williams and H. N. McMurray, *Journal of The Electrochemical Society*, vol. 148, 10, p. B377, 2001.

[10] J. Sinko, *Progress in Organic Coatings*, vol. 42, 267–282, 2001.

[11] G. Williams, S. Geary, and H. N. McMurray, *Corrosion Science*, vol. 57, 139–147,. 2012.

[12] M. L. Zheludkevich, S. K. Poznyak, L. M. Rodrigues, D. Raps, T. Hack, L. F. Dick, T. Nunes, and M. G. S. Ferreira, *Corrosion Science*, vol. 52, 2, 602–611, 2010.

[13] G. Williams, H. N. McMurray, and M. J. Loveridge, *Electrochimica Acta*, vol. 55, 5, 1740–1748, 2010.

[14] G. Williams and H. N. McMurray, *Electrochemical and Solid-State Letters*, vol. 6, 3, B9, 2003.

[15] G. Williams, H. N. McMurray, and D. A. Worsley, *Journal of The Electrochemical Society*, vol. 149, 4, B154, 2002.

[16] M. Rohwerder and A. Michalik, *Electrochimica Acta*, vol. 53,. 3, 1300–1313, 2007.

[17] G. Paliwoda-porebska, M. Stratmann, and M. Rohwerder, *Corrosion Science*, vol. 47, 3216–3233, 2005.

[18] D. Borisova, H. Möhwald, and D. G. Shchukin, *ACS nano*, vol. 5, 3, 1939–46, 2011.

[19] D. Snihirova, S. V Lamaka, M. Taryba, A. N. Salak, S. Kallip, M. L. Zheludkevich, M. G. S. Ferreira, and M. F. Montemor, *ACS applied materials & interfaces*, vol. 2, 11, 3011–22, 2010.

[20] D. V. Andreeva, E. V. Skorb, and D. G. Shchukin, *ACS Applied Materials & Interfaces*, vol. 2,. 7, 1954–1962, 2010.

[21] J. Marsh, J. D. Scantlebury, and S. B. Lyon, *Corrosion Science*, vol. 43, 2001.

[22] W. Fürbeth and M. Stratmann, *Corrosion Science*, vol. 43, 2,. 229–241, 2001.

[23] W. Fürbeth and M. Stratmann, *Progress in Organic Coatings*, vol. 39, 1,. 23–29, 2000.

[24] J. Coleman, A, H. N. McMurray, G. Williams, A. Afseth, and G. M. Scamans, *Electrochemical and Solid-State Letters*, vol. 10, 5, C35, 2007.

[25] G. Williams, a. Gabriel, a. Cook, and H. N. McMurray, *Journal of The Electrochemical Society*, vol. 153, 10, B425, 2006.

[26] M. Stratmann, *Corrosion Science*, vol. 27, 8, 869–872, 1987.

[27] W. Fürbeth and M. Stratmann, *Progress in Organic Coatings*, vol. 39, 23–29, 2000.

[28] M. Rohwerder, S. Isik-Uppenkamp, and C. a. Amarnath, *Electrochimica Acta*, vol. 56, 4, 1889–1893, 2011.

[29] R. Hausbrand, M. Stratmann, and M. Rohwerder, *Journal of The Electrochemical Society*, vol. 155, 7, C369, 2008.

[30] R. Hausbrand, M. Stratmann, and M. Rohwerder, *Corrosion Science*, vol. 51, 9, 2107–2114, 2009.

[31] G. Williams, R. J. Holness, D. A. Worsley, and H. N. McMurray, *Electrochemistry Communications*, vol. 6, 6, 549–555, 2004.

[32] L. D. Freedman and G. O. Doak, *Chem Rev*, vol. 57, no. 479, 1957.

Chapter Four.

An SVET study of the corrosion of hot dip galvanised steel immersed in phenyl phosphonic acid-containing electrolyte.

4.1 Introduction

The detrimental health effects of the traditional, highly effective anti-corrosion technologies based on sparingly soluble salts of chromium (VI) anions are widely known [1]. As such, legislative pressure to implement alternative environmentally friendly coating systems calls for research into this area. The benefits of chromate based systems for corrosion protection are as follows:

a) Leachable, highly soluble and mobile ions, such as Cr(VI) oxyanions, that provide a 'self-repairing' effect.
b) The self reducing Cr(VI) to Cr(III) reaction that forms passivating oxides at surface layer defects providing a barrier affect [2].
c) Stability of surface layers, such as Cr_2O_3, across a wide pH range [3].

Localised corrosion activity occurring over a commercial grade HDG surface immersed in aqueous sodium chloride electrolyte has been mapped using the SVET. Concentrations of H_2PP were systematically added to the experimental electrolyte in order to establish an optimum by assessment of its influence on the corrosion of the surface. Further experiments to determine the influence of pH on inhibition by H_2PP at its optimum concentration were then carried out.

4.2 Experimental

4.2.1 Materials

All HDG steel was supplied by Tata Steel UK and comprised of 0.7 mm gauge mild steel coated on both side with a 20 μm zinc layer cut into 50 mm x 50 mm square coupons. All chemicals were supplied by Sigma-Aldrich Chemical Co. and were of analytical grade purity.

4.2.2 Sample preparation

Prior to each experiment, abrasive cleaning was carried out, as described in Section 2.1.3, using an aqueous slurry of 5 μm polishing alumina followed by washing with aqueous surfactant and finally rinsing with distilled water and then ethanol. Samples were then prepared for immersion by being completely covered using 90 μm thick extruded PTFE 5490 tape (3M Ltd.), leaving exposed only the 10 mm x 10 mm test area on one face. All experimental electrolyte was prepared using analytical grade reagents

obtained from Alrdrich Chemical Co. and distilled water. Solution pH was adjusted by the drop-wise addition of either HCl (aq) or NaOH (aq).

4.2.3 Methods

SVET experiments were carried out as described in Section 2.3 with half-hourly scans over a period of 24 h. Time-dependent free corrosion measurements were performed using a Solartron SI 1280B Electrochemical Workstation and carried out as described in Section 2.15.

Mass loss experiments were carried out by first cutting the HDG material into a coupon of approximately 20 mm x 20 mm. Coupons were then cleaned and weighed and subsequently taped using 90 μm thick extruded PTFE 5490 tape (3M Ltd.) leaving a 10 mm x 10 mm exposed surface. Samples were then fully immersed in the relevant electrolyte for a period of one week. Samples, still taped, were then immersed in an etchant (made up of 50 ml H_3PO_4, 20 g CrO3 and 1 L H_2O)[4] at a temperature of ca. 80°C for a period of 5 min. All taping was then removed and samples were cleaned using ethanol and oven-dried at ca.100°C for 10 min. All samples were then weighed again.

4.3 Results and discussion

4.3.1 Corrosion inhibition of hot dip galvanised steel by phenyl phosphonic acid in neutral conditions

In situ SVET scanning was used to determine the current density distributions, as a function of time, above the surface of unpolarised HDG samples freely corroding in uninhibited 5% wt/v aqueous NaCl at pH 7. Representative current density maps obtained at times between 1 h and 24 h after initial sample immersion are shown in fig 4.1. It can be observed that corrosion activity occurs with the development of a single anode and a single cathode. For the duration of the 24 h experiment, the large cathode occupies roughly one third of the test area and the anode remains localised throughout. The photographic image presented in fig 4.1(f) shows white rust corresponding to the anodic region observed on the current density maps. Figs 4.2 to 4.4 show the respective sets of current density maps for SVET experiments carried out in electrolyte of H_2PP concentrations $1x10^{-3}$ mol dm^{-3}, $1x10^{-2}$ mol dm^{-3}, and $5x10^{-2}$ mol dm^{-3}, neutralised to pH 7. The current density surface maps given in fig 4.2, for additions of $1x10^{-3}$ mol dm^{-3}

H_2PP, indicate that at low concentration levels of H_2PP, inhibition is incomplete and thus an intense local anode is present. The corresponding photographic image, given in part (d), shows that the surface has been stripped away in a small region represented by the anodic activity on the current density maps. The photograph also shows a protective film on the remaining area of the sample. Fig 4.3, showing the results for experiments carried out in H_2PP concentrations of $1x10^{-2}$ mol dm^{-3}, shows a very similar finding but the local anode is smaller and less intense at this higher concentration. The current density maps presented in fig 4.4 indicate that, at the higher H_2PP concentration of $5x10^{-2}$ mol dm^{-3}, inhibition is complete and no corrosion activity is observed. The photographic image shows that no corrosive surface tarnishing has occurred.

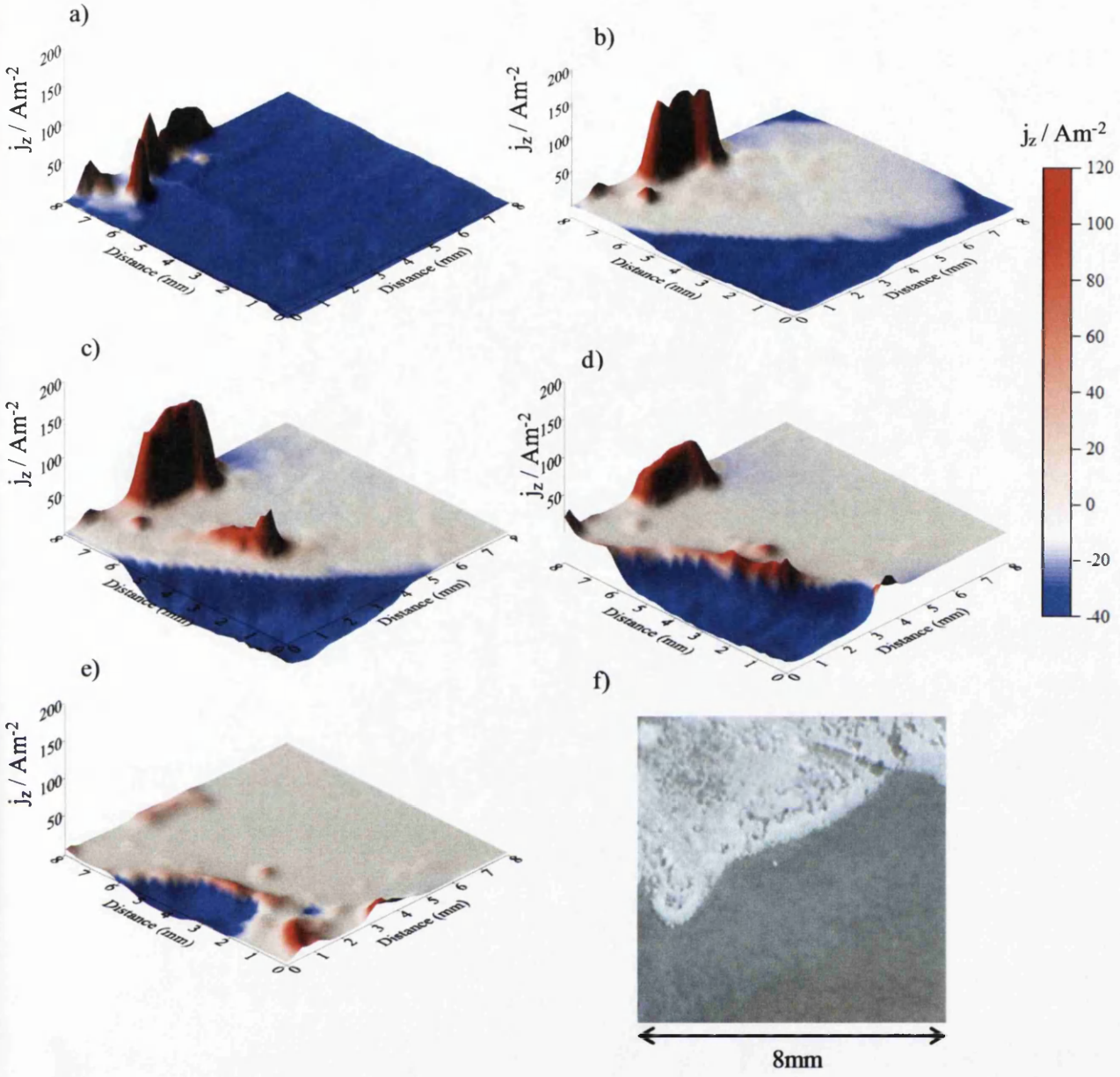

Fig 4.1 SVET-derived current density surface maps of unpolarised HDG obtained following immersion in aerated 5% (w/v) NaCl (aq) at pH 7 at time a) 1h b) 2 h, and c) 6 h where d) 12 h e) 24 h and f) shows a photographic image of the sample after 24h immersion.

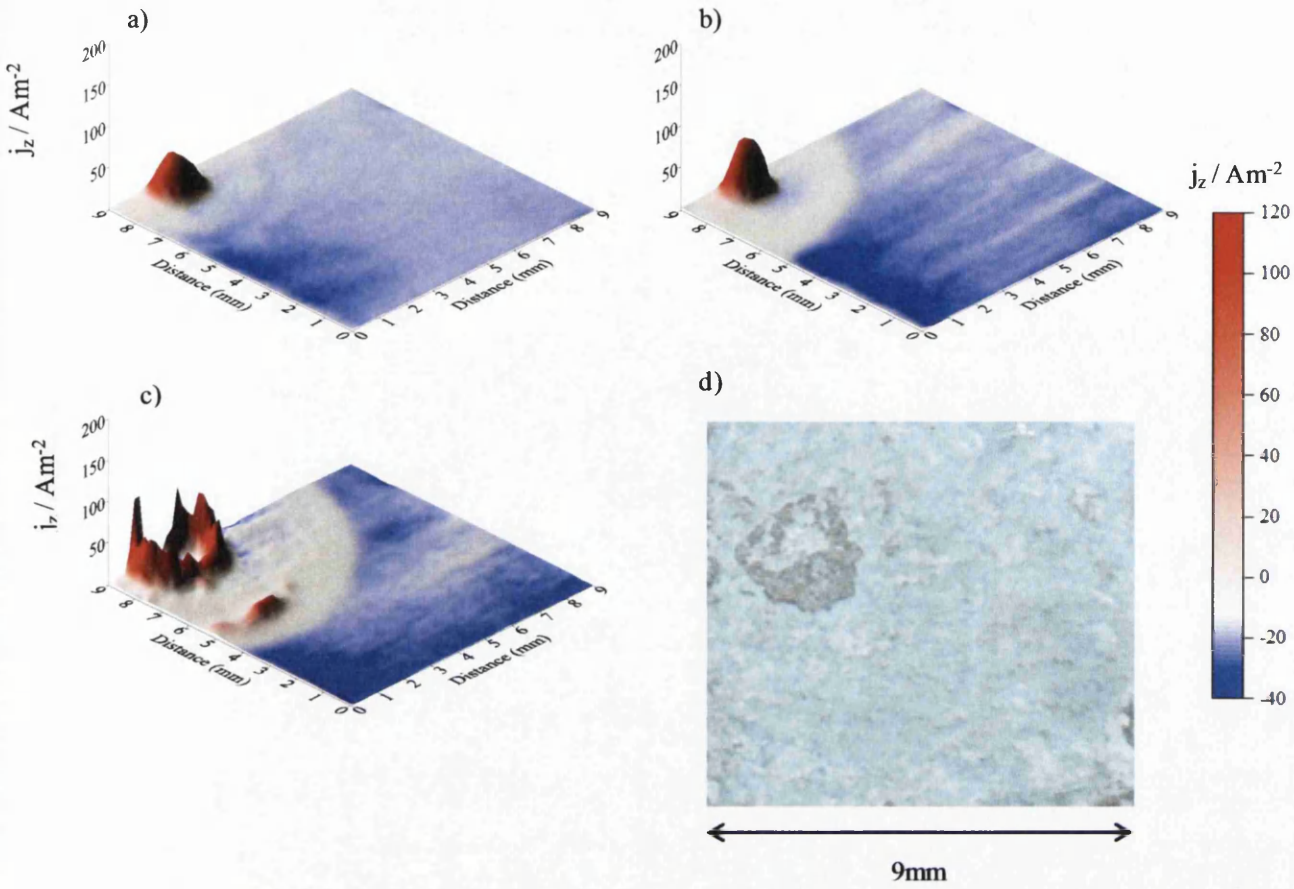

Fig 4.2 SVET-derived current density surface maps of unpolarised HDG obtained following immersion in aerated 5% (w/v) NaCl (aq) at pH 7 containing additions of $1x10^{-3}$ mol dm^{-3} H_2PP at times a) 30 min b) 6 h c) 24 h where d) is a photographic image of the sample after 24 h of immersion.

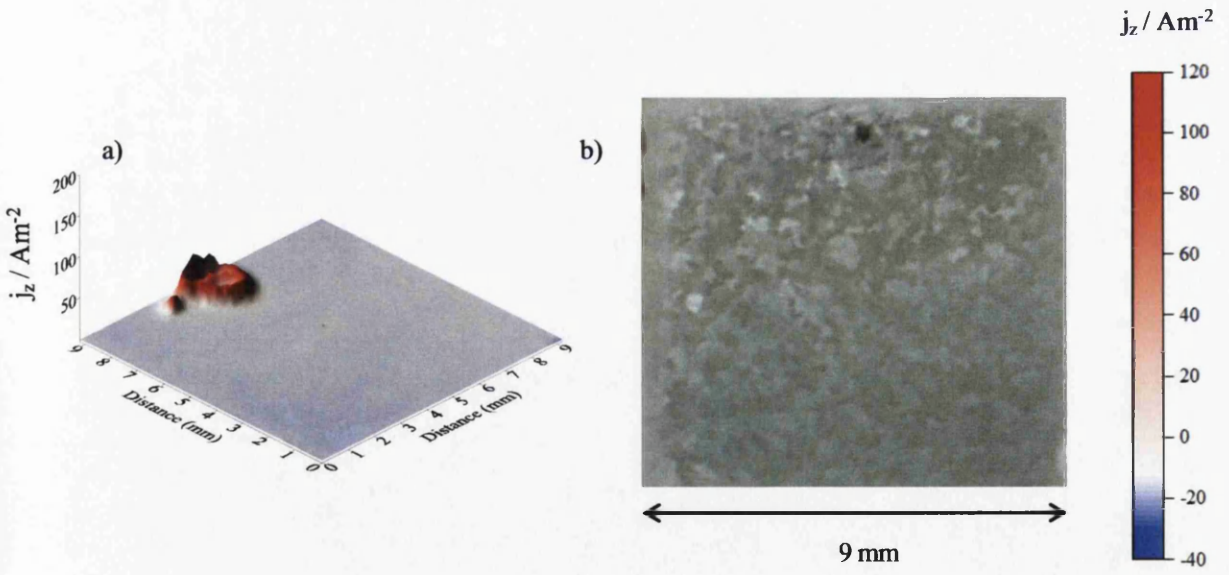

Fig 4.3 a) SVET-derived current density surface map of unpolarised HDG obtained following immersion in aerated 5% (w/v) NaCl (aq) at pH 7containing additions of $1x10^{-2}$mol dm^{-3} H_2PP at time 24 h where d) is a photographic image of the sample after 24 h of immersion.

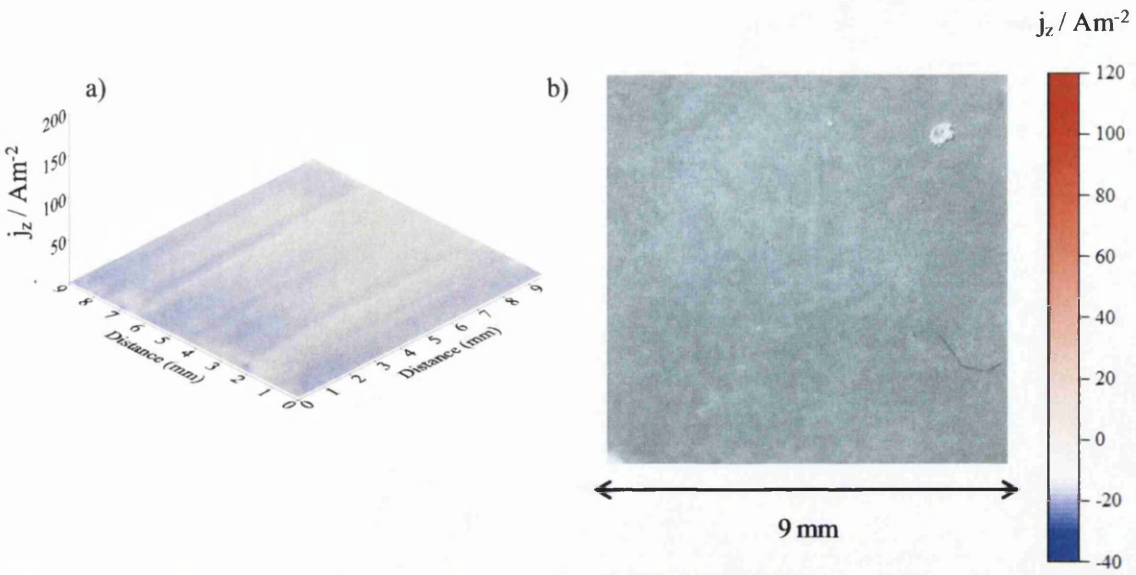

Fig 4.4 SVET-derived current density surface maps of unpolarised HDG obtained following immersion in aerated 5% (w/v) NaCl (aq) at pH 7containing additions of $5x10^{-2}$mol dm^{-3} H_2PP at 24 h where d) is a photographic image of the sample after 24 h of immersion.

Area-averaged, integrated SVET-derived anodic current density plotted as a function of time for uninhibited, $1x10^{-3}$ mol dm^{-3} H_2PP, $1x10^{-2}$ mol dm^{-3} H_2PP, and $5x10^{-2}$ mol dm^{-3} H_2PP concentrations is given in fig 4.5. The data was obtained by the numerical area integration of j_z distributions to give an estimation of time-dependent total local corrosion currents. This is described in full in Section 2.1.14. A progressive decrease in integrated current density can be observed with increasing concentrations of H_2PP. Plot (i) shows the integrated current density at a concentration level of $5x10^{-2}$mol dm^{-3} H_2PP and indicates that very little anodic activity was measured. From area-averaged anodic J_{at} current density values, the total equivalent zinc loss is calculated using:

(4.3)

where F is Faradays constant. Values of zinc loss after 24 h immersion time are presented in fig 4.6 given in gm^{-2}. It can be observed that, with increasing concentration levels of PP^{2-} dissolved in the electrolyte, the mass of zinc dissolved from the sample is progressively reduced. At a concentration of $5x10^{-2}$ mol dm^{-3} H_2PP, the measured zinc lost is reduced by ca. 96% when compared with the control sample.

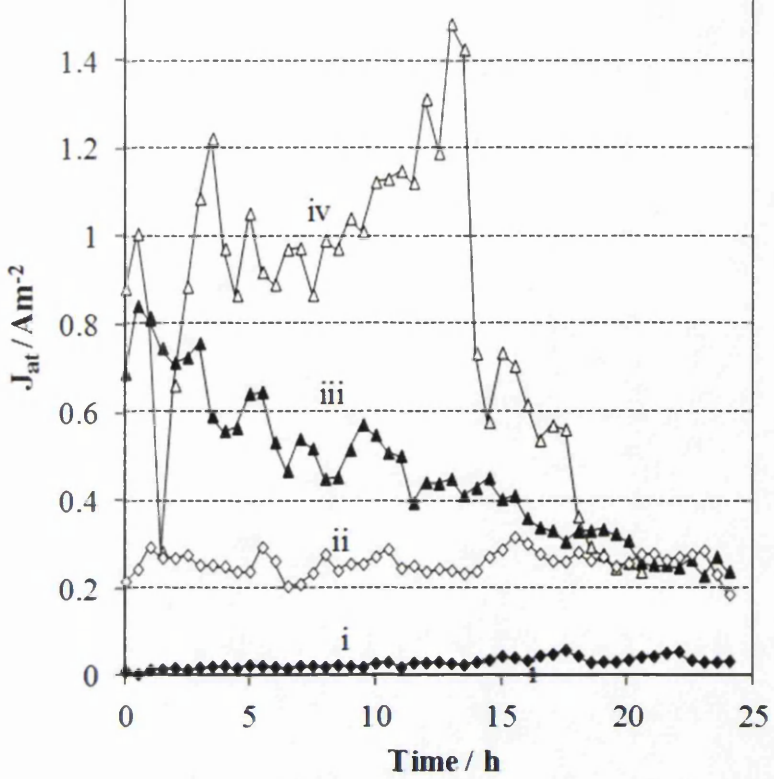

Fig 4.5 Area-averaged, integrated SVET-derived anodic current density vs. time profiles obtained for HDG immersed in aerated 5% (w/v) NaCl (aq) at pH 7 containing (i) $5x10^{-2}$ mol dm^{-3} (ii) $1x10^{-2}$ mol dm^{-3} (iii) $1x10^{-3}$ mol dm^{-3} additions of H_2PP. Curve (iv) was obtained in the absence of inhibitor.

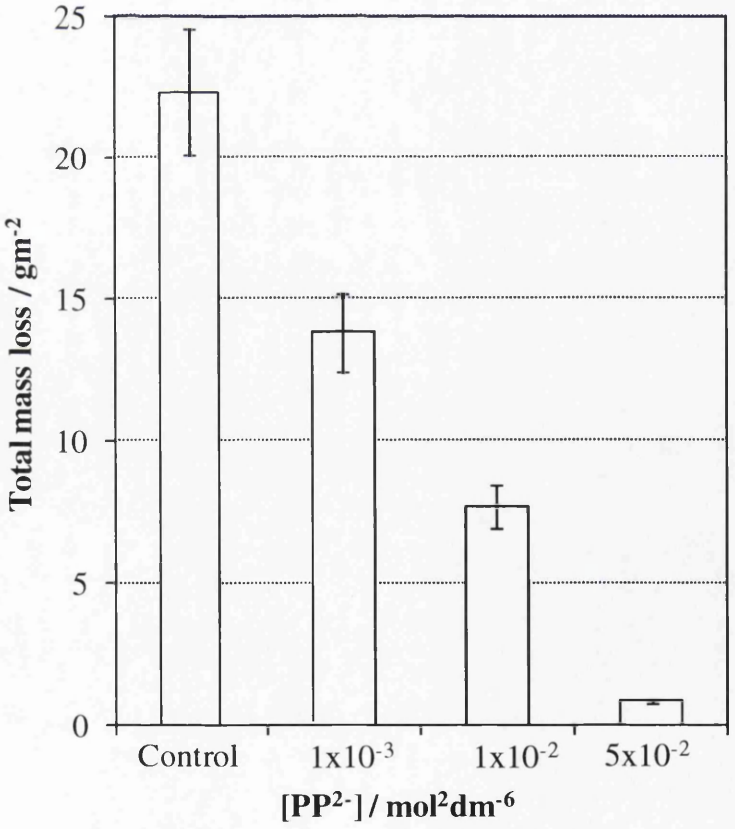

Fig 4.6 Summary of measured corrosion mass loss over 24 h as a function of [PP^{2-}].

Error! Reference source not found. 4.7 shows a plot of the open circuit potential (OCP) of HDG measured in a series of systematic experiments where H_2PP was present in concentrations ranging from $1x10^{-3}$ to $5x10^{-2}$ mol dm^{-3} in 5% wt/v $NaCl_{(aq)}$ experimental electrolyte neutralised to pH 7. The dashed line represents the eventual OCP value measured where no H_2PP was present in the electrolyte. It can be observed that this control result displays an E_{corr} value near the equilibrium value of zinc. It can be observed that the presence of H_2PP at concentrations of $1x10^{-3}$ mol dm^{-3} had no significant effect on the final potential.

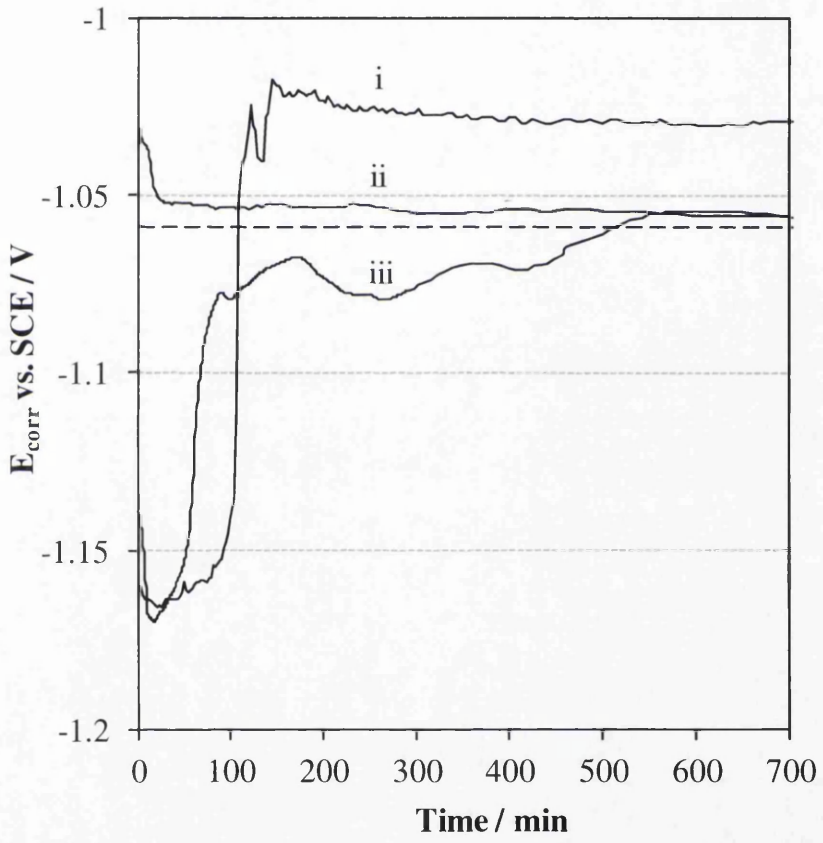

Fig 4.7 Plot of E_{corr} with respect to time for HDG immersed in aerated 5% wt/v NaCl (aq) electrolyte at pH 7 containing (i) $5x10^{-2}$ mol dm^{-3} (ii) $1x10^{-3}$ mol dm^{-3} (iii) $1x10^{-2}$ mol dm^{-3} additions of H_2PP. The dashed line represents the eventual value obtained in the absence of inhibitor.

The initial period up to ca. 100 min indicates predominant net cathodic inhibition where samples were immersed in $[PP^{2-}]$ of $5x10^{-2}$mol dm^{-3} and $1x10^{-3}$mol dm^{-3} shown in plots (i) and (ii). The possible mechanism by which this occurs is represented schematically in Fig. 4.8. When the HDG sample is initially immersed in the inhibited electrolyte, the localised corrosion activity is represented by Fig. 4.8(a) where low level anodic activity, distributed over large areas of the exposed surface is galvanically coupled with intense

cathodic sites. Fig 4.8(b) shows a high pH zone in the vicinity of the local cathode which results in the conversion of bulk $HPP^{-}_{(aq)}$ anions to $PP^{2-}_{(aq)}$. Zn^{2+} ions produced by Reaction (4.1) migrate to the sites of local cathodic activity and, by combining with free PP^{2-} anions, they form a solid Zn(PP) film thus stifling ongoing interfacial electron transfer as illustrated in Fig.4.8(c).

Beyond the 100 min immersion time it can be observed that plot (i), showing the result for $5x10^{-2}$ $molL^{-2}$ $[PP^{2-}]$ additions to the electrolyte, rapidly increases to more positive E_{corr} values suggesting a conventional anodic inhibitor mechanism where an insoluble Zn(PP) film is formed at the anodic sites.

Phosphorus oxyacids undergo a series of stepwise deprotonations and, with each step; a progressively higher pK_a is exhibited. The deprotonation equilibria for H_2PP are as follows [4]:

$$H_2PP_{(aq)} \rightleftharpoons HPP^{-}_{(aq)} + H^{+}_{(aq)} \qquad (pK_{a1} = 2.3) \qquad (4.4)$$

$$HPP^{-}_{(aq)} \rightleftharpoons PP^{2-}_{(aq)} + H^{+}_{(aq)} \qquad (pK_{a2} = 7.8) \qquad (4.5)$$

The following equation can be used to calculate the $[Zn^{2+}]$ threshold at which ZnPP will precipitate:

$$[Zn^{2+}][PP^{2-}] = k_{sp} \qquad (4.6)$$

where k_{sp} in the solubility product which, through a series of titrations described in the previous chapter, was calculated to be $1x10^{-6}$ mol^2dm^{-6}.

Under aqueous conditions, the pH-dependent concentration of PP^{2-} ($[PP^{2-}]$) is given by:

$$[\mathbf{PP^{2-}}] = \frac{[\mathbf{PP}]_{\mathbf{tot}}}{\mathbf{1 + 10^{(-pH+7.8)} + 10^{(-2pH+7.8+2.3)}}} \qquad (4.7)$$

where $[PP]_{tot}$ is the total concentration of the phenyl phosphonate species. From Eq. 4.7 it can be shown that $[PP^{2-}] = 6.8 \times 10^{-3}$ $[PP]_{tot}$ at pH 7. By applying this value and the k_{sp} value to Eq. 4.6 a $[Zn^{2+}]$ threshold can be calculated for the precipitation of solid Zn(PP) where a value of 1.46×10^{-4} mol^2dm^{-6} is obtained.

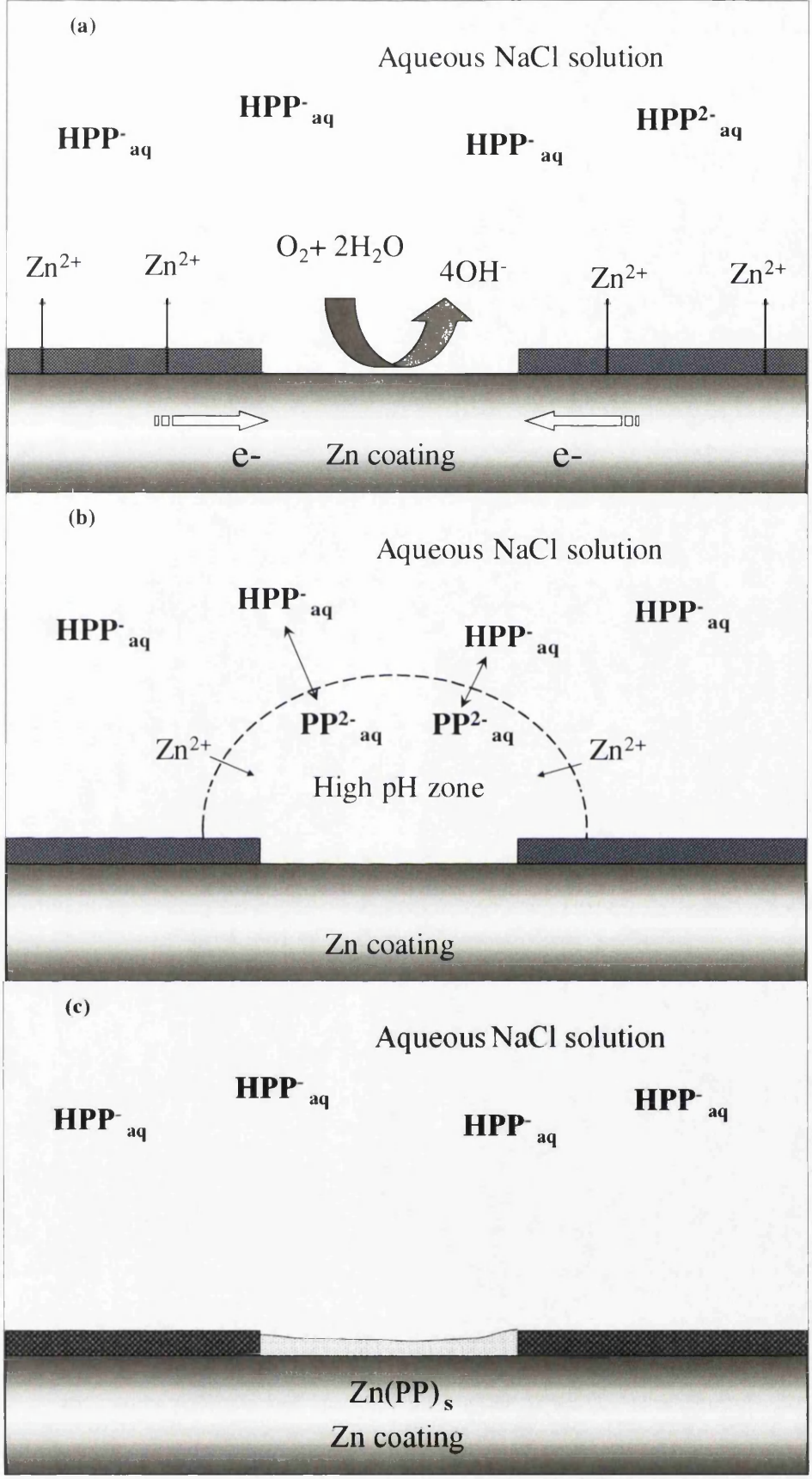

Fig 4.8 Schematic representation of the mechanism of zinc corrosion inhibition by aqueous phenyphosphonate ions at neutral pH, showing (a) localisation of the early stages of corrosion, (b) phosphonate speciation in the vicinity of the local cathode and (c) the deposition of an insoluble film.

4.3.2 pH Dependence of a phenyl phosphonic acid inhibitor

The Pourbaix diagram (fig 1.5) given in Section 1.2.3 shows the reaction conditions of zinc immersed in water at various pH and potential values. According to the Pourbaix diagram, when zinc is immersed in electrolyte of low pH, an abundance of Zn^{2+} ions should be present. Where additions of H_2PP are made to an electrolyte of low pH, it is expected that $[PP^{2-}]$ levels would be insufficient to form a solid film with the Zn^{2+} ions. This is shown by the pk_a value given for Eq. 4.4 suggesting that inhibition efficiency should drop with decreasing pH. Conversely, at high pH levels, a high level of $[PP^{2-}]$ would be expected in the electrolyte according to Eq. 4.5. However, the corrosion product formed at high pH according to the Pourbaix diagram is the highly soluble zincate anion (ZnO_2^{2-}). Therefore, even with sufficient $[PP^{2-}]$, without the presence of Zn^{2+} ions it would not be possible for a solid Zn(PP) film to form.

In the current section corrosion activity occurring on a bare HDG surface was studied when fully immersed in uninhibited electrolyte at both pH 2 and pH 11.5 for comparison with neutral conditions. Fig 4.9 shows SVET derived current density surface maps for unpolarised HDG immersed in aerated 5% wt/v $NaCl_{(aq)}$ electrolyte altered to pH 2 at various immersion times between 1 h and 24 h. In contrast to the corrosion activity shown in fig 4.1, where the test was carried out in at pH 7, general anodic and cathodic activity can be observed. Due to the lack of OH^- in the acidic electrolyte no 'white rust' corrosion product is observed in the photographic image given in fig 4.10(d) which shows the sample surface after 24 h immersion. However, a tarnishing of the surface corresponding to the anodic regions visible in the current density surface maps can be observed.

Fig 4.10 shows SVET derived current density surface maps for unpolarised HDG immersed in aerated 5% wt/v NaCl electrolyte altered to pH 11.5 shown at various immersion times between 1 h and 24 h. It can be observed that a single cathode and single anode situation prevails. However, in this case, the anodic region is initially localized to one confined region but, after approximately five hours, can be seen to spread in a wave-like manner across the substrate so the anodic and cathodic regions occupy approximately half the test area each. The photographic image given in 4.9(f)

shows the appearance of the HDG surface after 24 h immersion; the paler areas can be related to the anodic region shown in Fig. 4.10(e).

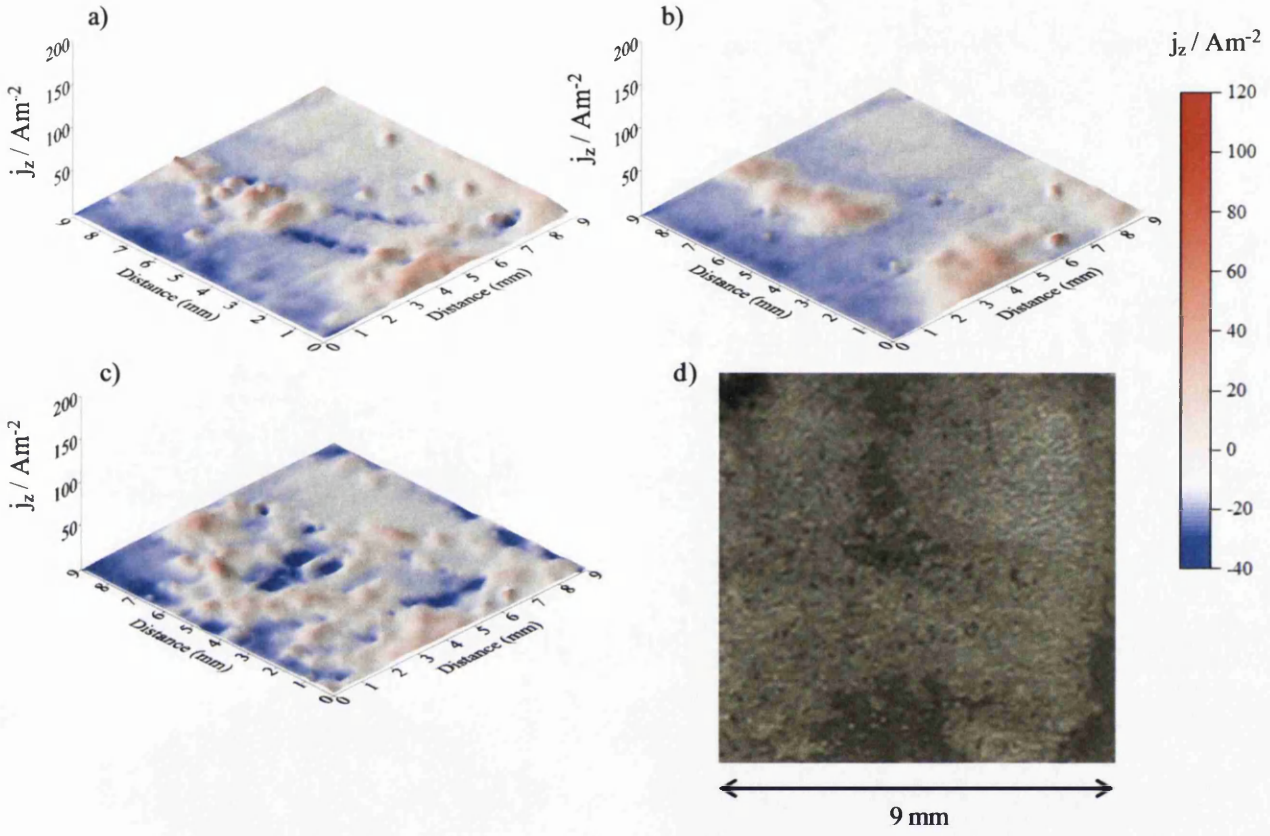

Fig 4.9 SVET-derived current density surface map of unpolarised HDG obtained following immersion in aerated 5% (w/v) NaCl (aq) at pH 2 at time a) 1h b) 14 h, and c) 24 h where d) shows a photographic image of the sample after 24h immersion.

Fig. 4.11 shows a summary of area-averaged, integrated SVET-derived anodic current density (J_{at}) versus time profiles obtained for HDG immersed in aerated 5% (w/v) $NaCl_{(aq)}$ at a range of pH where no inhibitor additions have been made to the electrolyte. It can be observed that the highest J_{at} values are observed in those experiments carried out at high pH. The Pourbaix diagram suggests that there should be a passive region due to the formation of a $Zn(OH)_2$ in alkali conditions. However, in the experimental conditions used here, the presence of 5% NaCl may provide Cl^- anions that destroy any passive film. Unexpectedly, those tests carried out in acidic conditions show lower J_{at} values than those carried in both alkali and neutral conditions. This will be discussed further where experiments carried out in inhibitor-containing electrolyte are presented.

In summary, it can be shown that the pH of the electrolyte has a significant effect on the corrosion behaviour of a bare HDG surface when immersed in aerated 5% wt/v $NaCl_{(aq)}$ electrolyte for 24 h. In neutral conditions the anodic region is shown to be highly localised and isolated. At high pH a moving anode region has been recorded. In acidic conditions general corrosion is observed where anodic and cathodic regions are highly interspersed. The effect on corrosion in these conditions will now be discussed with regards to the presence of an H_2PP inhibitor.

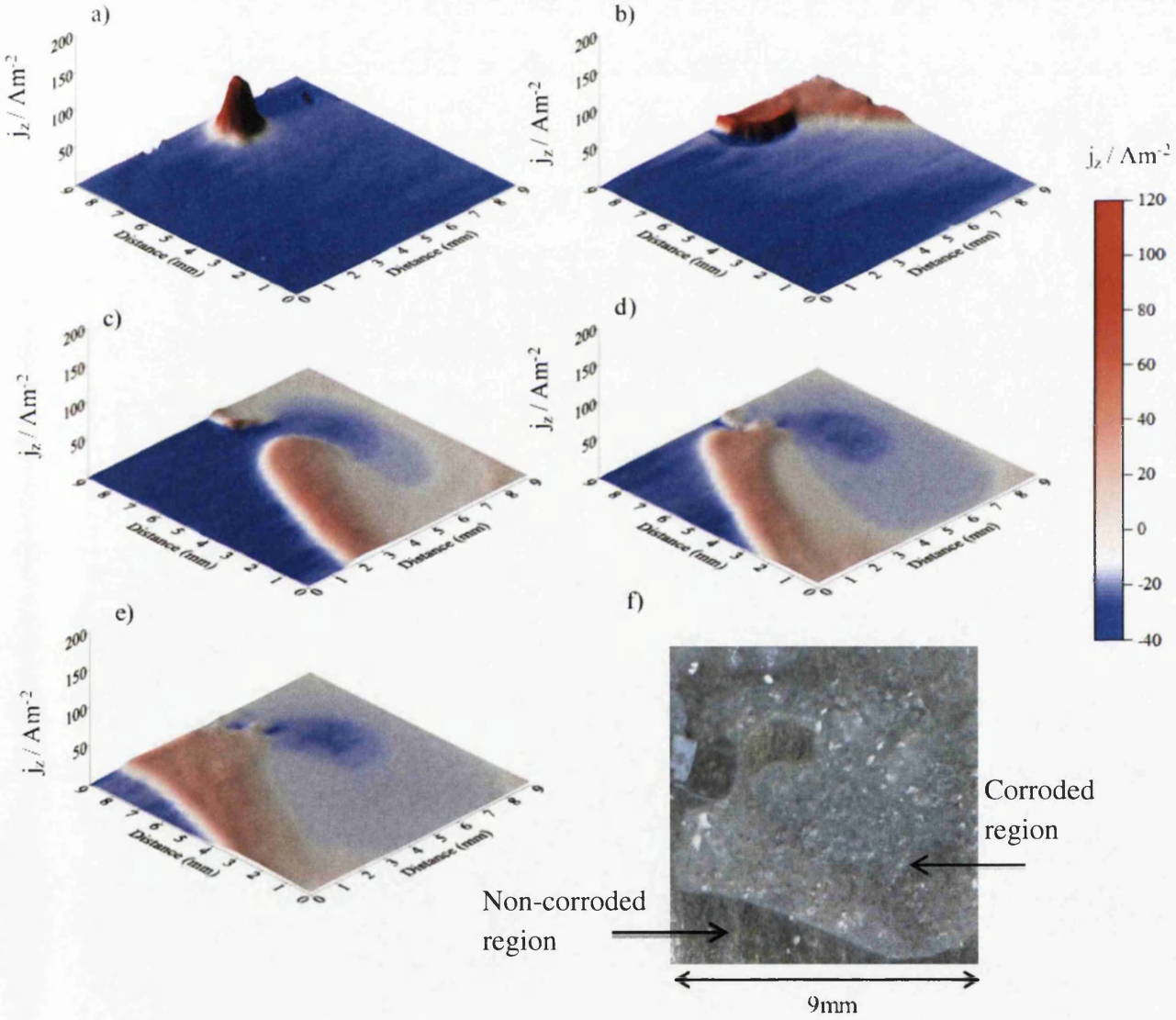

Fig 4.10 SVET derived current density surface map of unpolarised HDG obtained following immersion in aerated 5% (w/v) NaCl (aq) at pH 11.5 at time a) 1 h b) 6 h, c) 14 h, d) 22 h and e) 24 h where d) shows a photographic image of the sample after 24 h immersion.

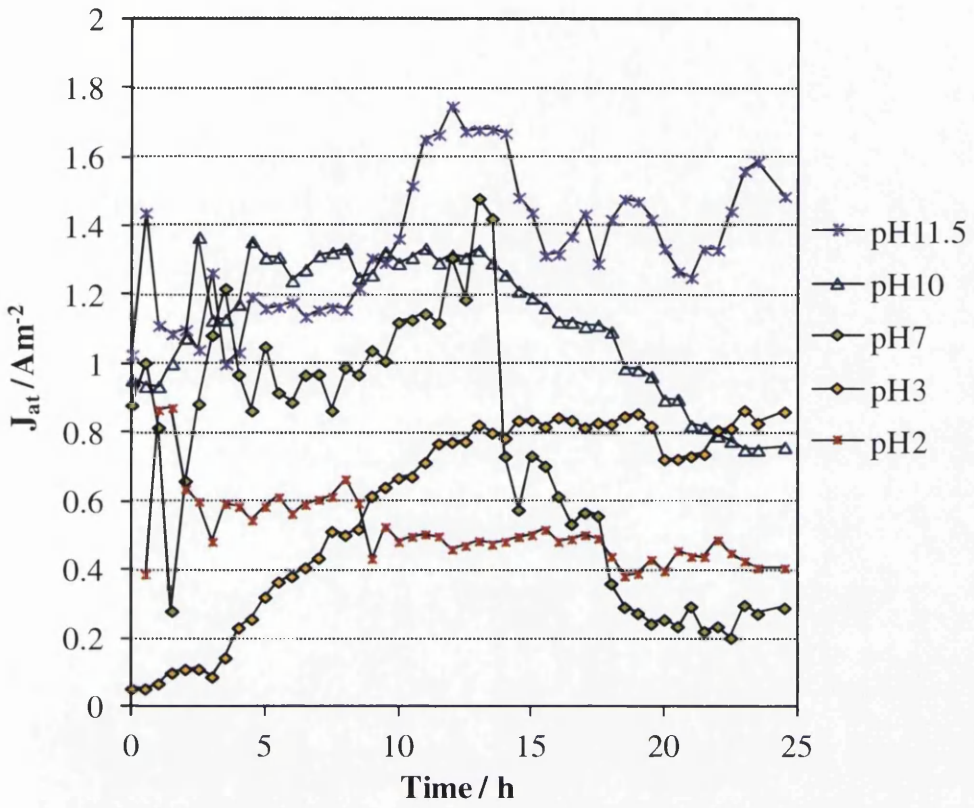

Fig 4.11 Summary of area-averaged, integrated SVET-derived anodic current density versus time profiles obtained for HDG immersed in aerated 5% (w/v) $NaCl_{(aq)}$ at a range of pH where no inhibitor additions have been made to the electrolyte.

Fig 4.12 shows SVET derived current density surface maps for unpolarised HDG immersed in aerated 5% wt/v $NaCl_{(aq)}$ electrolyte altered to pH 2 containing additions of $5x10^{-2}$ mol dm^{-3} H_2PP shown at various times between 0.5 h and 24 h. The SVET surface maps show general corrosion that appears to be more intense than that shown for the uninhibited test in fig 4.9.

Fig 4.13 shows SVET-derived current density surface maps for unpolarised HDG immersed in aerated 5% wt/v NaCl electrolyte altered to pH 11.5 containing additions of $5x10^{-2}$ mol dm^{-3} H_2PP shown at various times between 0.5 h and 24 h. It can be observed that a strong anodic peak forms on the surface and passivates after ca. 6 h. A further anodic region is shown to form at ca. 22 h. The photographic image given in fig 4.13(f) shows the substantial amount of corrosion product formed on the sample surface. The result given in fig 4.14(b) for pH 11.5 shows that as the H_2PP concentration is increased the J_{at} is progressively decreased. However, at the higher

concentration of H_2PP, it can be observed that intense localised anodic activity occurs in between periods of total inhibition. This is shown by the anodic spikes that initiate at immersion times of approximately 2 h and 22 h and remain for approximately 3 h. It is suggested that, in alkaline conditions, H_2PP acts as an adsorption inhibitor whereby the PP^{2-} anion adsorbs onto the HDG surface and reinforces the $Zn(OH)_2$ layer. This layer disfavours Cl^- adsorption thus preventing the anions from destroying this passive layer. However, the periods of intense, highly localised anodic activity, show that this layer is only partially protective.

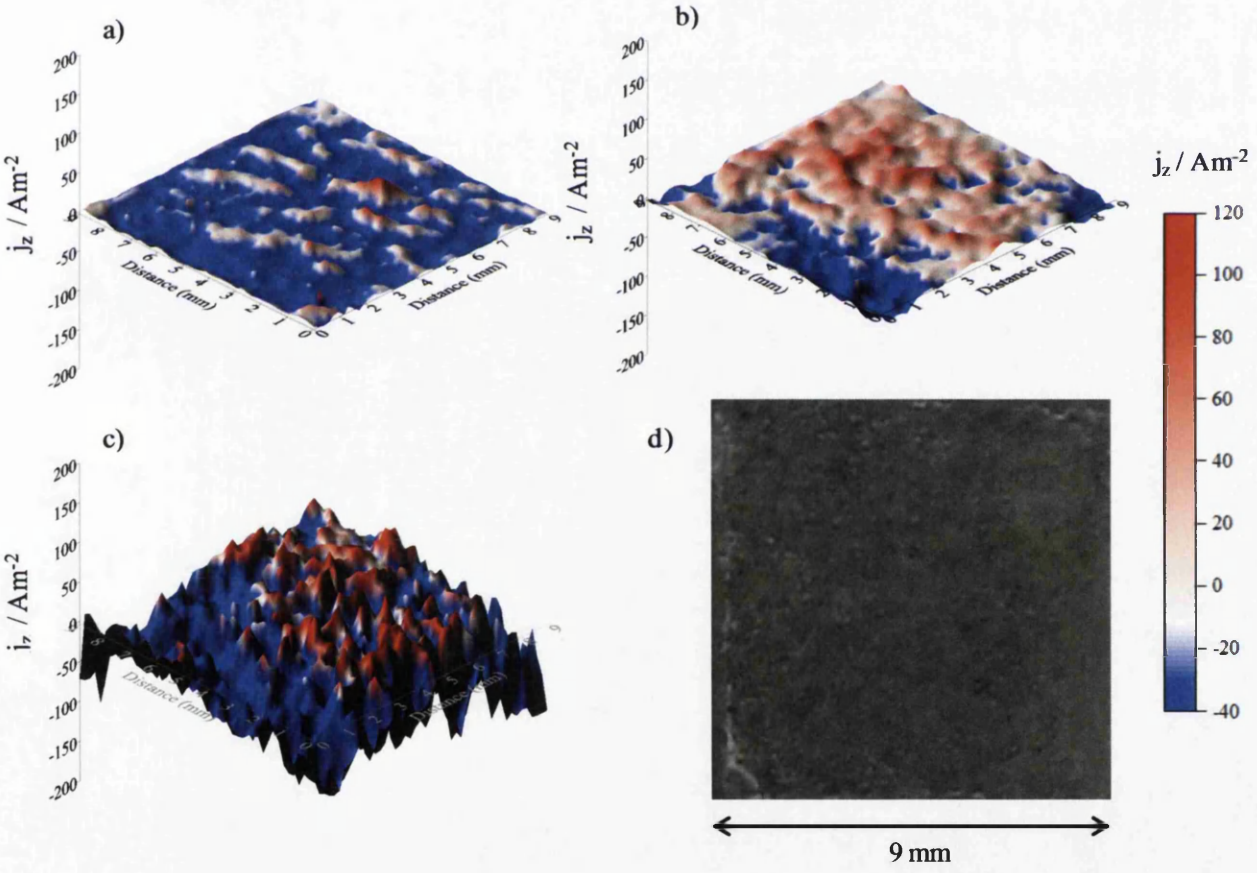

Fig 4.12 SVET derived current density surface map of unpolarised HDG obtained following immersion in aerated 5% (w/v) NaCl (aq) at pH 2 containing $5x10^{-2}$mol dm^{-3} H_2PP at (a) 30 mins, (b) 2.5 h, c) 22 h where (d) shows a photographic image of the sample after 24h immersion.

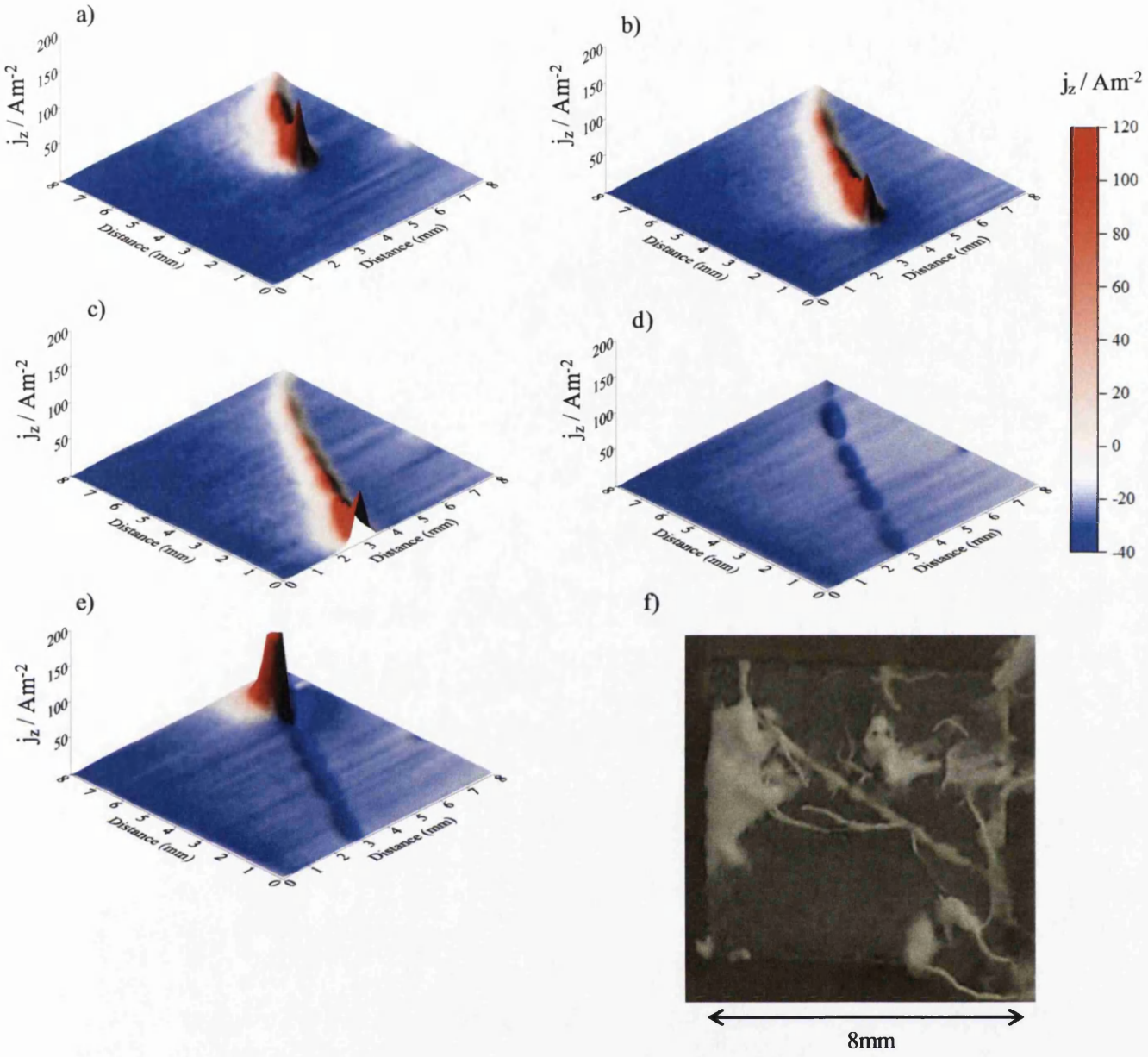

Fig 4.13 SVET derived current density surface map of unpolarised HDG obtained following immersion in aerated 5% (w/v) NaCl (aq) at pH 11.5 containing $5x10^{-2}$mol dm^{-3} H_2PP at (a) 2 h, (b) 3.5 h, c) 4 h, (d) 6 h, (e) 22 h, where (f) shows a photographic image of the sample after 24h immersion.

Fig 4.14 gives a summary of area-averaged, integrated SVET-derived anodic current density (J_{at}) vs. time profiles for samples immersed in electrolyte containing no inhibitor, $1x10^{-2}$ mol dm^{-3} H_2PP and $5x10^{-2}$ mol dm^{-3} H_2PP at (a) pH 2 and (b) pH 11.5. It is shown by the plots presented in 4.14(a) that, where a high H_2PP concentration is present, J_{at} is initially less than that of the uninhibited experiment, but after

approximately 17 h J_{at} progressively increases to extremely high values. At the lower H_2PP concentration very little corrosive activity was observed.

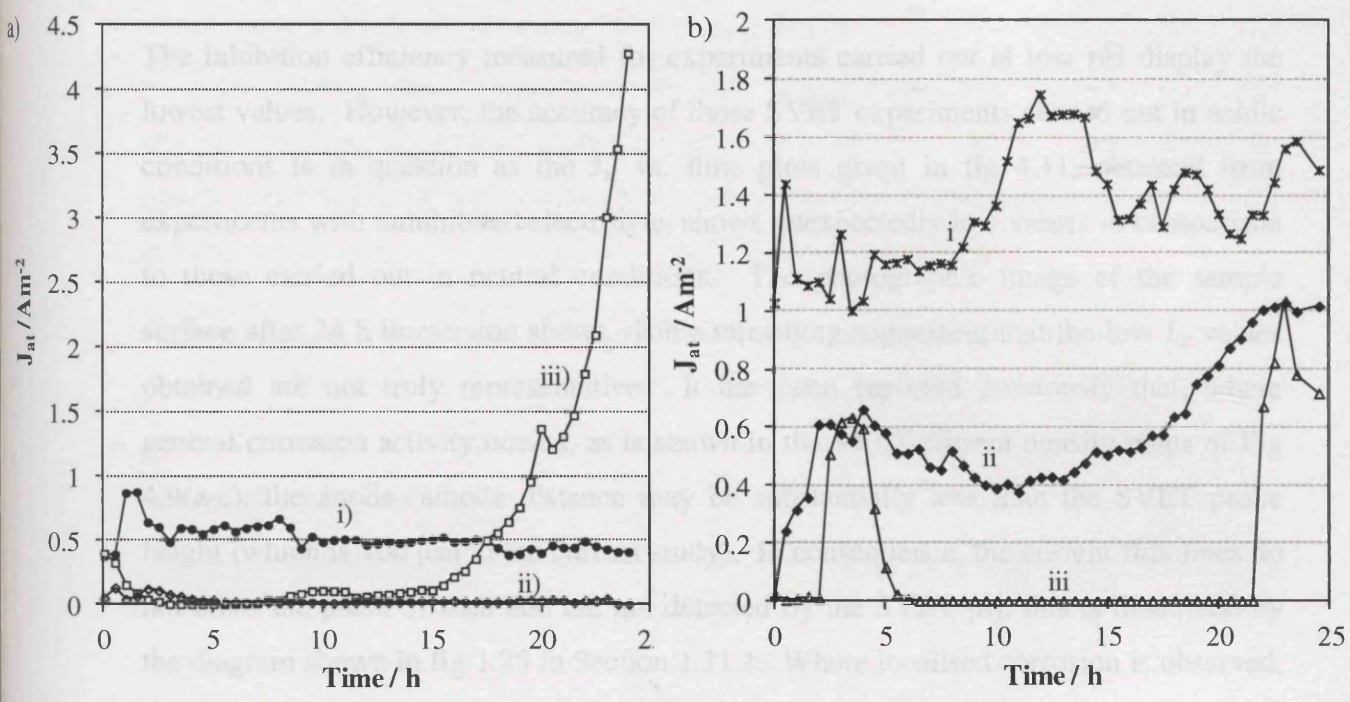

Fig 4.14 Area-averaged, integrated SVET-derived anodic current density vs. time profiles obtained for HDG immersed in aerated 5% (w/v) $NaCl_{(aq)}$ with i) no H_2PP additions and H_2PP additions of ii) 10^{-2}mol dm^{-3} and iii) $5x10^{-2}$mol dm^{-3} where the bulk pH of the experimental electrolyte has been altered to (a) pH 2 and (b) pH 11.5.

The inhibition efficiency (%) of H_2PP with respect to pH is presented in the plot given in fig 4.15. Efficiency was calculated as follows:

$$\textbf{Inhibition efficieny}\ (\%) = \frac{\textbf{mass loss}_c - \textbf{mass loss}_i}{\textbf{mass loss}_c}\textbf{x100} \qquad (4.8)$$

where 'mass loss$_c$' and 'mass loss$_i$' are the total mass of zinc lost after 24 h immersion in uninhibited electrolyte and electrolyte containing $5x10^{-2}$ mol dm^{-3} H_2PP respectively. Values were calculated from SVET-derived data using Eq. 4.3. It is expected that inhibition efficiency would be the highest in neutral conditions with a reduction observed with increasing or decreasing pH. The plot shows an efficiency of 96% in neutral conditions. The general trend is for efficiency to be reduced where pH is above and below neutral. However, pH 11.5 shows an efficiency of 90%. As shown in fig

4.13 and 4.14(b), the intense anodic activity is highly damaging and occurs for short periods of time. In the remaining time no anodic activity is recorded so, although the surface has been attacked and protection is only partial, the efficiency appears close to that at pH 7 for the SVET-derived efficiency data.

The inhibition efficiency measured for experiments carried out at low pH display the lowest values. However, the accuracy of those SVET experiments carried out in acidic conditions is in question as the J_{at} vs. time plots given in fig 4.11, obtained from experiments with uninhibited electrolyte, shows unexpectedly low values in comparison to those carried out in neutral conditions. The photographic image of the sample surface after 24 h immersion shows visible tarnishing suggesting that the low J_{at} values obtained are not truly representative. It has been reported previously that, where general corrosion activity occurs, as is shown in the SVET current density maps of Fig 4.9(a-c), the anode-cathode distance may be substantially less than the SVET probe height (which is 100 μm in the current study). In consequence, the current flux lines do not cross the plane of scan and are not detected by the SVET [6]; this is illustrated by the diagram shown in fig 1.25 in Section 1.11.1. Where localised corrosion is observed, the distance between anode and cathode is typically greater than that of the probe height providing good accuracy of results.

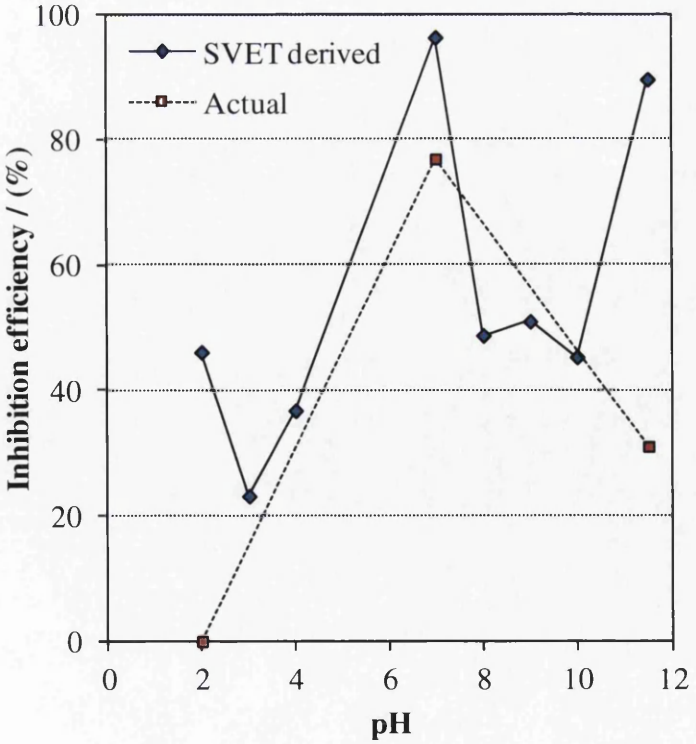

Fig 4.15 Plot showing the inhibition efficiency (%) of H_2PP with respect to pH.

To verify this notion, actual mass loss experiments were carried out as described in Section 4.2.3. The results are presented as a percentage of Zn mass loss in the bar chart shown in fig 4.16. Samples were immersed for a period of one week in 5% wt/v $NaCl_{(aq)}$ containing either no inhibitor, $5x10^{-2}$ mol dm^{-3} H_2PP or $1x10^{-2}$ mol dm^{-3} H_2PP where each inhibitor concentration level was tested at pH 2, pH 7 and pH 11.5. It can be observed that, where no inhibitor was present, a very similar Zn loss (%) value was recorded for samples immersed in the three levels of pH. This is in contrast to the results presented in fig 4.11 where the J_{at} values for experiments conducted in pH 2 are substantially lower.

Efficiency values have also been calculated for actual mass loss data at pH 2, pH 7 and pH 11.5. These are also summarised in fig 4.15. The Actual inhibition efficiency measured at pH 2 is substantially lower than that derived from the SVET. It is suggested, therefore, that the SVET derived J_{at} results presented for pH 2 immersion conditions cannot be taken as accurate, however, the observation of a change from localised to general corrosion is still an important result. A trend showing a progressive decrease in mass loss with increasing inhibitor concentration is shown for tests carried out in pH 7 electrolyte. This is in agreement with the J_{at} values presented in fig 4.5 and SVET-derived mass loss data presented in fig 4.6.

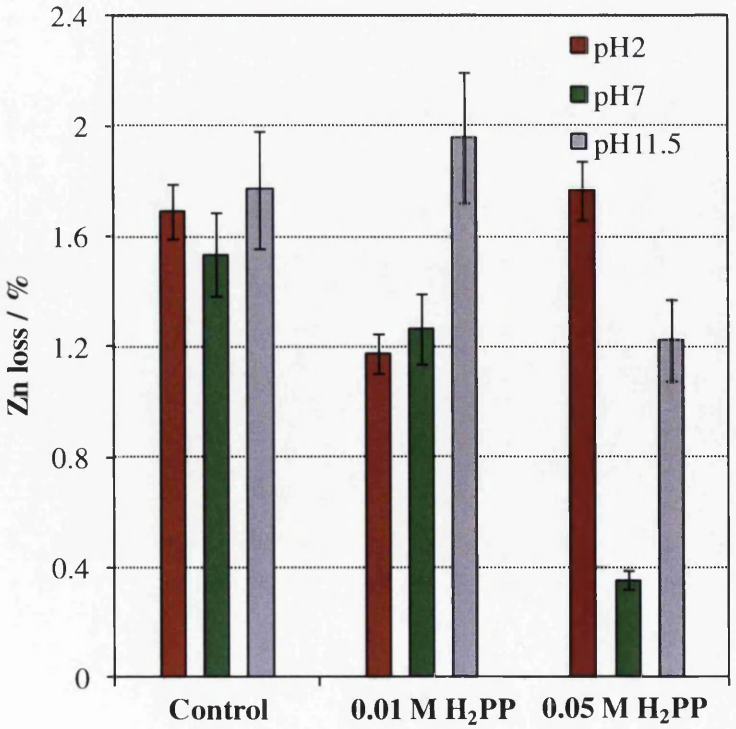

Fig 4.16 Bar chart showing Zinc loss (%) from HDG samples after one week of immersion in aerated 5% (w/v) $NaCl_{(aq)}$ at pH 2, pH 7 and pH 11.5 where no additions and $1x10^{-2}$ mol dm^{-3} H_2PP and $5x10^{-2}$mol dm^{-3} H_2PP additions have been made at each pH level.

4.3.3 Corrosion inhibition of hot dip galvanised steel by sodium phosphate

Having identified an optimum H_2PP concentration value of $5x10^{-2}$ mol dm^{-3} for the effective inhibition of a HDG surface, further experiments were carried out to compare the inhibition efficiency of H_2PP with sodium phosphate (Na_3PO_4). Figs 4.17(i) [a-c] show the SVET derived current density surface maps of unpolarised HDG samples after 24 h immersion in aerated 5% (w/v) NaCl (aq) containing $5x10^{-2}$ mol dm^{-3} Na_3PO_4 where electrolyte was adjusted to pH 2, pH 7 and pH 11.5 respectively. Photographic images taken after this 24 h period are given in fig 4.17(ii) [a-c].

The photographic image shown in fig 4.17(b)(ii) for the experiment carried out at pH 7 suggests that inhibition is only partial. A protective layer is visible over the whole surface but localised corrosive metal attack can be observed isolated in a small area. This is confirmed by the anodic region shown in the same corner of the surface of the SVET map of fig 4.17(a)(i). In comparison, the same test carried out with H_2PP additions of identical concentration showed full inhibition on the surface. The area-averaged, integrated SVET-derived anodic current density vs. time profiles for immersion over 24 h, are given in Fig 4.18[a-c]. The results presented in (b) for the experiment carried out at pH7 shows hourly J_{at} values much lower than those of the uninhibited case throughout the 24 h period.

Hydrolysed corrosion product was produced in the experiment carried out at pH11.5. This is shown in the photographic image given in Fig 4.17(c)(ii). It can also be observed that, as with the experiment carried out at pH 7, all visible corrosion activity is constrained to an isolated region and the remainder of the surface is corrosion-free. The SVET surface map however shows several local anodes in a region covering half the test area. The J_{at} vs. time profile given in Fig 4.18(c) shows that, in comparison to a relatively constant J_{at} value of around 1.25 Am^{-2} recorded throughout the 24 h experiment in uninhibited conditions, when Na_3PO_4 is present initial J_{at} values are extremely low. After approximately 4 h J_{at} begins to increases reaching that of the

uninhibited case at ca. 15 h. This increase in J_{at} continues to progresses over the remaining time period. Unlike the same experiment carried out with H_2PP, no re-passivation of the surface is observed after the occurrence of anodic activity where J_{at} values return to approximately 0 Am^{-2}.

In contrast to the experiment carried out with H_2PP at pH 2, the equivalent experiment presented here shows no sign of inhibition as the J_{at} values, given in 4.17(a), are substantially higher than that of the uninhibited case throughout the 24 h time period.

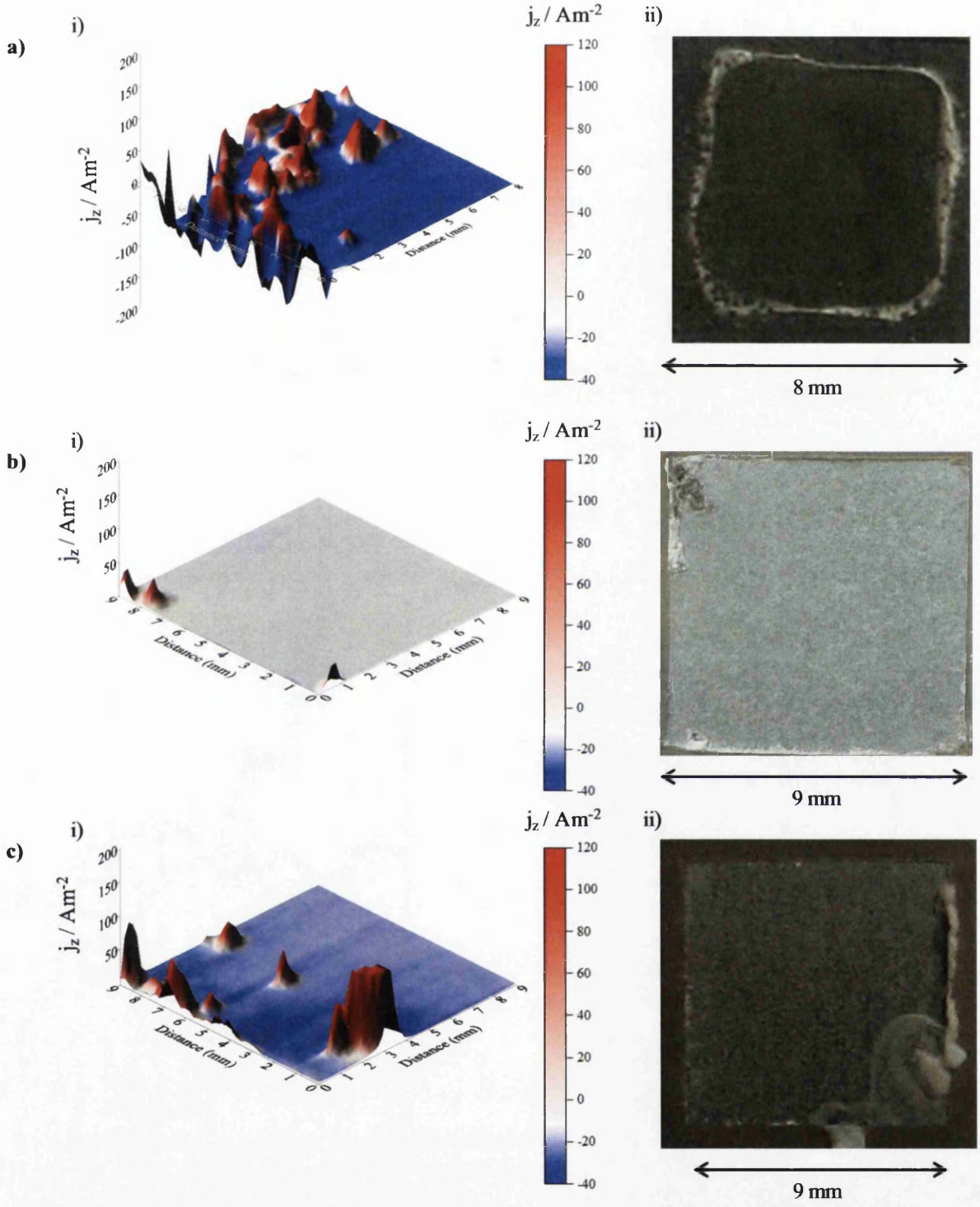

Fig 4.17 i) SVET-derived current density surface maps of unpolarised HDG obtained following immersion in aerated 5% (w/v) NaCl (aq) containing $5x10^{-2}$ mol dm^{-3} Na_3PO_4 after 24 h and ii) a photographic image of the sample after 24 h immersion where the bulk electrolyte was adjusted to a) pH 2, b) pH 7 and c) pH 11.5.

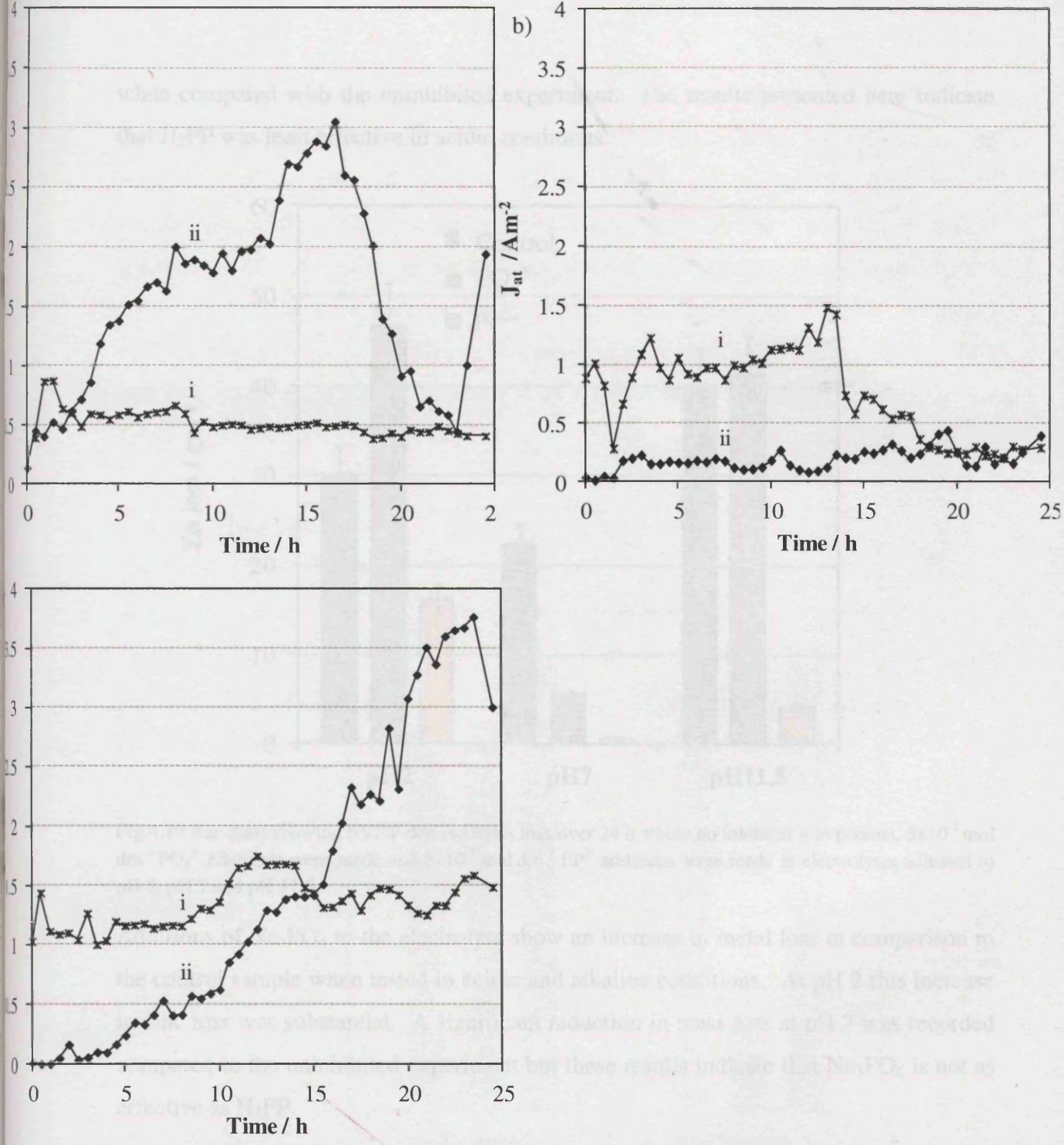

Fig 4.18 Summary of area-averaged, integrated SVET-derived anodic current density versus time profiles obtained for HDG immersed in aerated 5% (w/v) NaCl (aq) containing i) no inhibitor and ii) $5x10^{-2}$ mol dm^{-3} PO_4^{3-} adjusted to a) pH 2 b) pH 7 and c) pH 11.5.

Zinc mass loss values were derived, using Eq. 4.3, from the SVET experiments carried out in electrolyte adjusted to pH 2, pH 7 and pH 11.5 containing Na_3PO_4, H_2PP and no inhibitor additions. This is presented in fig 4.19 where, in all cases, it can be shown that zinc mass loss is at the lowest where experiments were carried out in neutral conditions. In all pH conditions, additions of H_2PP to the electrolyte show a reduction in zinc loss

when compared with the uninhibited experiment. The results presented here indicate that H_2PP was least effective in acidic conditions.

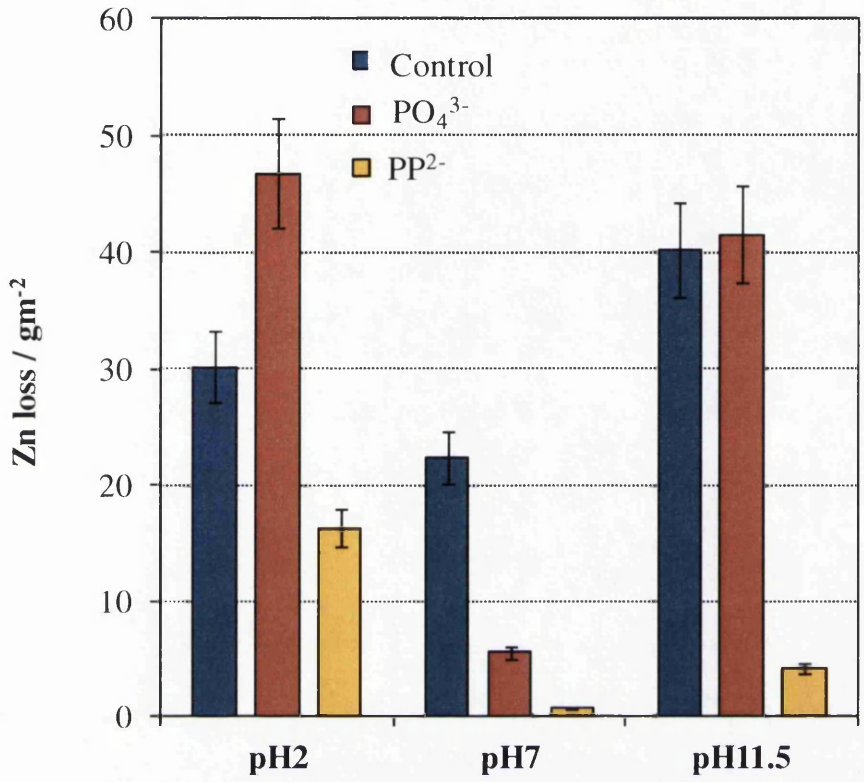

Fig 4.19 Bar chart showing SVET-derived mass loss over 24 h where no inhibitor was present, $5x10^{-2}$ mol dm^{-3} PO_4^{3-} additions were made and $5x10^{-2}$ mol dm^{-3} PP^{2-} additions were made in electrolytes adjusted to pH 2, pH 7 and pH 11.5.

Additions of Na_3PO_4 to the electrolyte show an increase in metal loss in comparison to the control sample when tested in acidic and alkaline conditions. At pH 2 this increase in zinc loss was substantial. A significant reduction in mass loss at pH 7 was recorded compared to the uninhibited experiment but these results indicate that Na_3PO_4 is not as effective as H_2PP.

Further actual mass loss experiments were carried out to determine whether the SVET derived results may be considered reliable. These were, again, carried out in electrolyte adjusted to pH 2, pH 7 and pH 11.5 with and without additions of $5x10^{-2}$ mol dm^{-3} Na_3PO_4. The results are presented in Fig 4.20 where it can be observed that, as with the SVET-derived data, a substantial decrease in mass loss is observed where Na_3PO_4 is present in neutral conditions. As with the SVET data, in both acidic and alkali conditions, it can be shown that Na_3PO_4 additions result in an increase in zinc loss when compared with uninhibited experiments. However, the actual mass loss recorded in

acidic conditions shows only a slight increase in zinc mass loss where Na_3PO_4 was present in comparison to the SVET derived data where this increase was substantial. As suggested in the previous section, the generalised anodic activity occurring in uninhibited, acidic conditions may be undetectable by the SVET. This suggests that, if the amount of zinc lost in the uninhibited experiment has been underestimated by the SVET-derived data, it may be more realistic to suggest that Na_3PO_4 is simply ineffective at low pH rather than an accelerant of corrosion. Efficiency values of 75% and 73% for SVET-derived and actual mass respectively were calculated using Eq. 4.8 for the experiments carried out at pH 7.

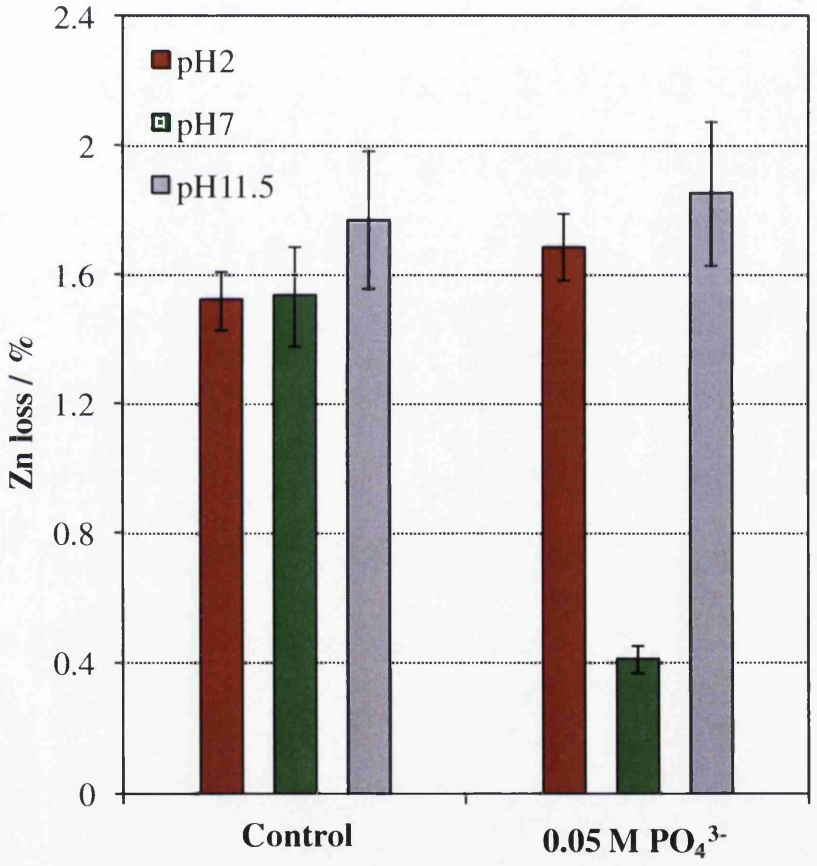

Fig 4.20 Bar chart showing zinc loss (%) from HDG samples after one week of immersion in aerated 5% (w/v) $NaCl_{(aq)}$ adjusted to pH 2 , pH 7 and pH 11.5 where no additions and $5x10^{-2}$ mol dm^{-3} PO_4^{3-} additions have been made at each pH level.

H_2PP appears to be a more effective inhibitor than Na_3PO_4 in the experiments presented here. Phosphorus oxyacids undergo a series of stepwise deprotonations and, with each step; a progressively higher pK_a is exhibited. The first, second and third pK_a values are 2.0, 6.9 and 12.3 respectively for H_3PO_4 [5]. The following equation can be used to calculate the $[Zn^{2+}]$ threshold at which $Zn_3(PO_4)_2$ will precipitate:

$$[Zn^{2+}]^3[PO_4^{3-}]^2 = k_{sp} \qquad [4.7]$$

where k_{sp} is $9x10^{-33}$ $mol^2dm\text{-}6$. Under aqueous conditions, the pH-dependent concentration of PO_4^{3-} ($[PO_4^{3-}]$) is given by:

[4.8]

---

where $[PO_4]_{tot}$ is the total concentration of the phosphate species, in this case $5x10^{-2}$ mol^2dm^{-6}. Eq. 4.8 may be used to show that $[PO_4^{3-}] = 8.8 \times 10^{-8}$. By applying this value and the k_{sp} value to Eq. 4.7 a $[Zn^{2+}]$ threshold can be calculated for the precipitation of solid $Zn_3(PO_4)_2$ where a value of 5.38×10^{-5} mol^2dm^{-6} is obtained. This is lower than the predicted $[Zn^{2+}]$ threshold value for the precipitation of ZnPP which is 1.46×10^{-4} mol^2dm^{-6}; this result suggests that Na_3PO_4 should be the more effective inhibitor. However, it is proposed that the incomplete inhibition observed in this case, where availability of PO_4^{3-} is not limited, results from precipitation of $Zn_3(PO_4)_2$ in solution above the sites of anodic zinc dissolution and not directly on the corroding surface. This is represented schematically in fig 4.20. Zn^{2+}, therefore, does not migrate to sites of local cathodic activity, as was the case with ZnPP (illustrated in fig 4.8b), to instigate the deposition of blocking films of $Zn_3(PO_4)_2$ directly on these regions. This was observed previously by Williams et al where the effect of a phosphate inhibitor on a corroding magnesium surface was assessed [7].

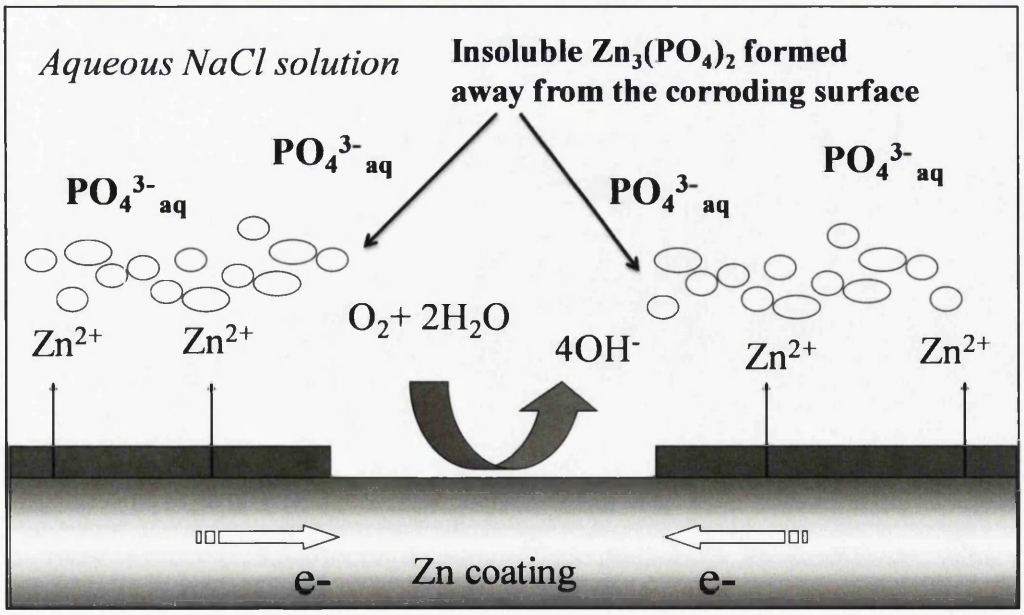

Fig 4.21 Schematic representation of a locally corroding HDG surface in the presence of phosphate ions.

4.4 Conclusions

The current chapter assesses the effectiveness of phenyl phosphonic acid (H_2PP) as a corrosion inhibitor for hot dip galvanised steel (HDG) surfaces immersed in 5%wt/v $NaCl_{(aq)}$ electrolyte containing additions of H_2PP. The work presented here demonstrates, using the in situ scanning vibrating electrode technique (SVET), and through a series of open circuit potential experiments, that increasing the concentration of H_2PP made to electrolyte progressively decreases the corrosion activity on the HDG surface. At a concentration of $5x10^{-2}$ mol^2dm^{-6}, H_2PP has been shown to keep a bare HDG surface free from white corrosion product for up to 24 h with an efficiency, measured using SVET-derived data, of 96%. The suggested inhibition mechanism is the formation of a Zn(PP) salt film that forms initially on cathodic sites and subsequently on anodic sites. Where a zone of high pH evolves at a cathodic site a conversion of bulk $HPP^-_{(aq)}$ anions to $PP^{2-}_{(aq)}$ may be expected. A combination of free PP^{2-} anions with Zn^{2+} ions produced by the anodic dissolution of zinc at the anodic sites forms a solid Zn(PP) film which stifles any ongoing interfacial electron transfer.

It was expected that H_2PP would be less effective as a corrosion inhibitor at non-neutral pH. At low pH, $[PP^{2-}]$ levels would be insufficient to form a solid film with the abundance of Zn^{2+} ions present. At high pH insufficient Zn^{2+} would be available to combine with the abundance of available PP^{2-} anions as a presence of the soluble zincate anion (ZnO_2^{2-}) tends to prevail according to the Pourbaix diagram (given in fig 1.5 of Section 1.2.3) . It has been shown in the work presented here that, in both acidic and alkaline conditions, corrosion activity is present where additions of $5x10^{-2}$ mol^2dm^{-6} H_2PP have been made. Anodic activity has been shown to change from isolated and localised in neutral conditions to moveable when in alkali conditions and highly general when in acidic conditions. The nature of the general corrosion observed visually in experiments carried out at low pH meant that SVET detection was poor. However, through photographing the sample surface and carrying out actual mass-loss experiments it can be concluded that H_2PP additions made to acidic media are less effective than in neutral conditions.

Partial inhibition was observed in alkaline conditions where it is thought that H_2PP acts as an adsorption inhibitor. The PP^{2-} anion adsorbs onto the zinc surface and reinforces the $Zn(OH)_2$ layer that disfavours Cl^- adsorption thus preventing the anions from

destroying this passive layer. The intermittent periods of high anodic activity showed that this layer must be partially protective only.

Finally, in situ SVET experiments carried out with sodium phosphate (Na_3PO_4) at the same concentration showed only partial protection of the HDG surface in neutral conditions and an SVET-derived efficiency of 75% was calculated. From this it can be concluded that H_2PP is more effective at this concentration. This was unexpected as the calculated $[Zn^{2+}]$ threshold value for solid $Zn_3(PO_4)_2$ precipitation to occur was substantially lower than the value of 1.46 x 10^{-4} mol^2dm^-6 calculated for Zn(PP) precipitation. However, it is suggested that precipitation of $Zn_3(PO_4)_2$ does not occur directly on the corroding surface but rests in solution in the regions above as has been observed previously [7]. Furthermore, Na_3PO_4 additions at both low and high pH were found it be relatively ineffective inhibitors.

The SVET has proved to be a useful tool in determining the effective corrosion inhibition of HDG surfaces immersed in electrolyte containing H_2PP at a concentration of $5x10^{-2}$ mol^2dm^{-6} in neutral conditions. The previous Chapter showed that, where additions of H_2PP were made to a polyvinyl butyral (PVB) coating, underfilm delamination was stifled and the delamination rate reduced substantially. One suggested inhibition mechanism was the leaching of H_2PP, PP^{2-} and HPP^- from the edge of the coating/defect boundary in to the $NaCl_{(aq)}$ electrolyte at the exposed zinc surface. The work presented in the current Chapter suggests that this is indeed a possible mechanism as additions of H_2PP present in electrolyte at the optimum level have been shown to keep a surface of exposed HDG free from white rust for a period of 24 h.

4.5 References

[1] S. A. Katz, *Environ. Health Perspect.*, vol. 92, 13–6, 1991.

[2] X. Zhang, C. Van Den Bos, W. G. Sloof, A. Hovestad, H. Terryn, and J. H. W. de Wit, *Surf. Coatings Technol.*, vol. 199, 1, 92–104, 2005.

[3] S. Thomas, N. Birbilis, M. S. Venkatraman, and I. S. Cole, *Corros. Sci.*, vol. 69, 11–22, 2013.

[4] T. H. Muster, W. D. Ganther, and I. S. Cole, *Corros. Sci.*, vol. 49, 4, 2037–2058, 2007.

[5] G. Williams, a. Gabriel, A. Cook, and H. N. McMurray, *J. Electrochem. Soc.*, vol. 153, 10, B425, 2006.

[6] G. Williams, A. J. Coleman, and H. N. McMurray, *Electrochim. Acta*, vol. 55, 20, 5947–5958, 2010.

[7] G. Williams, H. N. McMurray, and R. Grace, *Electrochim. Acta*, vol. 55, 27, 7824–7833, 2010.

Chapter Five.

Inhibition of corrosion-driven organic coating delamination on iron by phenyl phosphonic acid.

5.1 Introduction

In the current Chapter a non-chromate inhibitor, organic phenyl phosphonic acid (H_2PP), is added to a polyvinyl butyral (PVB) polymer solution. In Chapter three, such a system was shown to prolong the delamination initiation time (t_i) by ca. 1200 min and reduce the delamination rate (k_{del}) by 94% on a hot dip galvanised (HDG) steel surface where additions of 10% H_2PP were made to the PVB coating.

The primary aim of the work presented in this Chapter is to investigate the influence of H_2PP on both coating disbondment and filiform corrosion, when dissolved in an organic 'primer' PVB coating, applied to an iron substrate. The effect of H_2PP on underfilm delamination has been studied using two different experiments and, in both cases, the SKP technique has been employed to carry out measurements. The first type of experiment was carried out using the technique pioneered by Stratmann et al where the coating is partially lifted from the substrate and exposed to a large defect-containing electrolyte [1]. The experimental conditions are harsh and uninhibited coating delamination rates are high; this allows for a clear distinction between delamination rates where different levels of H_2PP are present. The second type of delamination experiment represents a realistic scenario where electrolyte is added to a small, penetrative scratch and first allowed to dry being exposed to a humid environment. This approach will establish whether H_2PP is a viable inhibitor in an environment that mimics a typical in-service defect. Further investigation using a series of SVET and OCP experiments will assess whether the leaching of H_2PP into electrolyte has an effect on the corrosion of bare iron. Furthermore, the effectiveness of in-coating H_2PP at halting FFC will be assessed.

FFC experiments have been carried out in the current chapter using the technique that is described in Section 5.2. The filament propagation rate has been assessed with regards to levels of H_2PP additions made to a PVB coating and, hence, the effectiveness of H_2PP as an inhibitor for FFC has been determined.

5.2 Experimental procedure

5.2.1 Materials

Iron foil samples (99.9% Fe) of 1.5 mm thickness were obtained from Goodfellow Metals Ltd and were received as 50 mm square coupons. Polyvinyl butyral (PVB) solutions were prepared in ethanol (15.5% w/w) MW 70,000-100,000 and the required amount of phenyl phosphonic acid (H_2PP) was added and thoroughly mixed. All chemicals were supplied by Sigma-Aldrich Chemical Co and were of analytical grade purity.

5.2.2 Sample preparation

All samples in the current chapter were cleaned as described in Section 2.2.1. The first set of SKP experiments were carried out using a standard delamination cell as described in Section 2.2.1.1 and well document elsewhere in literature published by Stratmann et al [2,3]. For the second set of SKP experiments, samples were prepared as described in Section 2.2.1.1 and documented elsewhere by Williams et al [4]. For SVET and OCP testing samples were prepared as described in Section 2.3.1.

5.2.3 Methods

For the Standard delamination testing, an electrolyte of 5% wt/v $NaCl_{(aq)}$ was used. The SKP reference probe was scanned in four lines of 12 mm over the coated surface, normal and adjacent with the defect-coating boundary. Scanning commenced immediately on the addition of electrolyte and thereafter at hourly intervals over a period of 24 h. A 100 μm reference probe-to-air gap was used with E_{corr} data points recorded at 20 per mm. In all delamination experiments the temperature and humidity were kept constant at 25°C and 95% r.h. The full description of SKP instrumentation, calibration procedure, set-up and subsequent analysis can be found in Sections 2.2.2 to 2.2.5.

For the second type of delamination experiment, a defect 2 mm in length was scribed into the PVB layer using a scalpel blade. Corrosion was initiated using 2 µl of 0.05 M $NaCl_{(aq)}$ solution introduced into the scribed region and allowed to dry in room air. The sample was then placed in the SKP chamber maintained at a constant 95% relative humidity and 20°C. Scans were carried out at hourly intervals thereafter on a 12 mm x 12 mm area centred around the scribe. Fig 5.1 shows a diagram of a prepared sample with defect, scan area and scan direction.

The SVET testing was carried out as described in Section 2.3 where a full description of SVET instrumentation, calibration procedure and set-up can be found. In all cases solution pH was adjusted to neutral by the drop-wise addition of $NaOH_{(aq)}$.

FFC experiments and subsequent analysis were carried out as described in Section 2.4. In summary, a 10 mm penetrating scribe was made into the PVB coating containing the relevant levels of H_2PP. In all cases, FFC was initiated by introducing a volume of 2 µl of aqueous 0.005 M $FeCl_2$ to the scribe and allowing to dry in room air. Samples were then placed in an environment chamber that was maintained at a constant 93% relative humidity and 20°C.

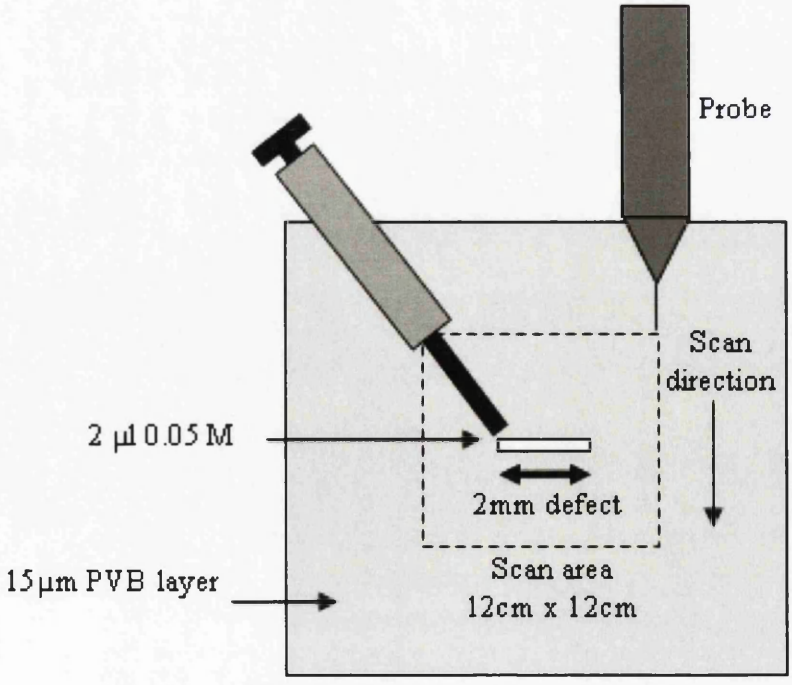

Fig 5.1 Diagram of iron sample showing 2 mm scribed defect scan area and scan direction

5.3 Results and discussion

5.3.1 SKP study of Cathodic delamination using a standard delamination cell

5.3.1.1 Cathodic delamination of uninhibited PVB coatings on iron

Delamination experiments were carried out using the approach pioneered by Stratmann et al [1]. Initial experiments were conducted using uninhibited PVB coatings to establish the baseline delamination kinetics. Upon the establishment of equilibrium with the humid experimental atmosphere, uniformly high E_{corr} values over the intact coating surface were obtained. The values were representative of those measured over an uncoated iron surface in the same conditions i.e. ca. 0.1–0.2 V vs. SHE. Delamination of the coating typically initiated within 1 h of the addition of 5% w/v NaCl (aq) electrolyte to the defect. The distinctive time-dependent E_{corr} – distance profiles proceeded to develop and progress thereafter as can be observed in fig 5.2. The E_{corr} values measured in the vicinity of the defect are approaching the hypothesised equilibrium potential of reaction 5.2 i.e. ca. -0.44 V vs. SHE. The mechanism by which cathodic disbondment on iron substrates occurs is described in full in Section 1.4.2.

A further experiment was carried out where the PVB coating remained uninhibited but in this case additions of 0.05 M H_2PP, adjusted to pH 7, were made to the experimental electrolyte. A plot of x_{del} vs. (t_{del} - t_i), where t_{del} is the delamination time following application of electrolyte and t_i is the delamination initiation time, are given in fig 5.3. It can be observed that there is very little difference between the two curves and both display parabolic kinetics suggesting that cation migration remains the rate-limiting step in the presence of H_2PP in the electrolyte. Furthermore, no increase in t_i was observed. This suggests that any leaching of in-coating H_2PP would have little effect on the anodic reaction (Reaction 5.2) occurring at the defect. These findings are in contrast to the observations of Chapter 3 Section 5.3.1 where the same experiment was carried out on a hot dip galvanised (HDG) steel substrate and an increase in t_i by 1140 min was observed.

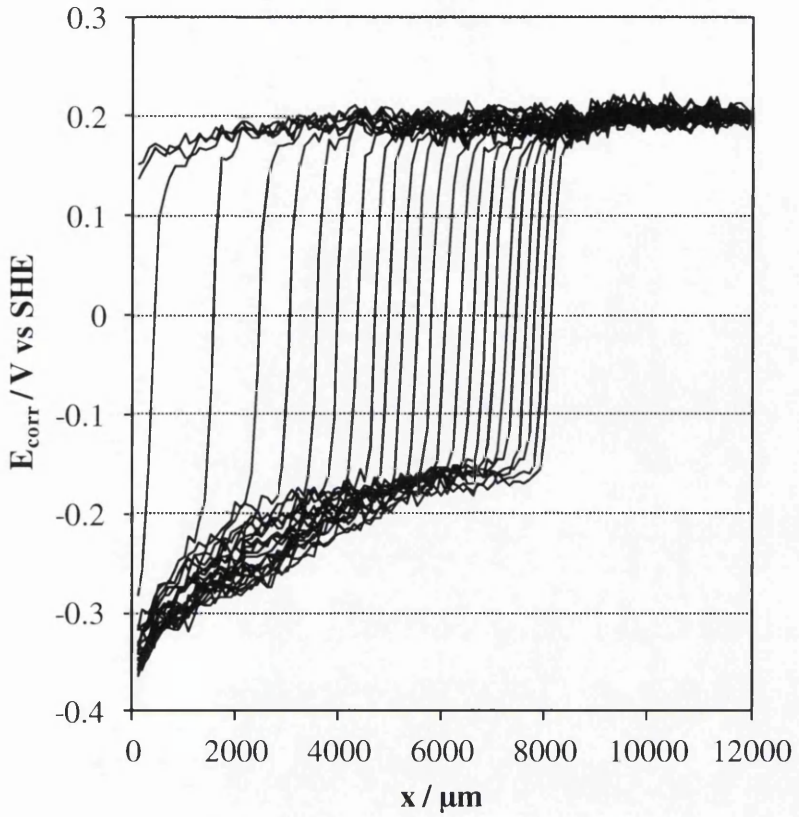

Fig 5.2 Profile of time dependant E_{corr} vs. SHE (V) measurements against distance from the penetrative coating defect (µm) for a PVB coated iron surface from 0h (left) to 24h (right) shown at hourly intervals following initiation with 5% $NaCl_{(aq)}$ electrolyte.

It has been shown elsewhere that, in a similar experiment, additions of CrO^{2-}_4 made to the initiating electrolyte of a Stratmann delamination cell showed only a 25% reduction in k_{del} of an uninhibited coating on a zinc surface in this instance. Despite the profound inhibition of an exposed, bare metal surface in the region of the penetrative coating defect by CrO^{2-}_4 anions, it was reported that defect-coating margin anodic metal dissolution persisted resulting in the onset of delamination [2]. In the current study, E_{corr} values were found to be slightly more positive in the region in close proximity to the defect (initially ca. -0.2 V vs. SHE increasing to -0.1 V vs. SHE after 24 h) when compared with the control experiment. This suggests that partial inhibition of the bare iron surface occurs. Further experiments to determine the inhibitory efficiency of H_2PP on bare iron when fully immersed in electrolyte containing H_2PP additions at various concentrations will be presented in the proceeding sections. Even if it is found that high inhibition efficiency occurs at the concentration studied here, it is suggested that anodic iron dissolution is able to persist in a delamination situation at the coating-defect margin.

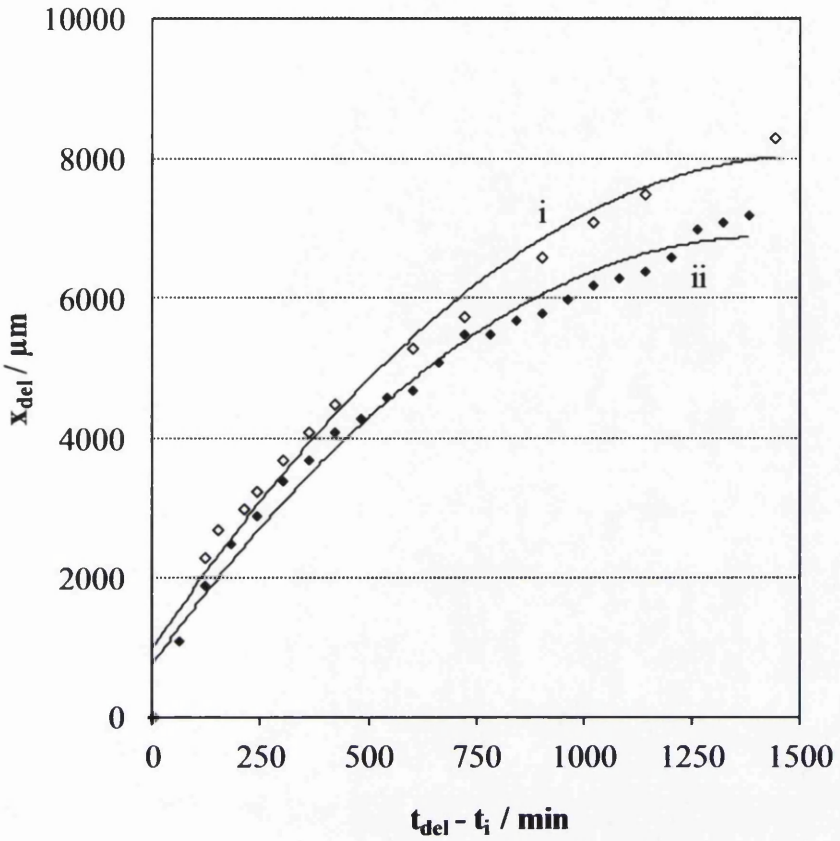

Fig 5.3 Plots of x_{del} vs. (t_{del} - t_i) for uninhibited PVB coated iron substrates where electrolyte adjusted to pH 7 where a concentrations of (i) 0 M and (ii) 0.05M H_2PP has been added to an external defect.

5.3.1.2 Inhibition of cathodic delamination with in-coating H_2PP

A series of experiments were carried out where different amounts of H_2PP were systematically added to the PVB coatings. Representative potential profile plots, over a period of 24 h, are given in figs 5.4 and 5.5 where 5% and 10% additions of H_2PP have been made respectively. It can be observed that the progression of the delamination front is reduced over the 24 h period where additions of in-coating H_2PP are present when compared to the control experiment. No variation of E_{intact} is observed at any level of H_2PP addition when compared with the control experiment suggesting that the presence of in-coating H_2PP has minimal effect on the steady-state delamination-cell potentials.

The delamination kinetics have been quantified as a plot of x_{del} vs. (t_{del} - t_i); this is given in fig 5.6. Curve (i) shows that, in the absence of in-coating H_2PP, delamination propagation kinetics best fit a parabolic curve and a delamination rate (k_{del})(dx_{del}/dt) of

6.39 μm.min after 24 h is measured upon differentiation of the curve. The linear kinetics shown in the plots that represent samples containing in-coating H_2PP additions show a reduction in k_{del}; however this is not substantial. The maximum reduction in k_{del} was 55% where additions of 10% H_2PP were made and an increase in t_i of 540 min was observed. A summary of t_i and k_{del} values plotted as a function of in-coating H_2PP amount (%) is given in fig 5.7. The plot illustrates the reduction in k_{del} and an increase of t_i with increasing levels of H_2PP. Actual values are also given in Table 5.1.

The observed change from parabolic to linear kinetics shown in fig. 5.6, for uninhibited and inhibitor-containing coatings respectively is a phenomenon observed in several previous studies on both polyaniline and smart-release bentonite-pigmented systems [4,5]. This was also reported in Chapter 3 where delamination of PVB coatings from HDG substrates in the presence of in-coating H_2PP was studied. It is proposed that this transformation is due to the formation of an interfacial layer that blocks electron transfer and subsequently suppresses the underfilm cathodic oxygen reduction reaction. It is suggested that this change in delamination kinetics occurs because, where H_2PP is added to the coating, the underfilm oxygen reduction reaction replaces the previously mentioned cation migration process as the rate-limiting step. The formation of this blocking interfacial layer is thought to proceed when the PVB/H_2PP ethanolic solution is first applied to the iron substrate. H^+ derived from the dissociation of H_2PP causes an acid etch of the iron surface generating Fe^{2+} cations at the metal-coating interface via Reaction 5.2. This is shown in the following series of equilibria:

$$H_2PP_{(aq)} \rightleftharpoons HPP^-_{(aq)} + H^+_{(aq)} \qquad (pK_{a1} = 2.3) \qquad (5.3)$$

$$HPP^-_{(aq)} \rightleftharpoons PP^{2-}_{(aq)} + H^+_{(aq)} \qquad (pK_{a2} = 7.8)[8] \qquad (5.4)$$

$$Fe^{2+} + PP^{2-} \rightleftharpoons [Fe^{2+}PP^{2-}]_s \qquad (5.5)$$

Provided local concentrations of the aforementioned ions exceed the estimated solubility product (K_{sp}) of 10^{-8} mol^2 dm^{-6}, subsequent combinations of Fe^{2+} cations with PP^{2-} produced by (5.4) will give an insoluble salt of $Fe^{2+}PP^{2-}$. This salt precipitate film, formed as the metal is coated, acts as a barrier to underfilm electron transfer and blocking cathodic oxygen reduction.

As shown in Reaction 5.1, the production of OH^- ions from the reduction of oxygen in a cathodic delamination cell renders the underfilm pH highly alkaline. In the case of iron values of pH >>10 are reported and, a maximum measurement of pH 14 recorded [7,8]. A second possible mode of underfilm inhibition is proposed by which the in-coating H_2PP additions moderate the underfilm pH to prevent or reduce the base-catalysed polymer degradation and base-catalysed hydrolysis of interfacial bonds. This is according to the corresponding series of acid/base equilibria given in reaction 5.3, where the pK_a values for first and second deprotonation steps given above are 2.3 and 7.8 respectively. Therefore the in-coating H_2PP provides a reservoir of H^+ cations which may provide some neutralisation of the hydroxide product of the underfilm cathodic reaction shown in reaction 5.1 and thus prevent loss of adhesion [8].

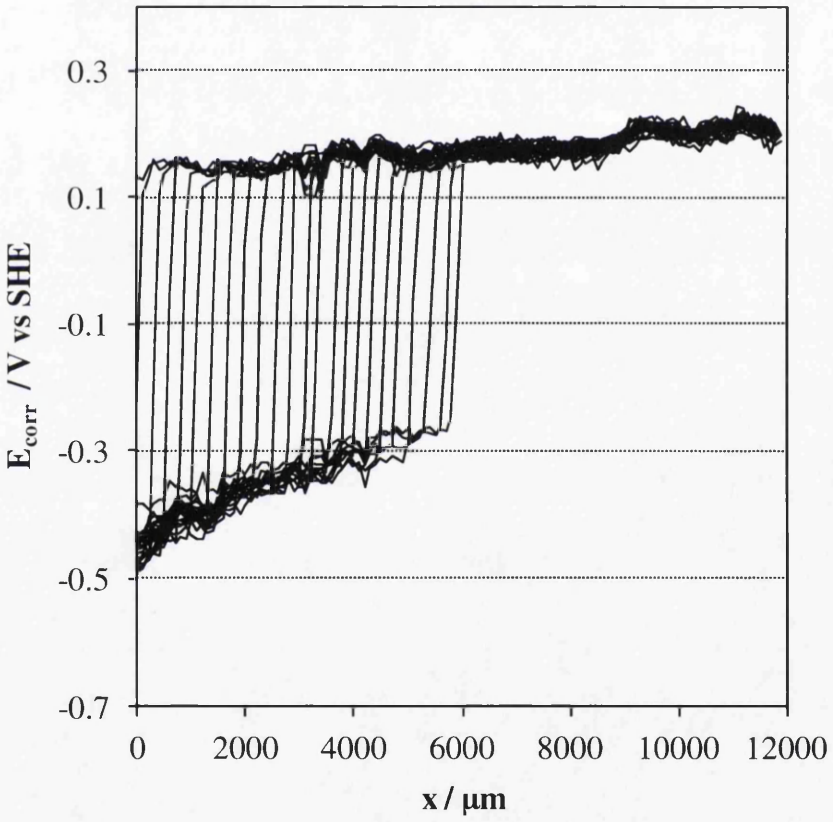

Fig 5.4 Profile of time dependant E_{corr} vs. SHE (V) measurements against distance from the penetrative coating defect (µm) for an iron surface coated with PVB containing additions of 5% H_2PP from 4 h (left) to 24 h (right) shown at hourly intervals following initiation with 5% $NaCl_{(aq)}$ electrolyte.

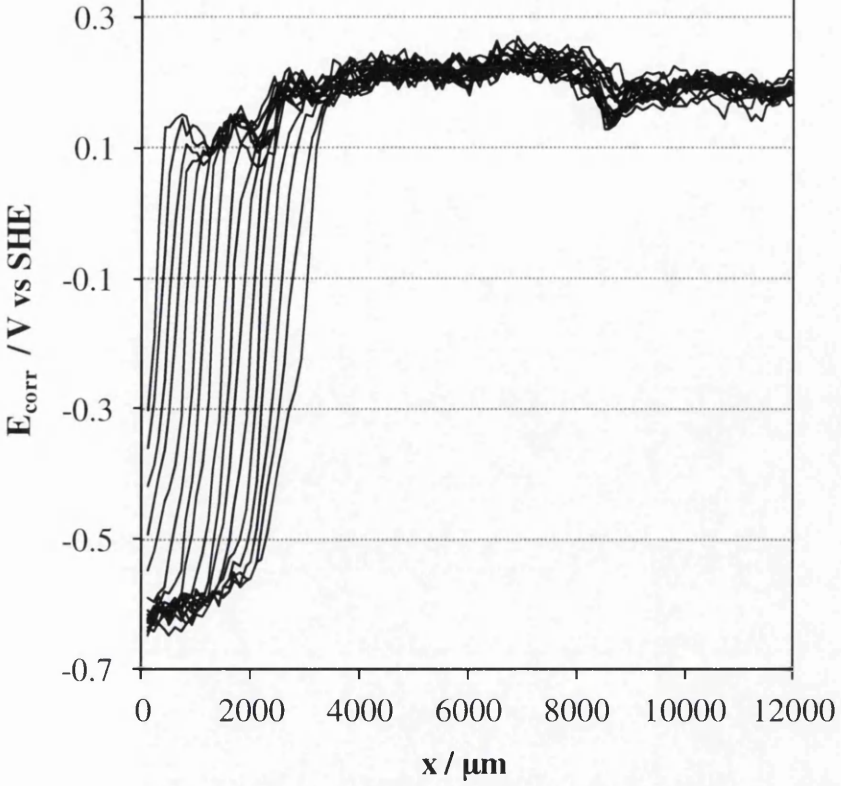

Fig 5.5 Profile of time dependant E_{corr} vs. SHE (V) measurements against distance from the penetrative coating defect (µm) for an iron surface coated with PVB containing additions of 10% H_2PP from 9 h (left) to 24 h (right) shown at hourly intervals following initiation with 5% $NaCl_{(aq)}$ electrolyte.

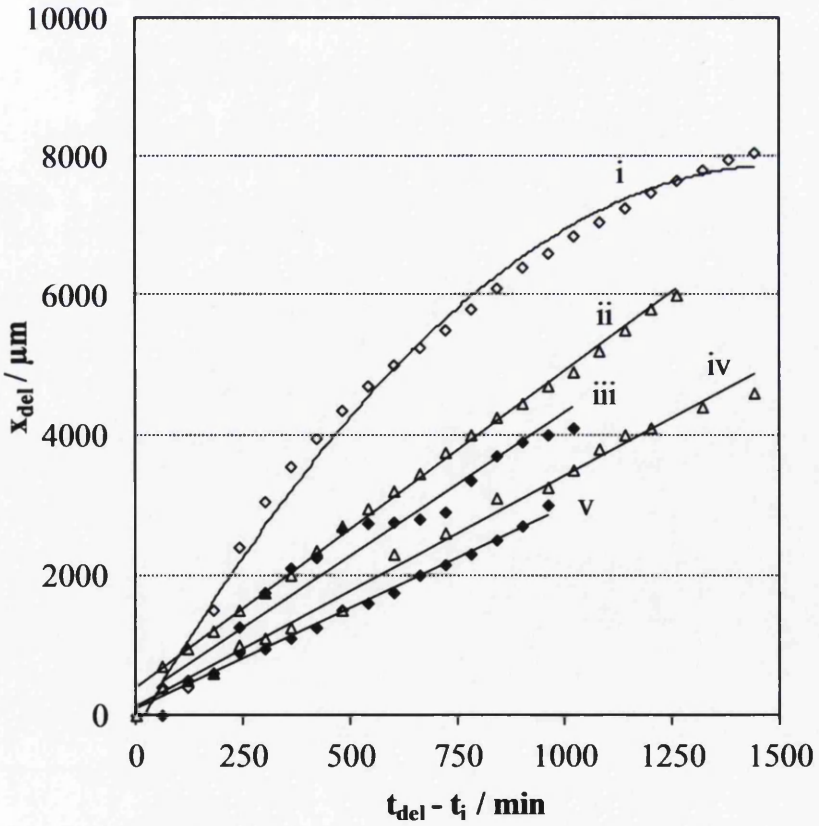

Fig 5.6 Plots of delamination distance (x_{del}) vs. (t_i - t_{del}) for 10 µm PVB coatings on an iron substrate containing i) no additions ii) 2% iii) 5% iv) 8% and v) 10% H_2PP additions following initiation with 5% $NaCl_{(aq)}$ electrolyte.

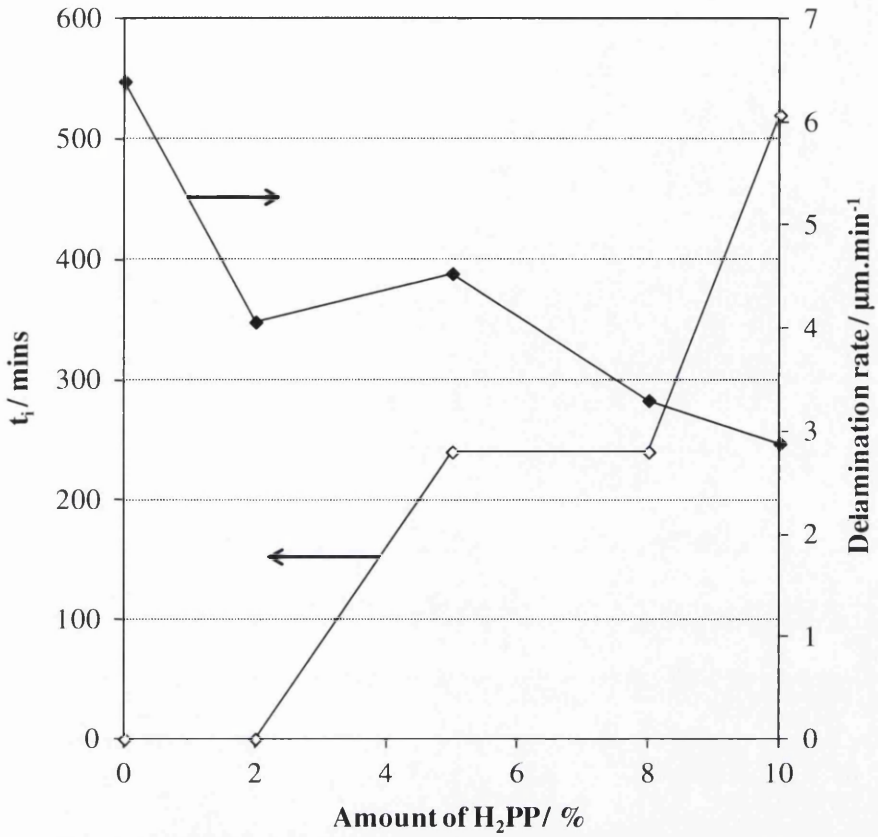

Fig 5.7 Summary plots of delamination initiation time values (t_i) and k_{del} values both plotted as a function of H_2PP levels (%) added to 10 µm PVB coatings delaminating from iron substrates; the latter are plotted using a secondary y-axis.

Table 5.1 Values of parabolic rate constant and time to delamination determined for PVB coatings containing various values of H_2PP on HDG substrates.

%H_2PP	k_{del} (µm.min)	Δk_{del} (%)	t_i (min)
0	6.39	0	0
5	4.53	29	240
8	3.3	48	240
10	2.88	55	540

5.3.2 Comparison of cathodic delamination inhibition by in-coating H_2PP on HDG steel and iron substrates

Chapter 3 investigated the effect of H_2PP on underfilm delamination of a PVB coating on a HDG substrate and it was found that the delamination initiation time (t_{del}) was increased by 1200 min and the delamination rate was reduced by 94% where in-coating additions of 10% H_2PP were made. In the current chapter it has been shown that the same amount of in-coating H_2PP provides a t_{del} value of 540 min and a reduction in k_{del} of only 55% when applied to an iron substrate. Although this is an improvement on the control sample, H_2PP does not appear to inhibit underfilm delamination as effectively

on iron as it does on a HDG substrate. Fig 5.8 gives summary plots of the reduction in k_{del} (%), for both iron and HDG substrates, as a function of in-coating H_2PP amount (%). This shows that even the lowest level of in-coating H_2PP provides superior inhibition on HDG in comparison to the maximum level of H_2PP applied to an iron substrate. It is suggested that a major factor may be that the underfilm pH on an iron surface, as described in the previous section where values of up to pH 14 have been recorded [7,8], is much higher than that of a HDG (pH 10-11[9]) substrate when delamination is taking place. Any pH buffering provided by the aforementioned reservoir of H^+ cations to neutralise the hydroxide product of the underfilm cathodic reaction, shown in reaction 5.1, would therefore not be as effective on the extremely highly alkaline rendered iron surface. A further mechanism that promotes loss of adhesion on an iron surface is the strongly potential dependent composition of iron-oxides, reported by Grundmeier et al, caused by the flipping of valence states (Fe^{2+} and Fe^{3+}) in the cation sublattice [3].

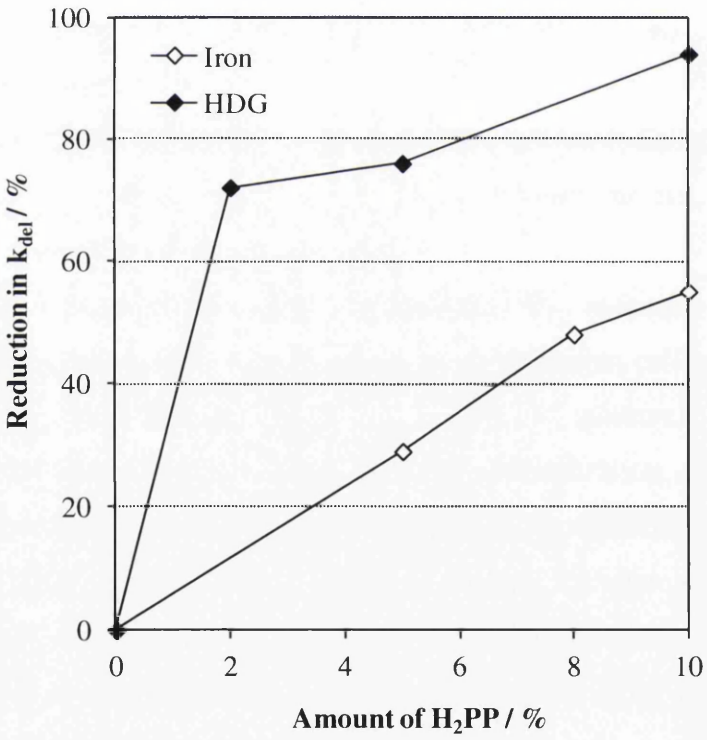

Fig 5.8 Summary plots showing the reduction in delamination rate (k_{del}) as a function of H_2PP levels (%) added to 10 μm PVB coatings on iron and HDG substrates where delamination was initiated using 5% w/v $NaCl_{(aq)}$.

Furthermore, HDG surfaces benefit from the additional inhibitory effect of free Zn^{2+} cations produced by the initial acid etch as reported by Williams et al [9]. It was

suggested that, in the alkaline underfilm electrolyte, Zn^{2+} aquocations become hydrolysed to precipitate solid zinc hydroxide ($Zn(OH)_2$) via the following reaction:

$$Zn^{2+}(aq) + 2OH^{-}(aq) \rightleftharpoons Zn(OH)_2(s) \qquad (5.6)$$

and improve delamination inhibition by further blocking the cathodic reaction. Without this mechanism the iron surface is protected only by the Fe_2PP layer and any H_2PP in contact with the metal surface as a result of leaching into the electrolyte.

5.3.3 SKP study of Cathodic delamination from a penetrative scribe defect

5.3.3.1 Cathodic delamination of uninhibited PVB coatings on iron

In the current section SKP experiments were carried out to mimic a realistic scenario, an alternative to the harsh conditions set up in the Stratmann cell experiments of the previous section. A similar study was carried out in previous work by Williams et al and it was reported that, when initiated with $NaCl_{(aq)}$, two types of corrosion are observed [4], namely:

i) Cathodic disbondment (phase I) - this will be studied in the current section.

ii) Anodic disbondment (phase II) via filiform corrosion (FFC) - this will be studied in the proceeding section.

Delamination experiments using uninhibited PVB coatings were carried out to determine baseline kinetics and establish the delamination cell characteristics. Fig 5.9 shows the profiles of time dependant E_{corr} vs. SHE (V) measurements plotted against the distance from the penetrative coating defect, measured in μm, for the PVB coated iron surface containing no inhibitor following initiation with 0.05 M $NaCl_{(aq)}$. The E_{corr} values recorded in the vicinity of the scribed defect are approaching -0.44 V vs. SHE, the expected value for anodically active iron. The recorded under-film distributions were entirely similar to those recorded by Stratmann et al for cathodic organic coating delamination on iron [1].

Fig 5.10 (a–d) shows a series of corresponding grey-scale E_{corr} distribution maps recorded using in situ SKP at various times up to 24 h. The images show the control sample where no H_2PP additions have been made to the PVB coating. The progression of the radially expanding delaminated area can be clearly observed.

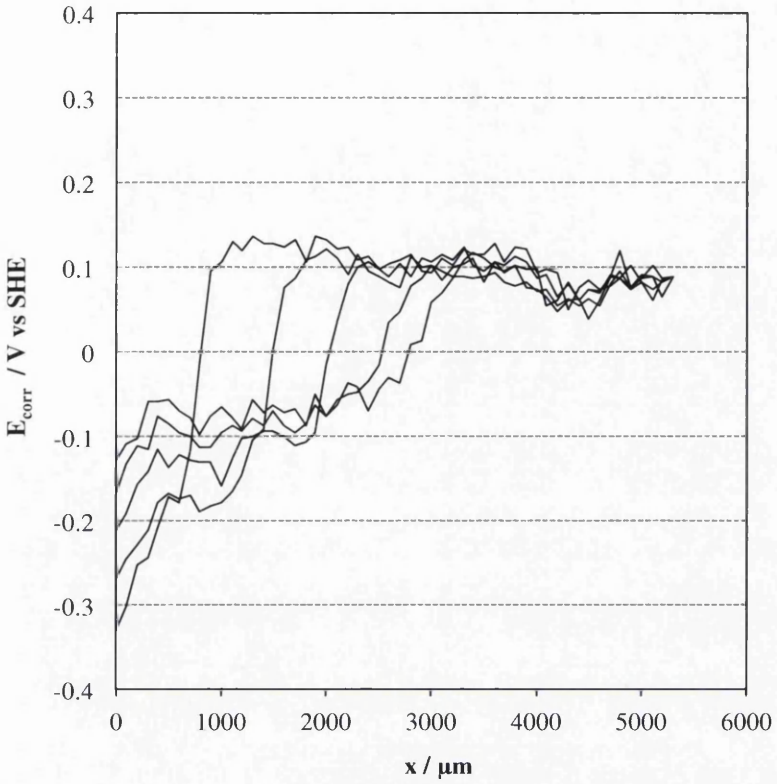

Fig 5.9 Profiles of time dependant E_{corr} vs. SHE (V) measurements against distance from the penetrative coating defect (mm) for a PVB coated iron surface containing no H_2PP at time intervals from 0h (left) in three hour intervals through to 12h (right) following initiation with 2 μl 0.05 M $NaCl_{(aq)}$ electrolyte added to a 2 mm scribed defect.

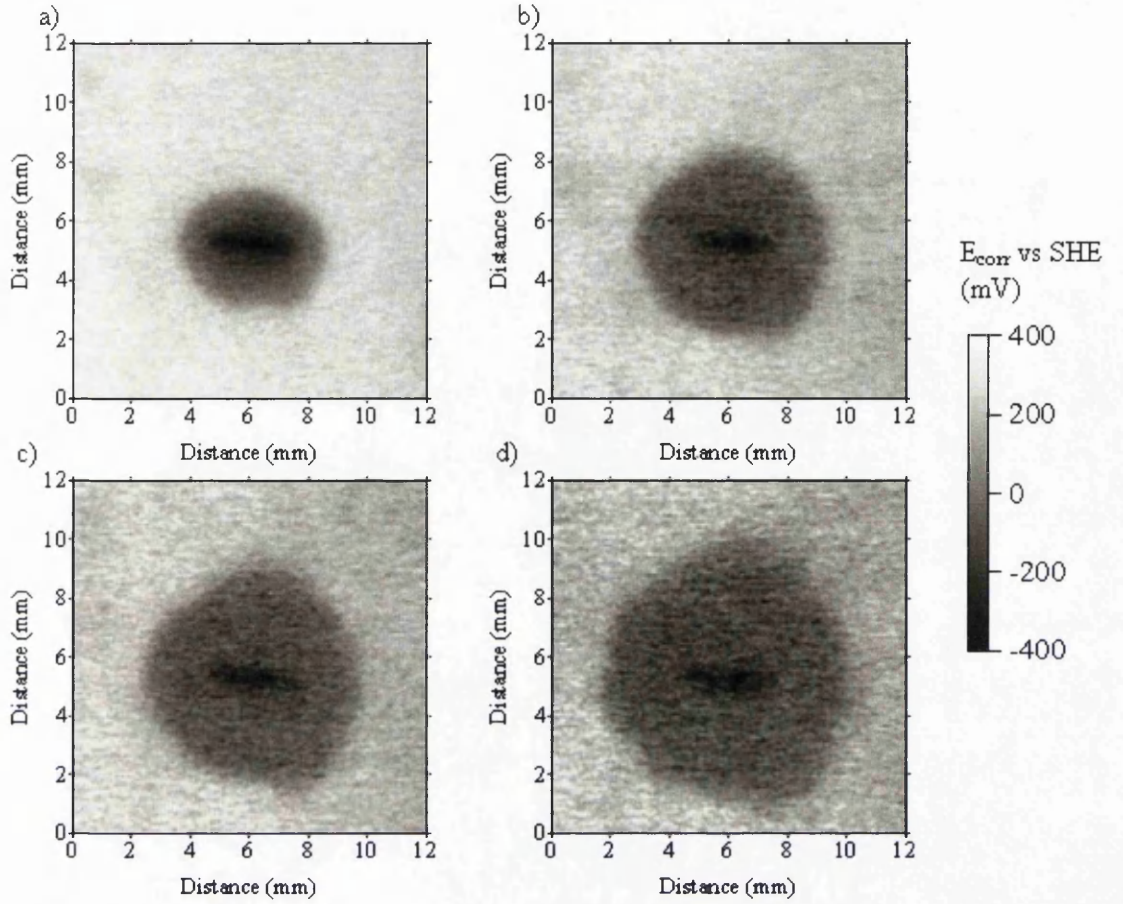

Fig 5.10 Interpolated grey-scale maps showing E_{corr} distributions measured over a PVB coated iron surface with dispersions of 2% H_2PP showing times (a) 1, (b) 4, (c) 8 (d) 12 hours following initiation using 2µl of 0.05 M NaCl (aq) to a scribed defect.

Experiments were carried out with additions of H_2PP at levels of 1%, 2%, 5% and 10% to the PVB coatings. Fig 5.11(a–d) shows a series of grey-scale E_{corr} distribution maps for the sample in which the PVB coating contains a dispersion of 2% H_2PP. The images show that delamination initiates but, after a 24 h period, the area of radial expansion is substantially less than that of the control sample.

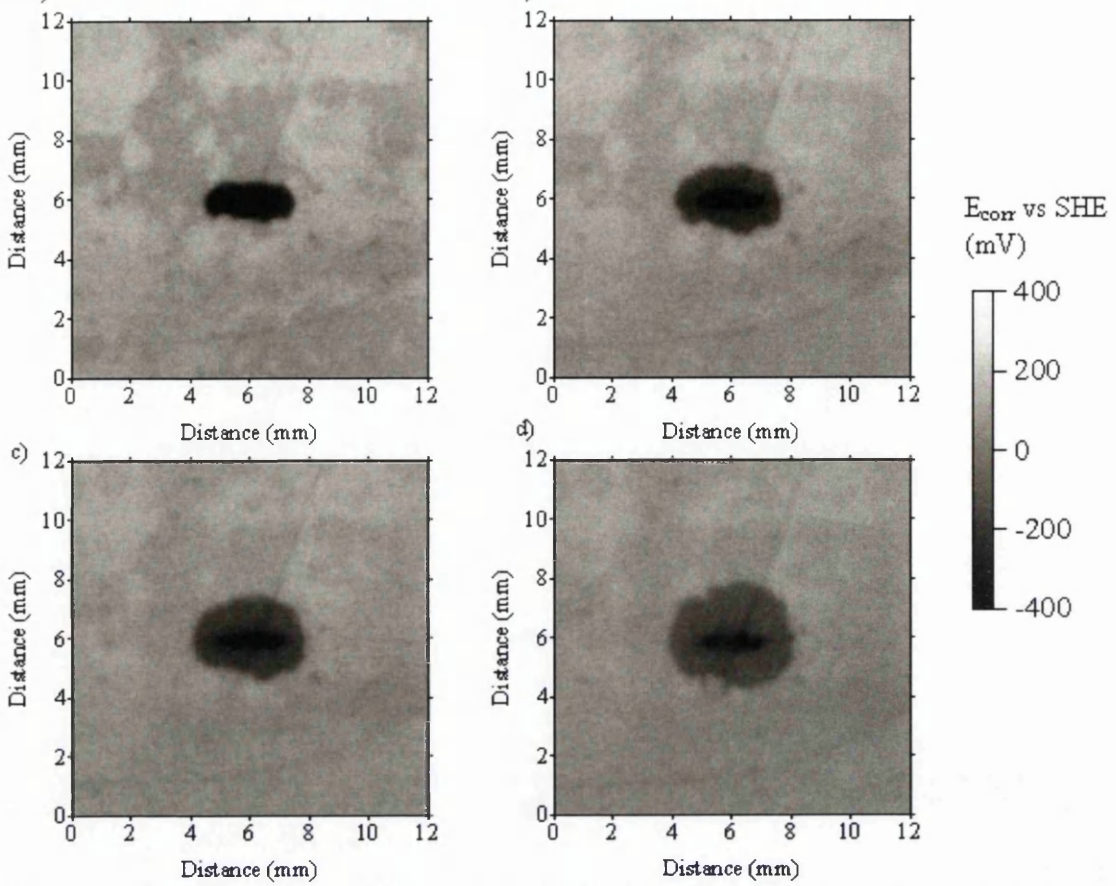

Fig 5.11 Interpolated grey-scale maps showing E_{corr} distributions measured over a PVB coated iron surface with dispersions of 2% H_2PP showing times (a) 1, (b) 4, (c) 8 (d) 24 hours following initiation using 2µl of 0.05 M NaCl (aq) to a scribed defect.

Figs 5.12 and 5.13 show the profiles of time dependant E_{corr} vs. SHE (V) measurements, at various time intervals, plotted against the distance (in µm) from the penetrative coating defect. The results are for a PVB coated iron surface containing dispersions of 2% H_2PP and 5% H_2PP respectively. The delamination kinetics have been quantified as a plot of x_{del} vs. $(t_{del} - t_i)$; this is shown in fig 5.14. Curve (i) shows that, as in the previous section, delamination propagation kinetics best fit a parabolic curve where measurements have been taken in the absence of H_2PP coating to the coating. Where additions of H_2PP have been made to the PVB coating, a change from parabolic to linear kinetics can be observed in the x_{del} vs. $(t_{del} - t_i)$ plots given in fig 5.12. This is entirely similar to that observed in the Stratmann cell experiments carried out in the previous section. Fig 5.15 summarises the t_i and k_{del} values plotted as a function of in-coating H_2PP amount (%). The plot shows a reduction in k_{del} and an increase in t_i with increasing levels of H_2PP. Actual values are given in Table 5.2. The realistic experiments carried out in the current section show a promising result for the inhibition of corrosion on iron with in-coating H_2PP where 10% additions halted delamination for a period of 24 h and reduced the delamination rate by 99% upon initiation.

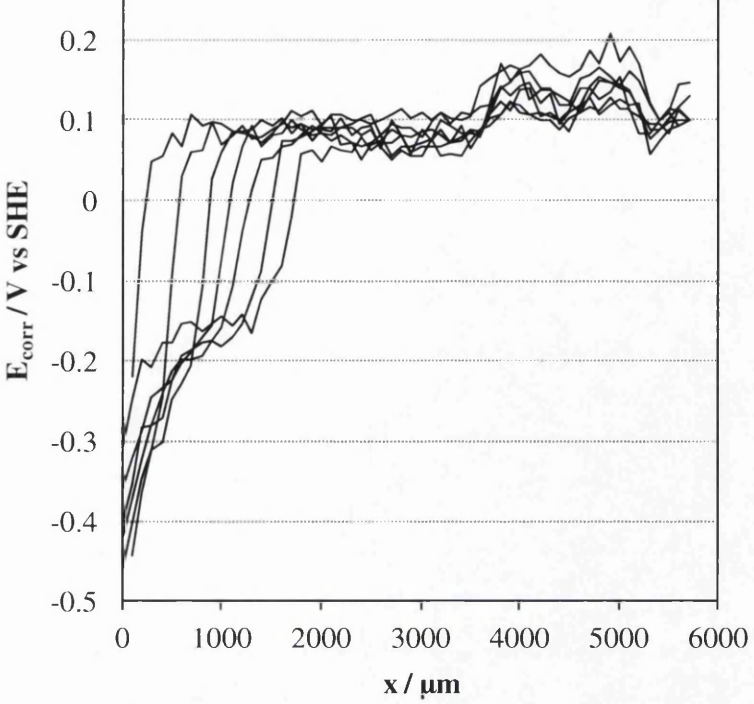

Fig 5.12 Profile of time dependant E_{corr} vs. SHE (V) measurements against distance (x) in μm from the penetrative coating defect for a PVB coated iron surface containing additions of 2% H_2PP at 3 h time intervals starting at 2 h (left) and ending at 20 h (right) following initiation with 2 μl 0.05 M $NaCl_{(aq)}$ electrolyte added to a 2 mm scribed defect.

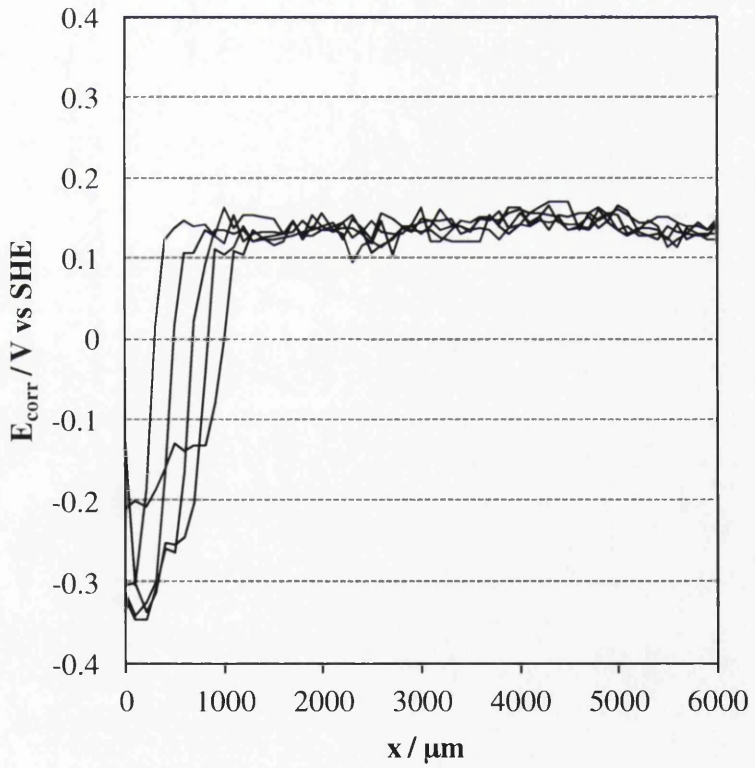

Fig 5.13 Profiles of time dependant E_{corr} vs. SHE (V) measurements against distance (x) in μm from the penetrative coating defect for a PVB coated iron surface containing a dispersion of 5% H_2PP at time 3 h (left) followed by 4 h, 5 h, 6 h and 10 h following initiation with 2μl 0.05M$NaCl_{(aq)}$ electrolyte added to a 2 mm scribed defect.

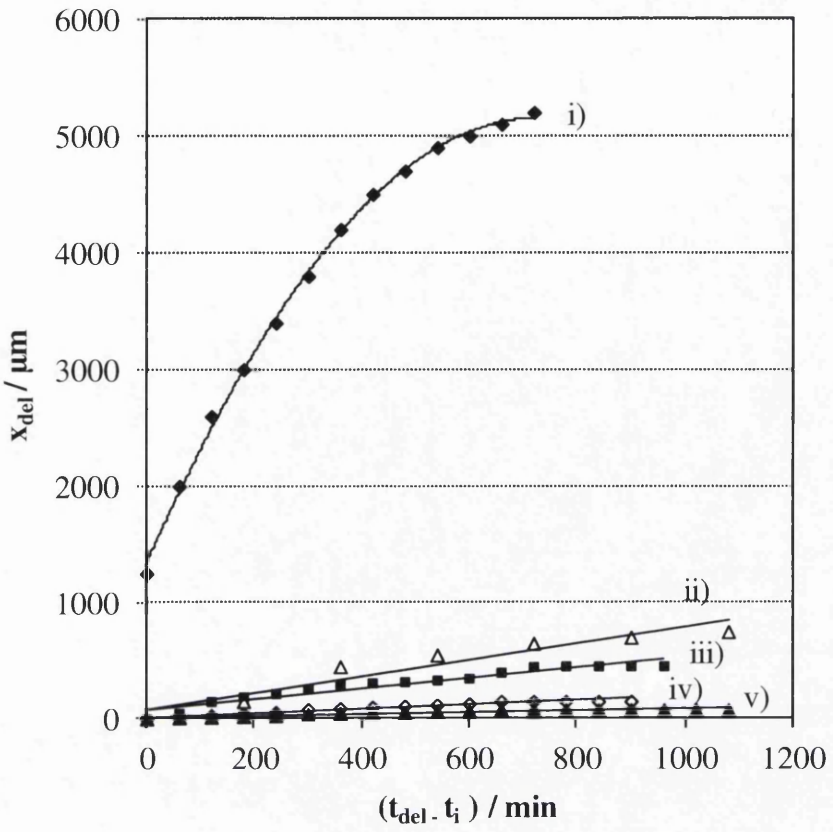

Fig 5.14 Plots of delamination distance (x_{del}) vs. (ti - t_{del}) for 15 µm PVB coatings on an iron substrate containing i) 0% ii) 1% iii) 2% iv) 5% and v) 10% H_2PP additions following initiation with 2µl 0.05M$NaCl_{(aq)}$ electrolyte added to a 2mm scribed defect.

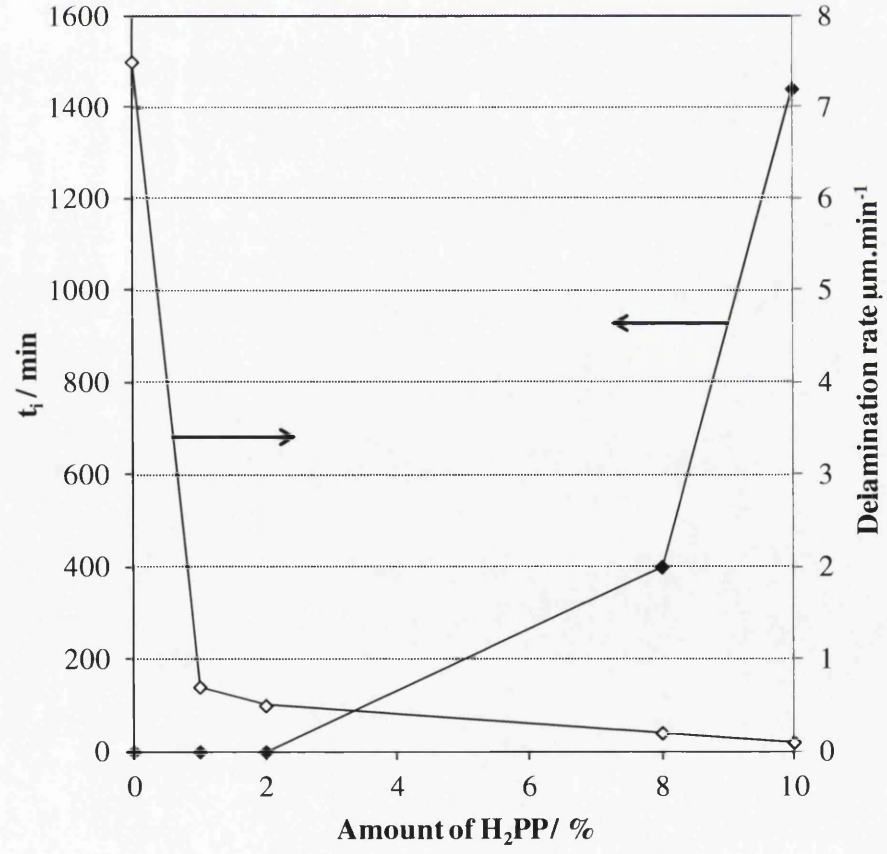

Fig 5.15 Values of time to delamination (t_i) and summary plots of k_{del} both plotted as a function of H_2PP levels (%) added to 10 µm PVB coatings on iron substrates where delamination was initiated using 5% w/v $NaCl_{(aq)}$; the latter are plotted using a secondary y-axis

Table 5.2 Values of parabolic rate constant and time to delamination determined for PVB coatings containing various values of H_2PP on iron substrates.

$\%H_2PP$	k_{del} (μm.min)	Δk_{del} (%)	t_i (mins)
0	7.5	0	0
1	0.7	91	0
2	0.5	94	0
5	0.2	98	400
10	0.1	99	-

5.3.3 Inhibition of filiform corrosion-driven anodic delamination by with in-coating H_2PP

As described in Section 1.4.6, filiform corrosion (FFC) may be recognised as a thread-like corrosion product deposited under organic films found on organic-coated aluminium and iron substrates. In the previous Section phase I underfilm cathodic delamination, as described by Williams et al [4], was studied where in-coating H_2PP was shown to retard the delamination rate when 0.05 M aqueous NaCl was used to initiate corrosion through application to a penetrative defect. As FFC, observed in phase II, is slow to develop, the current section assesses the effect of in-coating H_2PP where corrosion is initiated by aqueous $FeCl_2$. Williams et al showed that by initiating with $FeCl_2$ only phase II will commence and, as such, the experiments may be carried out over a shorter time scale [4].

Figs 5.16 and 5.17 show the appearance of PVB coated iron samples in (a) the absence of H_2PP and (b–e) the presence of H_2PP at levels of 2%, 5%, 10% and 12% respectively at 672 h and 1344 h. Fig 5.18 gives the plots of measured corroded area with respect to time for all levels of H_2PP additions. The uninhibited sample shown in both fig 5.16(a) and fig 5.17(a) was chosen as a good representation from all the repeat experiments. It can be observed that only five filaments are present and four of these cease to progress further than the distance covered after 672 h. One filament progresses and subsequently doubles in length by 1344 h. Where additions of 2% H_2PP have been made to the PVB coating (b), it can be observed that FFC filaments are much narrower but a substantial increase in the number of filaments can be observed. These filaments continue to grow in length over the period measured and new filaments can be seen to initiate. Interestingly, the filaments observed where 5% H_2PP is present in the PVB coating are approaching the thickness of those observed on the control sample. Filament

propagation exceeds that of the control sample. Both 2% and 5% H_2PP additions to the PVB coating result in an increase in corrosion rate, by 300% and 140% respectively, when compared to the control sample over the time period of 1008 h.

Where additions of 10% and 12% H_2PP are present, it can be observed that the filaments are extremely narrow. A high number of filaments initiate in both cases, however, after 672 h only very short filaments can be observed. Where 12% H_2PP additions are present, the filaments propagate over time and appear to change direction more frequently than those in the presence of H_2PP at other amounts. Additions of 12% H_2PP show the initiation of a large amount of narrow filaments but propagation is substantially limited and a decrease in corrosion rate of 76% is recorded. This is shown in fig 5.18 where plots of anodically delaminated area vs. time are shown for iron coated with PVB containing additions of H_2PP the various concentrations. Table 5.3 provides a summary of the values for the rate of FFC propagation.

As FFC is an anodic process it is likely that the formation of an insoluble Fe^{2+}/phenylphosphonate salt layer at the substrate/coating interface is not sufficient to prevent the initiation of FFC filaments. Where additions of a very high level of H_2PP are made to the PVB coating the suppression of the cathodic reaction might be enough to subsequently reduce the anodic reaction and hence reduce the corrosion rate but not prevent initiation entirely. In all cases, where in-coating H_2PP is present, the number of filaments is shown to dramatically increase and, in most cases, the filaments are much thinner. It is suggested that, due to partial protection of an insufficient Fe_2PP salt film that forms during casting, an increase in the number of initiation points occurs. Where additions of H_2PP have been made to the coating at lower levels, e.g. 2% - 10%, localised attack by Cl^- is possible. When enough H_2PP is present, such as with 12% additions, and a Fe_2PP layer forms that is capable of acting as a barrier to prevent Cl^- adsorbing onto the iron surface, only then is a reduction in progression rate observed. Furthermore, the acidic (pH 2) underfilm conditions in a filament head mean that no PP^- will be available to react with Fe^{2+} if leaching does occur. Fig 5.19 shows a schematic representation of the mechanism where the F_2PP salt layer is insufficient to prevent the adsorption of Cl^- onto the surface and, hence, corrosion is able to progress.

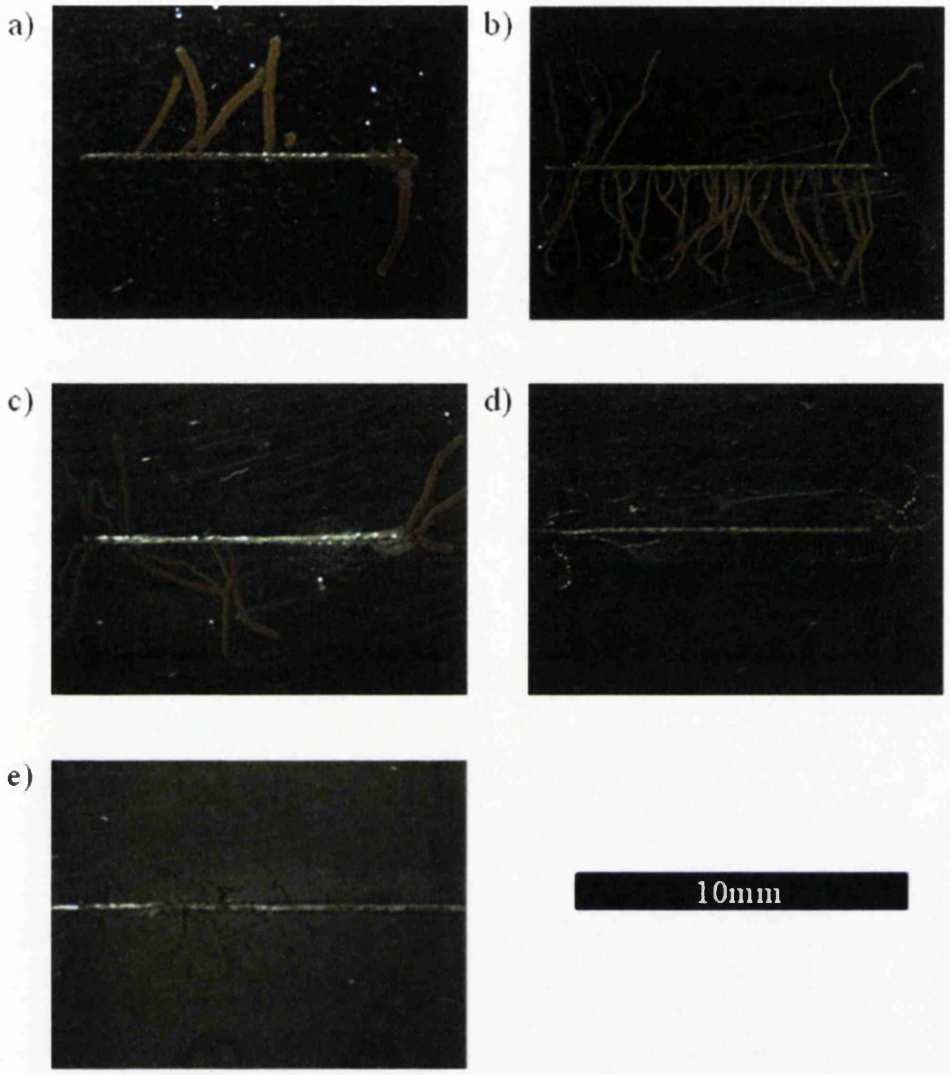

Fig 5.16 Photographic images of filiform experiments carried out on iron substrates coated with PVB containing additions of H_2PP at levels of a) 0% b) 2% c) 5% d) 10% e) 12% after 672h.

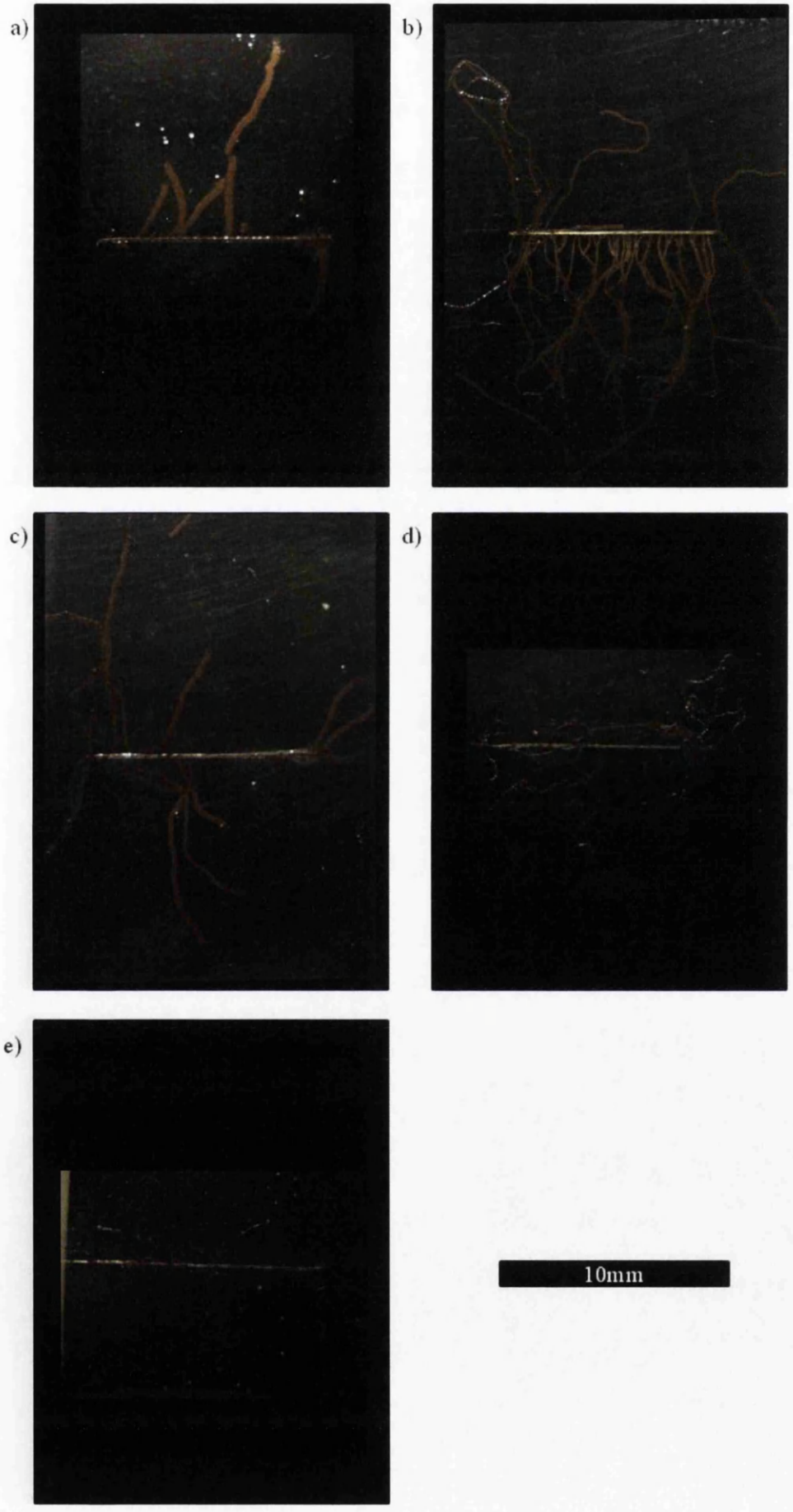

Fig 5.17 Photographic images of filiform experiments carried out on iron substrates coated with PVB containing additions of H_2PP at levels of a) 0% b) 2% c) 5% d) 10% e) 12% after 1344h.

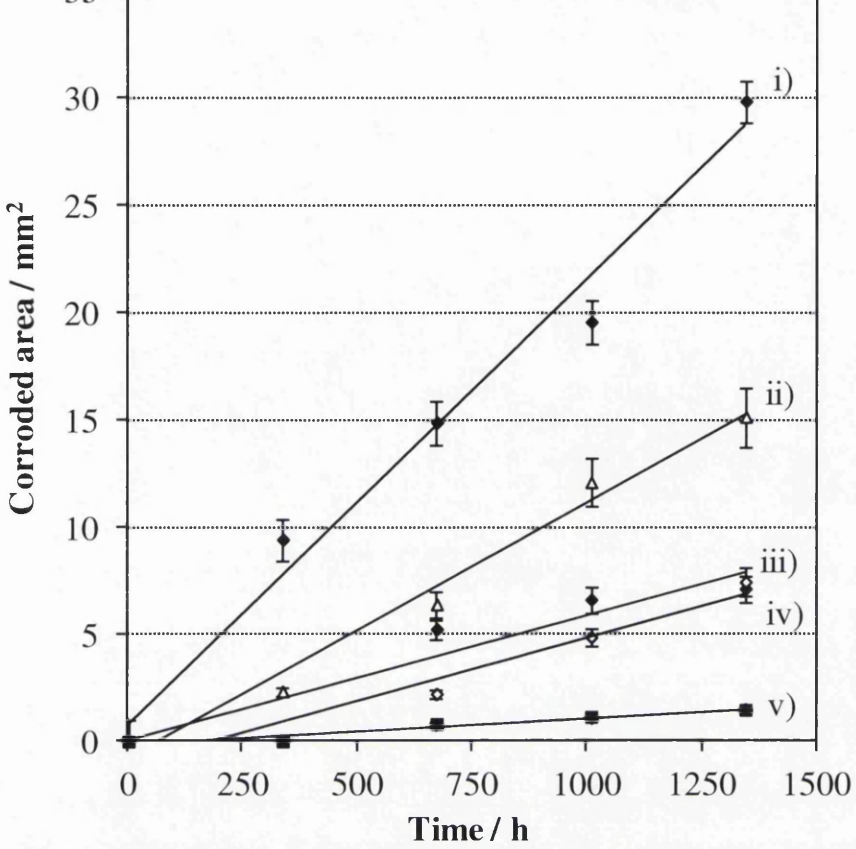

Fig 5.18 Time dependant FFC delaminated area for iron coated with PVB containing additions of H_2PP at concentrations of: i) 2% w/w ii) 5% w/w iii) 0% w/w iv) 10% w/w v) 12% w/w

Table 5.3 Values for the rate of FFC propagation for PVB containing various concentrations of H_2PP on iron

H_2PP (%)	Corrosion rate (mm^2.h)	Change in corrosion rate (%)
0	0.005	0
2	0.02	-300
5	0.012	-140
10	0.0059	-18
12	0.0012	76

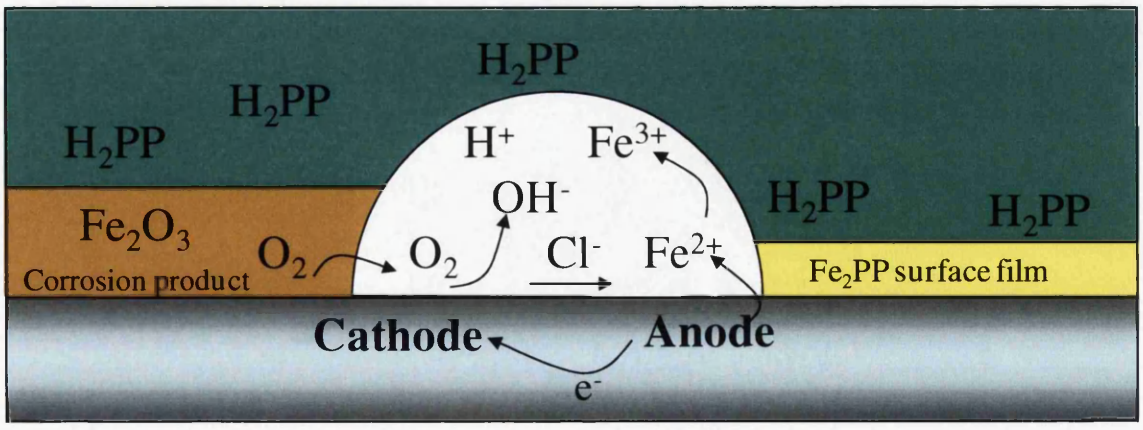

Fig 5.19 Schematic representation of filiform corrosion mechanism where an insufficient Fe_2PP surface film provides partial protection.

5.3.4 Corrosion inhibition of bare iron by phenyl phosphonic acid

The effect on corrosion of an iron surface where in-coating H_2PP, HPP^- or PP^{2-} leaches to the coating/defect region is explored in the current section. Experiments were carried out using SVET to determine if H_2PP had an effect, over a sustained time period, on the corrosion of bare iron surface fully immersed in 5% w/v $NaCl_{(aq)}$ electrolyte containing additions of the inhibitor.

Firstly, in situ SVET scanning was used to determine the current density distributions as a function of time above the surface of unpolarised iron samples freely corroding in 5% wt/v $NaCl_{(aq)}$ at pH 7. Representative current density maps obtained at times 2 h, 12 h and 24 h after immersion are shown in fig 5.20. It can be observed that activity occurs with the development of a single anode and a single cathode where the anode remains stationary and localized throughout. The photographic image shown in Fig 5.20(d) shows the thick layer of red rust that developed at the anodic site.

Figs 5.21 and 5.22 show the respective sets of current density maps for scans carried out where concentrations of $1x10^{-2}$ mol^2dm^{-6}, and $5x10^{-2}$ mol^2dm^{-6} H_2PP were present in the experimental electrolyte which was neutralised to pH 7. The photographic image given in fig 5.19(d) shows that some red rust was present after immersion over a 24 h period where additions of $1x10^{-2}$ mol^2dm^{-6} were made. In contrast to the control sample where a region of thick corrosion product was observed, a fine layer covering the entire surface was present after the 24 h period. However, the current density maps show negligible corrosive activity so this cannot be considered an accurate representation. A transformation from highly localised corrosion when the electrolyte is uninhibited, to general corrosion where H_2PP is present, appears to occur. The SVET is incapable of detecting the anodic and cathodic regions where generalised corrosion occurs as the resolution is not great enough - this is described full in Section 1.8.1.

The photographic image in fig 5.22(d) shows that no red rust is observed on the iron surface after an immersion period of 24 h where a concentration of $5x10^{-2}$ mol^2dm^{-6} H_2PP was present in the electrolyte. This, along with the negligible anodic activity shown by the current density maps, indicates that H_2PP at $\geq$ 0.05 M can effectively inhibit the corrosion of iron in such conditions up to a period of 24 h.

Fig 5.23 shows the result where additions of Na_3PO_4 were made to the electrolyte at a concentration of $5x10^{-2}$ mol^2dm^{-6}. A very sparse layer of red rust can be observed in the photographic image given in fig 5.23(d). As with fig 5.21, it cannot be certain whether the anodic activity shown in the current density maps gives a true representation of the anodic activity occurring on the iron surface. It can, however, be concluded that general corrosion, as opposed to localised corrosion is occurring.

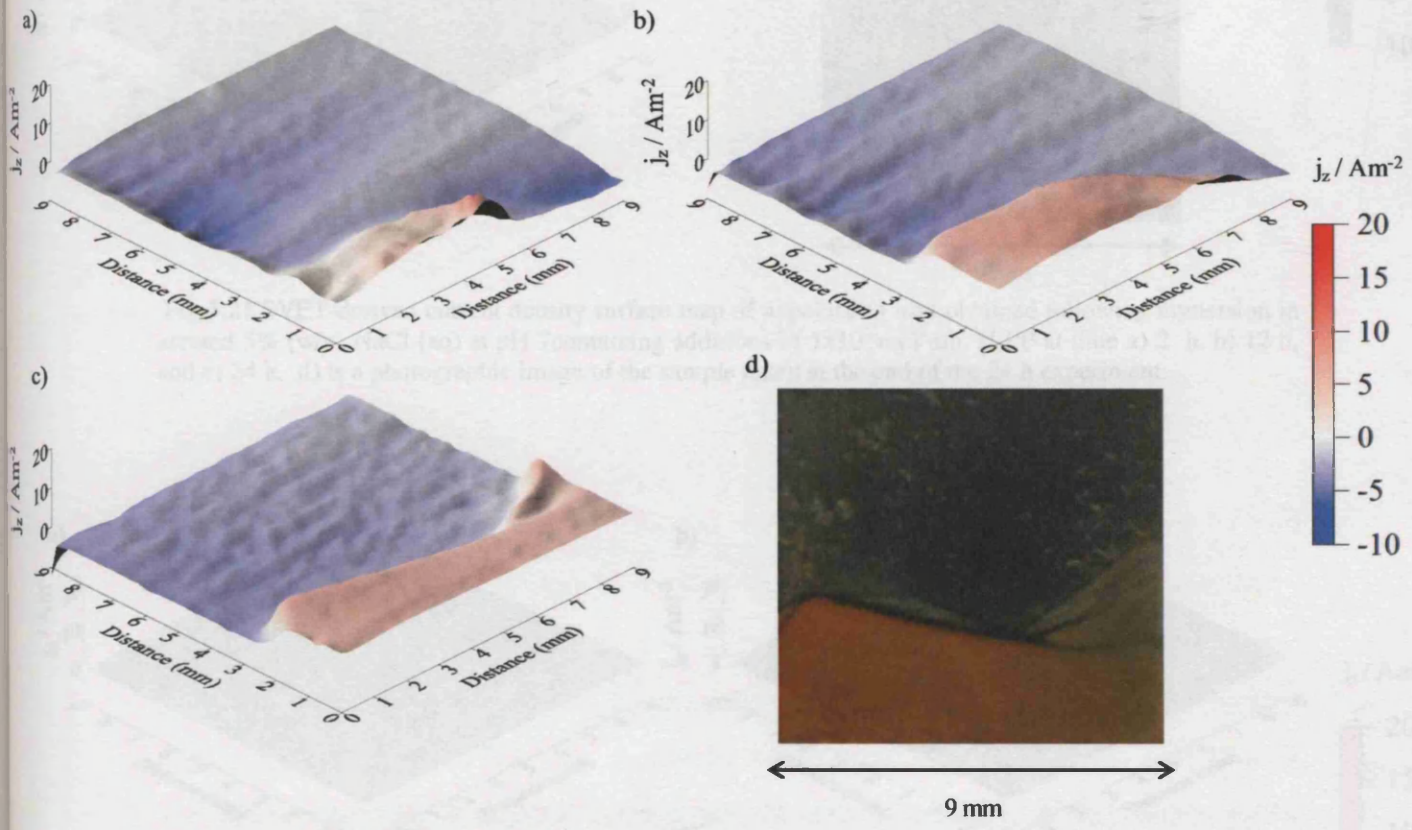

Fig 5.20 SVET-derived current density surface map of unpolarised iron obtained following immersion in aerated 5% (w/v) NaCl (aq) at pH 7 at time a) 2 h, b) 12 h, and c) 24 h. d) is a photographic image of the sample taken at the end of the 24 h experiment.

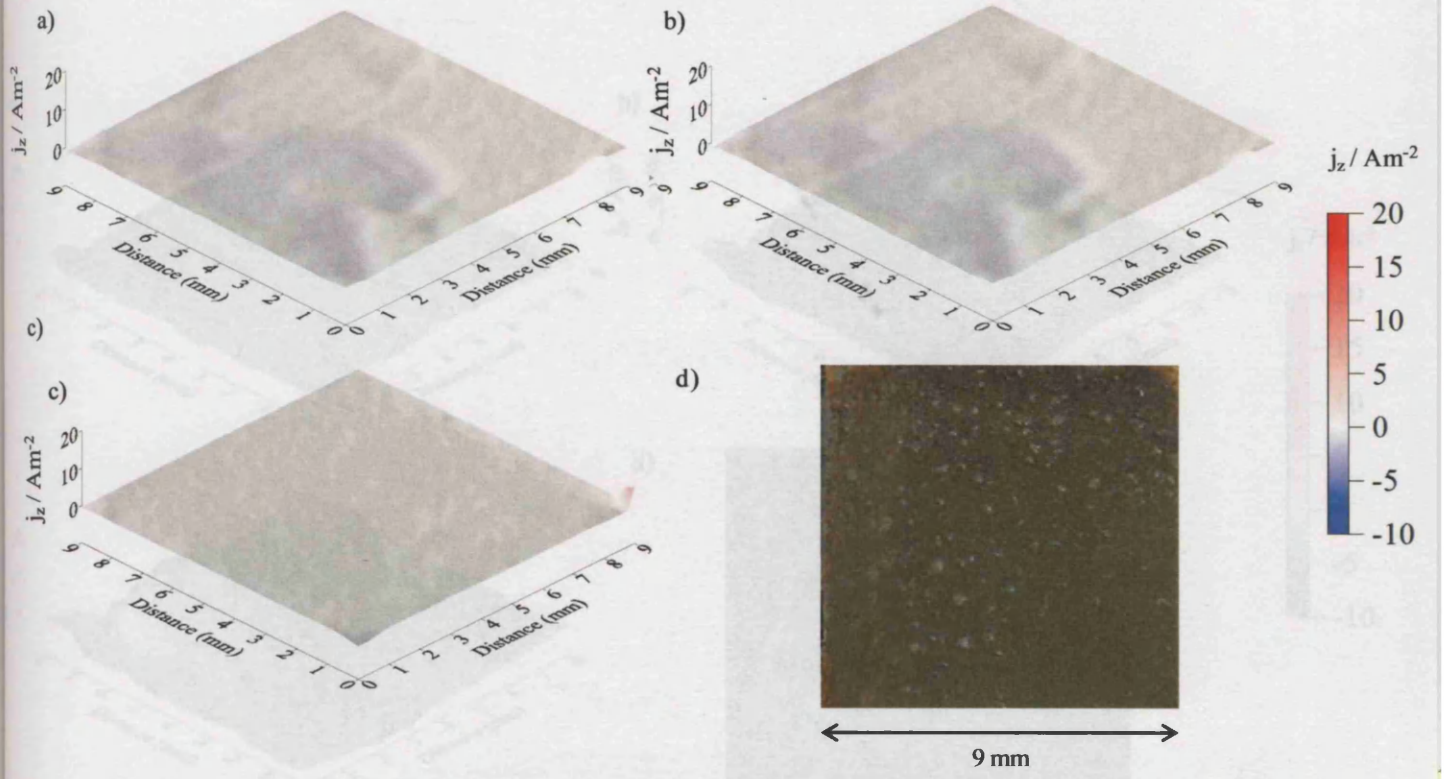

Fig 5.21 SVET-derived current density surface map of unpolarised iron obtained following immersion in aerated 5% (w/v) NaCl (aq) at pH 7containing additions of $1x10^{-2}mol^2dm^{-6}H_2PP$ at time a) 2 h, b) 12 h, and c) 24 h. d) is a photographic image of the sample taken at the end of the 24 h experiment.

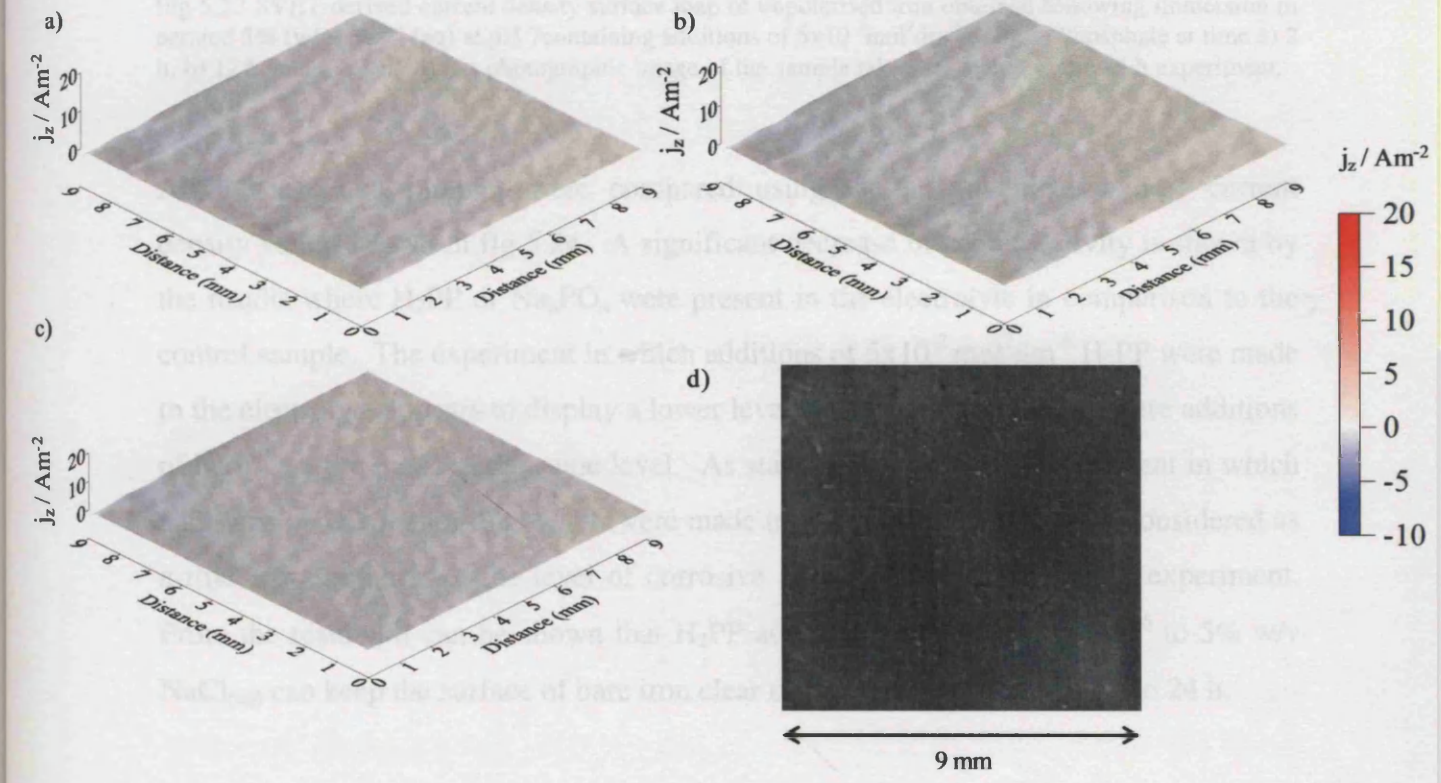

Fig 5.22 SVET-derived current density surface map of unpolarised iron obtained following immersion in aerated 5% (w/v) NaCl (aq) at pH 7containing additions of $5x10^{-2}mol^2dm^{-6}H_2PP$ at time a) 2 h, b) 12 h, and c) 24 h. d) is a photographic image of the sample taken at the end of the 24 h experiment.

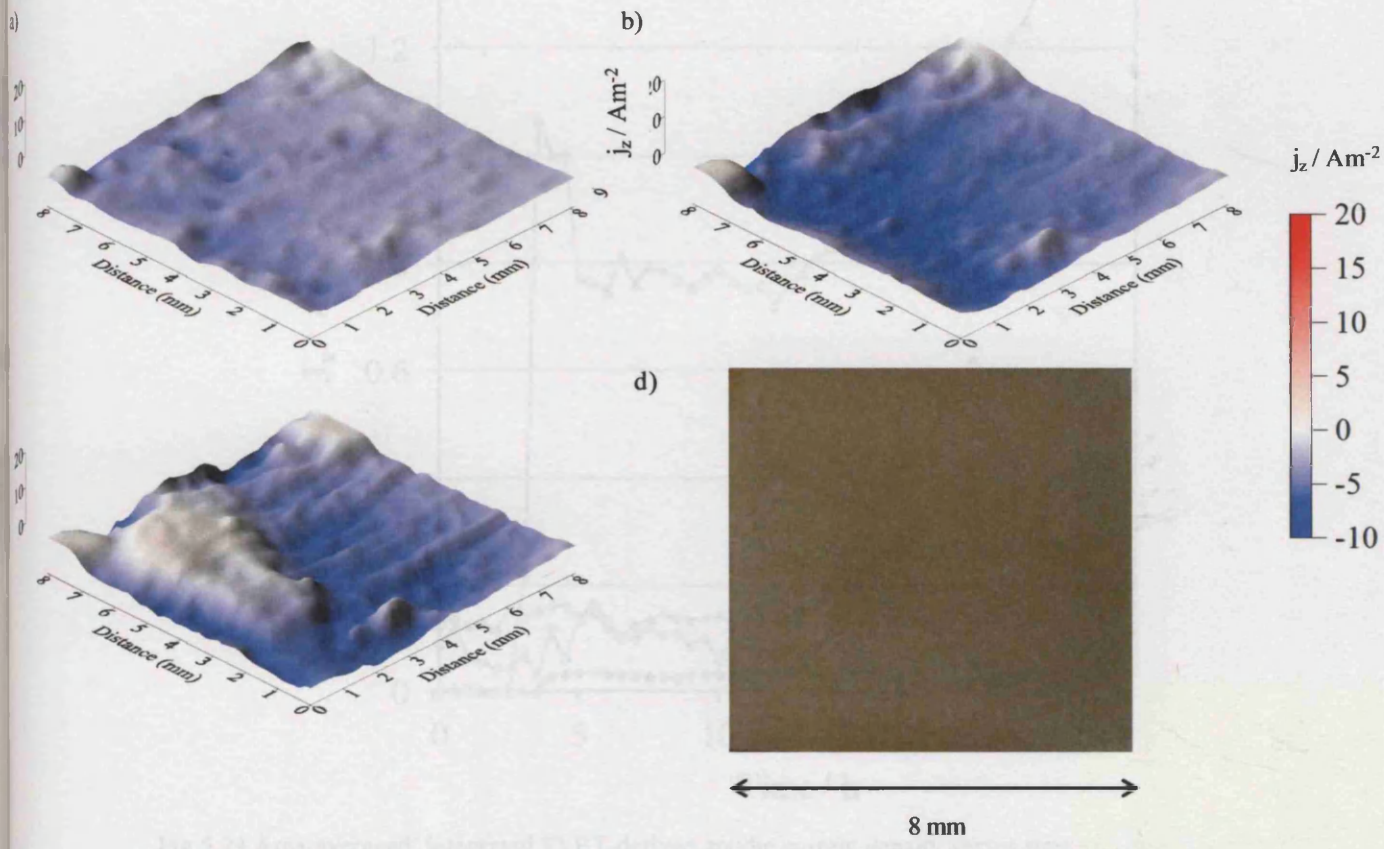

Fig 5.23 SVET-derived current density surface map of unpolarised iron obtained following immersion in aerated 5% (w/v) NaCl (aq) at pH 7containing additions of $5x10^{-2}mol^2dm^{-6}$ Sodium Phosphate at time a) 2 h, b) 12 h, and c) 24 h. d) is a photographic image of the sample taken at the end of the 24 h experiment.

All experimental samples were compared using the area-averaged anodic current density values shown in fig 5.24. A significant decrease in anodic activity is shown by the results where H_2PP or Na_3PO_4 were present in the electrolyte in comparison to the control sample. The experiment in which additions of $5x10^{-2}$ mol^2dm^{-6} H_2PP were made to the electrolyte appears to display a lower level of anodic current than where additions of Na_3PO_4 were made at the same level. As stated previously, the experiment in which additions of $1x10^{-2}$ mol^2dm^{-6} H_2PP were made to the electrolyte cannot be considered as a true representation of the level of corrosive activity taking place in the experiment. From the results, it can be shown that H_2PP additions of $\geq 5x10^{-2}mol^2dm^{-6}$ to 5% w/v $NaCl_{(aq)}$ can keep the surface of bare iron clear of red rust for periods of up to 24 h.

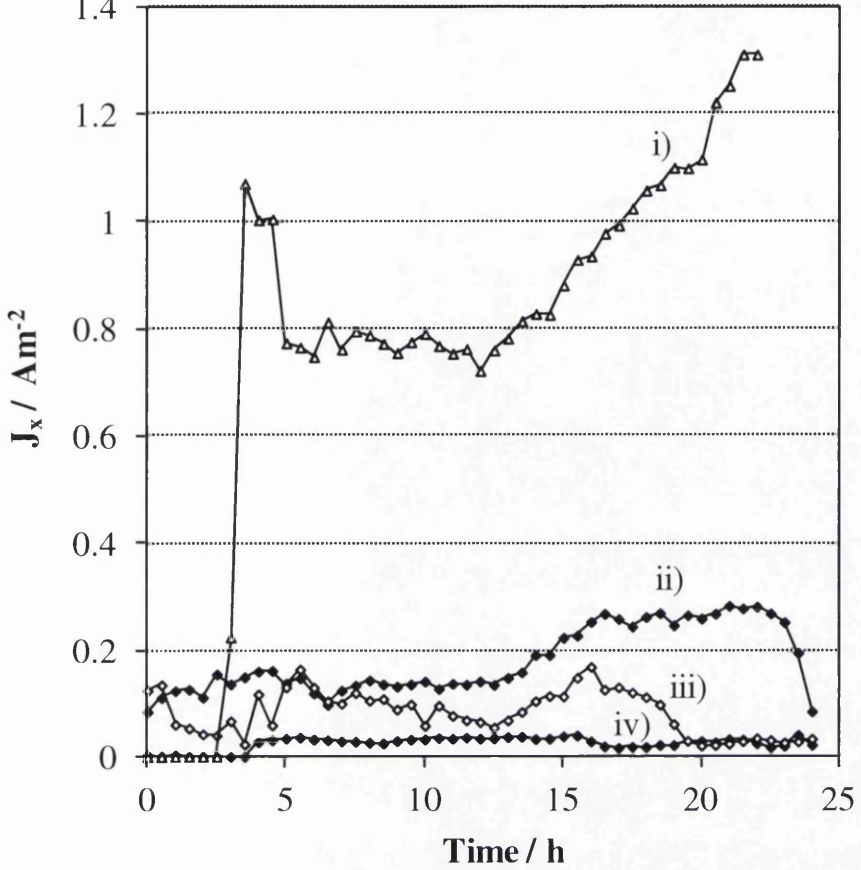

Fig 5.24 Area-averaged, integrated SVET-derived anodic current density versus time profiles obtained for iron immersed in aerated 5% (w/v) NaCl (aq) at pH 7 containing (i) no inhibitor (ii) $5x10^{-2}mol^2dm^{-6}$ Na_3PO_4 (iii) $1x10^{-2}mol^2dm^{-6}$ H_2PP additions and (iv) $5x10^{-2}mol^2dm^{-6}$additions of H_2PP.

Values for iron loss, given in gm^{-2}, recorded after 24 h immersion time are presented in fig 5.25. The plot shows that, with increasing concentration levels of PP^{2-} dissolved in the electrolyte, the mass of iron dissolved from the sample is progressively reduced. Where a concentration of $5x10^{-2}$ mol^2dm^{-6} H_2PP is present the measured iron loss is reduced by ca. 97% when compared with the control sample.

In order to determine the mode through which inhibition occurs, a systematic study of the open circuit potential (OCP) of bare iron samples was recorded with respect to time. Concentrations of H_2PP ranging from $5x10^{-3}$ mol^2dm^{-6} to $5x10^{-1}$ mol^2dm^{-6} were added to 5% wt/v $NaCl_{(aq)}$ experimental electrolyte, which was neutralised to pH 7, the results were compared with that of an uninhibited example. Fig 5.26 shows a plot of OCP vs. time curves recorded in both the presence and absence of H_2PP. The uninhibited control experiment gave an eventual value of -0.45V vs. SHE, this is represented by the dashed line. The potentials recorded at low H_2PP concentrations shown by plot (iii) and (iv), where additions of $2x10^{-2}$ mol^2dm^{-6} and $5x10^{-3}$ mol^2dm^{-6} were made respectively, show cathodic inhibition. At the higher H_2PP concentrations of $5x10^{-1}$ mol dm^{-3} and

$1x10^{-1}$ mol dm^{-3} shown by plots (i) and (ii) initially show mixed inhibition but principally anodic inhibition can be observed after ca. 900 s and 2300 s respectively.

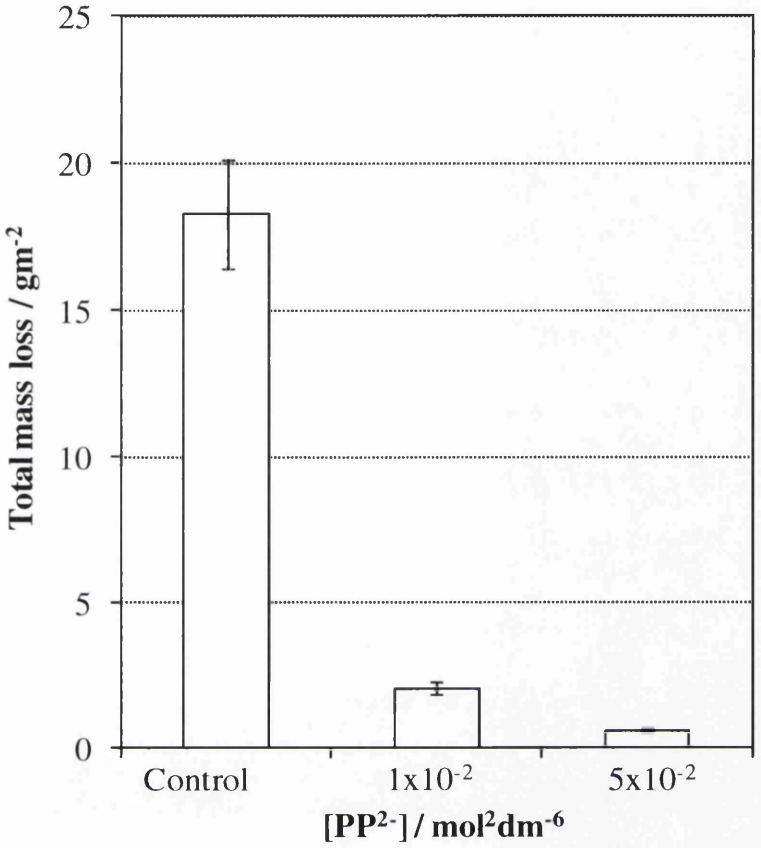

Fig 5.25 Summary of measured corrosion mass loss over 24 h as a function of $[PP^{2-}]$.

With regards to cathodic delamination, this suggests that the H_2PP concentrations added to the initiating electrolyte in Section 5.3.1.1 were not sufficient to provide any anodic inhibition in the defect region.

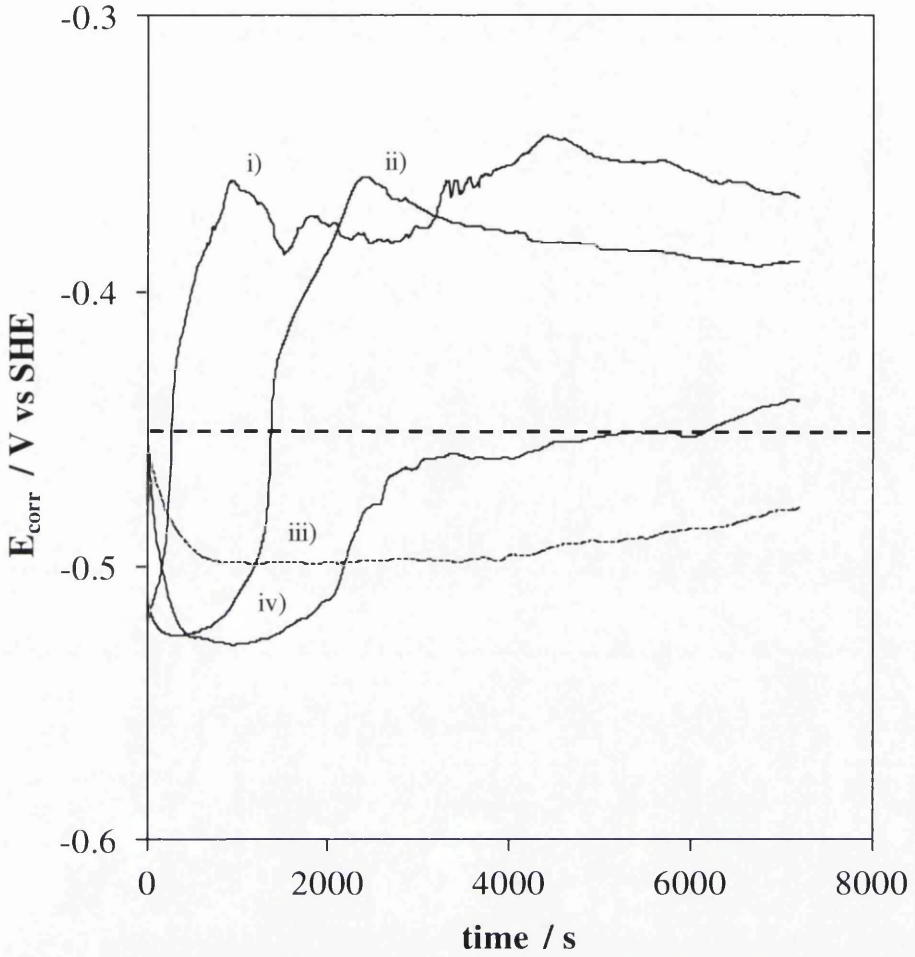

Fig 5.26 Plot of E_{corr} with respect to time for iron immersed in aerated 5% wt/v NaCl (aq) electrolyte at pH 7 containing (i) $5x10^{-1}$ mol^2dm^{-6}, (ii) $1x10^{-1}$ mol^2dm^{-6} (iii) $5x10^{-3}$ mol^2dm^{-6}, (iv) $2x10^{-1}$ mol^2dm^{-6} additions of H_2PP. The dashed line represents the eventual value obtained in the absence of inhibitor.

5.4 Conclusions

Where standard Stratmann delamination cell experiments were carried out, additions of phenyl phosphonic acid (H_2PP) dissolved in a 10 μm poly vinyl butyral (PVB) primer at 10% are shown to reduce the delamination rate (k_{del}) by 55% and increase the delamination initiation time (t_i) by 550 min when applied to an iron substrate. It is suggested that the formation of an insoluble Fe^{2+}/phenylphosphonate salt layer at the substrate/coating interface blocks the cathodic oxygen reduction reaction thus suppressing coating delamination. It is thought that this salt layer forms upon coating but also from the leaching of H_2PP, PP^{2-} and HPP^{-} after coating. Although some improvement is observed, this result compares poorly to the same experiment presented in Chapter 3 carried out on hot dip galvanised (HDG) steel where the same amount of in-coating H_2PP showed a decrease in k_{del} of 94% and an increase in t_i of 1200 min. This is thought to be due to the extremely high pH values recorded on iron (up to pH 14[11,12]) which are higher than those found on HDG in a delamination cell (typically

pH 10-11). As the dissociation of H_2PP results in an abundance of H^+ cations, this can act as a buffer to neutralise the alkaline rendered underfilm region from the cathodic oxygen reduction reaction and reduces the rate at which, previously base-catalysed, polymer degradation and hydrolysis of interfacial bonds occurs. However, whilst this is effective on the lower pH values found in the delaminated regions on a HDG steel surface, the highly alkaline rendered underfilm conditions that occur on iron during the delamination process may prevent in-coating H_2PP additions from being fully effective in this way. Furthermore, where $5x10^{-2}$ mol^2dm^{-6} H_2PP was present in the initiating electrolyte, no change from the control experiment was observed other than a slight increase in E_{corr} values in the defect region. A study using the scanning vibrating electrode technique (SVET) showed that, where H_2PP was present in the 5% wt/v electrolyte at a concentration of $5x10^{-2}$ mol^2dm^{-6} a bare iron surface was kept free from red rust for 24 h. Open circuit potential measurements suggest that, below a H_2PP concentration threshold of $1x10^{-1}$ mol^2dm^{-6}, predominantly cathodic inhibition is observed.

A realistic experiment, in which electrolyte was added to a scribe defect and allowed to dry, showed more encouraging results with regards to the inhibition of delamination. The efficient inhibition of the propagation of a radially delaminated region was observed when 2 µl of 0.05 M $NaCl_{(aq)}$ electrolyte were added to a 2 mm scribed defect. In the absence of H_2PP this delaminated region expanded to a delamination distance (x_{del}), measured from the defect to the cathodic delamination front, of ~4.4 mm at 12 h after initiation. Where H_2PP was present in the coating at a dispersion of 2% w/w the delamination still initiates but the propagation rate is greatly reduced and ceased completely after ~20 h. Additions of 5% H_2PP showed a further reduction in the delaminated region with the final x_{del} reaching only 0.9 mm after a time of 12 h post initiation. Increasing the level of H_2PP beyond 5% showed a slight further reduction in x_{del} and the initiation of delamination can still be seen to occur.

In both types of experiment, when plotting x_{del} vs. t_{del} for both the uninhibited coating and a coating containing H_2PP additions, it can be shown that a transformation from parabolic delamination kinetics to linear kinetics occurs respectively. It is suggested that the formation of an insoluble Fe^{2+}/phenylphosphonate salt layer at the substrate/coating interface blocks the cathodic oxygen reduction reaction thus

suppressing coating delamination. It is thought that this salt layer forms both upon the initial casting of the coating. The delamination experiment in which H_2PP was added to the external electrolyte, shown in the plot given in fig 5.3, suggests that leaching of H_2PP, PP^{2-}, and HPP^- from the coating has little effect on inhibiting delamination.

With regards to FFC it was found that any additions of H_2PP made to the PVB coating less than 10% wt/v were found to increase the corroded area measured on the iron surface. Below this level localised attack by Cl^- is possible, when enough H_2PP is present and a Fe_2PP layer forms that is capable of acting as a barrier to prevent Cl^- adsorbing onto the iron surface, only then is a reduction in progression rate observed. It was found that, with any level of H_2PP additions, the filaments were reduced in thickness. However, the number of initiation sites was found to increase due to partial protection of an insufficient Fe_2PP salt film, that forms during casting, causing an increase in the number of initiation points. The acidic (pH 2) underfilm conditions in a filament head mean that no PP^- will be available to react with Fe^{2+} if leaching does occur. Where additions of 12 % are present, it is thought that a Fe_2PP layer forms that is capable of acting as a barrier to prevent Cl^- adsorbing onto the iron surface. At this level a reduction in the filament progression rate of 76% observed.

In conclusion, it has been shown that in-coating H_2PP reduces the delamination rate of a PVB coating from an iron surface and this is effective when in a realistic scenario. With regards to a harsher experimental environment, this coating system is much more effective on a HDG surface. At high in-coating H_2PP levels, the system can effectively reduce the filament propagation rate of FFC thus reducing anodic delamination.

5.5 References

[1] M. Stratmann, A. Leng, W. Fürbeth, H. Streckel, H. Gehmecker, and K.-H. Groβe-Brinkhaus, *Prog. Org. Coatings*, vol. 27, 1–4, 261–267, 1996.

[2] M. Stratmann, A. Leng, W. Fiirbeth, H. Streckel, and H. I. Gehmecker, *Farbe Und Lack*, 1–7, 1996.

[3] G. Grundmeier, W. Schmidt, and M. Stratmann, *Electrochim. Acta*, vol. 45, 2515 – 2533, 2000.

[4] G. Williams and H. N. Mcmurray, *Electrochem. commun.*, vol. 5, 871–877, 2003.

[5] G. Williams, a. Gabriel, a. Cook, and H. N. McMurray, *J. Electrochem. Soc*, vol. 153, 10, B425, 2006.

[6] G. Williams, S. Geary, and H. N. McMurray, *Corros. Sci.*, vol. 57, 139–147, 2012.

[7] J. Ritter and J. Kruger, *NACE* 28, 1981.

[8] R. J. Holness, G. Williams, D. A. Worsley, and H. N. Mcmurray, *J. Electrochem. Soc.*, vol. 152, 2, B425–B433, 2005.

[9] W. Fürbeth and M. Stratmann, *Prog. Org. Coatings*, vol. 39, 23–29, 2000.

Chapter Six.

A scanning Kelvin probe investigation of the interaction of PEDOT:PSS films with metal surfaces and potential corrosion protection properties.

6.1 Introduction

Poly(3,4-Ethylenedoixythiophene)-Poly(Styrene Sulphonate) (PEDOT:PSS) is employed in a variety of applications and is widely used as a transparent conductor in applications such as organic light-emitting diodes (OLED)[1-2] and organic solar cells [3]. Much research has been conducted into the replacement of the traditional Pt counter electrode (CE) of a dye-sensitised solar cell (DSSC) [4] due to the high costs involved. PEDOT:PSS is widely considered to be an ideal candidate due to its high conductivity, electrochemical stability and stability in the oxidized state where catalytic activity for the reduction of the I_2 to I^- mediator in the redox electrolyte is required in a DSSC CE [5-6]. In many applications there is a requirement for electrical contact to be made with the organic PEDOT:PSS layer. It is therefore of high importance to understand the interaction between PEDOT:PSS and various metals in order to gauge the long term stability of the metal-ICP interface. Currently Au and Ag are typically used as contacts [7–9] but, as with the DSSC CE, it is necessary to determine whether a more cost-effective alternative, such as Cu or Ni, would be equally inert when over-coated using PEDOT:PSS. The first aim of the current Chapter is to use in-situ SKP to measure the Volta potential differences of various PEDOT:PSS coated metal surfaces to identify instances where a reaction may be taking place at the metal-PEDOT interface. Various previous studies have used the SKP to carry out potentiometric investigations of metals coated with ICP [8,11,12].

The second aim is to investigate any corrosion protection capability of PEDOT:PSS coatings applied to technologically important metallic surfaces, in this case iron (as a substitute for cold reduced steel) and hot dip galvanized (HDG) steel using an in-situ scanning Kelvin probe (SKP). Protection will be evaluated under two different scenarios where:

1. coating failure by cathodic delamination dominates.
2. the principal failure mechanism is anodic disbondment in the form of filiform corrosion (FFC) - for iron surfaces only.

Previously reported resistance against marine corrosion by an epoxy-based coating containing additions of electrochemically generated PEDOT:PSS was attributed to the electrochemical stability and high electrical conductivity of PEDOT:PSS [13].

6.2 Experimental details

The Scanning Kelvin probe (SKP) was used in all experiments and a full description of operation and set up is described in Section 2.2. SKP calibration was carried out as described in Section 2.2.4 and, additionally, a PEDOT:PSS layer over-coated with PVB was placed over the Cu/Cu^{2+} calibration cell to determine any effect on the measured calibration value which was found to be negligible.

All metal samples for all experiments were prepared using the procedure described in section 2.1.3. PEDOT:PSS was supplied by AGFA (5.5% wt) and was applied to metal surfaces via bar coating where clear adhesive tape was used to make a trough with either single, double or triple layers to achieve final film thickness of 1 μm, 3 μm or 5 μm respectively. Oven curing was carried out at 130°C for ≥ 10 min. Dry film thickness of the PEDOT:PSS was measured using a Dektak profileometer.

For PEDOT:PSS-metal interaction experiments metal substrates were coated with PEDOT:PSS as shown in Fig 6.1. Experiments were carried out in ambient conditions, unless otherwise stated, i.e. 50 ± 10% r.h. at ~25°C where measurements were taken throughout using a Lascar humidity and temperature sensor. Hourly scanning was carried out over four lines of 10 mm length over a 24 h period as shown in Fig 6.2.

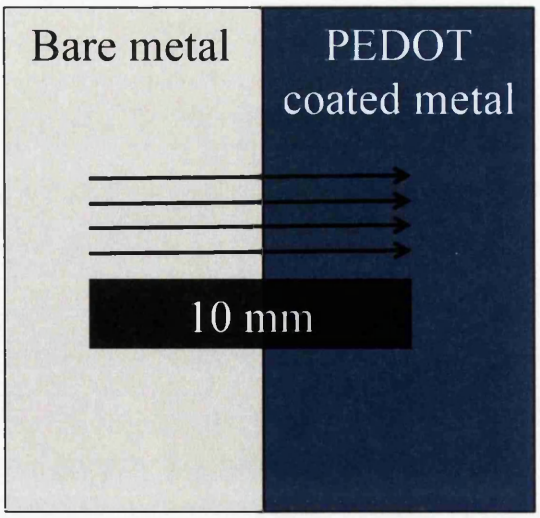

Fig 6.1 Schematic showing a metal sample coated with a PEDOT:PSS layer. The four arrows show the 10 mm scan length across the metal-PEDOT:PSS-coated metal boundary.

For delamination experiments metal substrates were coated with PEDOT:PSS, as shown in fig 6.2, at thicknesses 1 μm, 3 μm or 5 μm, and subsequently over-coated with PVB films of thickness 10±3 μm and prepared for delamination experiments as described in Section 2.2.1.1. SKP scanning was carried out as described in Section 2.2.3. For FFC experiments samples were prepared as shown in fig 6.3. Samples were coated with PEDOT:PSS layers of thicknesses 1 μm, or 5 μm with an exposed area of iron left in between the two coated strips. The entire sample surface was then over-coated with PVB films of thickness 10±3 μm. A 10 mm penetrating defect was scribed, using a scalpel, in the region with only a PVB layer. A syringe was then used to apply a volume of 2 μl of aqueous 0.005 M $FeCl_2$, which was allowed to dry in room air. Initiation was carried out with $FeCl_{2(aq)}$ as opposed to $NaCl_{(aq)}$ to avoid the phase I cathodic delamination described in Section 1.4.6.4 so experiments could be conducted over shorter time periods. Samples were placed in a humidity chamber at 93% r.h. and 20°C. Samples were photographed periodically using a Canon 600D camera.

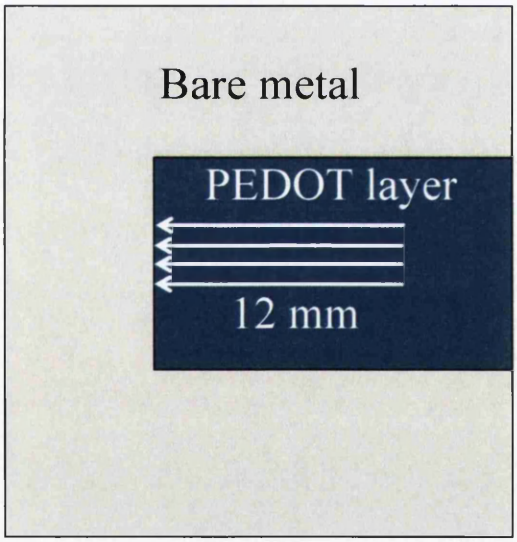

Fig 6.2 Schematic showing a metal sample coated with a PEDOT:PSS layer prior to over-coating with PVB. The four arrows show the 12 mm scan length across the PEDOT:PSS-coated metal surface up to the artificial defect.

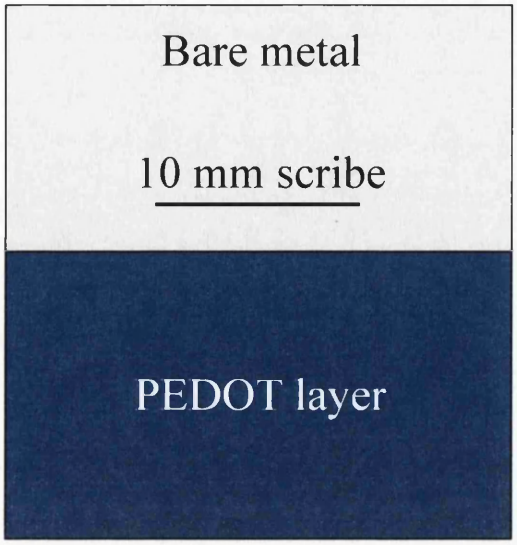

Fig 6.3 Schematic showing a metal sample coated with a PEDOT:PSS layer and over-coated with PVB. The 10 mm scribe is shown, where FFC is initiated, parallel to a PEDOT:PSS layer on the metal surface.

6.3 Results and discussion

6.3.1 Volta potential measurement of various PEDOT:PSS coated metal surfaces

The current study employs a wide range of metals spanning a large part of the electrochemical series. This was done to make a comparison between the more noble metals, such as Ag and Pt, that are typically used in conjunction with PEDOT:PSS for electronic applications, and reactive metals such as Mg and Al. Zn and Fe were chosen to gain an insight for the proceeding corrosion-driven delamination experiments. Cu and Ni were chosen for their 'intermediate' position in the electrochemical series and because they may potentially be utilised as electrical connections combined with PEDOT:PSS providing a less expensive alternative to Ag and Pt. The metals studied are listed in Table 6.1 where the standard reduction potentials (E^{o}) for each redox half-cell reaction are also given.

Table 6.1 The standard reduction potential (E^{o}) values for the relevant metals at 298K, 1mole, 1atm.

Metal	Half-reaction	E^{o} / V vs SHE
Pt	$Pt^{2+}_{(aq)}+2e^{-} \rightarrow Pt_{(s)}$	+1.20
Ag	$Ag^{+}_{(aq)}+e^{-} \rightarrow Ag_{(s)}$	+0.80
Cu	$Cu^{2+}_{(aq)}+2e^{-} \rightarrow Cu_{(s)}$	+0.34
Ni	$Ni^{2+}_{(aq)}+2e^{-} \rightarrow Ni_{(s)}$	-0.26
Fe	$Fe^{2+}_{(aq)}+2e^{-} \rightarrow Fe_{(s)}$	-0.44
Zn	$Zn^{2+}_{(aq)}+2e^{-} \rightarrow Zn_{(s)}$	-0.76
Al	$Al^{3+}_{(aq)}+3e^{-} \rightarrow Al_{(aq)}$	-1.68
Mg	$Mg^{2+}_{(aq)}+2e^{-} \rightarrow Mg_{(s)}$	-2.38

Experiments were conducted as described in Section 6.2 where PEDOT:PSS layers were applied at thickness of 1 μm, 3 μm and 5 μm on each metal substrate. Fig 6.4 [a-d] shows the E_{corr} (V vs. SHE) vs. distance profiles, taken as an average from four scanned lines, for the 'noble' metals Pt, Ag, Cu and Ni after 24 h holding time. In each case the blue dashed vertical line shows the boundary between the bare metal surface and the PEDOT:PSS-coated metal surface.

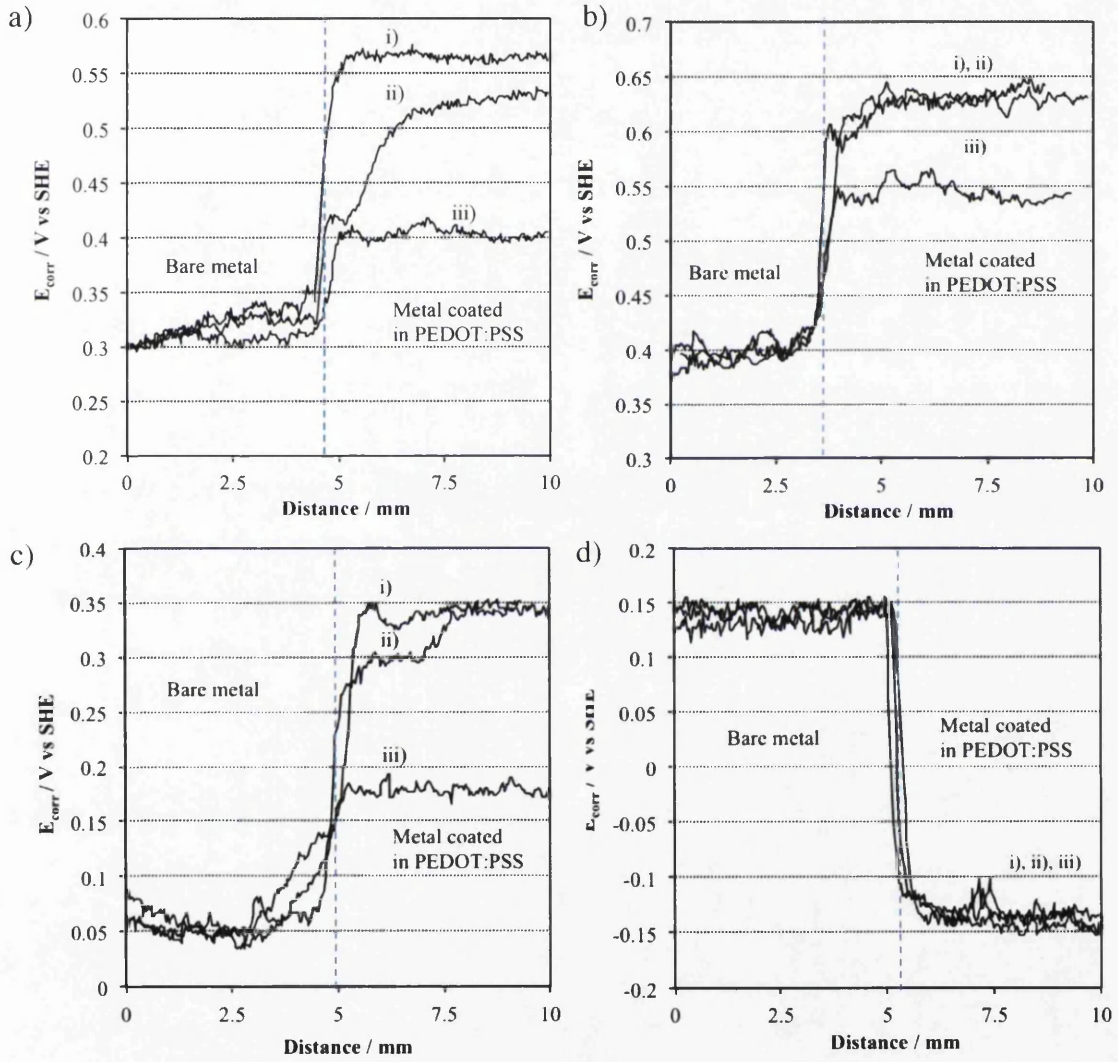

Fig 6.4 E_{corr} vs. distance profiles for substrates (a) Pt, (b) Ag, (c) Cu and (d) Ni where PEDOT:PSS layers were present at thicknesses of (i) 5 μm, (ii) 3 μm and (iii) 1 μm. Data was recorded after 24 h in ambient conditions.

In contrast to previous findings using PAni/PVB coatings, it can be observed that the values of E_{corr} recorded on each of the PEDOT:PSS coated metal surfaces (E_{intact}) are all unique [10]. In each case, with the exception of E_{intact} values measured on Ni, E_{intact}

values are more positive than the bare metal surface. It can be seen that the extent of this 'ennoblement' is dependent on film thickness. Whilst the values recorded for E_{intact} are wholly similar for PEDOT:PSS coatings of 3 μm and 5 μm, values measured on coatings of 1 μm for each metal were substantially less positive, again with the exception of Ni. It appears that a threshold thickness value of 3 μm exists where E_{intact} values measured in the presence of a coating of this thickness, or above, are wholly similar. Conversely, very similar values were recorded in experiments carried out on all three of the different PEDOT layers applied to a Ni surface and, importantly, a depression of E_{intact} measured in relation to the bare metal surface was observed.

Fig 6.5 [a – d] shows the E_{corr} (V vs. SHE) vs. distance profiles at 24 h for those metals at the more reactive end of the electrochemical series Fe, Zn, Al and Mg coated with PEDOT:PSS at film thicknesses of 1 μm, 3 μm and 5 μm. As with the previous fig, the dashed line shows the boundary between the bare metal surface and the PEDOT:PSS-coated metal surface. It appears that coating thickness has less of an influence on E_{intact} for Al, Ni and Zn as the values recorded on a layer of PEDOT:PSS at 1 μm seem to be entirely similar to those measured at 3 μm and 5 μm. It is suggested that the coverage of the metal surface is not uniform in those cases where E_{intact} values measured for a PEDOT:PSS layer of 1 μm do not approximate those measured at 3 μm and 5 μm.

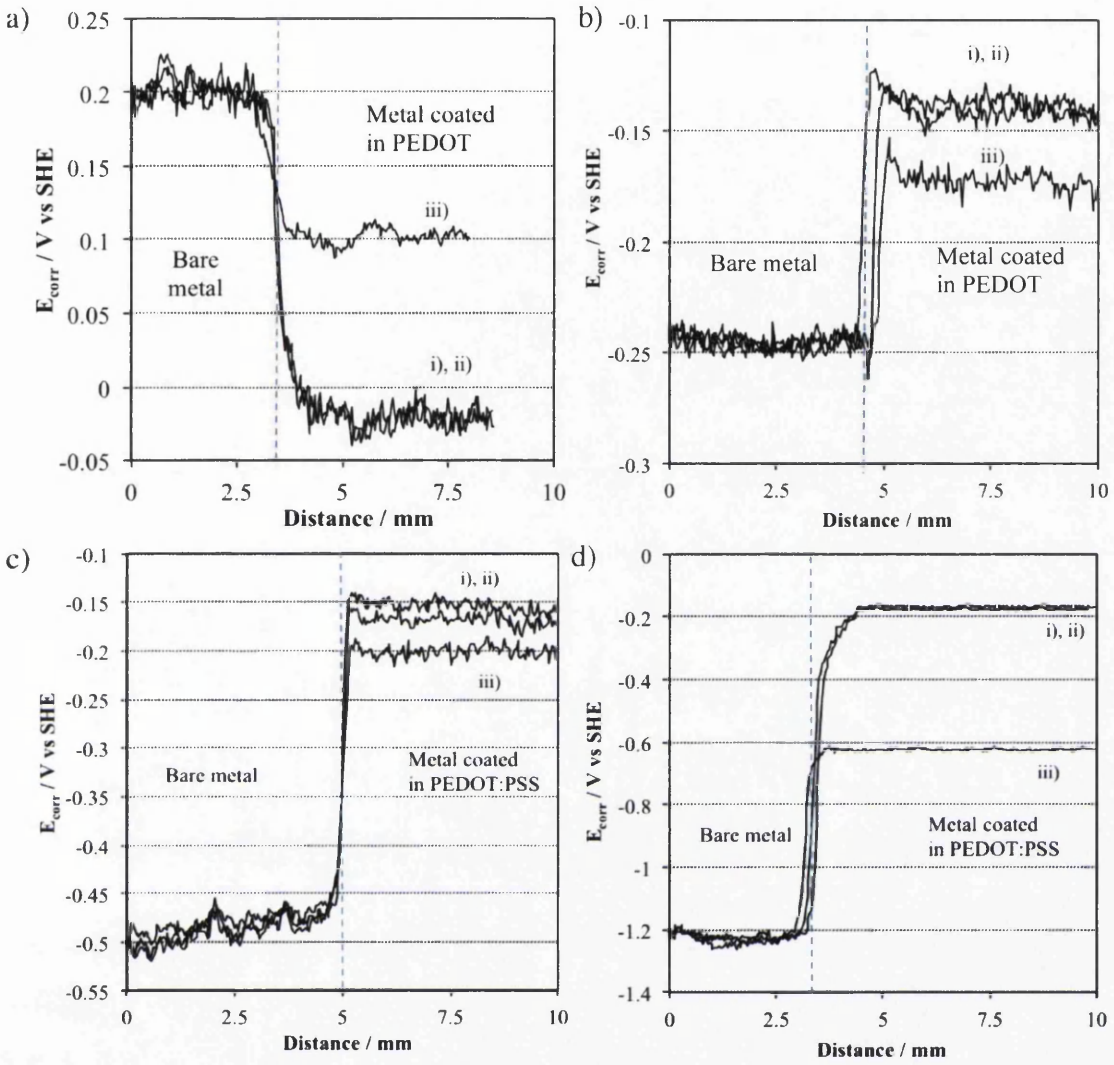

Fig 6.5 E_{corr} vs. distance profiles for substrates (a) Fe, (b) Zn, (c) Al and (d) Mg where PEDOT:PSS layers were present at thicknesses of (i) 5 μm, (ii) 3 μm and (iii) 1 μm. Data was recorded after 24 h in ambient conditions.

Fig 6.6 summarises the E_{corr} values measured over the metal-PEDOT:PSS coated metal interface for all the metals used in the current study when coated with a 5 μm PEDOT layer. The E_{corr} values recorded on the 'noble' metals, shown more closely in fig 6.7, are all more positive, with the exception of Fe, than the bare metal and display entirely dissimilar values.

Initial observations suggest that the Zn, Al and Mg substrates are simply ennobled by the PEDOT:PSS to a more positive E_{intact} value. However, as shown in fig 6.8, the established E_{intact} values all tend to a value of ca. -0.15 V vs. SHE. Furthermore, it can be observed that all those metals with an E^{o} value of $\leq$ -0.26 V vs. SHE (as given in Table 6.1) i.e. Ni and all subsequent metals with values more negative than this, are

'polarised' to this consistent value of ca. -0.15 V vs. SHE. For Ni and, to a lesser extent, Fe (fig 6.7), E_{intact} values are depressed relative to the E_{corr} measurements made on the bare metal surfaces. Again, these E_{intact} values tend towards -0.15 V vs. SHE. It seems reasonable to assume that this consistent E_{intact} value for PEDOT coated Ni, Fe, Mg, Al, Zn is due to the metal surface being 'polarised' to the potential governed by the $PEDOT:PSS_{(ox)}/PEDOT:PSS_{(red)}$ couple.

Ghilane et al report a switching value of -0.4 V vs. SCE (ca. -0.156 V vs. SHE) at which the potential of the PEDOT:PSS polymer film converts from the oxidized form to the reduced form. It is, therefore, further proposed that the consistent E_{intact} value observed on Ni, Al, Mg, Zn and, to some extent, Fe, is derived from the formation of a certain quantity of $PEDOT:PSS_{(red)}$. This arises because the $PEDOT:PSS_{(ox)}$ is capable of oxidizing the metal surface m (where m = Ni, Al, Mg, Zn and Fe) according to:

$$m \rightleftharpoons m^{n+} + ne^- \qquad (6.1)$$

$$PEDOT:PSS_{(ox)} + e^- \rightleftharpoons PEDOT:PSS_{(red)} \qquad (6.2)$$

Reaction 6.2, however, is written in a simplified form, as the PSS counterion is not included. It would be expected that, as the PEDOT:PSS becomes reduced from its radical cation state (as shown in the reaction scheme given in fig 6.10), electroneutrality would be preserved by the association of either metal cations (m^{n+}) or protons (H^+) with the negatively charged sulphonate groupings, this is represented in the reaction scheme given in fig 6.9.

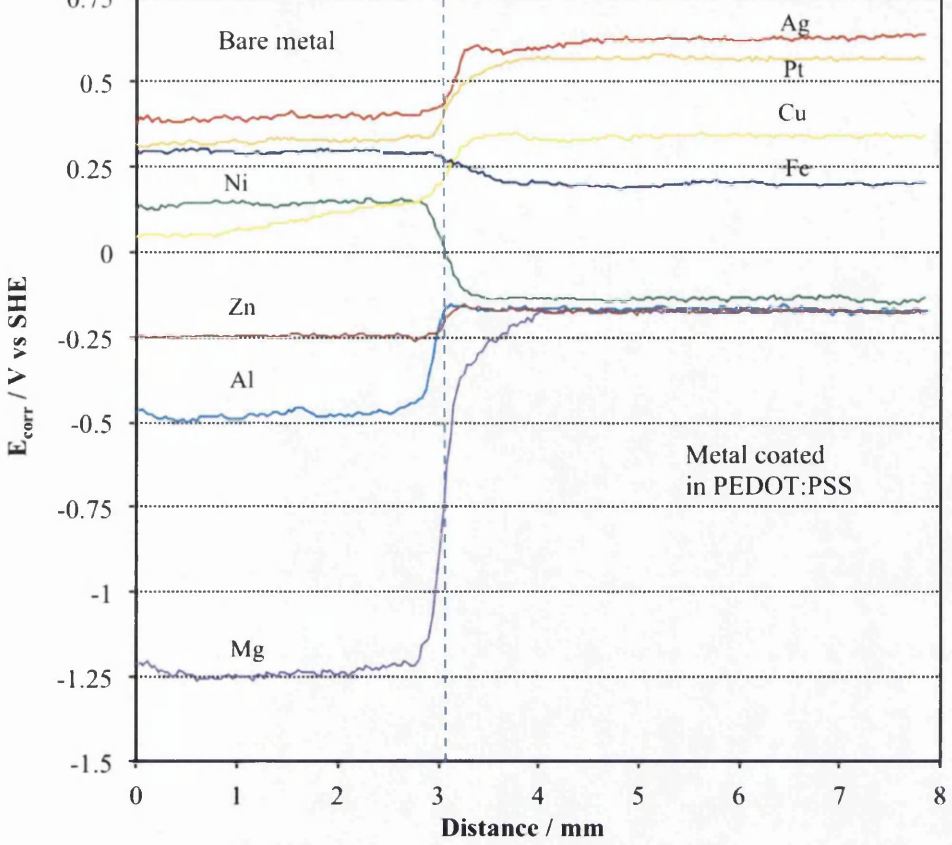

Fig 6.6 Summary plot of E_{corr} vs. distance profiles for all metals coated with PEDOT:PSS at a thickness of 5 μm.

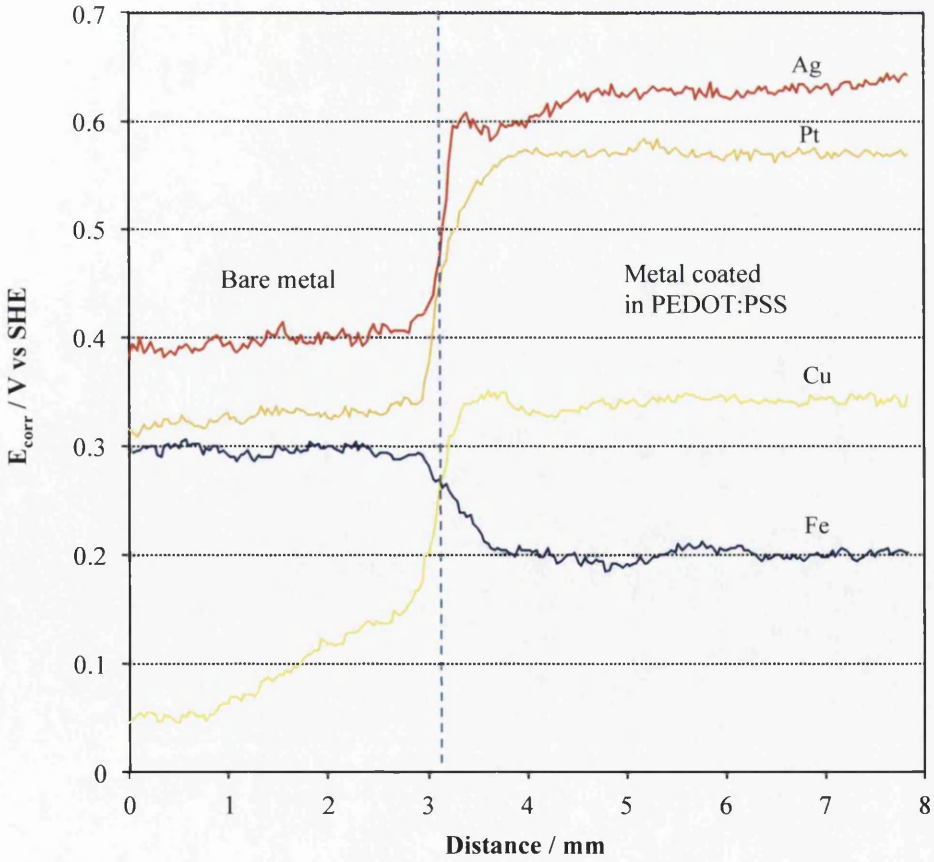

Fig 6.7 Summary plot of E_{corr} vs. distance profiles for the noble metals coated with PEDOT:PSS at a thickness of 5 μm.

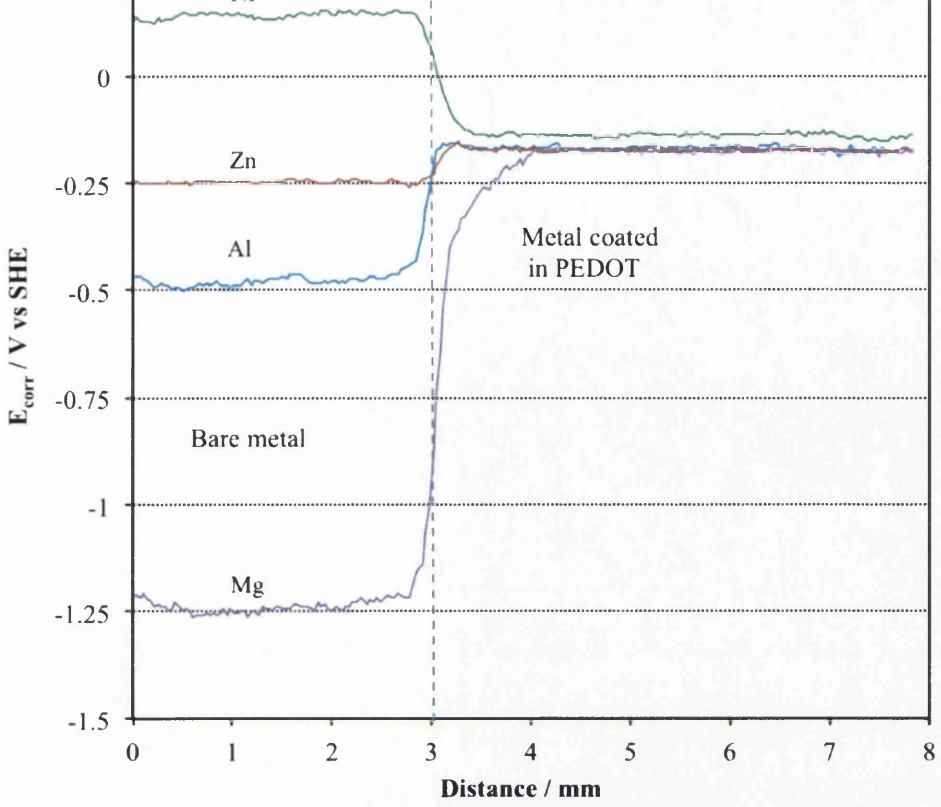

Fig 6.8 Summary plot of E_{corr} vs. distance profiles for the reactive metals coated with PEDOT:PSS at a thickness of 5 μm.

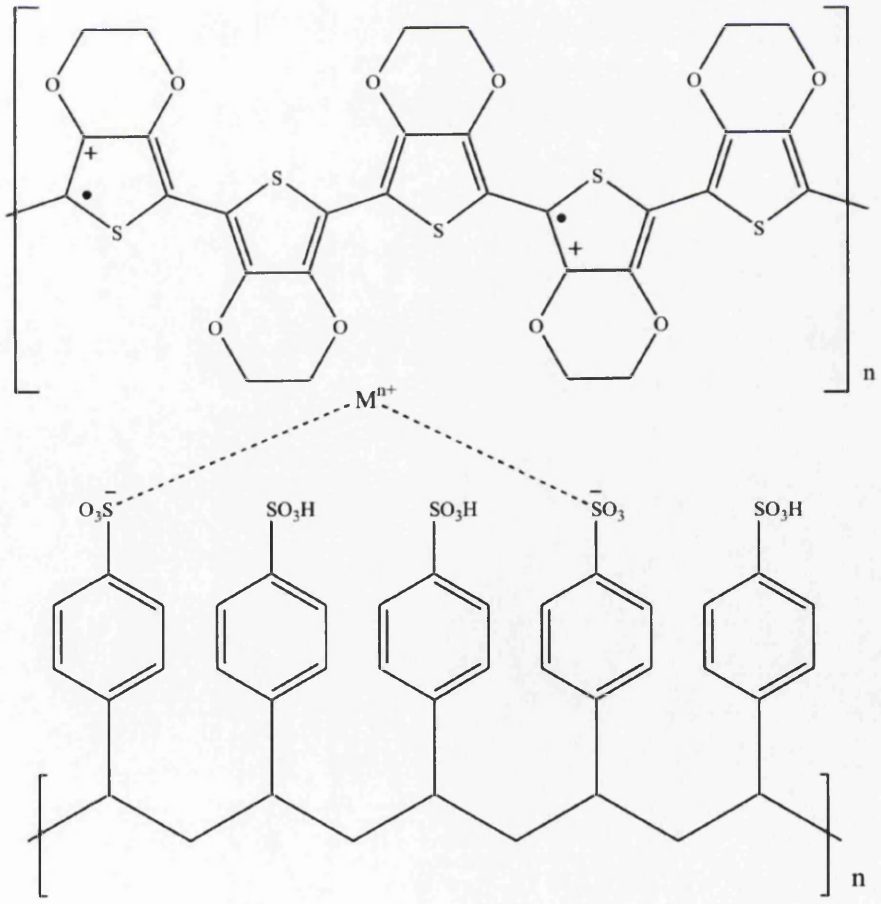

Fig 6.9 Reaction scheme showing PEDOT:PSS(red) stabilized by m^{n+} cation.

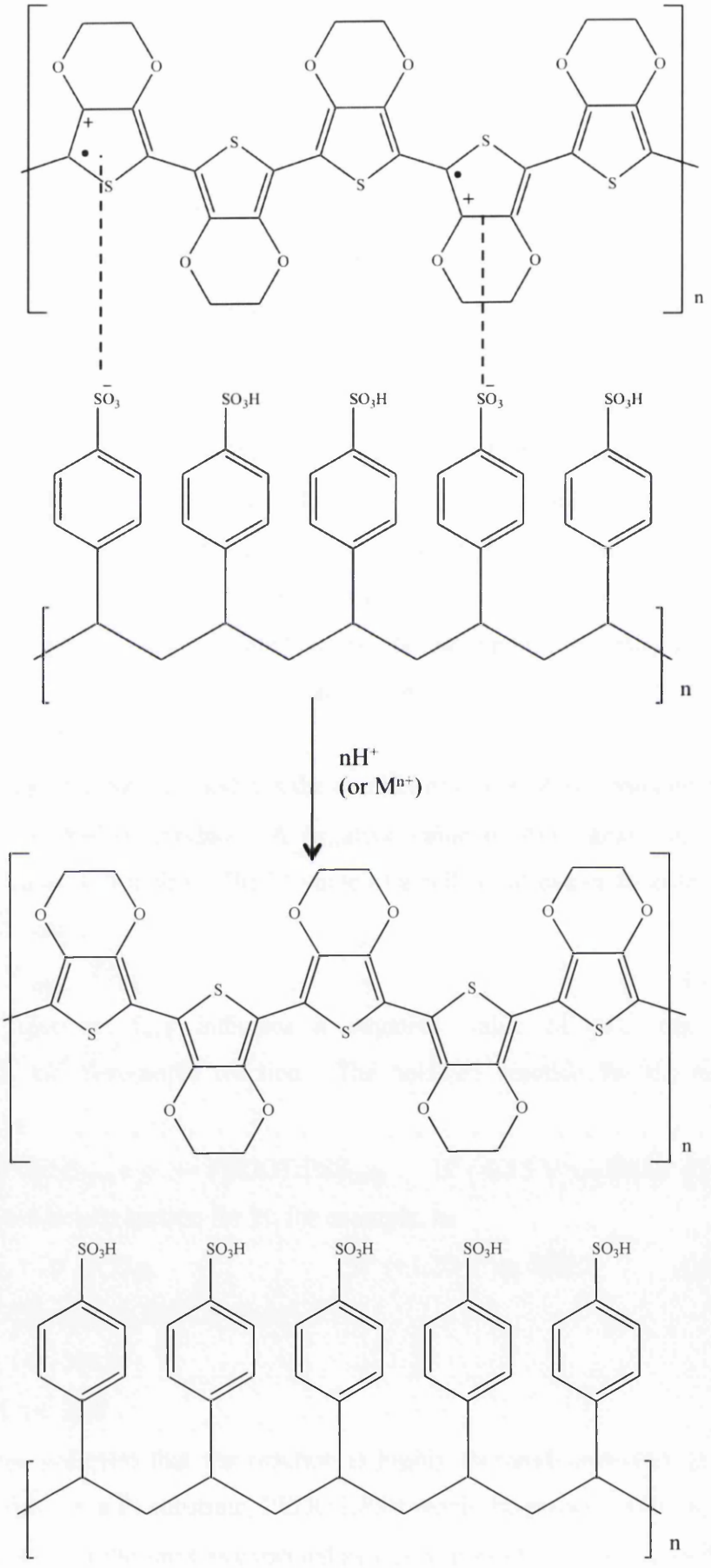

Fig 6.10 Reaction scheme showing the reduction of PEDOT:PSS.

The presence of a fraction of reduced PEDOT:$PSS_{(red)}$ in the coatings applied to the surface of a metal (m) allows a stable E_{intact} value to be established according to the Nernst equation:

$$E_{corr} = E^{o}\left(\text{PEDOT: PSS}\left(\frac{ox}{red}\right)\right) + \frac{2.303RT}{F}\log_{10}\frac{[\text{PEDOT:PSS(ox)}]}{[\text{PEDOT:PSS\{red)}]} \qquad (6.3)$$

For the 'noble' metals, e.g. Pt, Ag and Cu, the lack of any consistent E_{intact} values may be attributed to the fact that no redox reaction with PEDOT:$PSS_{(ox)}$ is established. As a result the PEDOT:PSS coating remains fully oxidized and the [$PEDOT_{(ox)}$]/[$PEDOT_{(red)}$] ratio is large, resulting in potentials that are consistently higher than E^{o}[$PEDOT_{(ox)}$]/[$PEDOT_{(red)}$]. This can be illustrated further by calculating the cell potential (E_{cell}) using the values of E^{o} (m/m^{n+}) and E^{o} (PEDOT:$PSS_{(ox)}$/ PEDOT:$PSS_{(red)}$) half-cells for each metal to determine whether the PEDOT:PSS reduction reaction ($E_{(red)}$) is thermodynamically favourable for each metal. The standard electrode potential is related to the thermodynamic quantity of Gibbs free energy change (ΔG^{o}) by the following relationship:

$$\Delta G^{o} = -nFE^{o} \qquad (6.4)$$

Where F is Faraday's constant and n is the number of moles of electrons involved in the cell reaction per mol of product. A negative value of ΔG^{o} means the reaction is thermodynamically favourable. The E^{o} value of a cell (E_{cell}) can be calculated by using the following equation:

$$E_{cell} = E_{(red)} - E_{(ox)} \qquad (6.5)$$

A positive value of E_{cell} indicates a negative value of ΔG^{o} and, hence, a thermodynamically favourable reaction. The half-cell reaction for the reduction of PEDOT:PSS is:

$E_{(red)}$ PEDOT:$PSS_{(ox)} + e^{-} \rightarrow$ PEDOT:$PSS_{(red)}$ E^{o} (-0.15 V vs. SHE) (6.6)

The half-cell oxidation reaction for Pt, for example, is:

$E_{(ox)}$ $Pt^{2+}_{(aq)} + 2e^{-} \rightarrow Pt_{(s)}$ E^{o} (+1.20 V vs. SHE) (6.7)

Applying this E^{o} value to Eq. 6.5 gives:

$E_{cell} = -0.15 - (+1.20)$

$E_{cell} = -1.35$ V vs. SHE

This E_{cell} value indicates that the reaction is highly thermodynamically unfavourable and suggests that, on a Pt substrate, PEDOT:PSS would be present in its oxidised form only. For Ag and Cu the same is expected as E_{cell} values of -0.95 V vs. SHE and -0.49 V vs. SHE are calculated respectively.

The half-cell oxidation reaction for Ni is:

$E_{(ox)}$ $Ni^{2+}_{(aq)}+2e^- \rightarrow Ni_{(s)}$ E^o (+0.26 V vs. SHE) (6.8)

Applying this E^o value to Eq. 6.5 gives:

$E_{cell} = -0.15 - (-0.26)$

$E_{cell} = +0.11$ V vs. SHE

This value indicates that the reaction is thermodynamically favourable and suggests that PEDOT:PSS on a Ni substrate would be present partially in its reduced form. For Al and Mg E_{cell} values of +1.53 V vs. SHE and +2.23 V vs. SHE respectively are calculated meaning that in both cases the reaction for the reduction of PEDOT:PSS is highly thermodynamically favourable.

Fig 6.11 (a) and (b) gives plots of E_{intact} vs. time over a period of 24 h for the two most noble metals, Pt and Ag, and the most reactive metals, Al and Mg, in 95% r.h. and ambient conditions respectively. After exposure to conditions at 95% r.h, PEDOT:PSS coated Mg and Al exhibit highly stable E_{intact} values in comparison to the more noble metals, Pt in particular. The plots presented in 6.11 (a) for Ag and Pt are selected purely to show the time dependence of E_{intact} over 24 h and are not a firm representation of repeat experiments as values measured were wholly different with each experiment. Unstable E_{intact} values measured over the 24 h period were observed each time. Al displays identical and stable values in both high r.h. and ambient conditions where a value approaching ca. -0.15 V vs. SHE is shown. However, where Mg was exposed to a high r.h, as shown in fig 6.11(a), the E_{intact} values were unexpectedly more negative than that of bare Mg. It was expected that, like Al, values around -0.15 V vs. SHE would be recorded. It is suggested that, at a high r.h. the $PEDOT:PSS_{(ox)}$/$PEDOT:PSS_{(red)}$ couple no longer exists and PEDOT:PSS exists in its fully reduced form under these conditions.

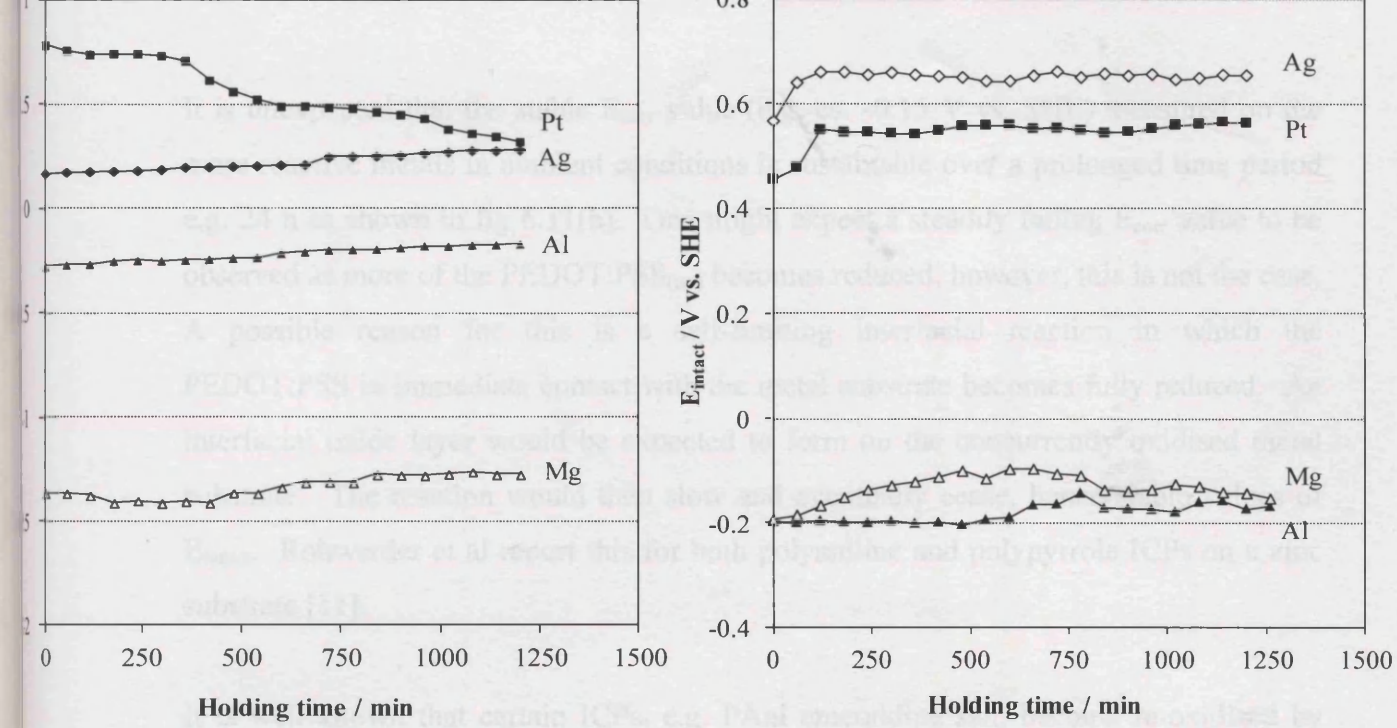

Fig 6.11 E_{intact} vs. time for PEDOT:PSS coated metals in air at a) 95% r.h. and b) 50% r.h.

This is demonstrated in fig 6.12 (a) and (b) that shows photographic images of Al and Mg surfaces respectively after one week in an environment chamber at 95% r.h. The right hand side of each image shows a section of the surface coated in PEDOT:PSS where the lower region has been removed using isopropanol. It can be seen in both cases that, in comparison to the bare substrate shown on the left hand side of each image, a surface oxide has developed. The E_{intact} values measured on the range of PEDOT:PSS-coated metals presented is not wholly governed by the redox potential as other factors, such as relative humidity, also have an influence.

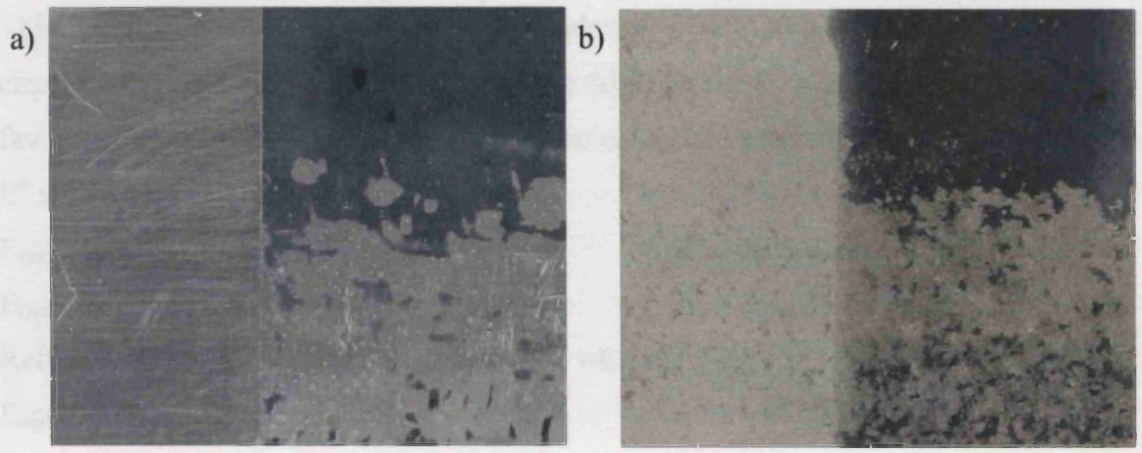

Fig 6.12 Photographic images of a) aluminium and b) magnesium substrates after one week in an environment chamber at 95% r.h. The right hand side has been coated with a 5 μm PEDOT:PSS and the lower portion removed using isopropanol. The left hand side shows the bare, uncoated metal surface.

It is unexpected that the stable E_{corr} value (e.g. ca. -0.15 V vs. SHE) measured on the more reactive metals in ambient conditions is sustainable over a prolonged time period e.g. 24 h as shown in fig 6.11(b). One might expect a steadily falling E_{corr} value to be observed as more of the PEDOT:$PSS_{(ox)}$ becomes reduced, however, this is not the case. A possible reason for this is a self-limiting interfacial reaction in which the PEDOT:PSS in immediate contact with the metal substrate becomes fully reduced. An interfacial oxide layer would be expected to form on the concurrently oxidised metal substrate. The reaction would then slow and eventually cease, hence stable values of E_{intact}. Rohwerder et al report this for both polyaniline and polypyrrole ICPs on a zinc substrate [11].

It is well known that certain ICPs, e.g. PAni emeraldine salt, become re-oxidised by atmospheric oxygen when in their reduced form [10]. A second hypothesis is that this is the case for PEDOT:PSS on the reactive metals. Fig 6.13 shows a plot of E_{intact} vs. time of an Al surface coated in PEDOT:PSS at a thickness of 5 μm where, upon the establishment of a stable E_{intact} value in 95% r.h. air, the environment chamber was flooded with N_2 remaining at 95% r.h. It can be observed that, when oxygen was removed from the chamber, the E_{intact} value decreased to a value of ca. -0.375 V vs. SHE. This value is approaching the values measured for bare Al as shown in fig 6.8 and represents a partial reduction of the oxide layer by the metallic Al underneath it; in air this reaction is prevented by the oxidizing potential of oxygen [11]. Upon reaching a stable E_{intact} value in the N_2 atmosphere, air was reintroduced into the chamber, again at 95% r.h. Importantly, the E_{intact} values returned to those recorded in air at 95% r.h. This result demonstrates the cyclic re-oxidation of PEDOT:PSS on Al. The E_{corr} changes observed are shown relative to bare Al in fig 6.14. Again, the thermodynamic favourability of this oxidation reaction can be calculated according to Eq. 6.4 where the E^o values for each half-cell are known:

$E_{(ox)}$ $PEDOT_{(red)}$ $\rightleftharpoons$ $PEDOT_{(ox)} + e^-$ E^o (-0.15 V vs. SHE) (6.9)

$E_{(red)}$ $O_2 + 4e^- + 2H_2O \rightarrow 4OH^-$ E^o (+0.44 V vs. SHE) (6.10)

Referring to Eq. 6.5, E_{cell} can be determined where:

$E_{cell} = +0.44 - (-0.15)$

$E_{cell} = +0.59$ V vs. SHE

which in turn gives a negative value of ΔG^o indicating that the oxidation of PEDOT:PSS is thermodynamically favourable.

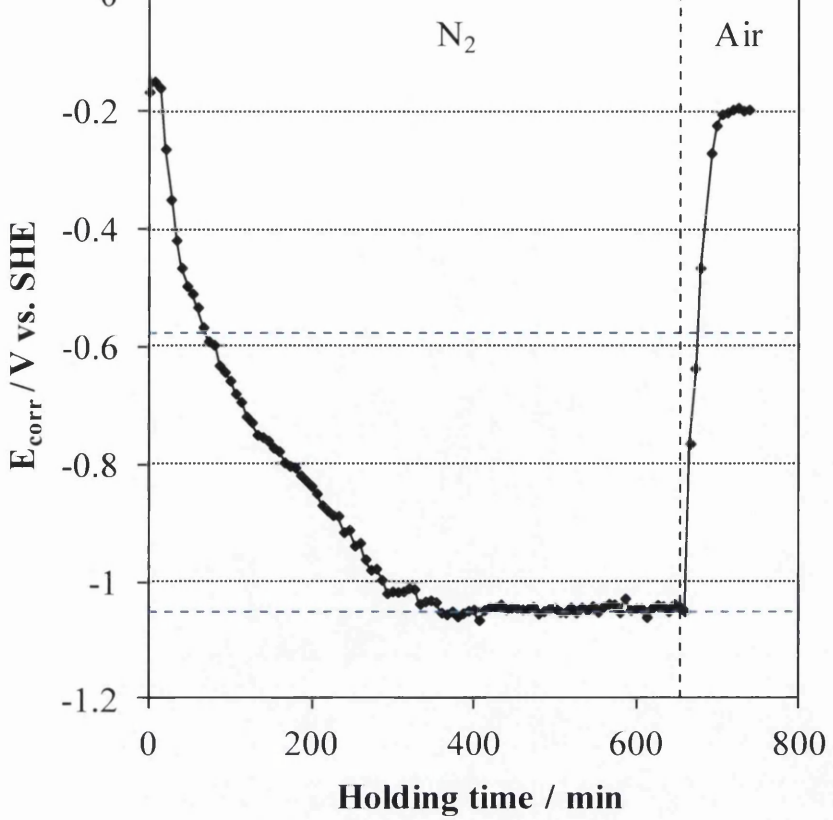

Fig 6.13 Plot of E_{intact} values with respect to time for an Al surface coated with a 5 µm PEDOT:PSS layer where the sample was kept in an environment chamber at 95% rh and 25°C throughout. Initial values were measured in air and immediately upon recording values the chamber was flooded with N_2. Air was reintroduced at approx. 650 min. The upper and lower dashed lines show the E_{corr} values recorded on bare Al in the absence of and presence of N_2 respectively.

6.3.2 Delamination of an uninhibited PVB coating from a bare HDG surface

Preliminary experiments were carried out to determine the baseline kinetics of unpigmented organic coating delamination from a bare HDG steel substrate. The Stratmann-type delamination cell procedure was carried out as outlined in Section 2.1.3 and four scan lines were taken hourly over a 24 h period. Upon reaching an equilibrium of 95% rh within the environmental chamber, values of E_{corr} for the undelaminated coating surface (E_{intact}) were approximately -0.4 V vs. SHE, similar to those recorded on an uncoated HDG surface in the same conditions and also in agreement with values reported within available literature [14]–[16]. Upon addition of an electrolyte of 5% aqueous NaCl to the defect area, the establishment of the distinctive time-dependent E_{corr}-distance (x) delamination profile was observed typically within 1-3 h denoting the onset of delamination. Fig 6.15 shows plots of time-dependent E_{corr} vs. distance profiles for a 10 µm PVB coating on HDG at hourly intervals from 0 h (left) to 24 h (right).

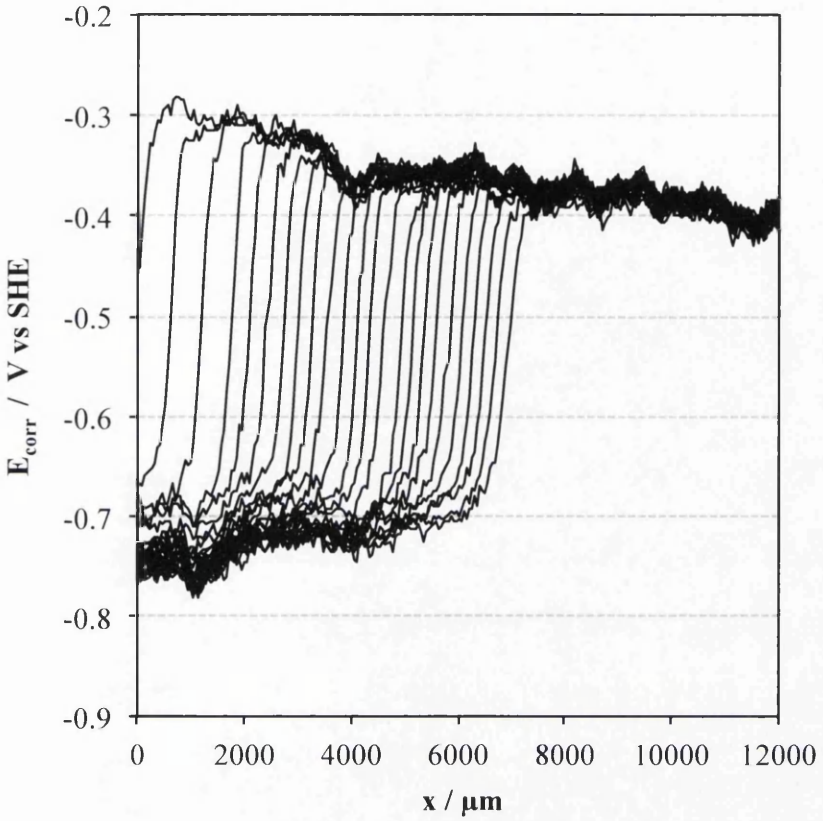

Fig 6.15 Plot of time-dependent E_{corr} vs. distance profiles for a 10µm PVB coating on HDG initiated at a defect with 5% (aq) electrolyte shown at hourly intervals from 0 h (left) to 24 h (right).

A sharp drop in potential of ca. 0.3 V is observed in the immediate vicinity of the delamination front. In the region linking the delamination front to the area adjacent to the defect, the potential reduces gradually and in an approximately linear manner finally reaching values as low as -0.7 to -0.8 V vs. SHE.

As described in Section 1.4.2 and in the available literature, a local cathode resulting from oxygen reduction due to O_2 reduction as in reaction 6.11, exists in the vicinity of the delamination front [29-30]. This is coupled with the anodic Zn dissolution reaction given in 6.12, that initially occurs at the defect only, by a thin layer of penetrating electrolyte. It is reported that the rate-determining step in cathodic delamination is typically the transport of cations from the external electrolyte and through the metal-coating interface.

$$O_2 + 2H_2O + 4e^- \rightleftharpoons 4OH^- \qquad (6.11)$$

$$Zn \rightleftharpoons Zn^{2+} + 2e^- \qquad (6.12)$$

The actual loss of adhesion of the organic coating is attributed to the high pH, reported to be pH 10-11 on HDG steel [18], that results in base catalysed polymer degradation and base catalysed hydrolysis of interfacial bonds. The Zn surface of HDG steel is also susceptible to the dissolution of the amphoteric metal oxide film at the metal-coating interface. This elevated pH leads to the formation of bizincate ($HZnO_2^-$) and zincate (ZnO_2^{2-}) corrosion product from anodic activity that eventually occurs in the underfilm region:

$$Zn(OH)_2(s) \rightleftharpoons HZnO_2^-(aq) + H^+(aq) \quad (6.13)$$

$$Zn(OH)_2(s) \rightleftharpoons ZnO_2^{2-}(aq) + 2H^+(aq) \quad (6.14)$$

Furthermore, a bare Zn surface exposed by the dissolution of zinc(hydroxide) has the potential to directly oxidize to bizincate via the following reaction:

$$Zn(s) + 2H_2O \rightleftharpoons HZnO_2^-(aq) + 3H^+(aq) + 2e^- \quad (6.15)$$

6.3.3 Delamination of PVB on a HDG steel surface with a PEDOT:PSS under-layer

Delamination experiments were carried out on HDG samples where a layer of PVB, of thickness 10 μm, was coated over a layer of PEDOT:PSS, of thickness 1 μm and 5 μm. The results are given in figs 6.16 and 6.17 where the time-dependent E_{corr} vs. distance profiles recorded at hourly intervals are plotted between 0 h and 24 h (right). The representative plot of time-dependent E_{corr} vs. distance profiles (fig 6.16) for a 1 μm PEDOT:PSS layer shows that values recorded in the vicinity of the defect region are ~-0.8 V vs. SHE approximating those values measured in the control experiment (fig 6.15). The drop in potential at the delamination front is also wholly similar to that shown for the control experiment. The E_{intact} values, however, are approximately 0.1 V vs. SHE higher than those recorded in the control experiment. For the experiment where a 5 μm PEDOT:PSS layer was present, represented by the plot given in fig 6.17, a very blurred potential drop is observed where the delamination front region appears to connect directly to the defect. Leng et al suggest in previous work that this is the result of the spreading of the corrosion conditions throughout the delaminated region as opposed to remaining localised, as is shown the control example (fig 6.15)[19]. Again, a slight increase in E_{intact} is observed when compared to the control experiment.

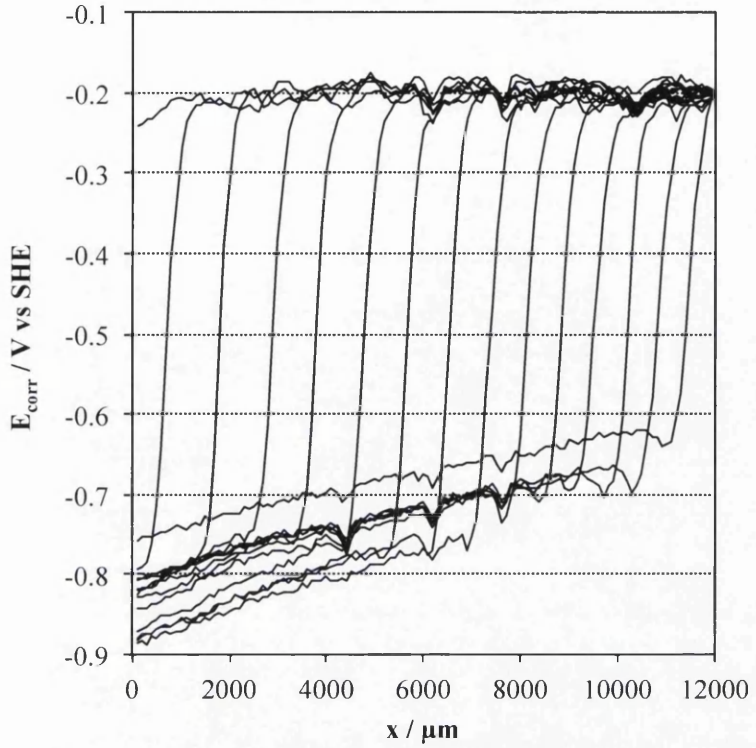

Fig 6.16 Plot of time-dependent E_{corr} vs distance profiles for a 10 µm PVB coating applied over a 1 µm PEDOT:PSS layer on HDG initiated at a defect with 5% (aq) electrolyte shown at hourly intervals from 0 h (left) to 14 h (right).

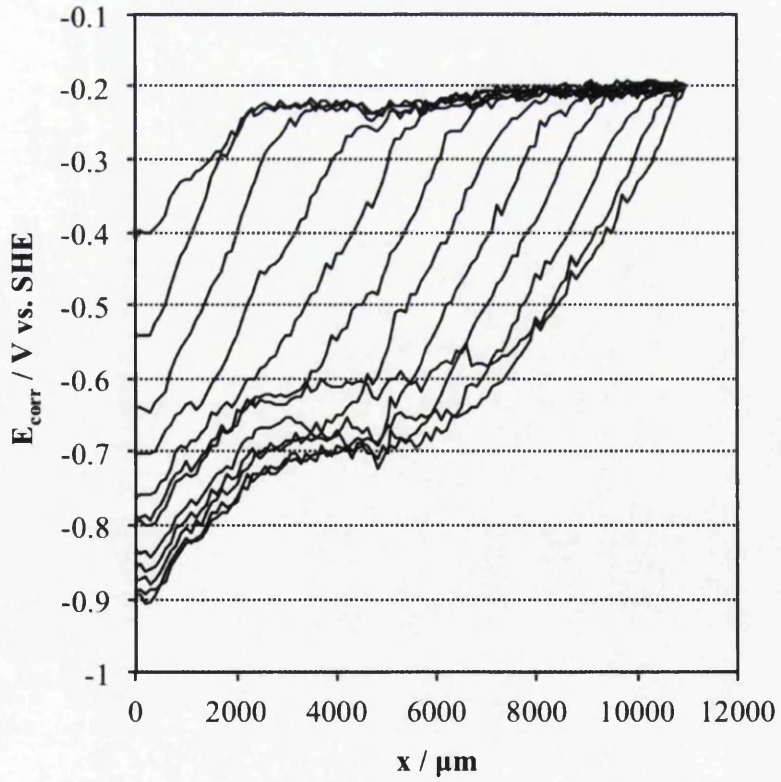

Fig 6.17 Plot of time-dependent E_{corr} vs. distance profiles for a 10 µm PVB coating applied over a 5 µm PEDOT:PSS layer on HDG where was initiated at a defect with 5% (aq) electrolyte from shown at half-hourly intervals from1 h (left) to 5.5 h (right).

The delamination rate (k_{del}) for the three experiments can be obtained from fig 6.18 where a plot of x_{del} vs. (t_{del} - t_i), is given where t_{del} is the delamination time following application of electrolyte and t_i is the delamination initiation time. As delamination kinetics remain parabolic it can be assumed that Na^+ cation migration remains the rate limiting process. The delamination rates (k_{del}) for each experiment are listed in Table 6.2. This shows that where a 1 μm PEDOT:PSS layer is present the delamination rate increases by ~113% in comparison with the control sample. Even more substantially, the presence of a 5 μm PEDOT:PSS layer increases the delamination rate by ~ 1860%.

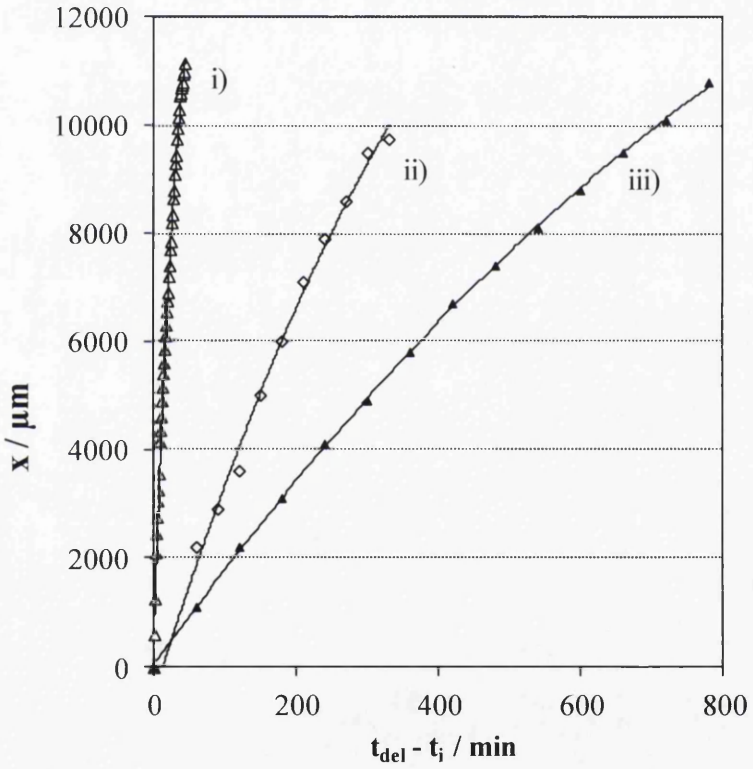

Fig 6.18 Delamination distance (x_{del}) plotted as a function of time (t_{del} – ti) for unpigmented PVB coatings where the defect electrolyte is 5% NaCl (aq) and layers of PEDOT:PSS have been applied directly to the HDG substrate at a thickness of i) 5 μm ii) 1 μm and iii) no PEDOT:PSS layer is present.

Image 6.19 shows photographic images of a typical Stratmann cell set up for the current experiment. A HDG surface coated in PEDOT:PSS at a thickness of 1 μm and over-coated with PVB at a thickness of 10 μm is shown (a) before the addition of electrolyte (b) after exposure to 95% r.h. over a period of 24 h where delamination was initiated with 5% wt/v aqueous NaCl and (c) where the PVB coating has been peeled back after

the experiment. Such a result was also typical where a PEDOT:PSS layer of 5 μm in thickness had been applied. An area of darker blue can be observed in fig 6.19(b) where delamination has occurred and electrolyte has ingressed underneath the coating. Furthermore, It can be observed, upon removal of the PVB coating (fig 6.19(c)), that the PEDOT:PSS has also been lifted from the HDG surface and attached to the PVB coating.

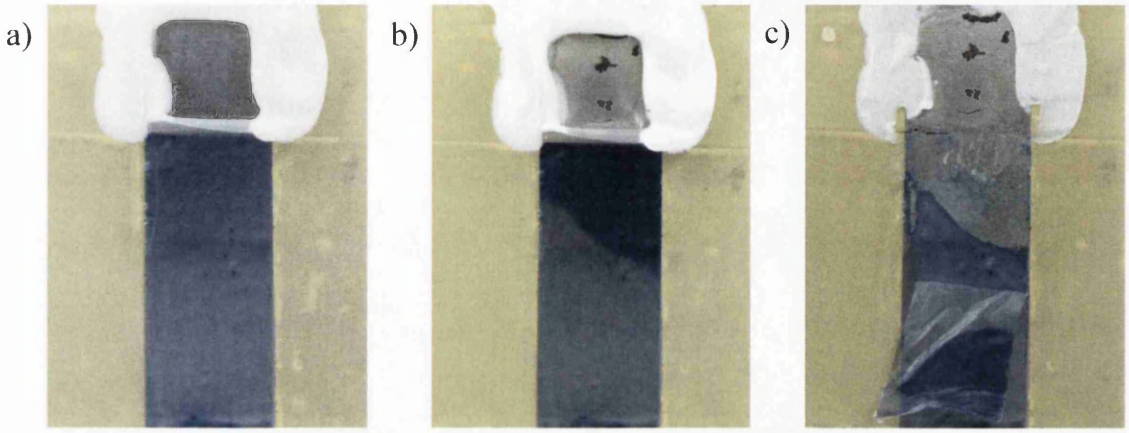

Fig. 6.19 Photographic images to show a Stratmann cell set up for a HDG surface coated in PEDOT:PSS at a thickness of 1 μm over-coated with PVB at a thickness of 10 μm (a) before the addition of electrolyte (b) after exposure to 93% r.h. over a period of 24 h where delamination was initiated with 5% wt/v aqueous NaCl and (c) with the PVB coating peeled back after the experiment.

Table 6.2 Values of the delamination rate (k_{del}) and time to delamination determined for PVB coatings applied over a PEDOT:PSS layer of various thicknesses on a HDG substrate.

PEDOT:PSS layer thickness (μm)	k_{del} (μm.min)	k_{del} change (%)	t_i (mins)
0	14	0	0
1	30	113	0
5	240	1860	0

Rohwerder et al hypothesise that enhanced corrosion observed in conjunction with ICP-based coatings is due to macroscopic percolation networks of the ICP leading to reduction of the ICP at an increased rate due to fast mobility of cations within the network [11]. It is stated that the above is true independent of the metal substrate upon which the ICP is coated. It is also reported that, in cases such as PEDOT:PSS, where the ICP may be re-oxidised by atmospheric oxygen, the enhancement of corrosion is likely to occur. Due to the acceleration of delamination it was unexpected that the E_{intact} values were in fact more positive.

6.3.4 Delamination of an uninhibited PVB coating from a bare iron suface

Initial delamination experiments were carried out using unpigmented PVB on a bare iron surface in order to establish baseline delamination kinetics. Stratmann-type experiments were carried out as outlined in Section 2.1.3 and, following equilibration with the humid experimental atmosphere, E_{intact} values were found to be uniformly high and approximated that of an uncoated iron surface in the same conditions i.e. ca. 0.1 – 0.2 V vs. SHE. Upon addition of 5% NaCl (aq) electrolyte to the defect area, the distinctive time-dependent E_{corr} vs. distance (x) delamination profile became established in one hour denoting the onset of delamination. A sharp drop in potential of ca. 0.4 to 0.5 V vs. SHE was observed in the immediate vicinity of the delamination front. In the region linking the delamination front to the region adjacent to the defect, an approximately linear and gradual potential reduction was observed. Values as low as -0.4 V vs. SHE were measured in the immediate vicinity of the defect. This is shown in fig. 6.20 which gives the plots of time-dependent E_{corr} vs. distance profiles for a 10 μm PVB coating on iron at hourly intervals from 0 h (left) to 24 h (right).

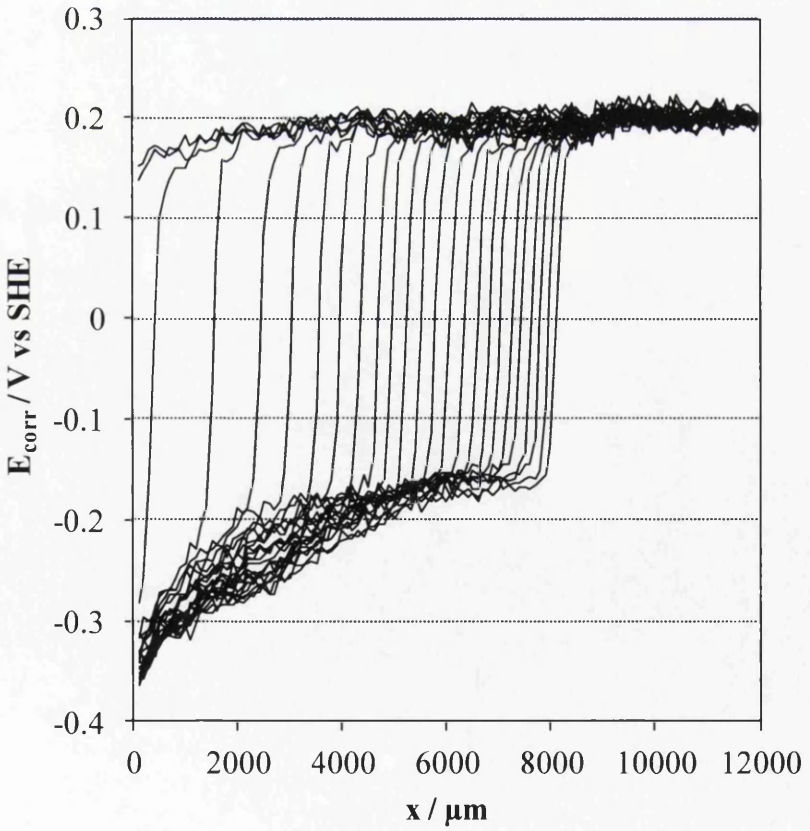

Fig 6.20 Plot of time-dependent E_{corr} vs. distance profiles for a 10 μm PVB coating on iron initiated at a defect with 5% $NaCl_{(aq)}$ electrolyte shown at hourly intervals from 0h (left) to 24h (right).

The corrosion-driven cathodic delamination of an organic PVB coating adherent to an iron substrate proceeds in a similar to manner to delamination from a HDG as described in Section 6.3.2. A thin layer of electrolyte ingresses underneath the coating coupling the anodic metal dissolution (Reaction 6.16) at the defect with cathodic oxygen reduction (Reaction 6.11) occurring in the proximity of the site of coating disbondment. On iron the alkaline environment that results from the cathodic oxygen reduction reaction has been recorded at values of > pH 10 up to pH 14 [20]; this is substantially higher than the values recorded for a zinc surface. It is this alkaline environment that is thought to cause the loss of coating adhesion by base catalysed polymer degradation and base catalysed hydrolysis of interfacial bonds.

$$Fe \rightleftharpoons Fe^{2+} + 2e^{-} \qquad (6.16)$$

6.3.5 Delamination of PVB on an iron surface with a PEDOT:PSS under-layer

Delamination experiments were carried out where a PEDOT:PSS layer was deposited, at thicknesses of 1 μm and 5 μm, on the iron surface prior to coating with a 10 μm PVB layer. Experiments were carried out as described in Section 2.1.3. In the case of a 1 μm PEDOT:PSS layer, addition of the 5% w/v NaCl (aq) electrolyte resulted in the initiation of delamination after five hours and a rapid progression of the delamination front is shown by the time-dependent E_{corr} vs. distance (x) delamination profiles plotted in fig 6.21. A delamination distance of 11000 μm was recorded after a period of 10 h. For the experiment where a 5 μm PEDOT:PSS layer was present delamination again progressed quickly and, in this case, the delamination profiles are similar to that of the control experiment shown in fig 6.22.

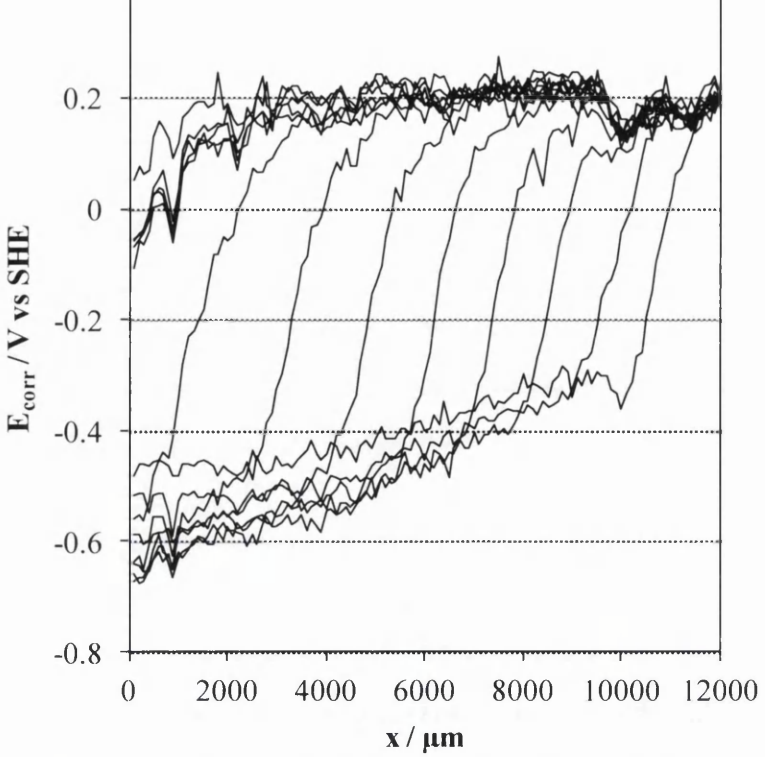

Fig 6.21 Plot of time-dependent E_{corr} vs. distance profiles for a 10 µm PVB coating applied over a 1 µm PEDOT:PSS layer on iron initiated at a defect with 5%$NaCl_{(aq)}$ electrolyte shown at hourly intervals from 0h (left) to 12h (right).

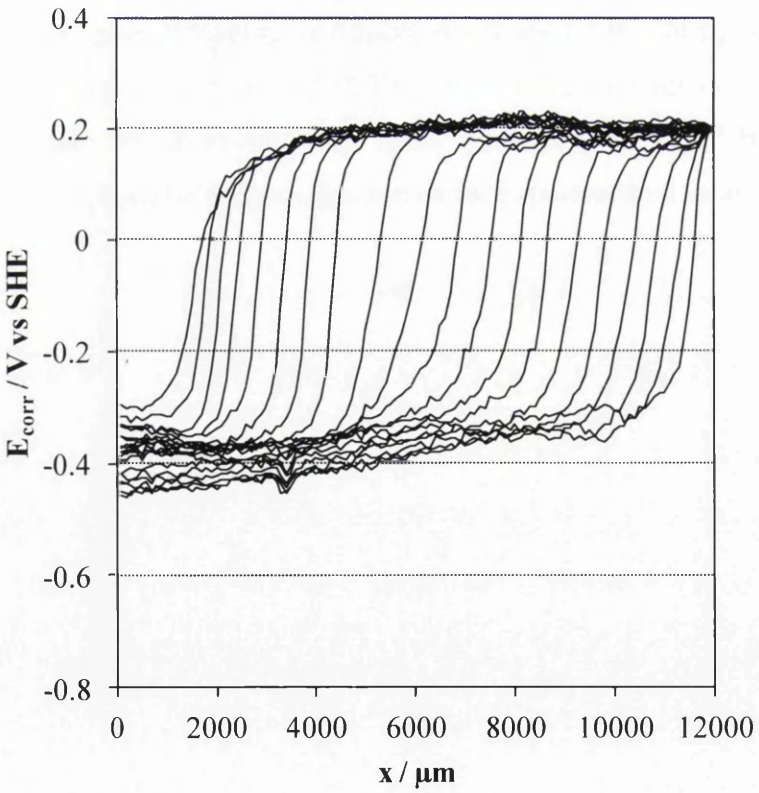

Fig 6.22 Plot of time-dependent E_{corr} vs. distance profiles for a 10 µm PVB coating applied over a 5 µm PEDOT:PSS layer on iron initiated at a defect with 5% $NaCl_{(aq)}$ electrolyte shown at hourly intervals from 4h (left) to 24h (right).

The delamination kinetics of the three experiments are summarised in fig 6.23 which shows a plot of x_{del} vs. (t_{del} - t_i). It can be observed that delamination kinetics remain parabolic meaning that Na^+ cation migration remains the rate limiting process. The delamination rates (k_{del}) for each experiment are listed in Table 6.3. This shows that, where a 5 μm PEDOT:PSS layer is present, the delamination rate increases by ~33% in comparison with the control sample but, even more substantially, the presence of a 1 μm PEDOT:PSS layer increases the delamination rate by ~ 167, albeit with a slightly prolonged initiation time %.

Fig 6.24 shows photographic images of a typical Stratmann cell set up for the current experiment. An iron surface coated in PEDOT:PSS at a thickness of 1 μm and over-coated with PVB at a thickness of 10 μm is shown (a) before the addition of electrolyte (b) after exposure to 95% rh over a period of 24 h where delamination was initiated with 5% wt/v aqueous NaCl. An area of darker blue can be observed in both cases where delamination has occurred and electrolyte has ingressed underneath the coating. Fig 6.25 (a) and (b) show photpgraphic images where the PVB coating has been peeled back after the experiment for layers of PEDOT:PSS at thicknesses of 1 μm and 5 μm respectively. It can be observed that, upon removal of the PVB coating, the PEDOT:PSS has also been lifted from the iron surface and attached to the PVB coating.

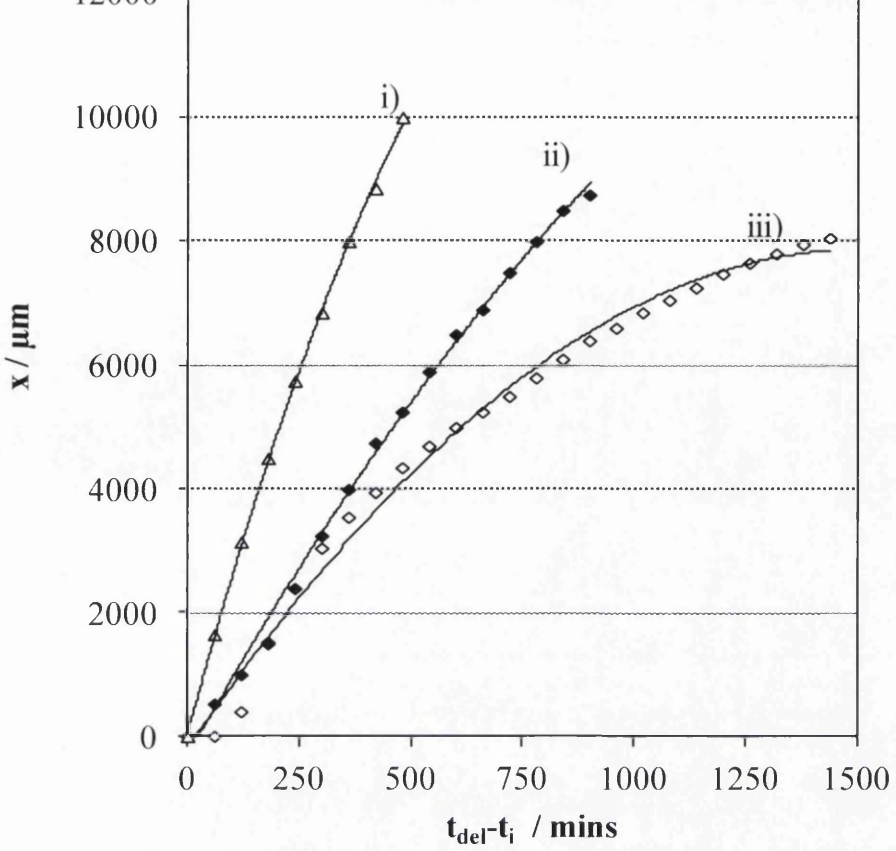

Fig 6.23 Delamination distance (x) plotted as a function of time ($t_{del} - t_i$) for unpigmented PVB coatings where the defect electrolyte is 5% NaCl (aq) and layers of PEDOT:PSS have been applied directly to the iron substrate at a thickness of i) 1 µm ii) 5 µm and iii) no PEDOT:PSS layer is present.

Table 6.3 Values of the delamination rate (k_{del}) and time to delamination determined for PVB coatings applied over a PEDOT :PSS layer of various thicknesses on an iron substrate

PEDOT:PSS layer thickness (µm)	k_{del} (µm.min)	k_{del} change (%)	t_i (mins)
0	7.5	0	0
1	20	167	300
5	10	33	120

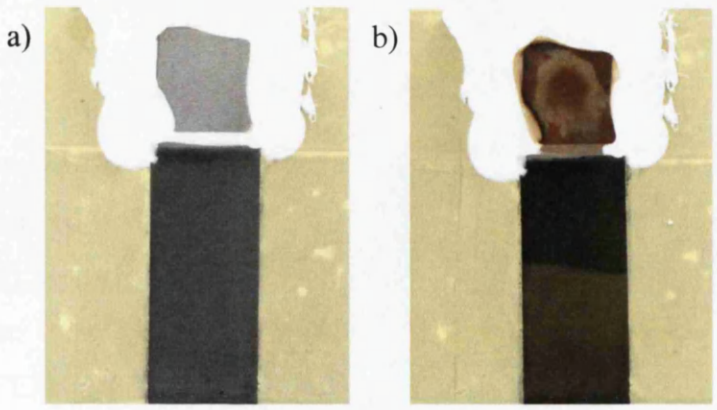

Fig. 6.24 Photographic images to show a Stratmann cell set up for an iron surface coated in PEDOT:PSS at a thickness of 1 µm over coated with PVB at a thickness of 10 µm (a) before the addition of electrolyte (b) after exposure to 93% r.h. over a period of 24 h where delamination was initiated with 5% wt/v aqueous NaCl.

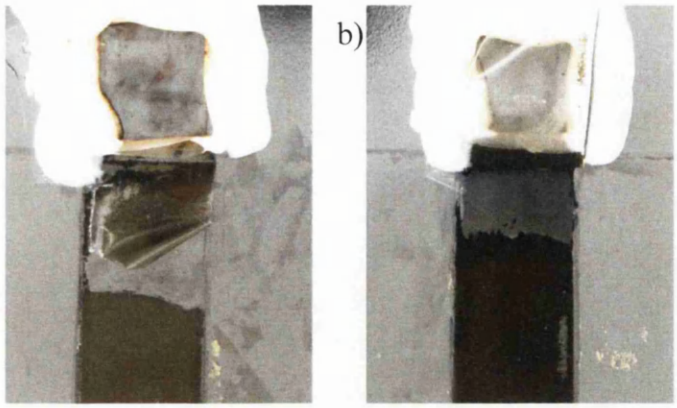

Fig. 6.25 Photographic images to show a Stratmann cell set up for an iron surface coated in PEDOT:PSS at a thickness of a) 1 μm and b) 5 μm where, in both cases, a 10 μm PVB coating has been peeled back. Both sample have been exposed to 93% r.h. for a period of 24 h and delamination was initiated with 5% wt/v aqueous NaCl.

As in the previous section, the acceleration of delamination, can be attributed to an accelerated reduction process caused by high cation mobility in a reduced polymer that becomes an "autobahn" for fast cation transport with the progression of the delamination frontier. Accelerated cation transport is thought to be promoted by high conductivity resulting from extended percolation networks of the conducting polymer.

6.3.6 Filiform corrosion on a PVB-coated iron surface with a PEDOT:PSS under-layer

In the current section filiform corrosion experiments were carried out where iron was coated in PEDOT:PSS at thickness of 1 μm or 5 μm and then over coated with PVB at a thickness of ca. 10 μm. FFC was then initiated by applying 0.005 M $FeCl_2$ to a scribed defect 10 mm in length. FFC was initiated both directly onto PVB coated iron where a PEDOT:PSS layer was present (6.26[a-b]) and also onto PVB coated on bare iron in a location parallel to, and 2 mm away from, a region coated with PEDOT:PSS (6.26 [c-d]). Samples were then held in an environment chamber at 95% rh for a period of four weeks. It was found that, on a substrate with a 1 μm thick layer of PEDOT:PSS, FFC initiation was greatly reduced in comparison to that initiated on PVB-coated bare iron (6.26 [c-d]). Furthermore, propagation of those filaments that did initiate can be seen to be extremely limited. Where filaments from the bare iron surface reach the PEDOT:PSS coated surface in fig 6.26 [a-b] it can be seen that, in most cases, filaments turn away from this layer. The same can be observed in fig 6.27 [a-b] where FFC filaments come into contact with a 5 μm layer of PEDOT:PSS. In this instance no penetration into this region occurred at all over the four-week experimental period.

Furthermore, no filament propagation occurred at all from the few initiation sites that formed on the PEDOT:PSS layer shown in fig 27.x [c-d].

It was first reported by Ruggieri and Beck that, upon coming into contact with the filament tail made of dry, porous corrosion product, a propagating filament head will not cross over this area and will instead change direction [21]. Williams et al carried out SKP measurements over a surface of propagating FFC filaments on an iron surface and recorded values of ca. +0.15 V vs. SHE in the filament tails [22]. In the current study SKP experiments were carried out where an iron surface coated with 10 μm PVB over a 5 μm PEDOT:PSS layer and was scanned every five hours over a period of one week in an environment chamber held at a constant rh of 95% as in the standard FFC experiments. The results are given in fig 6.28 where it can be observed that E_{intact} gradually increases to values more positive than that of a bare iron surface in the same conditions.

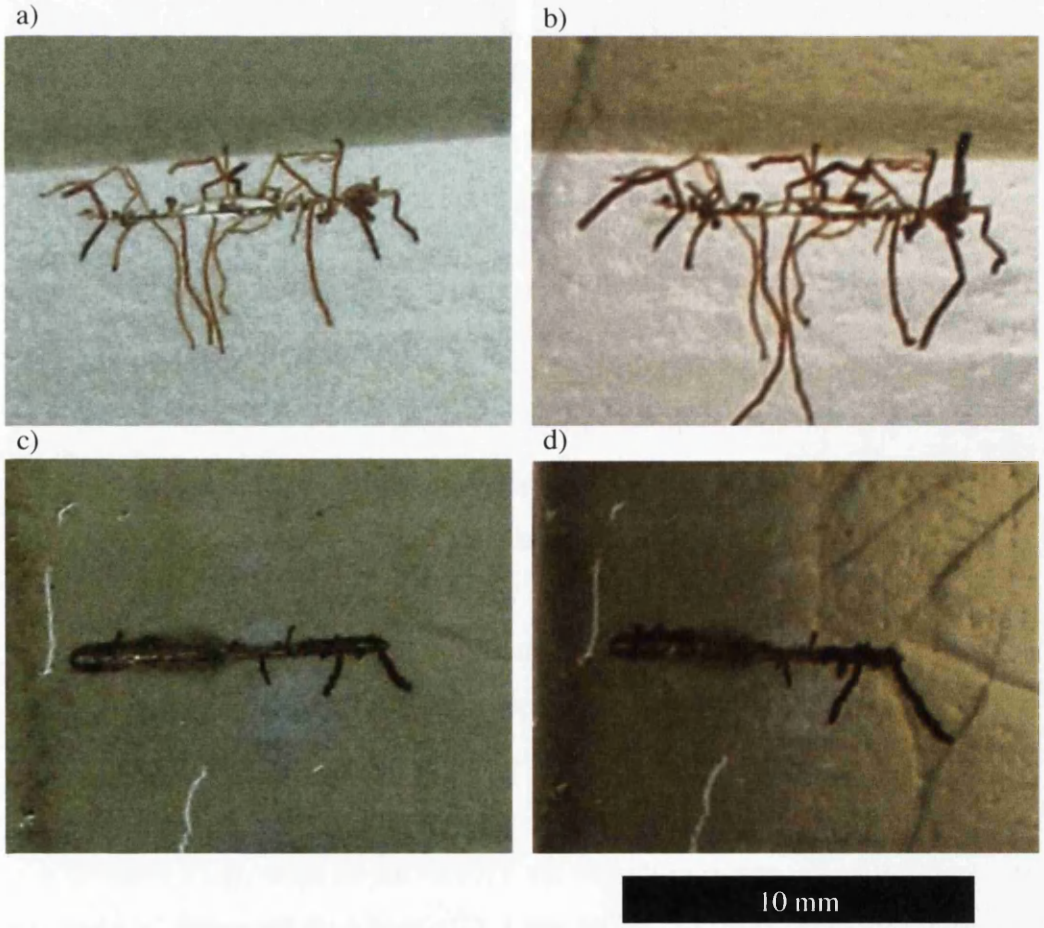

Fig 6.26 Photographic images showing FFC on a 10 μm thick PVB coated iron surface at two weeks (a and c) and four weeks (b and d) after initiation with 0.005 M $FeCl_2$ where samples have been held in an environment chamber at 95% r.h. Images a) and b) shows a defect made next to a 1 μm layer of PEDOT:PSS. Images c) and d) show a defect made directly over a layer of 1 μm PEDOT:PSS.

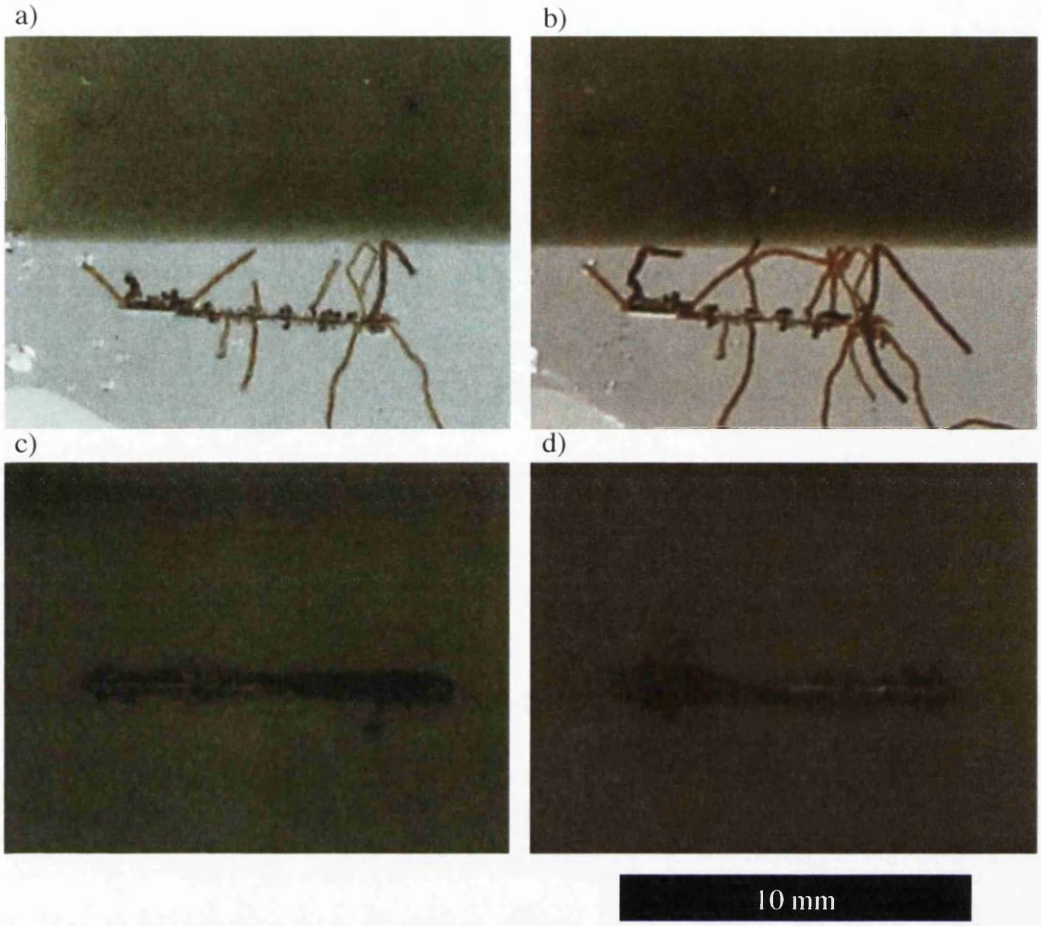

Fig 6.27 Photographic images showing FFC on a 10 μm thick PVB coated iron surface at two weeks (a and c) and four weeks (b and d) after initiation with 0.005 M $FeCl_2$ where samples have been held in an environment chamber at 95% r.h. Images a) and b) shows a defect made next to a 5 μm layer of PEDOT. Images c) and d) show a defect made directly over a layer of 5 μm PEDOT:PSS.

6.4 Conclusions

The aims of the current Chapter were, firstly, to use in-situ SKP to measure the Volta potential differences of various bare and PEDOT:PSS coated metal surface to identify instances where a reaction may be taking place at the metal-PEDOT:PSS interface. Secondly, an investigation into any corrosion protection capability offered by PEDOT:PSS coatings applied to iron and hot dip galvanized (HDG) steel surfaces was carried out. Evaluation was with regards to protection against cathodic delamination and, for iron, anodic disbondment in the form of filiform corrosion (FFC).

A consistent E_{intact} value of ca. -0.15 V vs. SHE was observed where PEDOT:PSS was applied at a threshold thickness of ≥ 3 μm on Ni, Al, Mg, Zn. On Fe a value tending towards ca. -0.15 V vs. SHE was observed. It is suggested that is derived from the formation of a certain quantity of $PEDOT:PSS_{(red)}$ arising because the $PEDOT:PSS_{(ox)}$ is

capable of oxidizing the metal surface in these cases. No consistent E_{intact} values were observed for the PEDOT:PSS-coated 'noble' metals, e.g. Pt, Ag and Cu, and this was attributed to the fact that no redox reaction with PEDOT:$PSS_{(ox)}$ was established. In such a case the PEDOT:PSS coating remains fully oxidized and the [PEDOT:$PSS_{(ox)}$]/[PEDOT:$PSS_{(red)}$] ratio is large, resulting in potentials that are consistently higher than E^{o}[PEDOT:$PSS_{(ox)}$]/[PEDOT:$PSS_{(red)}$]. An oxide layer was observed on the surface of Al and Mg when a PEDOT:PSS layer was removed after one week in 95% rh. Furthermore, the cyclic re-oxidation of PEDOT:PSS on an Al surface was demonstrated.

Experiments were carried out to determine the inhibitory properties of a PEDOT:PSS layer, applied at various thicknesses, to HDG steel and iron substrates. The delamination of a PVB layer, coated over the PEDOT:PSS layer, was studied. The acceleration of cathodic disbondment was observed in all cases when compared to a control experiment. Rohwerder et el reported previously that, intrinsically conducting polymers (ICPs) are suitable for corrosion protection only by the prevention of extended percolation networks in the polymer coating [23]. For PEDOT:PSS to provide effective inhibition of cathodic disbondment it may be needed to be electrochemically reduced in a cation containing solution, such as cerium chloride, after casting on the relevant substrate. However, a PEDOT:PSS layer under a PVB coating was found to be highly effective for the inhibition of filiform corrosion (FFC).

6.5 References

[1] W.-Y. Chou, S.-T. Lin, H.-L. Cheng, M.-H. Chang, H.-R. Guo, T.-C. Wen, Y.-S. Mai, J.-B. Horng, C.-W. Kuo, F.-C. Tang, C.-C. Liao, and C.-L. Chiu, "Polymer light-emitting diodes with thermal inkjet printed poly(3,4-ethylenedioxythiophene):polystyrenesulfonate as transparent anode," *Thin Solid Films*, vol. 515, no. 7–8, pp. 3718–3723, Feb. 2007.

[2] H. C. Neitzert, M. Ferrara, a. Rubino, S. Concilio, P. Iannelli, P. Vacca, L. Ferrara, and C. Minarini, "Monitoring of the initial degradation of oxadiazole based blue OLED's," *J. Non. Cryst. Solids*, vol. 352, no. 9–20, pp. 1695–1699, Jun. 2006.

[3] C. J. M. Emmott, A. Urbina, and J. Nelson, "Environmental and economic assessment of ITO-free electrodes for organic solar cells," *Sol. Energy Mater. Sol. Cells*, vol. 97, pp. 14–21, Feb. 2012.

[4] Y.-M. Xiao, J.-Y. Lin, J.-H. Wu, S.-Y. Tai, and G.-T. Yue, "Pulse potentiostatic electropolymerization of high performance PEDOT counter electrodes for Pt-free dye-sensitized solar cells," *Electrochim. Acta*, vol. 83, pp. 221–226, Nov. 2012.

[5] H. Sakamoto, S. Igarashi, M. Uchida, K. Niume, and M. Nagai, "Highly efficient all solid state dye-sensitized solar cells by the specific interaction of CuI with NCS groups II. Enhancement of the photovoltaic characteristics," *Org. Electron.*, vol. 13, no. 3, pp. 514–518, Mar. 2012.

[6] E. Tamburri, V. Guglielmotti, S. Orlanducci, and M. L. Terranova, "Structure and I2/I− redox catalytic behaviour of PEDOT–PSS films electropolymerized in aqueous medium: Implications for convenient counter electrodes in DSSC," *Inorganica Chim. Acta*, vol. 377, no. 1, pp. 170–176, Nov. 2011.

[7] J. Weickert, H. Sun, C. Palumbiny, H. C. Hesse, and L. Schmidt-mende, "Solar Energy Materials & Solar Cells Spray-deposited PEDOT : PSS for inverted organic solar cells," *Sol. Energy Mater. Sol. Cells*, vol. 94, no. 12, pp. 2371–2374, 2010.

[8] S. a. Mauger, L. Chang, C. W. Rochester, and A. J. Moulé, "Directional dependence of electron blocking in PEDOT:PSS," *Org. Electron.*, vol. 13, no. 11, pp. 2747–2756, Nov. 2012.

[9] F. Lasagni, J. L. Hendricks, C. M. Shaw, D. Yuan, D. C. Martin, and S. Das, "Applied Surface Science Direct laser interference patterning of poly (3 , 4-ethylene dioxythiophene) - poly (styrene sulfonate) (PEDOT-PSS) thin films," vol. 255, pp. 9186–9192, 2009.

[10] G. Williams and H. N. McMurray, "Factors Affecting Acid-Base Stability of the Interface Between Polyaniline Emeraldine Salt and Oxide Covered Metal," *Electrochem. Solid-State Lett.*, vol. 8, no. 9, p. B42, 2005.

[11] M. Rohwerder, S. Isik-Uppenkamp, and C. a. Amarnath, "Application of the Kelvin Probe method for screening the interfacial reactivity of conducting polymer based coatings for corrosion protection," *Electrochim. Acta*, vol. 56, no. 4, pp. 1889–1893, Jan. 2011.

[12] B. Wessling, "Corrosion prevention with an organic metal (polyaniline): Surface ennobling, passivation, corrosion test results," *Mater. Corros. und Korrosion*, vol. 47, no. 8, pp. 439–445, Aug. 1996.

[13] C. Ocampo, E. Armelin, F. Liesa, C. Alemán, X. Ramis, and J. I. Iribarren, "Application of a polythiophene derivative as anticorrosive additive for paints," *Prog. Org. Coatings*, vol. 53, no. 3, pp. 217–224, Jul. 2005.

[14] G. Williams and H. N. McMurray, "Chromate Inhibition of Corrosion-Driven Organic Coating Delamination Studied Using a Scanning Kelvin Probe Technique," *J. Electrochem. Soc.*, vol. 148, no. 10, p. B377, Oct. 2001.

[15] G. Williams, H. N. McMurray, and M. J. Loveridge, "Inhibition of corrosion-driven organic coating disbondment on galvanised steel by smart release group II and Zn(II)-exchanged bentonite pigments," *Electrochim. Acta*, vol. 55, no. 5, pp. 1740–1748, Feb. 2010.

[16] G. Williams, S. Geary, and H. N. McMurray, "Smart release corrosion inhibitor pigments based on organic ion-exchange resins," *Corros. Sci.*, vol. 57, pp. 139–147, Apr. 2012.

[17] G. Williams and H. N. McMurray, "Chromate Inhibition of Corrosion-Driven Organic Coating Delamination Studied Using a Scanning Kelvin Probe Technique," *J. Electrochem. Soc.*, vol. 148, no. 10, p. B377, 2001.

[18] W. Fürbeth and M. Stratmann, "Scanning Kelvinprobe investigations on the delamination of polymeric coatings from metallic surfaces," *Prog. Org. Coatings*, vol. 39, no. 1, pp. 23–29, Aug. 2000.

[19] L. A, S. H, H. K, and S. M, "The delamination of polymeric coatings from steel Part 2] Effect of the oxygen partial pressure on the delamination reaction and current distribution at the metal:polymer interface," *Corros. Sci.*, vol. 41, pp. 599–620, 1999.

[20] L. D. Freedman and G. O. Doak, "No Title," *Chem Rev*, vol. 57, no. 479, 1957.

[21] R. Ruggeri and T. Beck, "An analysis of Mass Transfer in Filiform Corrosion. Corrosion," in *NACE*, 1983, p. 39: 452.

[22] G. Williams and H. N. Mcmurray, "The mechanism of group (I) chloride initiated filiform corrosion on iron," *Electrochem. commun.*, vol. 5, pp. 871–877, 2003.

[23] M. Rohwerder, L. M. Duc, and a. Michalik, "In situ investigation of corrosion localised at the buried interface between metal and conducting polymer based composite coatings," *Electrochim. Acta*, vol. 54, no. 25, pp. 6075–6081, Oct. 2009.

Chapter Seven.

An alternative testing technique for corrosion protection by commercial thin organic coatings.

7.1 Introduction

The aim of the current chapter is to assess the viability of alternative corrosion testing techniques to be employed as complimentary tests to industry standard atmospheric corrosion tests. The potential of the in-situ scanning vibrating electrode technique (SVET) and time-lapse photography is assessed for implementation into the industrial research and development process for a new thin organic coating (TOC) system for cold reduced (CR) steel. Atmospheric corrosion testing, carried out according to BS 3900 [1] and analysed according to ASTM D610-08 [2], is the current corrosion assessment technique employed by TATA Steel UK for such product development studies; this is fully described in Section 2.7. A typical experimental length for this test is four weeks. The two test methods presented here need to provide reliable and repeatable data that can be produced over shorter time scales i.e. several days.

7.2 Experimental details

7.2.1 Sample preparation

All CR steel samples were received from pilot-line trials coated on one side with a TOC. For all time-lapse photography and SVET experiments, samples were cut into approximately 50 mm x 50 mm coupons with careful attention not to touch the TOC. Samples were then completely masked off using insulating extruded PTFE self-adhesive tape leaving an exposed area of 10 mm x 10 mm.

Samples for atmospheric corrosion testing were prepared as described in Section 2.7.1 according to BS 3900 – Part F2 [1].

7.2.2 Experimental method

All time-lapse photography testing was carried out as described in Section 2.6. In brief, prepared samples were fully immersed in 5% w/v $NaCl_{(aq)}$ electrolyte and photographed every 10 min. Photographic images were then edited and analysed as described in Section 2.6.3.

All SVET testing was carried out as described in Section 2.3. Prepared samples were immersed in 5% w/v $NaCl_{(aq)}$ electrolyte and scans taken every 30 min over a period of 24 h.

All atmospheric corrosion testing was carried out in accordance to BS 3900 – Part F2 [1] as described in Section 2.7.2. Evaluation was then carried out in accordance to ASTM D610-08 [2].

7.3 Results and discussion

7.3.1 Assessment of time-lapse photography and SVET immersion tests for TOCs on CR steel

The current study involves the assessment of two different coatings applied to CR steel on an industrial scale pilot line. Both were water-based coatings of ca. 1 μm dry film thickness (dft). Concerns that the edges of the CR steel strip were not being thoroughly coated were reported during a pilot line trial. Time-lapse photography and SVET were employed to assess:

1. The performance of both coatings with regards to corrosion protection.
2. Any apparent difference in the corrosion protection performance of the coating at the edge of the steel strip in comparison to the coating at the centre of the steel strip for both coating types.

For all experiments a 10 mm x 10 mm sample of each coating type was selected from both the edge and the centre of the steel strip. In all cases samples were fully immersed in 5% w/v $NaCl_{(aq)}$ solution for a period of 24 h. This is summarised in Table 7.1.

Table 7.1 Samples tested using SVET and time-lapse photography

Sample	Position on strip	Coating type
A	edge	1
B	centre	1
C	edge	2
D	centre	2

Time-lapse photography was employed to measure the sample area containing visible corrosion product as a percentage of the whole sample area. Photographic images were taken at 10 min time intervals over the 24 h immersion period. From this, images were selected at four-hourly intervals starting at 0 h immersion time. The corroded area (%) was then measured on each of these images. Corroded area (%) was then plotted with respect to immersion time (h). From this the samples were ranked according to the following:

1. Initial corrosion rate (% area / h) taken over the first 4 h of immersion.
2. Final corroded area (%)

In the experiments carried out using the SVET the samples were scanned on a half hourly basis over the 24 h period. The following could be established for each sample:

1. Profiles of area-averaged, integrated SVET-derived anodic current density vs. time.
2. The intensity and location of local anodes and cathodes.
3. Data for total metal mass loss over the 24 h period from which a ranking order could be established.

The data obtained in the current study will be used to assess the compatibility of time-lapse photography and the SVET for producing consistent quantitative and qualitative results.

7.3.1.1 Time lapse-photography as a technique for the assessment of corrosion performance of TOCs on CR steel

Prior to immersion, no difference in the coating quality was visible to the naked eye between the coated samples selected from the strip edge and the coated samples selected from the centre of the strip. Experiments were carried out in triplicate and representative images are presented in the current Section. Figs 7.1 and 7.2 show a typical selection of images taken throughout the 24 h period at time intervals of 2 h, 3 h, 6 h, 12 h and 24 h after immersion. Images have been selected at these immersion times for the purposes of comparison between the four different samples.

Every image presented in fig 7.1[a - e], representing the immersion tests carried out on Sample A, shows the presence of corrosion product in close proximity to the strip-edge (on the left-hand side of the photographs). The images show that this corrosion product develops over time into a well-defined region of corrosion product. Additional corrosion product on the remainder of the sample (i.e. away from the edge) appears to initiate after ca. 5 h immersion time. It can be observed that this occurs in the vicinity of the pre-corroded region at the strip-edge and spreads to the remainder of the sample area. The photographic images presented in fig 7.1[f - j] show Sample B, which was selected from the centre of the steel strip. Corrosion product can be observed generally on the sample area and can be seen to cover approximately the entire sample area at 24 h.

In contrast, it can be observed in the images given in fig 7.2 [a - e] for Sample C (selected from the edge of the steel strip) that a very faint line of corrosion product is present at the strip-edge. Furthermore, this does not appear to develop further, as with Sample A. Corrosion product can be observed to occur simultaneously elsewhere on the sample. When compared to the images presented in fig 7.2 [f - j], which show the result for Sample D, (selected from the centre of the same steel strip) it appears that wholly similar areas containing corrosion product are present at each time interval, other than the thin line at the strip-edge region shown in Sample C.

The progression of the corroded region with respect to time is plotted in fig 7.3 for all four samples. The corroded region, measured as a percentage of the total sample area, is plotted at 4 h time intervals over a 24 h period. From these plots the initial corrosion rate (corroded area(%) / h), measured for 4 h immersion time, and final corroded area (%) were measured and are summarised in Table 7.2. A performance ranking order, based on initial corrosion rate values, gave B>D>C>A where B displayed the lowest initial corrosion rate. The main performance ranking was order was based on the final corroded area (%)values recorded gave C>D>B>A value where Sample C showed the lowest amount of corrosion product present after 24 h immersion. The results show that, although ranked third, Sample B displayed the slowest initial corrosion rate (% area corroded / h) and, hence, acceleration in the corrosion rate must have occurred after this. Furthermore, the results show that Coating 1 performs better than Coating 2 with respect to corrosion protection.

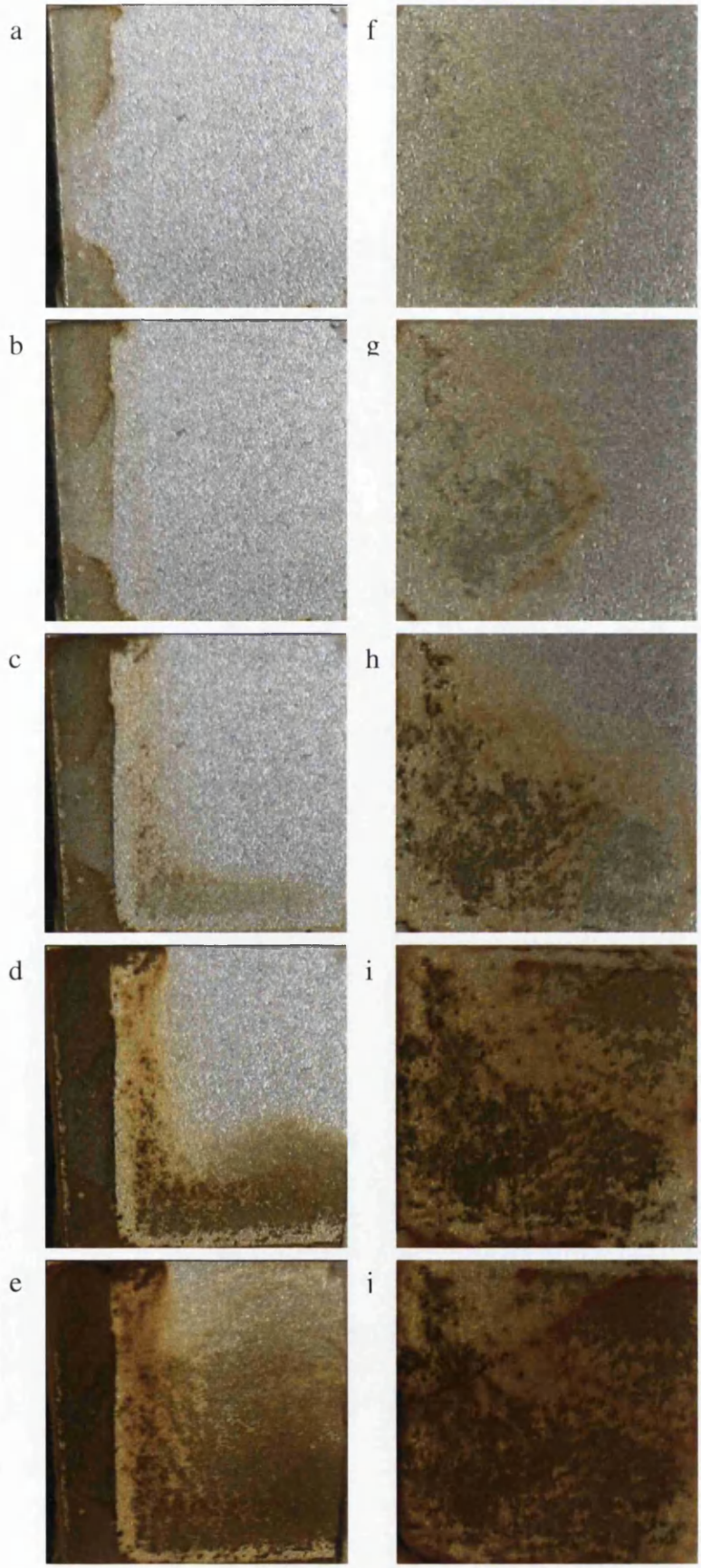

Fig 7.1 Photographic images of organically-coated CR steel fully immersed in 5% $NaCl_{(aq)}$ solution where [a - e] show sample A at immersion times a) 2 h, b) 3 h, c) 6 h, d) 12 h e) 24 h and [f - j] show sample B at immersion times a) 2 h, b) 3 h, c) 6 h, d) 12 h e) 24 h.

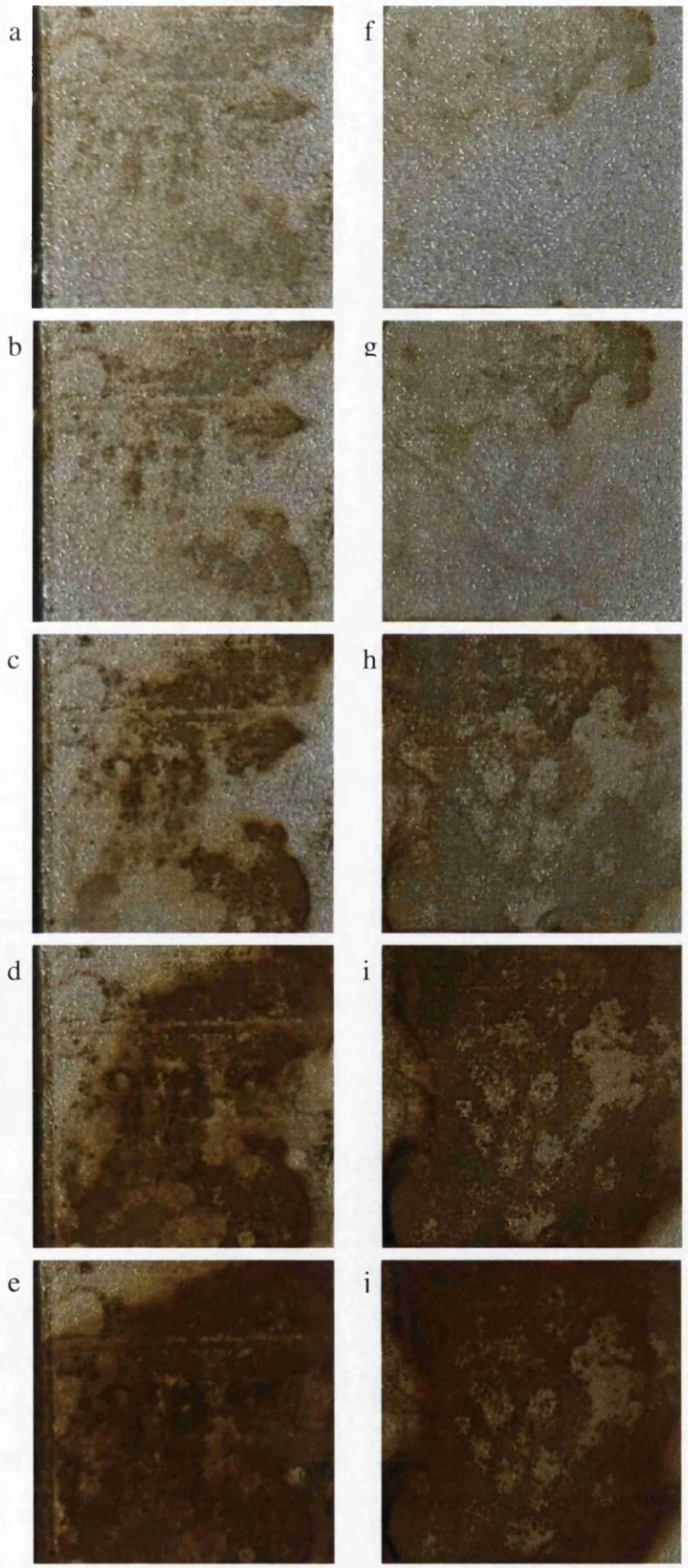

Fig 7.2 Photographic images of organically-coated CR steel fully immersed in 5% $NaCl_{(aq)}$ solution where [a - e] show sample C at immersion times a) 2 h, b) 3 h, c) 6 h, d) 12 h e) 24 h and [f - j] show sample D at immersion times a) 2 h, b) 3 h, c) 6 h, d) 12 h e) 24 h.

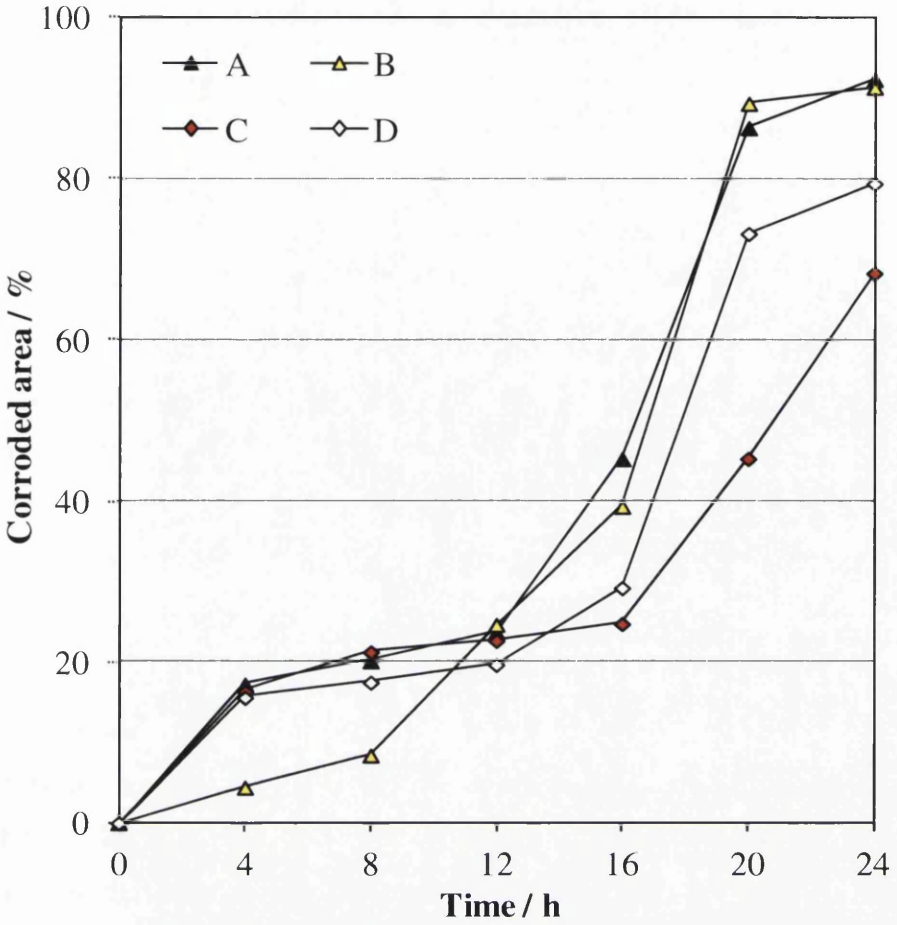

Fig 7.3 Corroded area (%) vs. time (h) plots for Samples A,B,C and D when fully immersed in 5% wt/v $NaCl_{(aq)}$ experimental electrolyte.

Table 7.2 Summary of performance ranking orders obtained from corroded area (%) vs. time data for samples A, B, C and D.

Sample	Initial corrosion rate (%Area corroded / h)	Ranking	Final corroded area (%)	Ranking
A	4.3	4	92	4
B	1.1	1	91	3
C	4.1	3	68	1
D	3.9	2	79	2

7.3.1.2 SVET as a technique for of the assessment of corrosion performance of TOCs on CR steel

The samples listed in Table 7.1 were studied using in-situ SVET in test conditions identical to those of the previous section. Experiments were carried out in triplicate and the results presented here have been selected as the best representation. Samples were scanned every 30 min over a 24 h period. Figs 7.5 - 7.8 show the SVET derived current density surface maps of unpolarised samples A, B, C and D respectively obtained following immersion in aerated 5% w/v $NaCl_{(aq)}$ at times a) 1 h b) 4 h, and c) 12 h. The scaling of the z-axis for all current density surface maps has been normalised to a maximum of 40 Am^{-2} to account for the maximum values recorded for Sample A given

in fig 7.5. This allows visual comparisons to be made between data for each sample. In all figs the photographic image shows the sample after 24 h immersion. The area-averaged anodic current density vs. time profiles for each sample is given in fig 7.9.

It can be observed in fig 7.4, which shows the set of SVET-derived current density surface maps for Sample A, that anodic action initiates at the strip-edge of the sample (the top left edge of the map) and subsequently spreads to the rest of the exposed area. Fig 7.4(c) indicates that by 12 h immersion time, anodic activity does not occur at the sample edge and has relocated to other areas of the sample. The photographic image given in fig 7.4(d) shows substantial corrosion product at the strip-edge of the sample and also on approximately half of the whole sample area. This highlights the fact that, although corrosion product may be visible in a particular area (i.e. the strip edge), it does not mean that anodic activity occurs in this area at all times. This is additional information provided by the SVET that is beyond the scope of time-lapse photography imaging. The results for Sample B (fig 7.5) indicate the occurrence of transient corrosion where anodically active sites are present in different regions on each of the current density surface maps. In each case large areas of non-active sites are also present. The final image shows that corrosion product covers almost the entire surface.

The current density surface maps for Samples C and D shown in figs 7.6 and 7.7 respectively show wholly similar results. For Sample C, which was selected from the strip-edge, anodic activity can initially be observed in this region (shown at the top left hand side of the image map) but this disappears in later scans. For both C and D, transient anodic activity can be observed in the initial scans and an anodic region covering the entire sample area can be observed after 12 h immersion. In both cases the photographic image shows complete coverage with corrosion product.

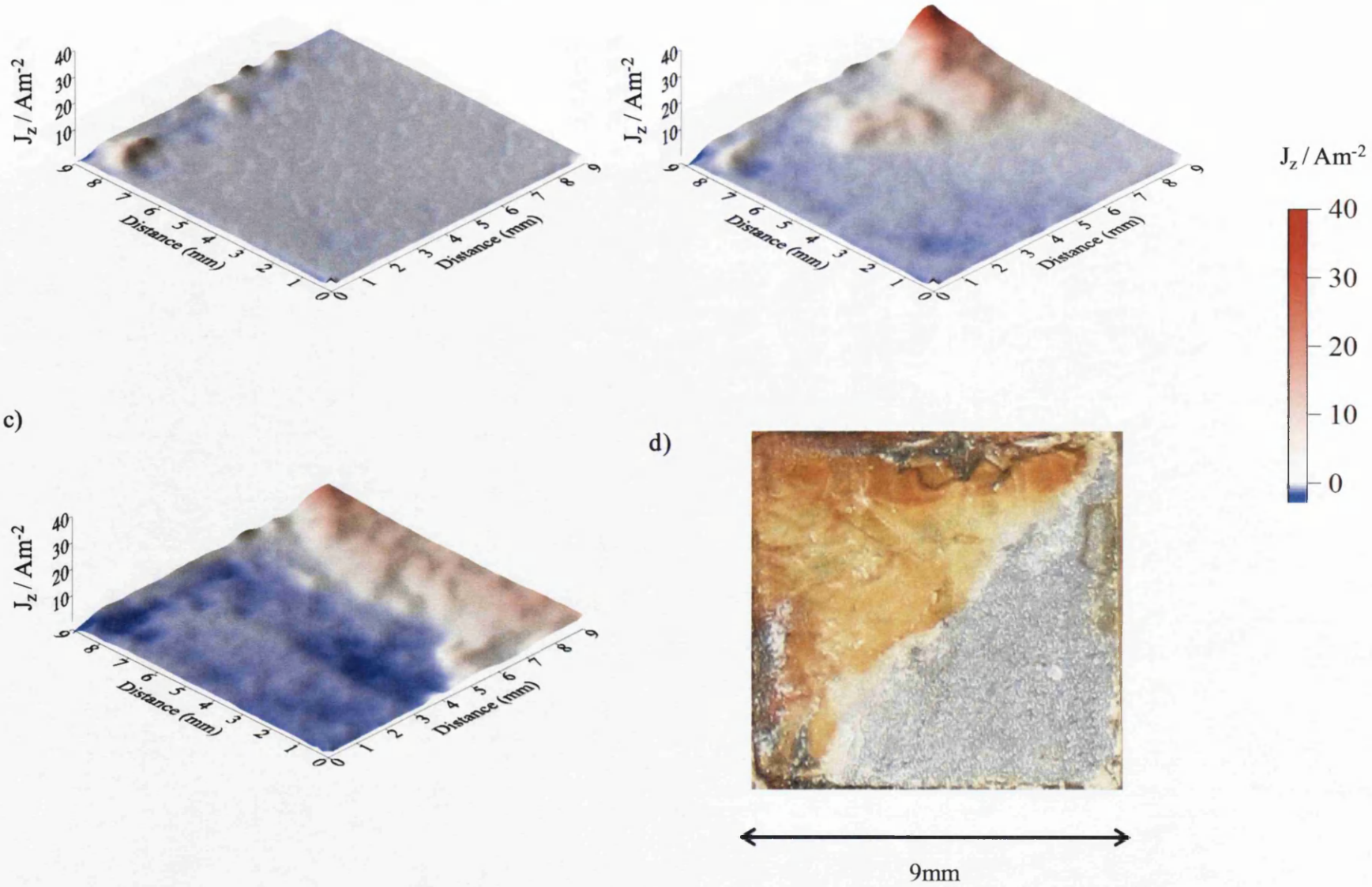

Fig 7.4 SVET derived current density surface map of unpolarised organically coated CR steel (Sample A) obtained following immersion in aerated 5% (w/v) NaCl (aq) at time a) 1h b) 4 h, and c) 12 h where the top left-hand edge is the strip-edge and d) is a photographic image of the sample after 24 h immersion where the strip edge is located on the left vertical side of the image.

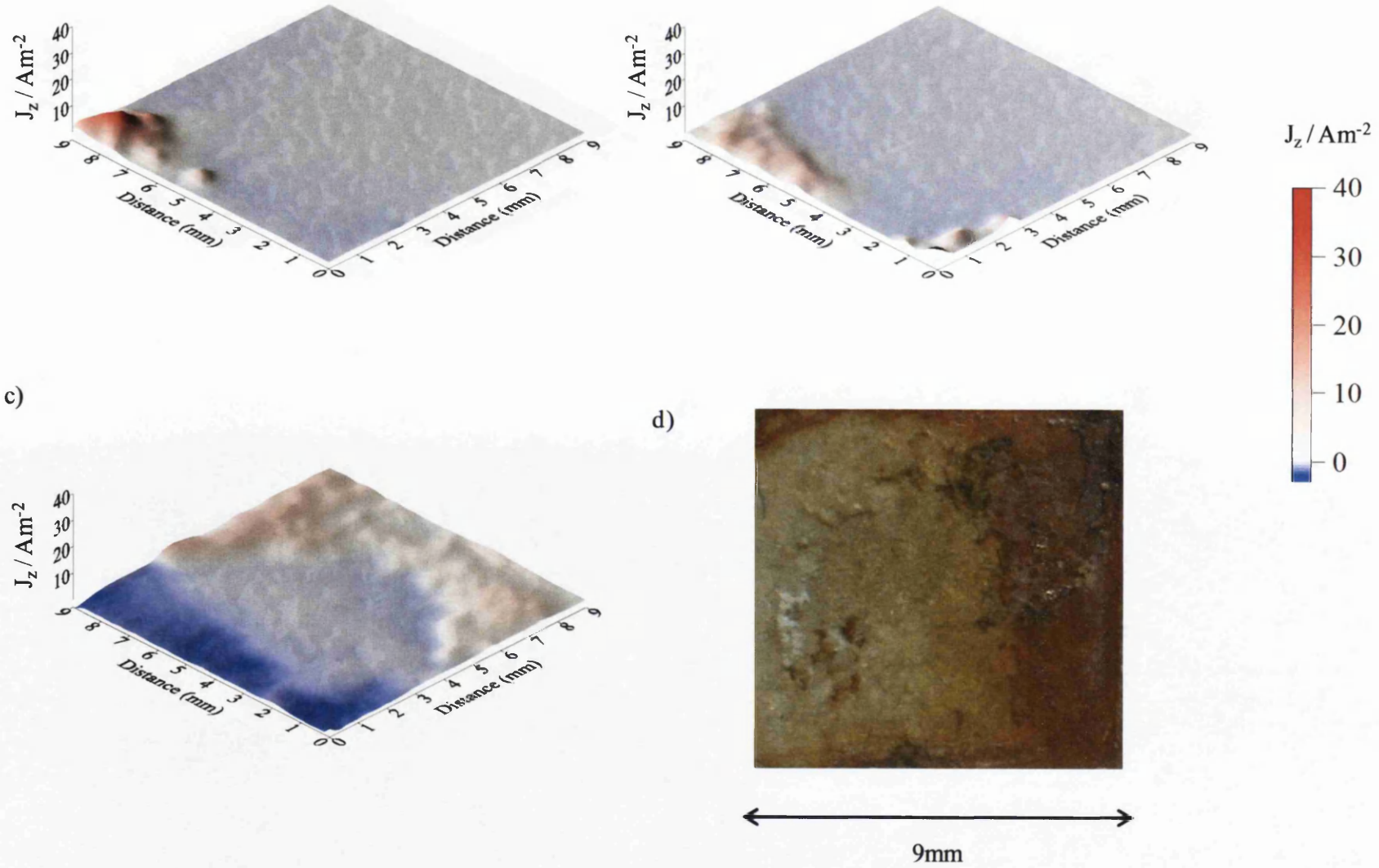

Fig 7.5 SVET derived current density surface map of unpolarised organically coated CR steel (Sample B) obtained following immersion in aerated 5% (w/v) NaCl (aq) at time a) 1h b) 4 h, and c) 12 h and d) is a photographic image of the sample after 24 h immersion.

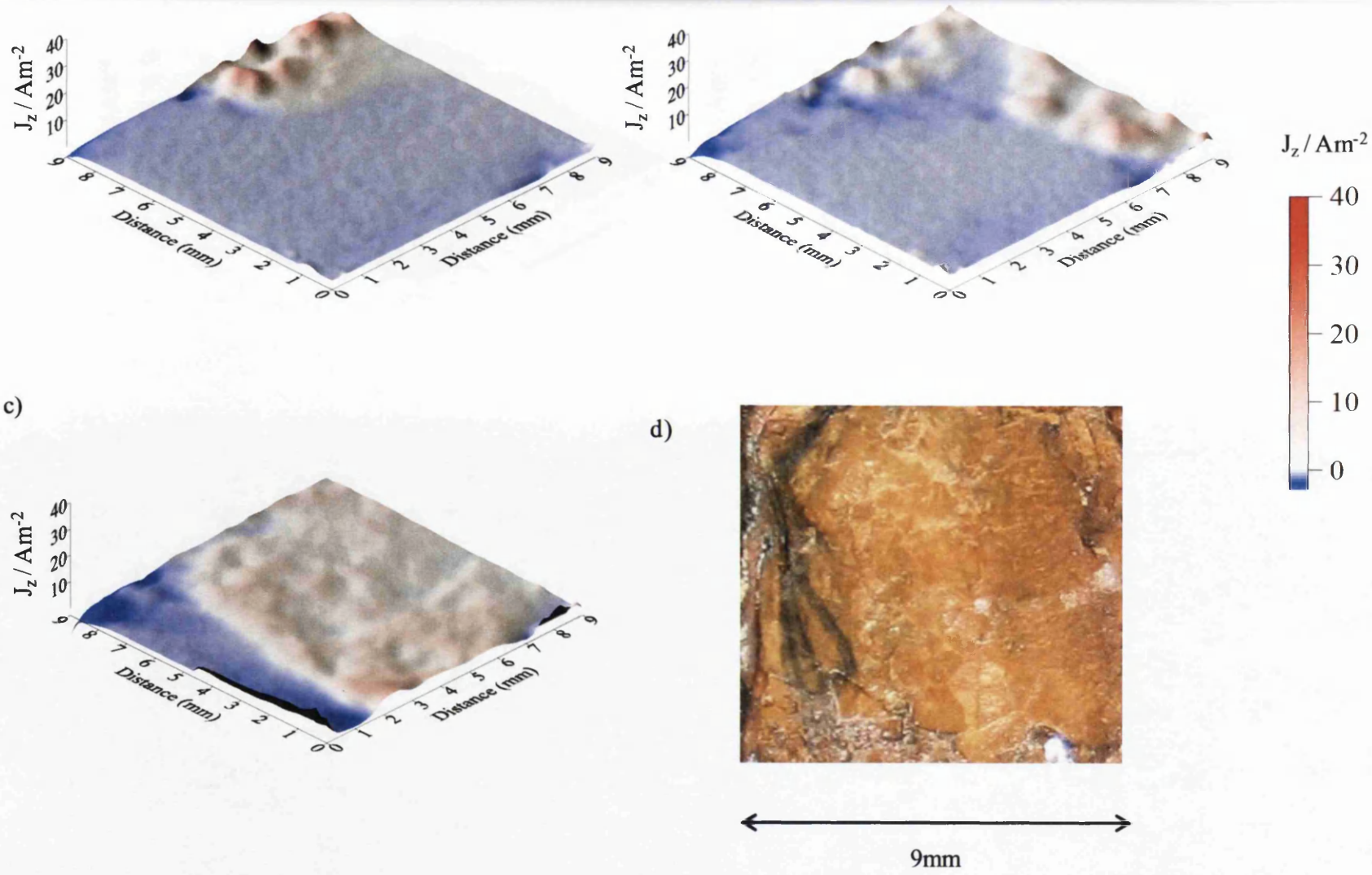

Fig 7.6 SVET derived current density surface map of unpolarised organically coated CR steel (Sample C) obtained following immersion in aerated 5% (w/v) NaCl (aq) at time a) 1h b) 4 h, and c) 12 h where the top left-hand edge is the strip-edge and d) is a photographic image of the sample after 24 h immersion and the strip edge is located on the left vertical side of the image.

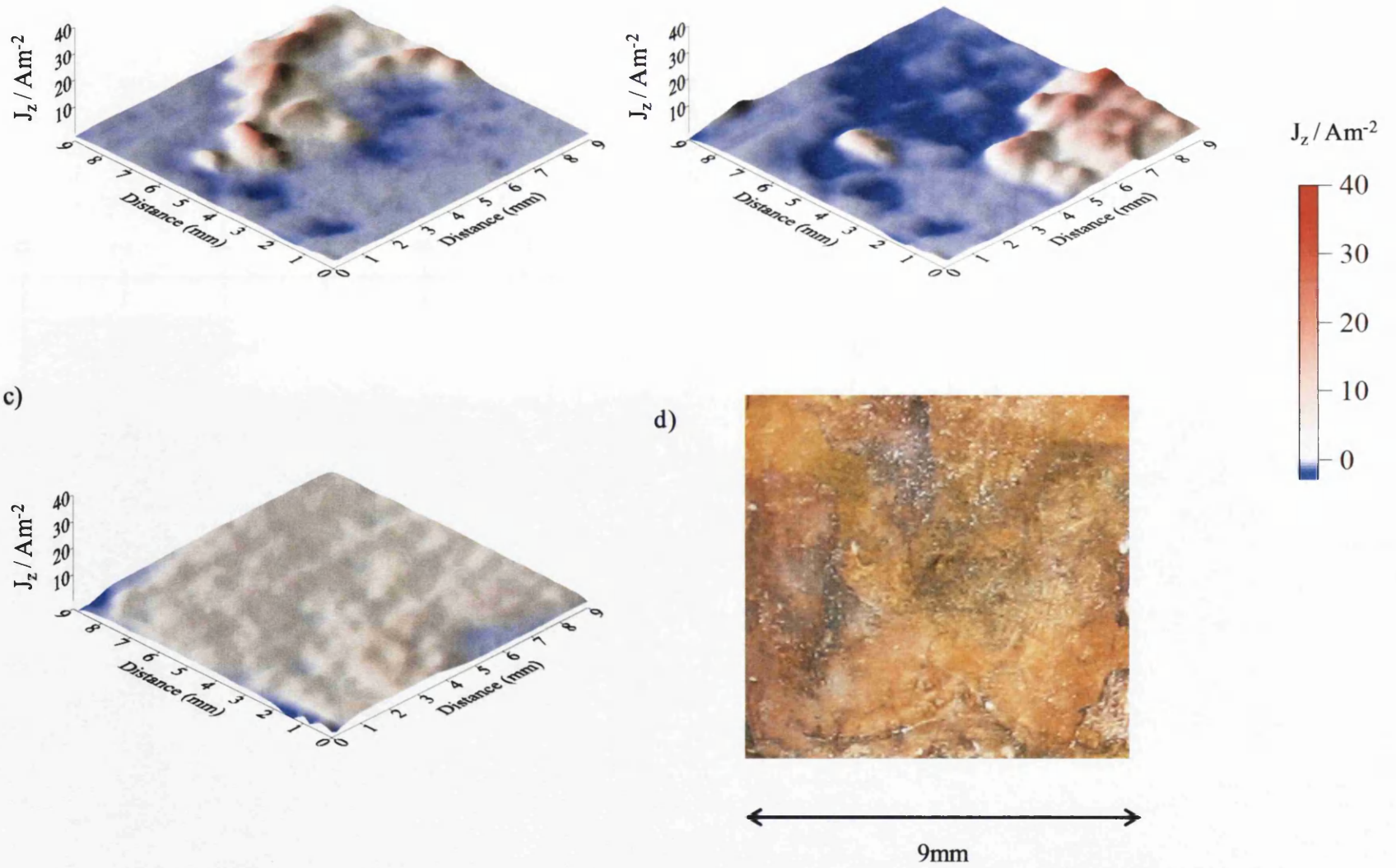

Fig 7.7 SVET derived current density surface map of unpolarised organically coated CR steel (Sample D) obtained following immersion in aerated 5% (w/v) NaCl (aq) at time a) 1h b) 4 h, and c) 12 h and d) is a photographic image of the sample after 24 h immersion.

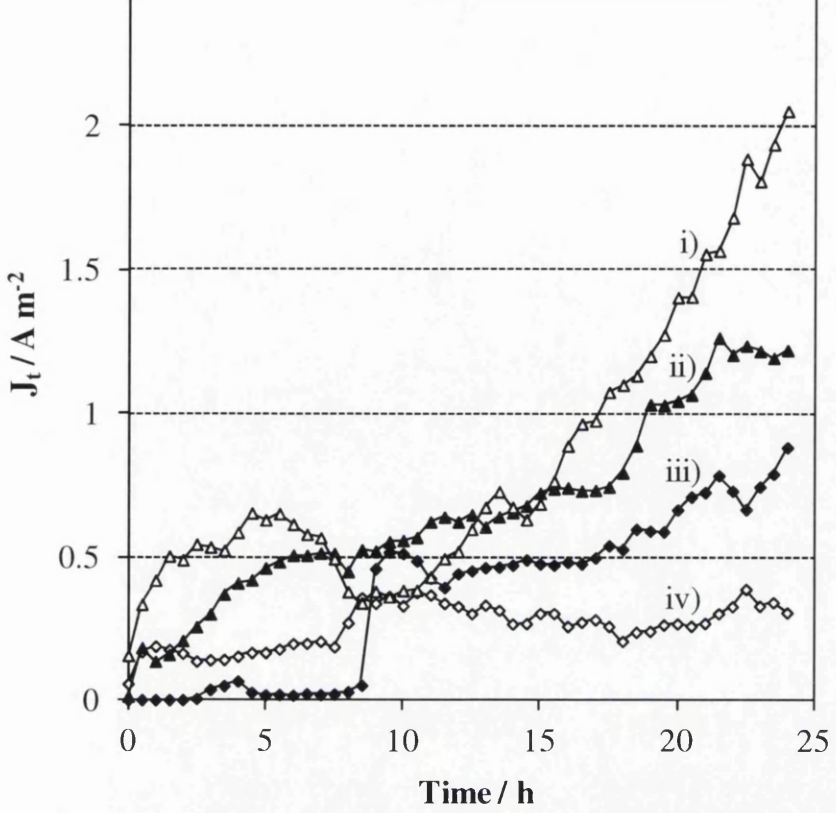

Fig 7.8 Area-averaged anodic current density versus time profiles obtained for samples i) D ii) C iii) A iv) B immersed in aerated 5% (w/v) NaCl (aq)

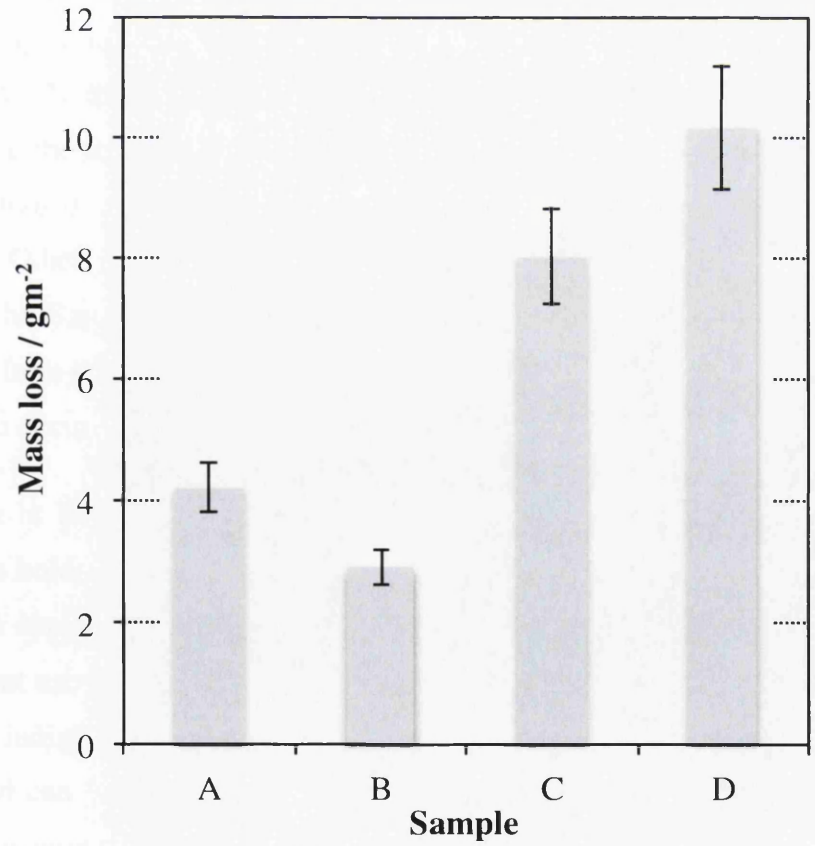

Fig 7.9 Bar chart showing SVET-derived mass loss over 24 h for coated CR samples A – D.

Fig 7.8 shows SVET-derived area-averaged anodic current density versus time profiles obtained for samples A, B, C and D after 24 h immersion in aerated 5% (w/v) $NaCl_{(aq)}$. The subsequent SVET-derived metal mass loss data for each sample is given in the bar chart shown in fig 7.9. A ranking order based on the SVET-derived mass loss data, where Sample B is considered the best performer with regards to corrosion protection, and B>A>C>D. When compared to the performance ranking order established through time-lapse photography, where Sample A was shown to have the least corroded final area and so A>B>D>C, it can be observed that in both cases coating 1 (i.e. Samples A and B) performs better than coating 2 (i.e. Samples C and D).

The current study highlights the major differences between the data obtained from in-situ SVET experiments and time-lapse photography tests. Although time-lapse photography can show the area occupied by corrosion product with respect to time, unlike SVET, it cannot detect where anodic activity is actually occurring at any one time.

In the current scenario time-lapse photography has proven to be highly useful for highlighting areas of poor coating quality, such as was shown at the strip-edge on Sample A. Both time-lapse photography and SVET indicated that corrosion initially occurred at the strip-edge for both coating 1 and coating 2. The time-lapse photography images studied at the strip edge of coating 2 showed only a thin line of corrosion product. Other than this corrosion appeared to progress in a wholly similar manner to that on the Sample selected from the centre of the steel strip. Qualitative results obtained from the SVET seem to be in agreement with this where corrosion activity can be seen to occur in all areas of the sample.

Although in both cases tests are carried out over 24 h, the time-lapse photography technique holds a distinct advantage over the SVET with respect to efficiency. For this particular application all samples (including repeats) may be tested in one single 24 h experiment using one set of equipment. For SVET testing each sample must be carried out in an individual test over 24 h meaning the total time for the entire set of tests to be completed can be many days. The equipment preparation and set-up and subsequent results rendering and analysis required for the SVET takes a substantially longer amount of time and is more complex.

The current study shows the compatibility of time-lapse photography and SVET where quantitative results were wholly similar when ranking the performance of two coatings. Furthermore, qualitatively, time-lapse photography highlighted the initiation point of corrosion product development and the resultant build-up and surface tarnishing effect; any visible coating failure was also recorded. SVET showed wholly similar results when identifying the location of anodic activity initiation points. The SVET provides the additional benefit of mapping the location and intensity of anodic activity at the time of occurrence. It is suggested that, for these test methods to be implemented into a research and development process, time-lapse photography could be used to test every sample and SVET could be employed only in circumstances where specific features and information about actual corrosion activity were required.

7.3.2 Assessment of time-lapse photography in comparison with industry standard atmospheric corrosion testing

The current study assesses the viability of time-lapse photography to be used in conjunction with standard atmospheric corrosion testing for a commercial TOC applied CR steel. Both testing techniques have been employed for a series of samples and a performance ranking order established. For time-lapse photography this is based on the final corroded area (%). For atmospheric corrosion tests this is based on the final grading after four weeks of testing; the grading system is fully explained in Section 2.4. Experiments were carried out on a set of six samples taken from a pilot-line trial where the line speed (m / min), squeegee roll roughness (CAMI grit designation) and pre-heat treatment were variables. Table 7.2 lists the samples and their relevant application method.

Table 7.2 Samples tested using humidity testing and time-lapse photography

Sample	Line speed (m/min)	Pre-heat?	Squeegee (CAMI grit designation)
19	100	Y	80
20	100	N	80
21	200	Y	80
24	100	Y	120
25	100	N	120
28	250	Y	120

7.3.2.1 Assessment of TOCs on CR steel using time lapse-photography

Time-lapse photography tests were carried out (in triplicate) as described in Section 2.4. The total experimental time for all samples was 40 h as one single test and one set of equipment was used for all. Figs 7.10 to 7.15 show a selection of typical photographic images taken throughout the 40 h period where the progression of corrosion product development can be observed with respect to time. These images have been chosen as the best representation out of the three repeat tests. In all samples both pin-point rusting and red rust can be observed. Fig 7.16 gives plots of measured corroded area (%) vs. time. From this, samples can be ranked, with regards to corroded area after the full 40 h testing time, as follows: 20>25>21>19>28>24 where Sample 20 showed the lowest corroded area after 40 h immersion. This is summarised in Table 7.3.

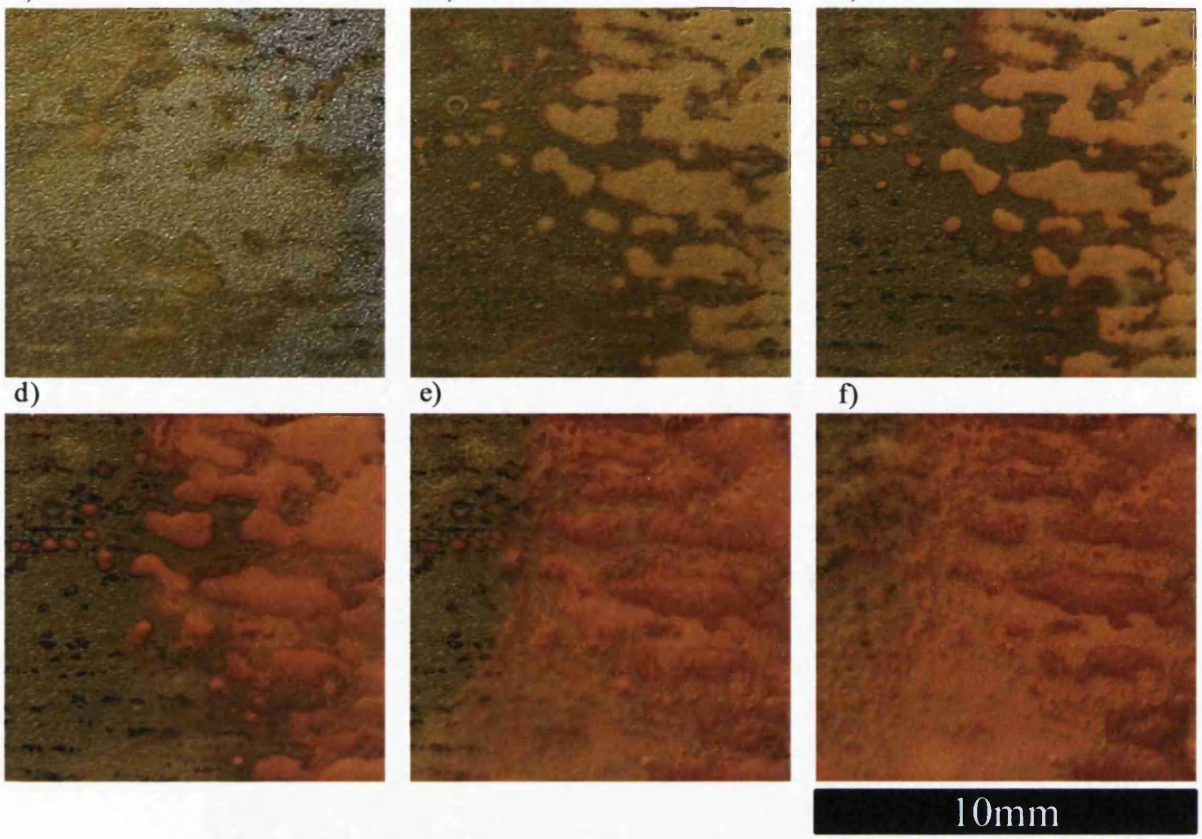

Fig 7.10 Photographic images of Sample 19 organically coated CR steel sample immersed in aerated 5% (w/v) NaCl (aq) at times a) 5 h, b) 8 h, c) 10 h, d) 20 h, e) 30 h and f) 40 h.

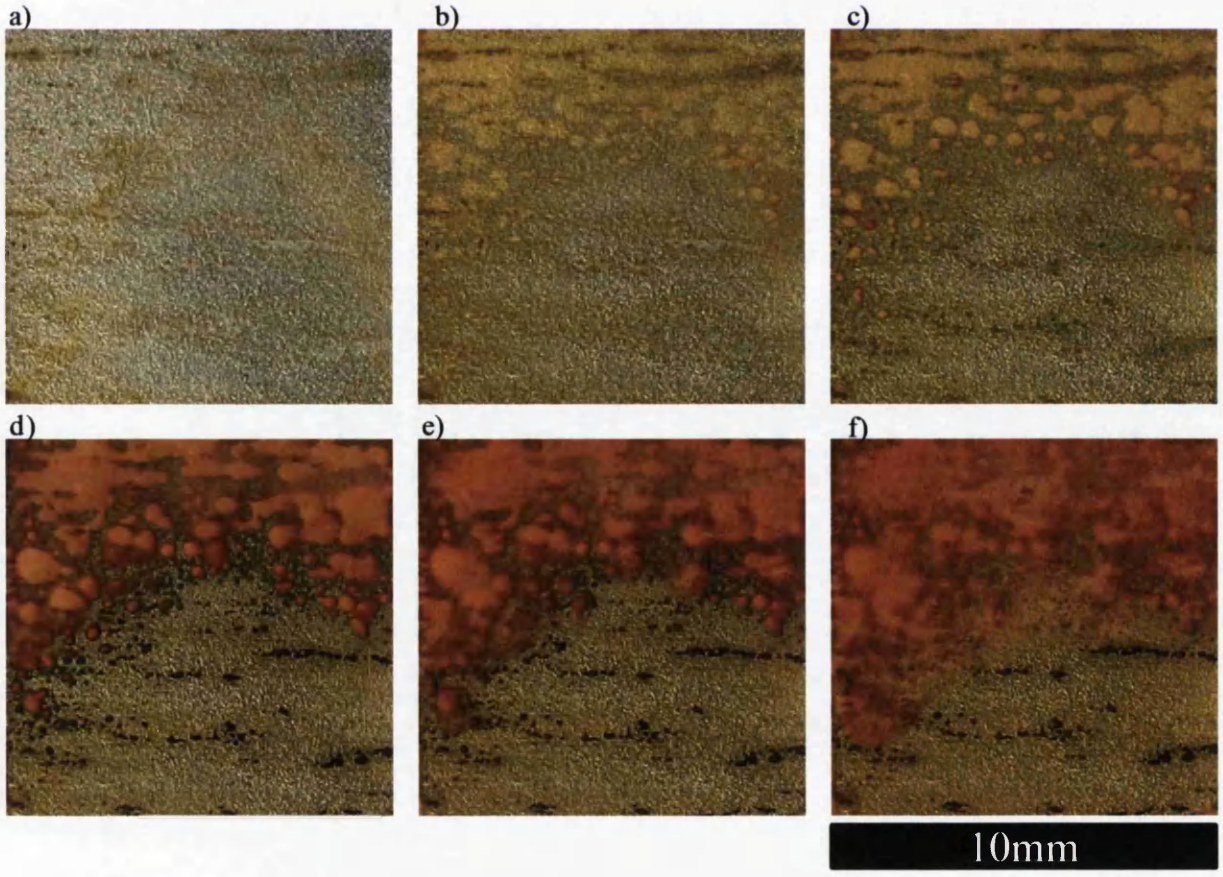

Fig 7.11 Photographic images of Sample 20 organically coated CR steel sample immersed in aerated 5% (w/v) NaCl (aq) at times a) 5 h, b) 8 h, c) 10 h, d) 20 h, e) 30 h and f) 40 h.

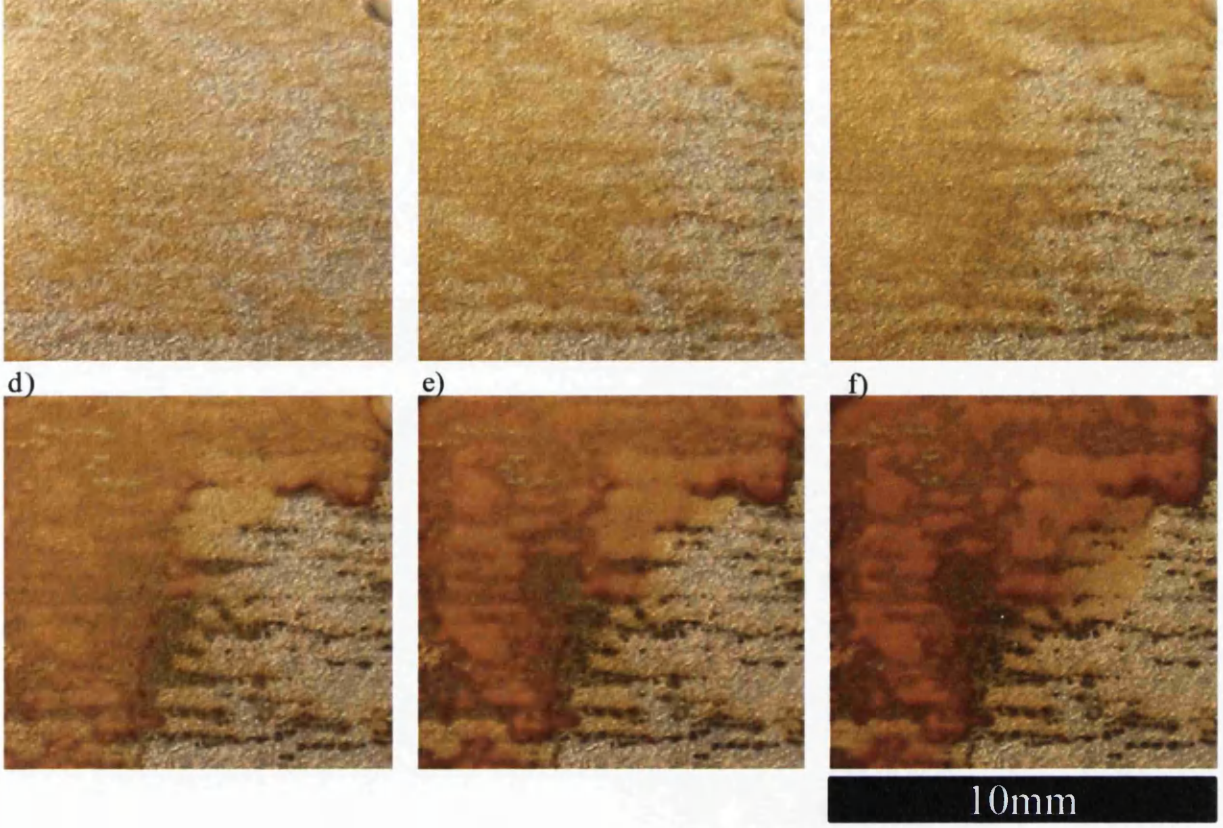

Fig 7.12 Photographic images of Sample 21 organically coated CR steel sample immersed in aerated 5% (w/v) NaCl (aq) at times a) 5 h, b) 8 h, c) 10 h, d) 20 h, e) 30 h and f) 40 h.

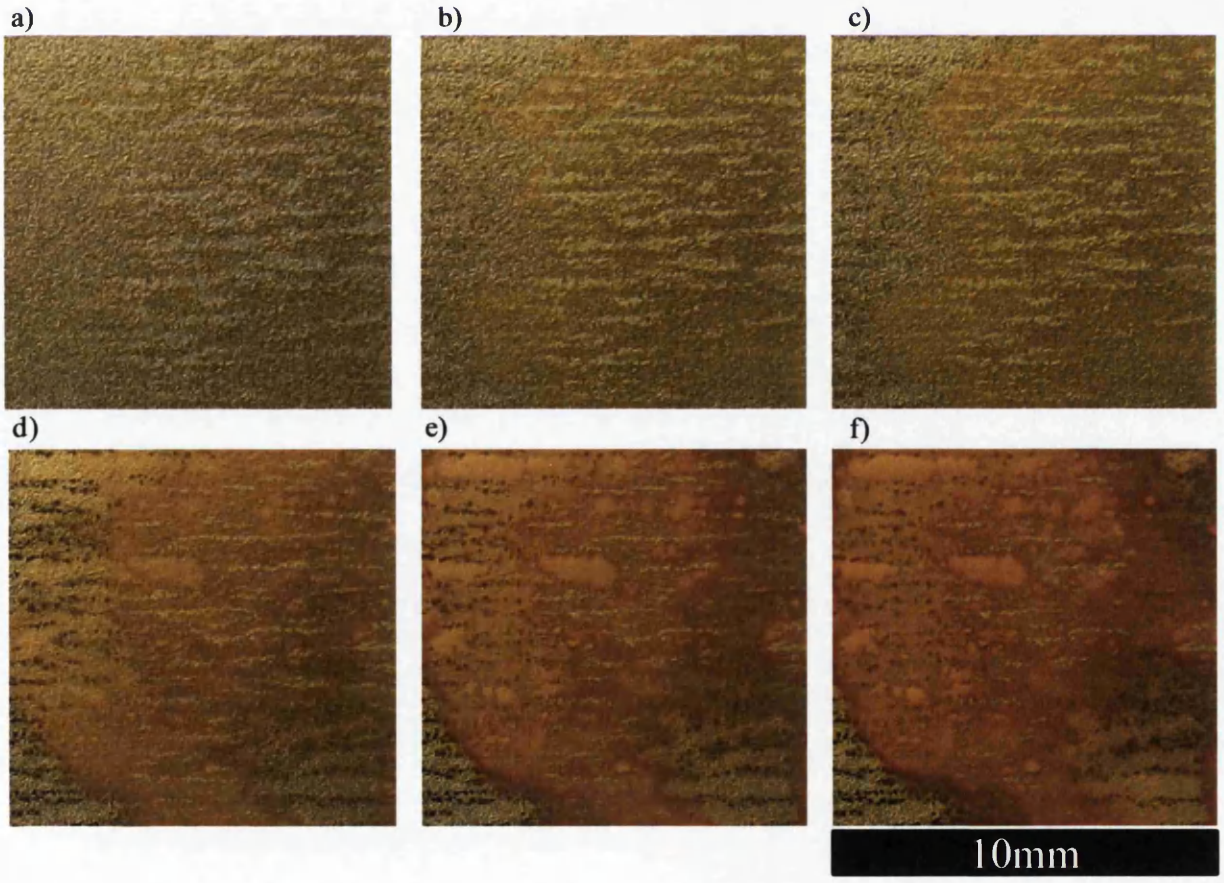

Fig 7.13 Photographic images of Sample 24 organically coated CR steel sample immersed in aerated 5% (w/v) NaCl (aq) at times a) 5 h, b) 8 h, c) 10 h, d) 20 h, e) 30 h and f) 40 h.

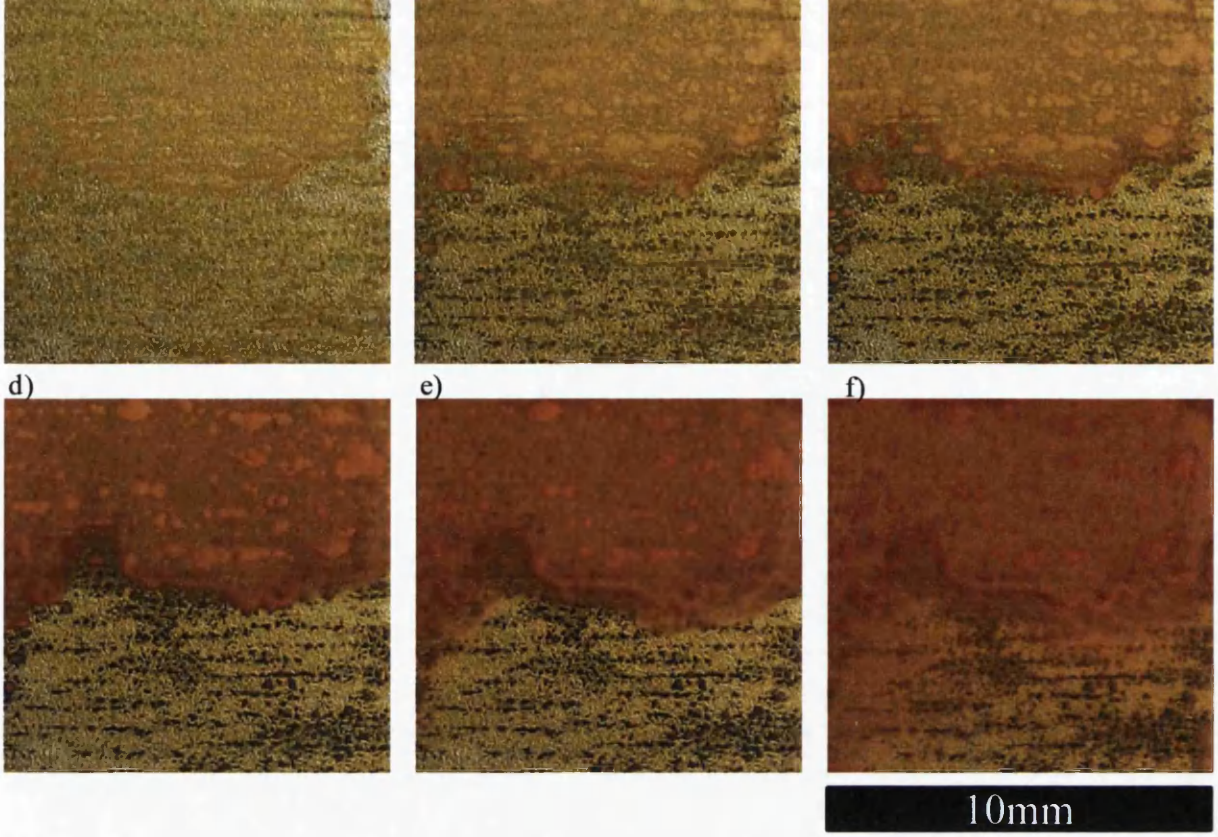

Fig 7.14 Photographic images of Sample 21 organically coated CR steel sample immersed in aerated 5% (w/v) NaCl (aq) at times a) 5 h, b) 8 h, c) 10 h, d) 20 h, e) 30 h and f) 40 h.

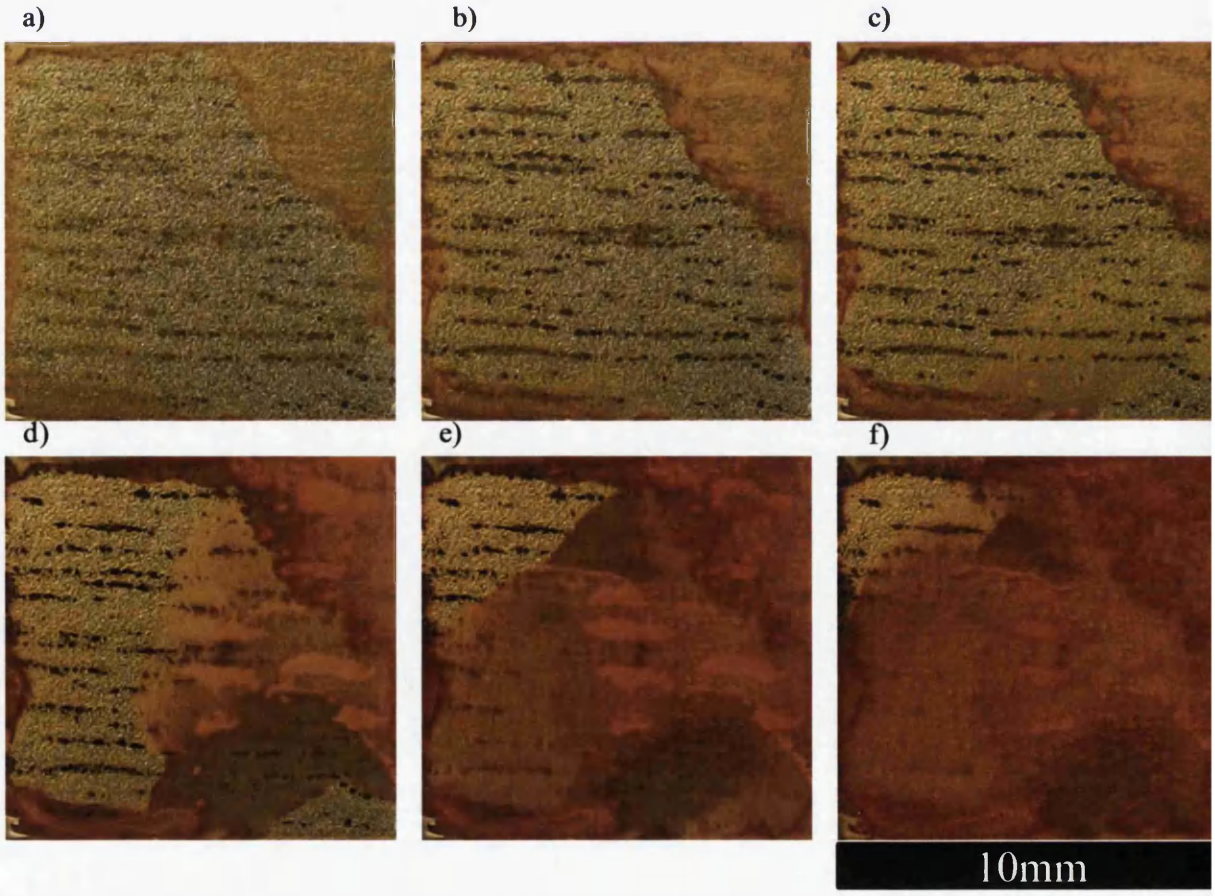

Fig 7.15 Photographic images of Sample 21 organically coated CR steel sample immersed in aerated 5% (w/v) NaCl (aq) at times a) 5 h, b) 8 h, c) 10 h, d) 20 h, e) 30 h and f) 40 h.

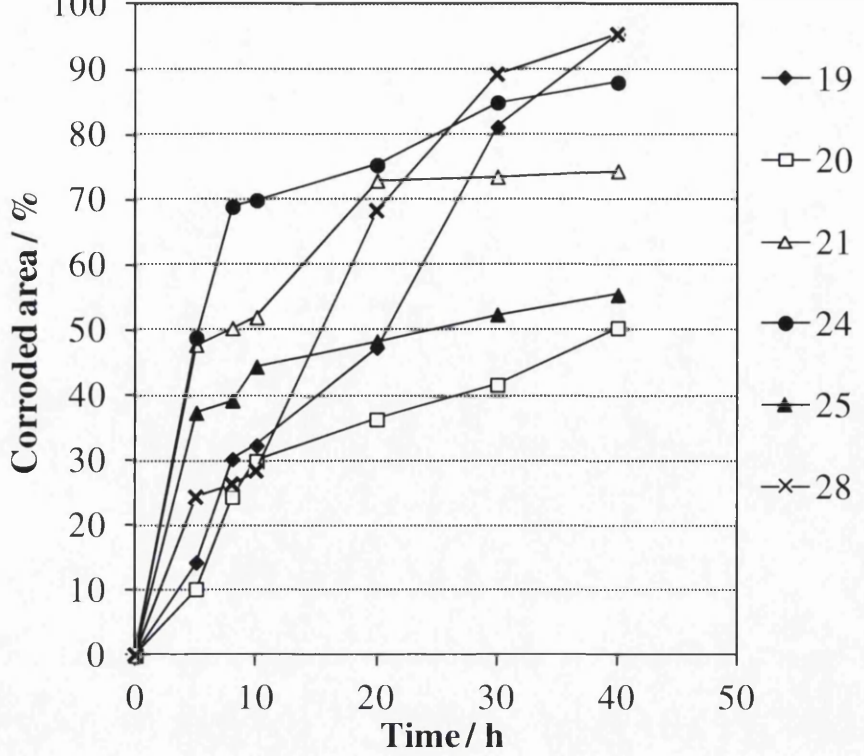

Fig 7.16 Corroded area (%) vs. time (h) plots for Samples 19, 20, 21, 24, 25 and 28 when fully immersed in 5% wt/v $NaCl_{(aq)}$ experimental electrolyte.

Table 7.3 Summary of performance ranking orders obtained from corroded area (%) vs. time data.

Sample	Initial corrosion rate (%corroded area / h)	Ranking	Final corroded area (%)	Ranking
19	2.9	2	95	6
20	2.0	1	50	1
21	9.6	5	74	3
24	9.8	6	88	4
25	7.5	4	55	2
28	4.9	3	95	5

7.3.2.2 Assessment of TOCs on CR steel using standard atmospheric corrosion testing

Atmospheric corrosion testing was carried out according to BS 3900 [1], this is fully described in section 2.4. All samples were tested in the same humidity chamber in duplicate. The total experimental testing time was two weeks. Figs 7.17 to 7.22 show photographic images for samples 19-28 after storage in a humidity chamber for a) 24 h and b) 2 weeks. The images have been evaluated according to ASTM D610-08 industry standards [2]. The results are recorded in Table 7.3. All samples display pinpoint rusting and, after two weeks testing, samples 20 and 25 can be graded 3-P and samples 19, 21, 24 and 28 are graded 2-P.

Fig 7.17 Photographic images of duplicate tests of Sample 19 held in a humidity chamber for a) 24 h and b) 2 weeks.

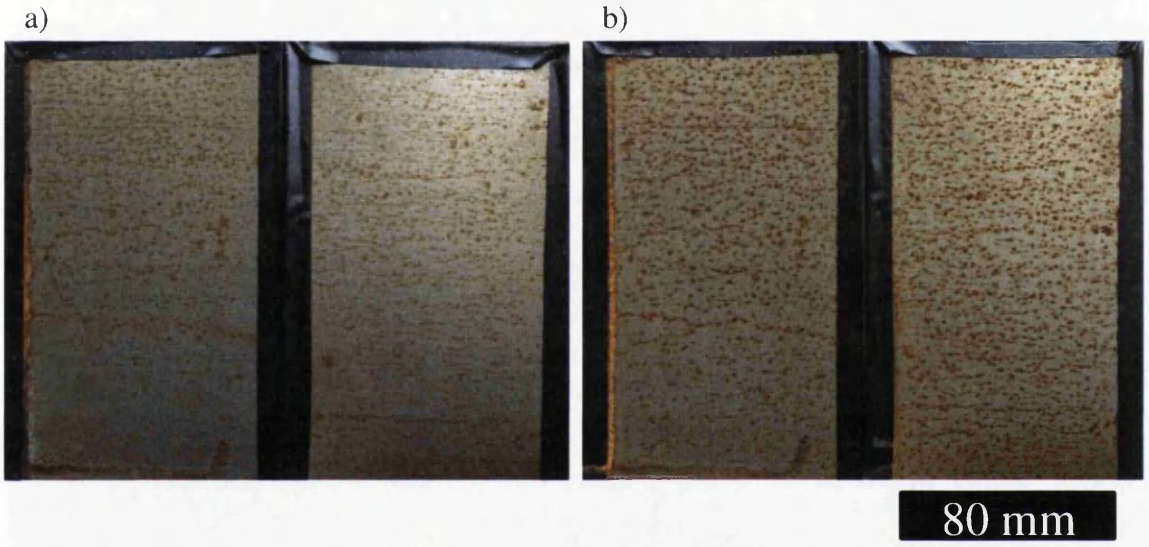

Fig 7.18 Photographic images of duplicate tests of Sample 20 held in a humidity chamber for a) 24 h and b) 2 weeks.

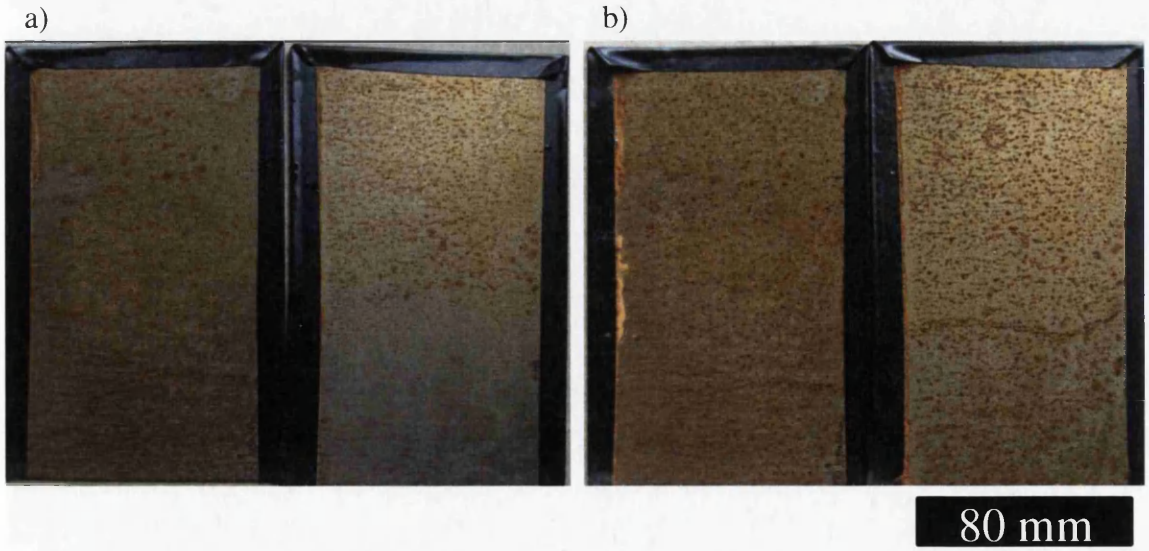

Fig 7.19 Photographic images of duplicate tests of Sample 21 held in a humidity chamber for a) 24 h and b) 2 weeks.

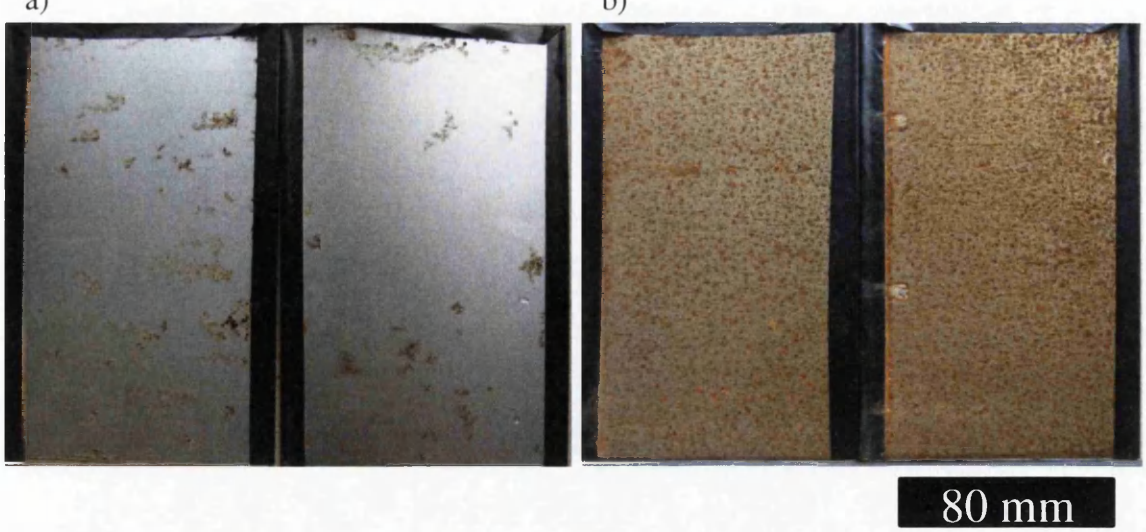

Fig 7.20 Photographic images of duplicate tests of Sample 24 held in a humidity chamber for a) 24 h and b) 2 weeks.

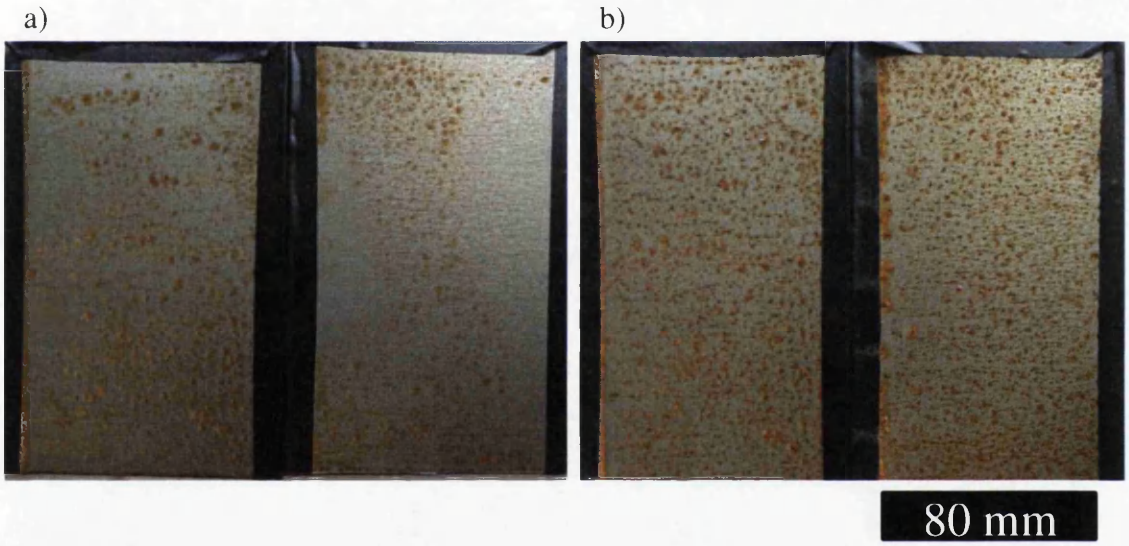

Fig 7.21 Photographic images of duplicate tests of Sample 25 held in a humidity chamber for a) 24 h and b) 2 weeks.

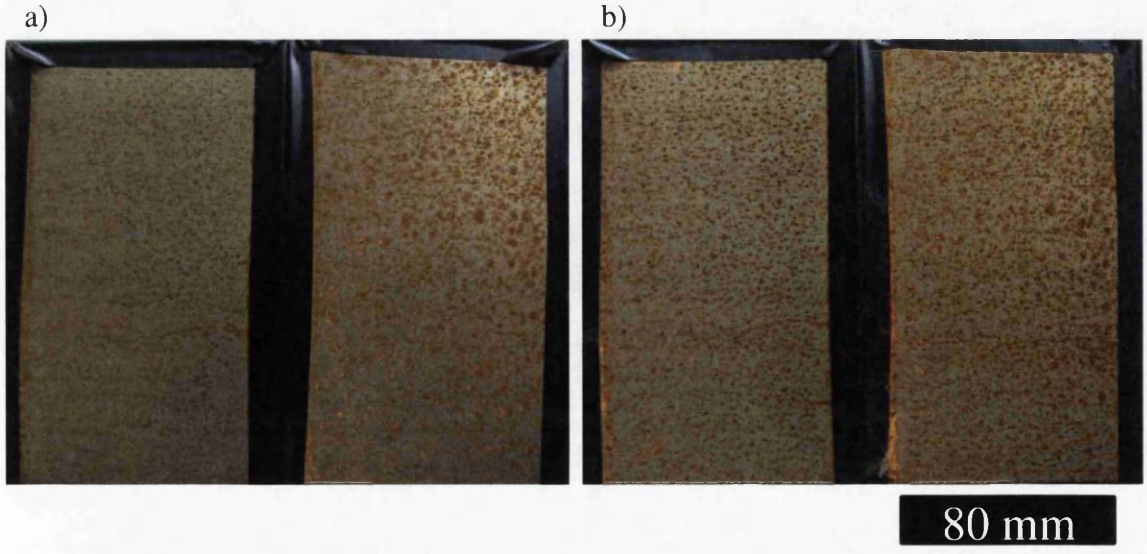

Fig 7.22 Photographic images of duplicate tests of Sample 28 held in a humidity chamber for a) 24 h and b) 2 weeks.

Table 7.3 Results of atmospheric corrosion tests for relevant samples evaluated according to ASTM standard D610 - 08

	24 h		120 h		1 week		2 weeks	
Sample	**% RR**	**Grade**	**% RR**	**Grade**	**% RR**	**Grade**	**% RR**	**Grade**
19	10-16	4/3-P	16	3-P	16-33	3/2-P	33	2-P
20	10	4-P	10	4-P	10	4-P	16	3-P
21	3	5-P	10	4-P	16	3-P	33	2-P
24	16	3-P	-	-	16-33	3/2-P	33	2-P
25	10-16	4/3-P	10-16	4/3-P	16	3-P	16	3-P
28	16-33	3/2-P	16-33	3/2-P	33	2-P	33	2-P

Atmospheric corrosion test analysis according to ASTM standard D610-08 places samples into a performance group; in this case either 2-P of 3-P. This means difficulties can arise when distinguishing between two particular samples. In this case the four worst performing samples were grouped together in 2-P. The time-lapse photography technique allows the exact corroded area (%) to be compared at any particular time and can be used to distinguish between every individual sample tested. As shown here, a ranking order between the six samples was established allowing the preferential parameters for coating application to be determined.

In both atmospheric corrosion testing and time-lapse photography testing, samples 20 and 25 had the highest performance-ranking showing that the results produced were wholly similar for both tests. Time-lapse photography technique testing can be carried out over a 24 h period which is a significant reduction in experimental time from two weeks. The data rendering involved with time-lapse photography is more time consuming than that of atmospheric corrosion testing due to an accurate measure of corrosion being established rather than grouping performance. However, the total time to carry out the experiment and data rendering is still substantially shorter than the 2 weeks required for industry standard atmospheric corrosion testing. Furthermore, a reduction in data rendering time can be realised by reducing the number of images analysed if required i.e. only photographs taken at 24 h immersion time could be analysed. It is suggested that the time-lapse photography technique could be used in conjunction with the industry standard atmospheric corrosion test where samples, such as the four poorest performers in the current study, are indistinguishable through when grouped as shown in the current study.

7.4 Conclusions

The validity of a time-lapse photography technique and in-situ scanning vibrating electrode technique (SVET), for corrosion testing of commercial TOCs applied to CR steel, has been assessed. Time-lapse photography technique was compared to both SVET and atmospheric corrosion testing using two different sets of samples. In all cases a ranking order, as far as possible, was established. When compared to both SVET and atmospheric corrosion tests, time-lapse photography results proved to be wholly similar. This suggests that, for the current application, viable data concerning the corrosion protection performance of TOCs applied to CR steel can be produced.

Firstly, an assessment of the coating quality at the strip edge was conducted for two separate coatings. Samples of each coating were selected for assessment where some samples were taken from the vicinity of the strip-edge and some were taken away from the strip-edge. Time-lapse photography and SVET were both employed to study corrosion during immersion in 5% wt/v $NaCl_{(aq)}$ electrolyte over a 24 h period. Both techniques showed wholly similar trends with regards to corrosion initiation when analysed qualitatively. Although time-lapse photography shows the location of corrosion product, the SVET can provide exact details of intensity and location of anodic activity occurring at a specified time. The quantitative results obtained from both techniques were in agreement that coating 1 performed better than coating 2.

Secondly, an assessment of the viability of time-lapse photography, to be used in conjunction with industry standard atmospheric corrosion testing of a commercial TOC applied CR steel, was carried out. Both testing techniques were employed to test a series of samples where a performance ranking order was established. The same coating was used on all six samples but the coating application processes were varied. Both tests indicated that Samples 20 and 25 performed the best with regards to corrosion protection. Both tests work on the same principal in that samples are held in corrosive conditions and periodically photographed to assess corrosion. Although the time-lapse photography technique is not a realistic test (i.e. the conditions samples are subject to do not reflect those of the natural environment in which an in-service TOC product would be used) the test conditions are constant amongst all samples to allow a comparison to be made. This also allows for alternative testing conditions to be applied i.e. a change in temperature or pH may be introduced in order to establish the corrosion

performance in such conditions. Where two samples produce a very similar corrosion performance re-testing in a lower salt concentration may be carried out to further distinguish between samples. Provided each sample is subjected to the same environment a comparison and, hence, a ranking order may be established. The major advantage of the time-lapse photography technique over atmospheric corrosion testing is the reduction in experimental time. It is suggested that the technique may be used alongside atmospheric corrosion testing in order to distinguish between those samples that fall into the same performance group.

It is suggested that, for time-lapse photography to be implemented into a research and development process, time-lapse photography could be used to test all samples to allow a faster throughput of data to provide short-term information whilst industry standard atmospheric corrosion tests are conducted. For in-situ SVET, although the typical experimental length of 24 h per sample is substantially shorter than the 2 – 4 weeks for industry standard tests, this represents an extensive time period if a large batch of samples were tested in duplicate. Therefore, the suggested use of the technique for industrial purposes would be to provide data for selected samples where information about specific features or verification of a corrosion mechanism was required.

7.5 References

[1] B. Standard, "Test for paints —," no. 1989.

[2] R. Coatings, "Standard Practice for Evaluating Degree of Rusting on Painted Steel Surfaces 1," 4–9, 2012.

Chapter Eight.

Conclusions and further work.

8.1 Conclusions

The current thesis presents an extensive study of the inhibitor phenyl phosphonic acid (H_2PP) with regards to the prevention of corrosion on industrially important materials hot dip galvanised (HDG) steel and iron, where the latter was used to represent cold reduced steel. The drive to expand the design of effective corrosion inhibitor systems for organic coatings applied to steel substrates derives from legislative pressure to replace traditional toxic inhibitors based on chromate. Phosphonates are well known anodic inhibitors and are also considered to be environmentally acceptable for use as inhibitors. H_2PP was selected for the current study as previous reports exhibit the inhibitors ability to strongly adsorb onto a surface oxide film; a benefit for corrosion inhibition as the incorporation of chloride ions becomes disfavoured.

The effectiveness of H_2PP as an in-coating inhibitor of delamination has been studied using a Scanning Kelvin probe (SKP) where the rate of delamination (k_{del}) was measured in comparison to an inhibitor-free coating. A standard experimental delamination cell set-up, was used and all coatings were made from a model coating polyvinyl butyral (PVB). It was found for both HDG steel and iron that, by systematically increasing the wt% of in-coating H_2PP additions, the delamination rate was progressively decreased. However, this reduction in k_{del} was found to be much more profound on HDG steel surfaces rather than iron surfaces where reductions of 97% and 55% were established respectively. In both cases the reduction in k_{del} is attributed to a metal/phenylphosphonate layer that forms on the metal surface during the initial casting of the PVB coating. This salt layer blocks the oxygen reduction reaction that occurs at the site of cathodic disbondment. This was determined by the delamination kinetics which transformed from parabolic for uninhibited coatings to linear for coatings containing H_2PP in all cases. It is suggested that the reason H_2PP is more effective on a HDG steel surface is due to the effect of the dissociation of H_2PP that results in an abundance of H^+ cations in the under-film region. This can act as a buffer to neutralise the alkaline-rendered underfilm region from the cathodic oxygen reduction reaction and reduces the rate at which previously base-catalysed polymer degradation, and hydrolysis of interfacial bonds, occurs. On a HDG steel surface, the underfilm pH has been measured at around pH 10-11 and so this buffering mechanism can potentially have a profound effect. Conversely, the underfilm conditions of a

coating delaminating from an iron surface tend to be much more alkaline and have been measured previously at pH 14. It is, therefore, suggested that the buffering effect is not as effective for iron substrates.

However, further studies were carried out into the effectiveness of H_2PP as an in-coating inhibitor for iron using a delamination cell set-up that represents a realistic scenario; that is less harsh than the previous experiments. As such a scribed defect is made to the coating and electrolyte is added and allowed to dry. A reduction of 98%, when compared to a control experiment, was observed where $\geq$ 5% H_2PP was added to the coating. Furthermore, where additions of 12% H_2PP were made to the PVB coating, a reduction in the filament propagation rate of filiform corrosion (FFC) filaments was observed. However, when added at values below 10%, in-coating H_2PP was found to enhance corrosion by creating an increase in filament initiation sites and an increase in filament propagation rate was observed.

H_2PP was also studied in immersion conditions where bare HDG steel substrates were placed in electrolyte containing various concentrations of the inhibitor. Localised corrosion activity occurring over a commercial grade HDG steel surface immersed in aqueous sodium chloride electrolyte was mapped using the in situ Scanning vibrating electrode technique (SVET). It was thus demonstrated using the SVET, and through a series of open circuit potential experiments, that systematically increasing the concentration of H_2PP made to the electrolyte progressively decreases the corrosive activity on the HDG steel surface. Furthermore, at a concentration of $5x10^{-2}$ mol^2dm^{-6}, H_2PP was shown to keep HDG steel free from white rust for a period of 24 h with an efficiency of 96%, measured using SVET-derived data. This was compared to a sodium phosphate (Na_3PO_4) inhibitor that was studied at the same concentration where an efficiency of 75% was measured using SVET-derived data. The results reported for this study reinforced a third suggested mechanism for the inhibition of underfilm cathodic delamination on HDG steel surfaces by H_2PP which was a leaching effect by which the anodic process occurring at the defect was inhibited, thus delaying the initiation and on-set of delamination. A further development of the study of the inhibitory effect of H_2PP presented here would be to extend this research to other metals of industrial interest, such as alloyed HDG steel.

Experiments to determine the influence of pH on inhibition by H_2PP at its optimum concentration showed that, in both acid (pH 2) and alkaline (pH 11.5) conditions, corrosion activity was present where additions of $5x10^{-2}$ mol^2dm^{-6} H_2PP were made. Anodic activity was shown to change from isolated and localised in neutral conditions to moveable when in alkali conditions and highly general when in acidic conditions.

A further study into inhibition of corrosion-driven cathodic delamination on HDG steel and iron surfaces explored the intrinsically conducting polymer (ICP) Poly(3,4-Ethylenedioxythiophene)-Poly(Styrene Sulphonate), also known as PEDOT:PSS. The results showed the failure of the PVB-PEDOT:PSS coating system where delamination was found to be accelerated when compared with control experiments. Such a result has been reported previously for ICPs and this was attributed to a fast reduction of the ICP, caused by fast mobility of cations in the network of the reduced polymer. This occurs due to macroscopic percolation networks. Although coatings based on ICPs may effectively inhibit corrosion in the presence of small defects, a coating breakdown is inevitable in the presence of large defects such as those employed for delamination experiments in this thesis. For PEDOT:PSS to provide effective inhibition of cathodic disbondment, it may need to be electrochemically reduced in a cation containing solution, such as cerium chloride, after casting on the relevant substrate. However, a PEDOT:PSS layer under a PVB coating was found to be highly effective for the inhibition of filiform corrosion (FFC) on coated iron surfaces.

Finally, a study into alternative industrial testing techniques was carried out. It was shown that a time-lapse photography immersion technique could produce reliable data for the corrosion resistance of thin organic coatings (TOCs) on CR steel in a much shorter time-scale than the industry standard atmospheric corrosion tests. It was also shown that the technique could provide further information with regards to corrosion initiation and coating failure. Furthermore, the in situ SVET was shown to provide further information, where experiments were again carried out on coated CR steel samples, with regards to corrosion activity. This provided further information where other techniques, using photographic imaging, could only measure the visible corrosion product.

8.2 Further work

In the previous Section various areas of further work have been highlighted. With regards to phenyl phosphonic acid (H_2PP), there is scope for further research into this inhibitor with regards to alternative industrially important substrates, such as alloyed HDG steels. Furthermore, research into the potential incorporation into water-based coating systems, such as those studied in Chapter 7 is suggested. This presents further problems, as the acidic nature of the inhibitor may not be compatible with a water-based resin. Further research into the use of PEDOT:PSS as an inhibitor of under-film cathodic delamination is suggested. The electrochemical reduction in a cation containing solution, such as cerium chloride, may be required for PEDOT:PSS to provide effective protection against coating delamination.